Dissertation

submitted to the

Combined Faculties of the Natural Sciences and Mathematics

of the Ruperto-Carola-University of Heidelberg, Germany

for the degree of

Doctor of Natural Sciences

Put forward by

M.Sc. Georg Schmid

born in Reutlingen

Oral examination: June 20, 2018

Two-Color Pump-Probe Experiments on Small Quantum Systems at the Free-Electron Laser in Hamburg

Referees: Priv.-Doz. Dr. Robert Moshammer

Prof. Dr. Andreas Wolf

Abstract - Within this thesis, the dynamical response of small quantum systems after the absorption of multiple extreme-ultraviolet (XUV) photons is studied via two-color pump-probe experiments at the free-electron laser (FEL) in Hamburg (FLASH) by employing many-particle recoil-ion momentum spectroscopy.
The multi-photon ionization of argon atoms is investigated at a photon energy of 27 eV and FEL intensities of $10^{13} - 10^{14}\,\mathrm{W/cm^2}$. The sequential ionization channel is found to dominate and intermediate resonances are revealed by a delayed infrared (IR) laser pulse.
Molecular hydrogen (H_2) is studied at a photon energy of 28.2 eV. Dissociation via excited states and fragmentation by sequential two-photon ionization are observed. In addition, it is shown how the ground-state dissociation of H_2^+ can be used as a tool to determine the temporal overlap between an XUV and IR laser pulse.
In the argon dimer, multiple interatomic relaxation processes are triggered by the absorption of several 27-eV-photons. Besides interatomic Coulombic decay (ICD), frustrated triple ionization and charge transfer at crossings of potential energy curves are observed. The lifetime of charge transfer is determined to be (531 ± 136) fs using an XUV-IR pump-probe scheme.
The employed reaction microscope is upgraded by an in-line XUV split-delay and focussing optics, which was designed and commissioned as part of this thesis.

Zusammenfassung - In dieser Arbeit wird die Dynamik kleiner Quantensysteme, welche durch die Absorption mehrerer extrem-ultravioletter (XUV) Photonen hervorgerufen wird, am Freie-Elektronen-Laser (FEL) in Hamburg (FLASH) untersucht. Dazu werden Pump-Probe Experimente mit Photonen zweier Farben und Mehrteilchen-Rückstoß-Ionen-Spektroskopie kombiniert.
Die Multiphotonenionisation von Argonatomen wird bei einer Photonenergie von 27 eV und FEL Intensitäten von $10^{13} - 10^{14}\,\mathrm{W/cm^2}$ untersucht. Dabei dominiert der sequentielle Ionisationskanal. Ein zeitlich verzögerter infraroter (IR) Laserpuls erlaubt zwischenliegende Resonanzen aufzudecken.
Untersuchungen an Wasserstoffmolekülen (H_2) werden bei einer Photonenenergie von 28.2 eV durchgeführt. Dabei wird Dissoziation mittels angeregter Zustände und Fragmentation durch sequentielle Zweiphotonenionisation beobachtet. Zudem wird gezeigt, dass die Grundzustandsdissoziation von H_2^+ verwendet werden kann, um den zeitlichen Überlapp zwischen XUV- und IR-Laserpulsen zu ermitteln.
In Argondimern werden unterschiedliche interatomare Relaxationsprozesse durch die Absorption mehrerer 27-eV-Photonen ausgelöst. Neben *Interatomic Coulombic Decay* (ICD) sind frustrierte Dreifachionisation und Ladungstransfer an Schnittpunkten von Potentialkurven wichtige Kanäle. Die Lebensdauer des Ladungstransfers von (531 ± 136) fs wird mit einem XUV-IR Pump-Probe Schema bestimmt.
In einem weiteren Teil dieser Arbeit wurde das verwendete Reaktionsmikroskop um einen Aufbau zur Spaltung, Verzögerung und Fokussierung von XUV-Pulsen verbessert.

Contents

1 Introduction

The formation and breakup of a molecule can be described as the time-dependent evolution of a few-body quantum system. Knowing the initial and final states of such reactions gives information about the type of reaction products and the branching ratios between specific channels. However, to extract information on intermediate states along the reaction path, the temporal and structural evolution of the system needs to be explored on its natural time and length scales: femtoseconds[1] and Ångströms[2]. In a quantum-mechanical treatment, molecular dynamics is commonly described within the Born-Oppenheimer approximation [23], which is based on the decoupling of electronic and nuclear motion. This approach is appropriate because the electrons' mass is much lighter (factor ~ 1800) compared to the nuclei. Hence, the electrons move in quasi-static potentials of the nuclei and the potential energy of the molecule is represented by so-called potential energy surfaces. In case of diatomic molecules, these reduce to one-dimensional potential energy curves (PECs), which depend only on the internuclear separation. The nuclear dynamics within the molecule is then described by wave packets, which are propagating on the PECs.
A wide-spread method to access real-time molecular dynamics is so-called pump-probe spectroscopy [291]. It employs ultrashort laser pulses to reach femtosecond temporal resolution and thus allows to trace, e.g., molecular vibrations and dissociation dynamics, which typically take place within tens to hundreds of femtoseconds. Pump-probe spectroscopy in terms of PECs can be described as follows (see also Fig. 1.1): a pump pulse excites a nuclear wave packet on a PEC. Then, the wave packet evolves freely in time. After a time-delay, the probe pulse promotes the wave packet onto a repulsive Coulomb curve. Consequently, the molecule fragments and the charged particles and corresponding kinetic energies can be measured. Via this so-called Coulomb-explosion imaging (CEI), the geometry of the molecule at the moment of the fragmentation, i.e, the action of the probe pulse, can be deduced [203]. By adjusting the relative arrival time between pump and probe pulse, the temporal evolution of the system can be recorded frame by frame.
The first ground-breaking pump-probe experiments on molecular dynamics in the 1980s are directly connected to the availability of femtosecond laser pulses and constitute the research field of laser femtochemistry [290]. By employing the technique of mode-locking [70, 76], Titanium:Sapphire[3] lasers operating in the infrared (IR)

[1] 1 femtosecond $\hat{=} 10^{-15}$ s.
[2] 1 Ångström $\hat{=} 10^{-10}$ m.
[3] Wavelength 800 nm, photon energy 1.55 eV.

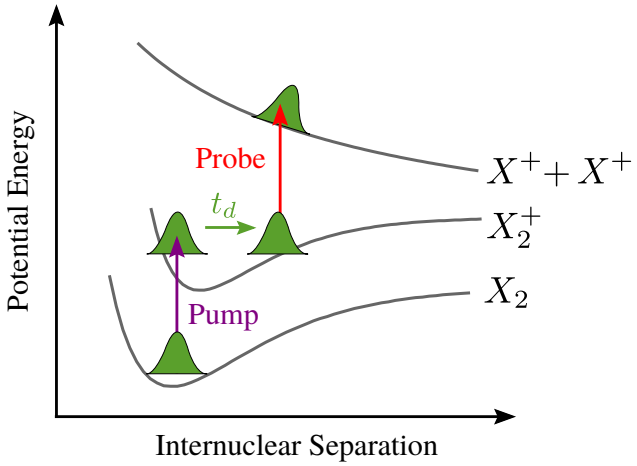

Figure 1.1: Illustration of pump-probe spectroscopy on the model diatomic molecule X_2 in terms of potential energy curves (PECs). The pump pulse (purple) ionizes the molecule and thereby launches a nuclear wave packet on the PEC of the bound ionic X_2^+ state. After a time delay t_d, the temporal evolution is probed by the second pulse (red). It promotes the wave packet onto a repulsive PEC and the molecule undergoes a Coulomb explosion into $X^+ + X^+$ fragments.

regime deliver pulses with femtosecond durations and became the work horses of time-resolved studies on ultrafast quantum dynamics. Using such laser pulses in an IR-IR pump-probe scheme, the dissociation of H_2^+ and D_2^+, i.e., the break-up of the most simple chemical bond, was traced on its natural time-scale of some tens of femtoseconds [54, 66]. Succeeding studies observed oscillation of vibrational wave packets in the cations of several diatomic molecules [43], isomerization of acetylene dications [161] and the break-up of a chemical bond [6] in real-time.
The aforementioned experiments are performed by ionizing the molecule in the pump and probe step. The ionization by IR lasers, however, occurs by the simultaneous absorption of multiple photons, which requires intense pulses. The corresponding induced electric fields are so strong that they modify the system and the dynamics of the studied process is disturbed by the measurement itself.
The restraints of ionization with IR lasers are overcome by using photons of higher energy, such as extreme ultraviolet (XUV) radiation. In this case, photoionization is caused by the absorption of single- and few-photons and can be described within a perturbative approach. In the last decades, two radiation sources have been developed and now provide short XUV pulses with laser properties: High harmonic generation (HHG) [166, 197] and free-electron lasers (FELs) [22, 200].
HHG allows to generate pulses in the XUV and soft X-ray energy range with durations below 100 attoseconds [83, 293]. Due to the generation processes, the higher harmonic pulses are intrinsically synchronized to the fundamental pulses of the driving laser, which results in the outstanding temporal resolution of XUV-IR pump-probe experiments based on HHG. This way, for example attosecond time delays

in atomic photoionization were measured by streaking [243] and interferometric techniques [134].
Although pioneering experiments were conducted [97, 267], the highest intensities of $\sim 10^{13}\,\mathrm{W/cm^2}$ [160, 223] reported for HHG-sources are nowadays not routinely available. This excludes these sources from inducing non-linear processes and thus from performing XUV pump-probe experiments on a daily basis [34].
In contrast, FELs are able to produce pulses with photon energies ranging from the XUV to the hard X-ray regime with peak intensities of $10^{16}\,\mathrm{W/cm^2}$ [5, 52, 58, 115]. This is about eight orders of magnitude higher than modern synchrotron sources [2]. Pulse durations of few tens of femtoseconds and a high degree of spatial and temporal coherence are properties of FEL radiation, which are only known from optical lasers. This makes FELs unique light sources to study non-linear light-matter interactions in an unexplored regime.
In particular, the research field of structural biology is strongly affected by the advent of FELs as they inspired the vision to image single biomolecules [190]. X-ray scattering is sensitive to the electronic density and thus to the structure of the molecule with atomic resolution, which is crucial to draw conclusions on the exact functionality of molecular complexes. In so-called single-particle imaging (SPI), a particle is illuminated by billions of photons at a time. The entirety of diffraction images recorded for different spatial orientations enables to reconstruct the three dimensional structure of the particle. SPI allows to use samples in their natural liquid environment. Hence, it tremendously expands the variety of possible samples by avoiding the so far existing problem that only large crystalline samples could be investigated using synchrotron radiation. The imaging of small crystalline samples (nano crystals) with intense femtosecond FEL X-ray pulses has already been accomplished [36, 261]. Recent examples are the structure determination of an enzyme [136] and investigations on the photosystem II [139].
A main prerequisite to obtain an in-situ image of the molecule is the so-called "diffract before destroy" principle. It refers to the problem of sample disintegration following the massive energy input by the absorption of many photons. The basic questions are how fast do the structural changes occur and whether the exposure time, i.e., the FEL pulse duration, is short enough to image an unperturbed molecule. To answer these questions, basic studies on energy and charge redistribution after the absorption of multiple high-energetic photons [56, 57, 238] are important from a fundamental perspective, but also of practical use to develop accurate models that account for radiation damage in SPI.
To this end, fundamental ionization, energy-redistribution and charge-transfer processes occurring in small quantum systems upon the absorption of multiple XUV photons are studied within this thesis. In order to distinguish specific mechanisms, the complexity of the system under investigation is successively increased: from atoms over diatomic molecules up to dimers. An XUV-pump IR-probe scheme is applied to follow the response of the systems in time. The XUV pulse causes a neg-

ligible perturbation in the pump step. Thus, the atomic and molecular excitations can be described within a perturbative picture and by the Franck-Condon principle. The synchronized IR laser pulse is especially sensitive to probe highly excited electronic states, which are hard to ionize by XUV photons.

In a first experiment, the multiple ionization of an atom upon the absorption of several XUV photons is investigated. Generally, one distinguishes two multi-photon ionization mechanisms. The sequential channel is understood as step-by-step single-photon absorptions via stationary intermediate ionic states, whereas the non-sequential channel is described by direct ionization through virtual intermediate states. In earlier studies, it was found that non-sequential ionization is dominant for low intensities ($I \lesssim 10^{12}\,\mathrm{W/cm^2}$) [120, 186] and the sequential channel takes over for higher intensities [188, 275]. It has also been shown that intermediate resonances need to be taken into account to describe the ionization pathway and the yields of distinct ion charge states [77, 106, 182].
The goal of the present study is to identify the multi-photon ionization mechanisms in atomic argon at a photon energy of 27 eV and intensities of $10^{13} - 10^{14}\,\mathrm{W/cm^2}$. Furthermore, it especially aims to reveal and understand the role of resonant states along the ionization pathway. Therefore, excited Ar^{+*} states just below the Ar^{2+} ionization threshold are prepared by resonant XUV absorption. By employing a delayed IR laser pulse, the excitation of these states is probed. The impact of this manipulation on the further ionization cascade is studied for different IR intensities and as a function of FEL intensity and pump-probe delay.

The second study presented in this thesis investigates XUV-induced dissociation and fragmentation of H_2, i.e., the smallest diatomic molecule. Despite its simple composition, H_2 is intensively studied as it serves as a model system to test fundamental properties of quantum mechanics and to benchmark state-of-the-art calculations. Experiments using XUV synchrotron radiation mostly looked into the dissociation dynamics of H_2^+ [116, 148, 159, 228, 279]. A different type of experiments uses strong femtosecond optical laser pulses and HHG-IR pump-probe schemes to study the dissociation and wave-packet dynamics of H_2^+ [53, 54, 65, 66, 206]. However, only few experiments on H_2 exploiting FEL radiation are reported in literature. The two-photon double-ionization of the deuterium molecule (D_2) was studied at 38 eV [123] and an XUV pump-probe experiment at the same photon energy mapped the nuclear wave-packet motion in D_2^+ [121].
Here, H_2 is studied at a photon energy of $\hbar\omega = 28.2\,\mathrm{eV}$ and intensities of about $10^{13}\,\mathrm{W/cm^2}$ in order to reveal and understand dissociation and fragmentation channels, which are present after one- as well as two-photon absorption. Furthermore, it is shown how the ground-state dissociation of H_2^+ can be exploited as an intrinsic tool to determine the temporal overlap between XUV and IR laser pulses. The scheme is general and suitable for any gas-phase XUV-pump IR-probe experiment

in the photon energy range $20 - 30\,\mathrm{eV}$ where commonly applied schemes like the fragmentation of nitrogen or oxygen cannot be used [270].

In the third experiment, interatomic relaxation processes are investigated in a weakly bound system: the argon dimer (Ar_2). An isolated excited atom usually relaxes to its ground state by emitting photons (fluorescence) or, if energetically possible, by the ejection of electrons (Auger decay [4, 168]). If, however, another atom is placed in the vicinity of the excited atom, it may relax by transferring its excess energy via a virtual photon to the neighbor. In 1997, Cederbaum *et al.* were the first to theoretically describe a new interatomic relaxation: Interatomic Coulombic Decay (ICD) [31]. Since then, ICD and related phenomena, like electron transfer mediated decay (ETMD) [72, 227, 297] and radiative charge transfer (RCT) [125, 225], were studied extensively from a theoretical [12, 230] as well as experimental perspective [119, 156, 237]. Making the step from pure understanding to application, ICD is nowadays proposed for cancer treatment in radiation biology [81]. In this scenario, the slow electrons accompanying ICD destroy the malign tissue by breaking DNA strands [24]. It was shown that ICD-type processes are omnipresent in weakly bound systems [101]. In this respect, Van-der-Waals clusters and dimers are perfect model systems to study such processes because they are bound by polarization forces at a larger internuclear distances compared to covalently bound molecules [196].
A large amount of studies is reported for Ar_2. In particular, ICD, ETMD and RCT are observed [133, 143, 184, 212, 213, 216, 225, 268, 286] and investigated by theory [178, 258]. In most of these studies, the argon dimer is excited by creating an inner-shell vacancy. Following Auger decay, a large variety of dimer states is populated. Consequently, many different intra-/interatomic relaxation pathways are enabled. In an experiment, it is often challenging to disentangle the different pathways. A more comprehensive approach, however, is to excite specific dimer states via direct dipole-transitions. By absorption of few high-energetic photons, distinct dimer states can be directly excited.
Within this thesis, the relaxation and fragmentation dynamics of argon dimers upon absorption of few photons of $27\,\mathrm{eV}$ is studied. The number of excited states is controlled by the number of absorbed photons by tuning the FEL intensity. Besides direct fragmentation and ICD, also other types of relaxation mechanisms are observed. At the crossing point of PECs, charge is transferred by the exchange of an electron. As this requires a strong overlap of electronic wave functions, nuclear motion prior to the transfer is essential. The charge transfer lifetime could be determined by an XUV-pump IR-probe experiment. The experimental results are compared to a classical simulation and to calculations based on Landau-Zener probabilities, The XUV-IR scheme is also applied to probe the fragmentation channel of so-called frustrated triple ionization. Beyond that, the fragmentation of dimers with sum charges up to 6+ is observed and compared to a Coulomb model.

All three experiments employ a reaction microscope (REMI) to detect the ionic fragments [270]. While the first experiment on atomic argon exploits the ion charge-state sensitivity of this instrument, the two other experiments are based on recoil-ion momentum spectroscopy. For this purpose, the initial ion momenta are measured and by employing momentum conservation, ionic fragments originating from the same molecule can be unambiguously assigned. This way, different fragmentation channels can be identified by their kinetic energy release.

While nuclear motion is encoded in the ionic fragments, the ejected electrons are sensitive to the electronic structure of the system under investigation. Thus, only the coincident detection of electrons and ions yields a kinematically complete and state-sensitive picture of the reaction. Although a REMI is capable of measuring electron-ion coincidences, so far the two-photon double-ionization of neon [141] was the only kinematically complete experiment employing a REMI at an FEL. On the one hand, the neon experiment is a static measurement and temporal information in terms of pump-probe spectroscopy could not be extracted. On the other hand, all time-resolved REMI studies at high FEL intensities [121, 124, 237, 238], i.e., beyond single-photon absorption, failed in measuring electrons in coincidence with ions. It turned out that stray light from undirected scattered photons and background from ionization of residual gas particles are the main sources preventing a detection of electron-ion coincidences. To address these problems and to overcome conceptual drawbacks of an existing setup, a new XUV split-delay and focussing optical setup has been developed in the framework of this thesis. It is integrated into the REMI endstation at the free-electron laser FLASH2 in Hamburg. Here, results from commissioning experiments show the working capacity in terms of small foci, stray light reduction, electron-ion coincidences and delay-dependent ion spectra.

This thesis is structured as follows. Ch. 2 provides the theoretical background to discuss the experimental results. The basic concept of photoionization of atoms is introduced and the built-up of many-electron atoms is discussed. The structure of diatomic molecules is presented and special emphasize is put on the Born-Oppenheimer approximation, which allows to describe nuclear dynamics on PECs. Interatomic relaxation mechanisms relevant for the argon dimer are summarized, before the formalism of Landau-Zener transitions is introduced. Ch. 3 contains relevant informations on FELs in terms of functionality and radiation properties. Ch. 4 is dedicated to explain the working principle and main components of a REMI. Furthermore, challenges of operating a REMI at an FEL are pointed out. The setup of the XUV-IR experiments is described in Ch. 5, before the results of the experiments on Ar, H_2 and Ar_2 are discussed in Ch. 6, 7 and 8, respectively. The design and commissioning results of the new XUV split-delay optics are presented in Ch. 9. The thesis closes with conclusive remarks and an outlook given in Ch. 10.

2 Theory

2.1 Interaction of Photons with Atoms

Generally in physics, the coupling between leptonic elementary particles is enabled by gauge bosons. Concerning the electromagnetic interaction, the photon is the gauge boson which couples to leptons. In this regard, the interaction of a single photon with a bound electron is the most fundamental light-atom interaction. If the energy of the incoming photon $\hbar\omega$ equals the energy difference $E_f - E_i$ between two bound atomic states i and f, and if the transition is allowed by selection rules, the electron is excited from one bound state to another. However, if the energy of the photon $\hbar\omega$ is higher than the binding energy E_b of an electron, the electron is released with an excess of kinetic energy $E_{\text{kin}} = \hbar\omega - E_b$ into the continuum and the atom is left as a charged ion. In 1905, Albert Einstein was the first to describe this radiative ionization in a quantum mechanical context and the phenomenon became prominent as the photoeletric effect [51].
Noble gases have a closed valence shell and show the highest binding energies compared to the other elements of their period. Among all noble gases, the $1s$ electron of helium has the largest binding energy of $E_b = 24.6\,\text{eV}$. This implies that photons with energies of few tens of eV are needed in order to ionize the valence electrons of all known elements by a single photon [221]. This photon energies correspond to extreme-ultraviolet (XUV) radiation[4], which is nowadays routinely delivered by accelerator-based light sources like synchrotrons or free-electron lasers (FELs) (see Ch. 3), or by high-harmonic generation (HHG) in the lab [25].
Different to the kinetic energy of the ejected electron, the calculation of transition and ionization cross sections, i.e., the probabilities of bound-bound and bound-continuum transitions, is not that straightforward. A common theoretical concept to compute transition rates is given within the framework of time-dependent perturbation theory. A perturbative approach, however, is only applicable, if the external perturbation is weak.
The mean quiver energy of a free electron in an electric light field, the so-called ponderomotive potential U_p, is proportional to $U_p \propto I\lambda^2 \propto I/(\hbar\omega)^2$, with I being the light intensity (see Sec. 2.1.2). As an example, one may consider a helium atom with a binding energy of $E_b = 24.6\,\text{eV}$ [137], a photon energy of $\hbar\omega = 62\,\text{eV}$ and a light intensity of $I = 10^{16}\,\text{W/cm}^2$ which is reached at FELs (see Sec. 3.5). Here, the

[4] $\hbar\omega_{\text{XUV}} = 10 - 124\,\text{eV}$, $\lambda_{\text{XUV}} = 10 - 121\,\text{nm}$ [265].

external perturbation $U_p = 0.37\,\mathrm{eV}$ is much smaller compared to the binding energy E_b. Thus, for XUV photons, a perturbative approach is usable.
In the following, time-dependent perturbation theory is applied to describe single- and two-photon absorption of an atom. For reasons of completeness and to point out conceptional differences, the formalism of strong field ionization is briefly presented in Sec. 2.1.2.

2.1.1 Single- and Two-Photon Absorption

The following derivations are done in a non-relativistic approximation up to second order perturbation theory for hydrogen-like ions, i.e., one electron and one nucleus. The mathematical formalism can be extended to multi-photon processes, many-electron atoms (see Sec. 2.2) or relativistic systems [19, 84]. The theory is developed for bound-bound transitions between discrete electronic states, but can also be expanded to describe bound-continuum transitions, i.e., photoionization processes. If not otherwise stated, atomic units (see Appendix A) are used in the following derivations which are compiled from Ref. [234], Ref. [236, Ch. 2.1] and Ref. [26, Ch. 4].
The perturbative approach treats the action of the vector potential of an electromagnetic plane wave of amplitude A_0, polarization vector ϵ, wave vector $\mathbf{k}$ and frequency ω,

$$\mathbf{A}(\mathbf{r},t) = A_0\epsilon\left(e^{\mathrm{i}(\mathbf{kr}-\omega t)} + e^{-\mathrm{i}(\mathbf{kr}-\omega t)}\right), \tag{2.1}$$

as a weak external time-dependent perturbation $\hat{H}_{\mathrm{ex}}(t) = \mathbf{p}\cdot\mathbf{A}(\mathbf{r},t)$ ($\mathbf{p}$ is the momentum operator) of the stationary atomic single-electron Hamiltonian

$$\hat{H}_0 = -\frac{1}{2}\nabla^2 - \frac{Z}{\mathbf{r}} \tag{2.2}$$

with the nabla operator ∇ and the Coulomb potential $-Z/\mathbf{r}$. The time-dependent Schrödinger equation reads:

$$\mathrm{i}\frac{\partial}{\partial t}\Psi(\mathbf{r},t) = \left(\hat{H}_0 + \alpha\hat{H}_{\mathrm{ex}}(t)\right)\Psi(\mathbf{r},t). \tag{2.3}$$

Here, the wavefunction $\Psi(\mathbf{r},t)$ is the general solution and α the perturbation parameter. It is assumed that the eigenstates $\psi_k(\mathbf{r})$ of the unperturbed Hamiltonian $\hat{H}_0$ are known and form a complete orthonormal basis set:

$$\hat{H}_0\psi_k(\mathbf{r}) = E_k\psi_k(\mathbf{r}). \tag{2.4}$$

Therefore, any time-dependent solution $\Psi(\mathbf{r},t)$ of the system can be expanded using this spectral basis:

$$\Psi(\mathbf{r},t) = \sum_k c_k(t)e^{-\mathrm{i}E_k t}\psi_k(\mathbf{r}). \tag{2.5}$$

The task is to find the expansion coefficients $c_k(t)$. By inserting Eq. 2.5 into Eq. 2.3, one ends up with a system of coupled differential equations:

$$\mathrm{i}\frac{\partial c_f(t)}{\partial t} = \sum_k \alpha c_k(t) \left\langle \psi_f \left| \hat{H}_{\mathrm{ex}}(t) \right| \psi_k \right\rangle e^{\mathrm{i}(E_f - E_k)t}. \tag{2.6}$$

In Eq. 2.6, the matrix element $\left\langle \psi_f \left| \hat{H}_{\mathrm{ex}}(t) \right| \psi_k \right\rangle$ is the transition amplitude from state ψ_k to ψ_f. To solve Eq. 2.6, one uses the perturbation approach, namely that the perturbation $\alpha\hat{H}_{\mathrm{ex}}(t)$ is weak and the coefficients $c_k(t)$ can be expanded in α:

$$c_k(t) = \alpha^0 c_k^{(0)}(t) + \alpha^1 c_k^{(1)}(t) + \alpha^2 c_k^{(2)}(t) + ... \tag{2.7}$$

This allows to solve the system of coupled differential equations (Eq. 2.6) iteratively by substituting the expansion series of Eq. 2.7 and integrating over time.
In Eq. 2.7, the element of n-th order is interpreted as the n-fold interaction of the perturbation with the unperturbed system, i.e., the number of exchanged photons. The element of zero-order corresponds to the case of no photon exchange and the expansion coefficient $c_f^{(0)}(0)$ is a constant. The second term of Eq. 2.7 accounts for transitions with exchange of one photon. The third term represents the interaction of two photons, i.e., two-photon absorption or two-photon emission.
If one considers a transition between an explicit initial state ψ_i to a final state ψ_f, the expansion coefficients $c_f^{(1)}(t)$ and $c_f^{(2)}(t)$ are expressed like:

$$c_f^{(1)}(t) = \frac{1}{\mathrm{i}} \int_0^t \mathrm{d}t' \left\langle \psi_f \left| \hat{H}_{\mathrm{ex}}(t') \right| \psi_i \right\rangle e^{\mathrm{i}(E_f - E_i)t'}, \tag{2.8}$$

$$c_f^{(2)}(t) = \left(\frac{1}{\mathrm{i}}\right)^2 \sum_k \int_0^t \mathrm{d}t' \int_0^{t'} \mathrm{d}t'' \left\langle \psi_f \left| \hat{H}_{\mathrm{ex}}(t') \right| \psi_k \right\rangle \left\langle \psi_k \left| \hat{H}_{\mathrm{ex}}(t'') \right| \psi_i \right\rangle \times e^{\mathrm{i}(E_f - E_k)t'} e^{\mathrm{i}(E_k - E_i)t''}. \tag{2.9}$$

In case of two-photon exchange (Eq. 2.9), one has to sum over k in order to account for intermediate transition states [82].
Moreover, by inserting the perturbation Hamiltonian $\hat{H}_{\mathrm{ex}}(t) = \mathbf{p} \cdot \mathbf{A}$ with the definition of the plane electromagnetic wave $\mathbf{A}(\mathbf{r}, t)$ (see Eq. 2.1), one obtains for photoabsorption[5] $E_f = E_i + \omega$:

$$1.\,\mathrm{order} : c_f^{(1)}(t) = \frac{A_0}{\mathrm{i}} \left\langle \psi_f \left| \mathbf{p} \cdot \epsilon\, e^{\mathrm{i}\mathbf{kr}} \right| \psi_i \right\rangle \int_0^t \mathrm{d}t' e^{\mathrm{i}(E_f - E_i - \omega)t'}, \tag{2.10}$$

[5]For photoemission $E_f = E_i - \omega$ and the following derivations are analogous.

$$2.\,\text{order} : c_f^{(2)}(t) = \left(\frac{A_0}{\mathrm{i}}\right)^2 \sum_k \left\langle \psi_f \left| \mathbf{p}\cdot\epsilon\, e^{\mathrm{i}\mathbf{kr}} \right| \psi_k \right\rangle \left\langle \psi_k \left| \mathbf{p}\cdot\epsilon\, e^{\mathrm{i}\mathbf{kr}} \right| \psi_i \right\rangle \times \int_0^t \mathrm{d}t' \int_0^{t'} \mathrm{d}t'' e^{\mathrm{i}(E_f - E_k - \omega)t'} e^{\mathrm{i}(E_k - E_i - \omega)t''}. \tag{2.11}$$

Generally, the absolute square of the expansion coefficients $c_f^{(n)}(t)$ denotes the probability $P_{if}^{(n)}(t)$ to find the system, which was at time $t' = 0$ initially in state ψ_i, at a time $t' = t$ in state ψ_f:

$$P_{if}^{(n)}(t) = \left| c_f^{(n)}(t) \right|^2. \tag{2.12}$$

Furthermore, the transition rate from state ψ_i to state ψ_f after a time interval T is given by

$$R_{if}^{(n)} = \frac{P_{if}^{(n)}(T)}{T}. \tag{2.13}$$

For first and second order, using Eq. 2.10 and 2.11 with Eq. 2.13, this results in the following proportionalities of the transition rates [236, Ch. 2.1.1]:

$$R_{if}^{(1)} \propto I \left| \left\langle \psi_f \left| \mathbf{p}\cdot\epsilon\, e^{\mathrm{i}\mathbf{kr}} \right| \psi_i \right\rangle \right|^2 \delta(E_f - E_i - \omega), \tag{2.14}$$

$$R_{if}^{(2)} \propto I^2 \left| \sum_k \frac{\left\langle \psi_f \left| \mathbf{p}\cdot\epsilon\, e^{\mathrm{i}\mathbf{kr}} \right| \psi_k \right\rangle \left\langle \psi_k \left| \mathbf{p}\cdot\epsilon\, e^{\mathrm{i}\mathbf{kr}} \right| \psi_i \right\rangle}{E_k - E_i - \omega} \right|^2 \delta(E_f - E_i - 2\omega). \tag{2.15}$$

The δ-functions follow from the integration over time of Eq. 2.10 and 2.11. The light intensity is denoted by I.
Considering Eq. 2.14 and 2.15, one sees that the transition rates for the interaction of photons with an atom can be traced back to the evaluation of matrix elements. For an one-photon transition, the matrix element can be calculated straightforward. For the two-photon case, one has to sum over the intermediate states k, which makes the evaluation more demanding. A common approach to account for the summation over k is to use the Green's function formalism [84, Ch. 3.6]. Please note that the intermediate states k are virtual states and therefore not necessarily eigenstates of the atom.
Up to now, only transitions from an initial bound state ψ_i to a bound final state ψ_f are considered. For photoionization, i.e., bound-continuum transitions, the computational task is more challenging, because one additionally has to sum over infinitely many final continuum states.

Beyond that, the dependence of the transition rate on the light intensity (see Eqs. 2.14 and 2.15), can be generalized by accounting for higher expansion orders of Eq. 2.7 [207]:

$$R_{if}^{(n)} \propto I^n. \tag{2.16}$$

Here, n is the number of absorbed photons.

Dipole Approximation and Electron Angular Distribution

The transition matrix element $M_{if} = \langle \psi_f \left| \mathbf{p} \cdot \epsilon \; e^{\mathbf{ikr}} \right| \psi_i \rangle$ can be evaluated by means of a multipole expansion of the electromagnetic plane wave:

$$e^{\mathbf{ikr}} = 1 + \mathrm{i}\mathbf{kr} + \frac{1}{2}(\mathrm{i}\mathbf{kr})^2 + ... \tag{2.17}$$

In the non-relativistic case and if the wavelength of the electromagnetic wave is large compared to the dimensions of the atom, $\mathbf{kr} \ll 1$ with $|\mathbf{k}| = 2\pi/\lambda$, the so-called dipole approximation considers only the first expansion term of Eq. 2.17 and the transition matrix element reduces to [26, Ch. 4.1]:

$$M_{if} \approx \langle \psi_f \left| \mathbf{p} \cdot \epsilon \right| \psi_i \rangle \, . \tag{2.18}$$

The dipole approximation $\mathbf{kr} \ll 1$ breaks down for relativistic systems like highly-charged ions and higher terms in the multipole expansion (see Eq. 2.17) need to be taken into account. This leads to higher multipole transitions [26, Ch. 4.5].
For one-photon ionization and within the dipole approximation, the angular distribution of emitted photoelectrons is given by [15, Ch. 1]:

$$\frac{\mathrm{d}\sigma}{\mathrm{d}\Omega}(\hbar\omega, \theta) = \frac{\sigma}{4\pi} \left[1 + \beta_2(\hbar\omega) P_2(\cos(\theta))\right] . \tag{2.19}$$

Here, P_2 is the second order Legendre polynomial and θ is the angle relative to the polarization axis, which is the only assigned direction for atomic photoionization. The anisotropy parameter $\beta_2(\hbar\omega)$ ranges from -1 to 2. The photoelectron angular distribution given by Eq. 2.19 is plotted in Fig. 2.1 for four different β_2 values.

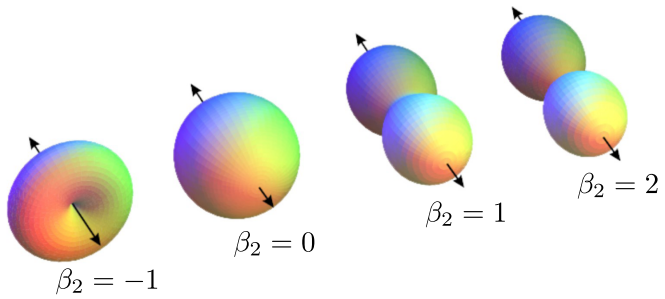

Figure 2.1: Photoelectron angular distribution for four different anisotropy parameters β_2. The arrows denote the polarization direction. Taken from Ref. [118].

2.1.2 Strong Field Ionization

The motion of an atom in an intense laser field can in first approximation be described by the quiver motion of a free electron in an oscillating electromagnetic field while the much heavier ionic core ($m_{\text{core}}/m_e \geq m_{\text{proton}}/m_e \approx 1800$) is assumed to stay at rest. This implies that the electron has oscillatory energy in addition to its kinetic energy. The mean energy of the oscillation is named ponderomotive potential and the derivation of it is based on the classical equations of motion of a free electron in an electromagnetic field[6]:

$$m_e \frac{\mathrm{d}v}{\mathrm{d}t} = eE_0 \cos(\omega t). \tag{2.20}$$

Here, m_e is the mass of the electron, v its velocity, e the elementary charge, E_0 the amplitude of the field and ω the frequency of the field.
Integrating Eq. 2.20 yields for the velocity of the electron:

$$v(t) = \frac{eE_0}{m_e\omega} \sin(wt). \tag{2.21}$$

The integration of Eq. 2.21 gives the displacement around the mid point x_0:

$$x(t) = \frac{eE_0}{m_e\omega^2} \cos(wt) = x_0 \cos(wt). \tag{2.22}$$

By using Eq. 2.21, the kinetic energy can be written as:

$$\frac{1}{2} m_e v(t)^2 = \frac{e^2 E_0^2}{2m_e\omega^2} \sin^2(wt). \tag{2.23}$$

The ponderomotive potential U_p is the mean energy:

$$U_p = \frac{1}{2} m_e \left\langle v(t)^2 \right\rangle = \frac{e^2 E_0^2}{2m_e\omega^2} \left\langle \sin^2(wt) \right\rangle = \frac{e^2 E_0^2}{4m_e\omega^2} = \frac{1}{4} m_e \omega^2 x_0^2. \tag{2.24}$$

It can also be written as a function of intensity $I = \frac{1}{2}\epsilon_0 c E_0^2$:

$$U_p = \frac{e_0^2 I}{2\epsilon_0 m_e c\omega^2} = \frac{e_0^2 I\lambda^2}{8\pi^2\epsilon_0 m_e c^3} \propto I\lambda^2. \tag{2.25}$$

Eq. 2.25 reveals the proportionality of the ponderomotive potential to the intensity I and the square of the wavelength λ^2. Consider for example the ionization of atomic argon with a first ionization potential of $I_p = 15.8\,\text{eV}$ [137] in case of IR ($\lambda = 800\,\text{nm}$) and XUV ($\lambda = 46\,\text{nm}$) radiation. For the same intensity of 5×10^{14} W/cm^2, the ponderomotive potential for the IR and the XUV case is $U_p^{\text{IR}} = 30\,\text{eV}$ and

[6] This section is compiled from Ref. [103, Ch. 8.5]. Here, SI and not atomic units are used.

$U_p^{\mathrm{XUV}} = 0.1\,\mathrm{eV}$, respectively. This means that $U_p^{\mathrm{IR}} > I_p$, which is a strong distortion and results in a bending of the atomic Coulomb potential. This regime is usually called strong field regime. For the XUV pulse, $U_p^{\mathrm{XUV}} < I_p$ and the atomic potential is only little perturbed and the picture of multi-photon absorption is more appropriate. In this regard, the Keldysh parameter γ [128] is a dimensionless quantity to distinguish both ionization regimes. It is defined as

$$\gamma = \sqrt{\frac{I_p}{2U_p}}. \tag{2.26}$$

For $\gamma > 1$, the ionization process can be described in the multi-photon picture. In literature, multi-photon ionization is also referred to "vertical" ionization, because the electron is excited by absorbing several photons along the vertical energy axis (see Fig. 2.2 (a)).
A Keldysh parameter $\gamma < 1$ is linked to the strong field picture, which is sometimes also referred to as "horizontal" ionization. In strong field ionization, two sub-regimes are further distinguished. In the tunnelling regime, the atomic potential is strongly bent, which results in a lowering of the potential barrier. Like this, the probability for bound electrons to tunnel through barrier is increased [8]. For even higher laser fields, the potential is bend so strongly that electrons are directly freed (see Fig. 2.2 (b)). This mechanism is called "over-the-barrier" ionization. The critical intensity I_{crit} can be calculated by equalizing the saddle point potential with the ionization potential [207][7].
It was shown that the transition between the multi-photon and the strong field regime is not very strict and experiments performed at $\gamma \approx 1$ usually feature signs of both ionization mechanisms [59, 171].

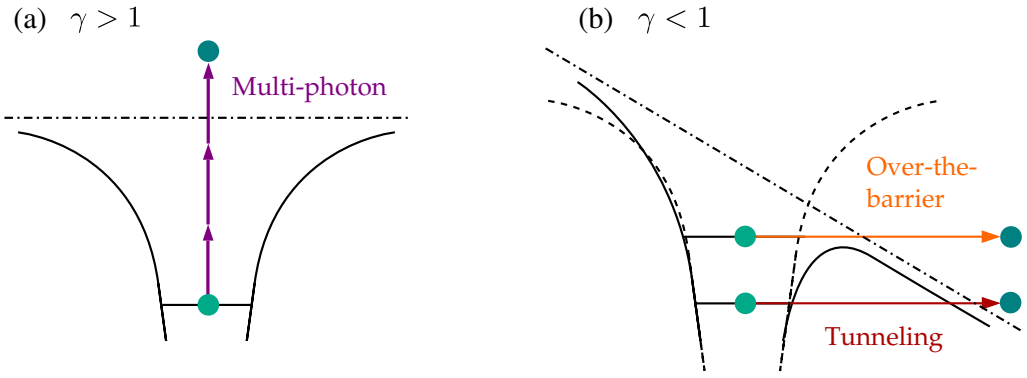

Figure 2.2: Scheme of different ionization pictures [207]. (a) Multi-photon regime ($\gamma > 1$). (b) Strong field regime ($\gamma < 1$).

[7] Critical intensity for over-the-barrier ionization: $I_{\mathrm{crit}} = \frac{\pi^2 c \epsilon_0^3}{2Z^2 e^6}\, I_p^4$, e.g., for atomic hydrogen $I_{\mathrm{crit}} \approx 1.4 \times 10^{14}\,\frac{\mathrm{W}}{\mathrm{cm}^2}$.

The commonly applied ADK-model (Ammosov-Delone-Krainov) [8] provides an analytic formula to describe tunnel ionization. It assumes the ionization to occur in a fraction of the optical cycle, so that the field can be regarded as quasi-static [207]. According to ADK-theory, the width of the ion momentum distribution along the laser polarization axis is given by

$$\Gamma(p_{||}) = A \cdot \exp\left(-(p_{||} - p_0)^2 \frac{\omega^2 (2I_p)^{3/2}}{3I^{3/2}}\right), \tag{2.27}$$

with amplitude A, momentum along the laser polarization $p_{||}$, central momentum p_0, laser frequency ω, ionization potential I_p and laser intensity I. In Sec. 6.2.1, the ADK-approach is used to estimate the intensity of the present IR laser.

2.1.3 Photoionization at FEL Intensities

In synchrotron experiments not more than one photon is absorbed within one light pulse [226]. This is in contrast to ionization by strong optical laser pulses, where many photons need to be absorbed to remove one electron (see Sec. 2.1.2). The systematic investigation of the ionization of a single atom by multiple high energetic photons is only enabled by the advent of FELs (see Ch. 3). To date, only FELs provide high enough intensities of X-ray/XUV photons to absorb several photons within one light pulse [214, 218, 253].
Two mechanism are distinguished in multi-photon ionization: sequential and non-sequential ionization. Fig. 2.3 illustrates the differences in terms of double-ionization of model atom X by two photons.

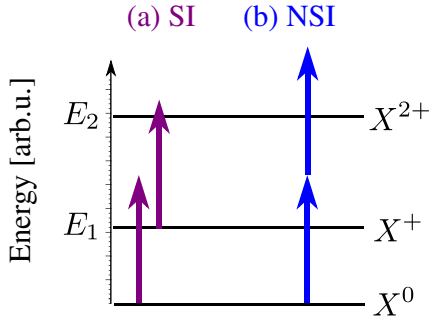

Figure 2.3: Photoionization of model atom X. (a) Sequential ionization (SI). In the first step, a photon (purple arrow) is absorbed to reach the stationary ionic X^+ state. From this intermediate state, a second photon is absorbed and the final X^{2+} state is reached. (b) Non-sequential ionization (NSI). Two photons (blue arrows) are directly absorbed and the final X^{2+} state is reached via a virtual intermediate state.

Sequential ionization (SI) occurs by step-by-step single-photon absorptions via stationary intermediate ionic states. In non-sequential ionization (NSI), two photons

are directly absorbed and the final state is reached via a virtual intermediate state. The lifetimes of these virtual states are very short as they are determined by Heisenberg's uncertainty relation. Therefore, the two photons need to be absorbed quasi-simultaneously. In the example of Fig. 2.3, both channels are energetically possible. However, depending on the photon energy and the intensity regime, one channel can dominant over the other.
In the X-ray regime, it was found that the multiple ionization predominantly happens by sequential absorption of single photons [189, 288] and that non-sequential ionization is a small contribution [46]. Depending on the system under investigation, the energy of one X-ray photon can be enough to ionize inner-shell and core electrons, which is usually accompanied by cascades of Auger electrons [78, 218].
In contrast to the X-ray-regime, several studies in the XUV photon energy range showed that besides the sequential, also the non-sequential channel plays a role to describe the ionization process [90, 120, 142, 144, 186, 220, 254, 275].
In order to reach the same ionic charge state, typically more photons are absorbed in the sequential than in the non-sequential channel. According to the power law $Y \propto I^n$, the ion yield Y increases non-linearly with intensity I [55, 218]. Thus, sequential ionization is expected to dominate at high intensities, where overall more photons are provided. The non-sequential channel is stronger at lower intensities, where less photons are available [144, 154]. Depending on the photon energy and the system under investigation, the power law $Y \propto I^n$ allows to distinguish the sequential from the non-sequential channel by "counting" the number n of absorbed photons. In Ch. 6, this is employed to investigate the pure and IR-assisted multi-photon ionization of atomic argon.

2.2 Many-Electron Atoms

In Sec. 2.1.1, time-dependent perturbation theory is applied to describe photoabsorption of hydrogen-like ions. The perturbation approach can be extended to many-electron atoms consisting of N electrons and a nucleus of charge Z. In difference to a single-electron system, the eigenstates of the many-electron system are N-particle states, which are eigenstates of the unperturbed Hamiltonian[8]:

$$\hat{H}_0 = \sum_{i=1}^{N} \left(-\frac{1}{2}\nabla_{r_i}^2 - \frac{Z}{r_i} \right) + \sum_{i \neq j}^{N} \frac{1}{r_{ij}} \tag{2.28}$$

Here, ∇_{r_i} is the single-electron nabla operator, r_i is the distance between electron i and the nucleus and $r_{ij} = |\mathbf{r}_i - \mathbf{r}_j|$ is the distance between electron i and j. Recapitulating the definition of the unperturbed single-electron Hamiltonian (see Eq. 2.2), the many-electron Hamiltonian additionally contains a term to describe the Coulomb interaction between the electrons.
The Schrödinger equation for the many-electron wave function $\Psi(\mathbf{r}_1, \mathbf{r}_2 ... \mathbf{r}_N)$ with the spatial coordinates[9] $\mathbf{r}_i$ reads:

$$\hat{H}_0 \Psi(\mathbf{r}_1, \mathbf{r}_2 ... \mathbf{r}_N) = E\Psi(\mathbf{r}_1, \mathbf{r}_2, ... \mathbf{r}_N). \tag{2.29}$$

Central Field Approximation and Independent Particle Model

In the central field approximation, the potential experienced by electron i is a combination of the potential of the nuclear charge Z and the mean field built up by the residual $N - 1$ electrons:

$$V_i(r_i) = -\frac{Z}{r_i} + \left\langle \sum_{i \neq j}^{N} \frac{1}{r_{ij}} \right\rangle. \tag{2.30}$$

Thus, the interaction between the electrons is conceptionally switched off by representing them as independent particles. This allows to decompose the many-electron wave function $\Psi(\mathbf{r}_1, \mathbf{r}_2 ... \mathbf{r}_N)$ into a product of single-electron wave functions $\phi_i(\mathbf{r}_i)$ which are named orbitals:

$$\Psi(\mathbf{r}_1, \mathbf{r}_2 ... \mathbf{r}_N) = \phi_1(\mathbf{r}_1)\phi_2(\mathbf{r}_2) ... \phi_N(\mathbf{r}_N). \tag{2.31}$$

In this way, the many-electron problem reduces to finding the single-electron wave functions $\phi_i(\mathbf{r}_i)$, which can be done by solving single-electron Schrödinger equations

[8] If not otherwise stated, this section is compiled from Ref. [26, Ch. 7], Ref. [103, Ch. 10.1] and Ref. [236, Ch. 2.2].

[9] As one is dealing with electrons, also the electrons' spin s_i needs to be considered in addition to the spatial coordinate $\mathbf{r}_i$ resulting in spatial-spin coordinates $q_i = (\mathbf{r}_i, s_i)$ [103, Ch. 10.1]. To keep the following derivations compact, only the spatial coordinate will be taken into account.

with the mean potential $V_i(r_i)$ (see Eq. 2.30). To get $V_i(r_i)$ accurately, one has to integrate over the wave functions of the remaining electrons. Those are ab initio not known and the Schrödinger equation needs to be solved iteratively following approaches like the Hartree method [103, Ch. 10.1.4]. Eventually, one ends up with a so-called electron configuration which is a set of N orbitals $|\phi_i(\mathbf{r}_i)\rangle$. The knowledge of the electron configuration allows to determine the total energy of the system

$$E = \left\langle \phi_1(\mathbf{r}_1)\phi_2(\mathbf{r}_2)...\phi_N(\mathbf{r}_N) \left| \hat{H} \right| \phi_1(\mathbf{r}_1)\phi_2(\mathbf{r}_2)...\phi_N(\mathbf{r}_N) \right\rangle . \tag{2.32}$$

2.2.1 Hartree-Fock Method

The Hartree-Fock (HF) method is a variational approach to find the wave function of an N-electron system. It is assumed that the N-electron wave function can be approximated by a single Slater determinant. By its definition, the Slater determinant accounts for the symmetry properties of the wave function, which are so far not taken into account. As electrons are indistinguishable fermions, they obey the Pauli principle and the total N-electron wave function needs to be antisymmetric. Therefore, it is convenient to express the N-electron wave function in terms of a single Slater determinant:

$$\Psi(q_1, q_2, ..., q_N) = \frac{1}{\sqrt{N!}} \begin{vmatrix} \phi_\alpha(q_1) & \phi_\beta(q_1) & ... & \phi_\nu(q_1) \\ \phi_\alpha(q_2) & \phi_\beta(q_2) & ... & \phi_\nu(q_2) \\ ... & ... & ... & ... \\ \phi_\alpha(q_N) & \phi_\beta(q_N) & ... & \phi_\nu(q_N) \end{vmatrix} . \tag{2.33}$$

Here, $1/\sqrt{N!}$ is a normalization constant and $\phi_\lambda(q_i)$ are single-electron wave functions, which generally depend on the spatial-spin coordinates $q_i = (\mathbf{r}_i, s_i)$. For simplicity, only the spatial coordinate $\mathbf{r}_i$ is considered in the following derivations, which are compiled from Ref. [236, Ch. 2.2], Ref. [103, Ch. 10.2] and Ref. [26, Ch. 7.4]. The HF Hamiltonian $\hat{H}_{\mathrm{HF}}$ is constructed by the sum of single-electron operators

$$\hat{H}_{\mathrm{HF}} = \sum_{i=1}^{N} \hat{h}_i + \hat{w}_i. \tag{2.34}$$

Here, $\hat{h}_i = -\frac{1}{2}\nabla_i^2 - \frac{Z}{r_i}$ is the Hamiltonian of a single electron in the Coulomb potential of the nucleus with charge Z. The operator $\hat{w}_i$ accounts for electron-electron interaction and is composed of the Coulomb operator $\hat{j}_i$ and the exchange operator $\hat{k}_i$. These operators are defined by their action on a single-electron wave function:

$$\hat{j}_i(\mathbf{r}_n)\phi_\lambda(\mathbf{r}_n) = \left(\int \phi_i^*(\mathbf{r}_m) \frac{1}{|r_{nm}|} \phi_i(\mathbf{r}_m) \mathrm{d}\mathbf{r}_m \right) \phi_\lambda(\mathbf{r}_n), \tag{2.35}$$

$$\hat{k}_i(\mathbf{r}_n)\phi_\lambda(\mathbf{r}_n) = \left(\int \phi_i^*(\mathbf{r}_m) \frac{1}{|r_{nm}|} \phi_\lambda(\mathbf{r}_m) \mathrm{d}\mathbf{r}_m \right) \phi_i(\mathbf{r}_n). \tag{2.36}$$

By using the Hamiltonian of Eq. 2.34, the N-electron wave function is obtained by solving the Hartree-Fock equation

$$\hat{H}_{\mathrm{HF}} \left|\Psi\right\rangle = E_{\mathrm{HF}} \left|\Psi\right\rangle . \tag{2.37}$$

This equation can be written in terms of the functional

$$E[\Psi] = \sum_{\lambda=1}^{N} I_\lambda + \frac{1}{2} \sum_{\lambda=1}^{N} \sum_{\mu=1}^{N} [J_{\lambda\mu} - K_{\lambda\mu}], \tag{2.38}$$

which is composed of a single-electron part

$$I_\lambda = \left\langle \phi_\lambda \left| \hat{h} \right| \phi_\lambda \right\rangle \tag{2.39}$$

and the electron-electron interaction parts

$$J_{\lambda\mu} = \left\langle \phi_\lambda \phi_\mu \left| \frac{1}{|r_{ij}|} \right| \phi_\lambda \phi_\mu \right\rangle \quad \text{and} \quad K_{\lambda\mu} = \left\langle \phi_\lambda \phi_\mu \left| \frac{1}{|r_{ij}|} \right| \phi_\mu \phi_\lambda \right\rangle . \tag{2.40}$$

$J_{\lambda\mu}$ is the so-called direct term, whereas $K_{\lambda\mu}$ is denoted exchange term.
The functional of Eq. 2.38 is now varied with respect to the wave functions ϕ_λ in order to minimize the total energy of the system [26, Ch. 2.8]:

$$E[\Psi] = \frac{\left\langle \Psi \left| \hat{H}_{\mathrm{HF}} \right| \Psi \right\rangle}{\langle \Psi | \Psi \rangle} \Rightarrow \delta E[\Psi] = 0. \tag{2.41}$$

Finally, one ends up in solving a system of coupled integro-differential equations to find the single-electron wave functions:

$$\hat{h}_i \phi_\lambda(\mathbf{r}_i) + \sum_\mu \hat{j}_\mu \phi_\lambda(\mathbf{r}_i) - \sum_\mu \hat{k}_\mu \phi_\mu(\mathbf{r}_i) = \epsilon_\lambda \phi_\lambda(\mathbf{r}_i). \tag{2.42}$$

Here, ϵ_λ is the energy of the orbital ϕ_λ. Using the explicit action of the operators, Eq. 2.42 can be rewritten like:

$$\left(-\frac{1}{2}\nabla_i^2 - \frac{Z}{r_i} \right) \phi_\lambda(\mathbf{r}_i) + \left(\sum_\mu \int \phi_\mu^*(\mathbf{r}_i) \frac{1}{r_{ij}} \phi_\mu(\mathbf{r}_i) \mathrm{d}\mathbf{r}_i \right) \phi_\lambda(\mathbf{r}_i) \tag{2.43}$$

$$- \left(\sum_\mu \int \phi_\mu^*(\mathbf{r}_i) \frac{1}{r_{ij}} \phi_\lambda(\mathbf{r}_i) \mathrm{d}\mathbf{r}_i \right) \phi_\mu(\mathbf{r}_i) = \epsilon_\lambda \phi_\lambda(\mathbf{r}_i). \tag{2.44}$$

This equation system can only be solved numerically in an iterative self-consistent way. The accuracy and the computational effort strongly depend on the chosen basis set of the wave functions. More details about the iterative procedure can be found in Ref. [208].

2.2.2 Configuration Interaction

Although the HF method (see Sec. 2.2.1) is a powerful tool, the obtained energies are still not the exact ones [26, Ch. 7.4]

$$E_{\text{exact}} = E_{\text{HF}} + E_{\text{corr}}. \tag{2.45}$$

The additional term E_{corr} accounts for electron-electron correlations that are not included in the HF formalism[10]. In Hartree-Fock formalism, the electrons are treated independently by approximating electron-electron interaction in terms of an average potential experienced by each electron. Electron correlations beyond this, which are for example responsible for phenomena like autoionization [174], are not included. To account for this, more advanced methods like configuration interaction (CI) are used [248]. In contrast to HF, where only the ground state electronic configuration is considered, CI approaches use a multi-configuration wave function in the initial and the final state. The many-electron wave function is now described by a linear combination of Slater determinants, $\Psi_{\text{total}} = \sum_n c_n \Psi_n$. The individual wave functions Ψ_n can be obtained by the HF method. The leading order of the expansion is typically the HF ground state configuration, followed by terms of excited electronic configurations. An example of such a calculation is given by Ref. [48], where the valence satellite binding energies of argon are computed by implementing a single-configuration ground state wave function and a multi-configuration wave function for the final state. In multi-reference CI, already the ground state is described by a multi-configuration wave function. Taking all excited states into account, one speaks of full CI calculations. Such calculations are very demanding from the computational side and can be only performed for small systems. An example is the calculation of valence satellite states of neon [37].
A drawback of approaches being based on Hartree-Fock is that the initial and final state need to be computed beforehand in order to calculate transitions. The Algebraic Diagrammatic Construction (ADC) method [232, 233] circumvents this problem by following the Green's function formalism [30, 42]. This allows to directly calculate energy differences and transition amplitudes between states. The Green's function for many-electron systems cannot be determined exactly and is calculated perturbatively in ADC. For this purpose, the Hamiltonian is decomposed in a non-perturbative and an interaction part. The perturbative order determines the accuracy, but also the costs of the calculations.
In the framework of this thesis, potential energy curves (PECs) (see Sec. 2.3.3) of argon dimers are computed by Ref. [177] using ADC(2) calculations. They are considered in Secs. 2.4.4 and 8.2.1.

[10] This section is compiled from Ref. [234] and Ref. [236, Ch. 2.2]

2.3 Diatomic Molecules

So far, the theoretical compilations concentrated on the electronic structure of a single atom. Compared to atoms, molecules consist of at least two nuclei, which comprise more degrees of freedom. To comprehensively describe the molecular system, the dynamics of the nuclei needs to be taken into account. Different to atoms, the nuclei of a molecule can vibrate around their equilibrium position and the entire molecule can undergo rotations. Adding the electronic motion, three types of motion need to be considered to describe a molecule.
In order to decrease the complexity of the problem, the electronic and the nuclear motions can be decoupled. The justification to do so lies in the much higher mass of the nuclei compared to the electrons. Already the lightest nucleus, the proton, is about 1800 times heavier than the electron. The Coulomb forces to which the electrons and nuclei are exposed, are, however, of comparable strength. As a result, the electrons move much faster and the nuclei seem to be at rest on the electronic time scale. These considerations give rise to the Born-Oppenheimer approximation [23], which is highlighted in Sec. 2.3.1. Based on this, the construction of molecular orbitals is introduced in Sec. 2.3.2. In Sec. 2.3.3, the concept of potential energy curves (PECs) is illustrated. Nuclear wave functions and the Franck-Condon principle are discussed in Sec. 2.3.4 and Sec. 2.3.5, respectively. The section closes with a brief discussion of Van-der-Waals molecules (see Sec. 2.3.6).

2.3.1 Born-Oppenheimer Approximation

A diatomic molecule consists of the two nuclei and N electrons[11]. Nucleus A has mass m_A and charge Z_A, whereas nucleus B is defined by mass m_B and charge Z_B. In the coordinate system depicted in Fig. 2.4, $\mathbf{R}_A$ is the vector pointing from the origin to nucleus A, the vector $\mathbf{R}_B$ points to nucleus B and $\mathbf{r}_i$ points to the i^{th} electron. The internuclear separation is $\mathbf{R} = \mathbf{R}_B - \mathbf{R}_A$ and the reduced mass of the nuclei is $\mu = (M_A M_B)/(M_A + M_B)$.

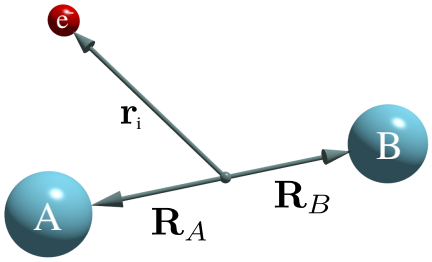

Figure 2.4: Coordinate system of a diatomic molecule with nuclei A and B. The depicted electron e^- represents the entirety of N electrons.

[11] This subsection is compiled from Ref. [104, Ch. 3] and Ref. [41].

The total molecular Hamiltonian

$$\hat{H} = \hat{T}_{\mathrm{n}} + \hat{T}_e + V(\mathbf{r}, \mathbf{R}) \tag{2.46}$$

includes the kinetic energy of the nuclei

$$\hat{T}_{\mathrm{n}} = -\frac{1}{2\mu}\nabla_R^2, \tag{2.47}$$

the kinetic energy of the N electrons

$$\hat{T}_e = \sum_{i=1}^{N}\left(-\frac{1}{2}\nabla_{r_i}^2\right), \tag{2.48}$$

and the Coulomb potential for all particles

$$V(\mathbf{r}, \mathbf{R}) = -\sum_{i=1}^{N}\frac{Z_A}{|\mathbf{r}_i - \mathbf{R}_A|} - \sum_{i=1}^{N}\frac{Z_B}{|\mathbf{r}_i - \mathbf{R}_B|} + \sum_{i<k}^{N}\frac{1}{|\mathbf{r}_i - \mathbf{r}_k|} + \frac{Z_A Z_B}{R}. \tag{2.49}$$

In order to determine the total energy E, the stationary Schrödinger equation

$$\hat{H}\Psi(\mathbf{R}, \mathbf{r}) = E\Psi(\mathbf{R}, \mathbf{r}) \tag{2.50}$$

needs be solved[12]. However, even for the simplest diatomic molecule, ionic hydrogen H_2^+, no analytic solutions for Eq. 2.50 do exist and numerical methods have to be applied. In order to do so, the complexity of Eq. 2.50 needs be reduced.
The most commonly used approximation is the Born-Oppenheimer (BO) approximation [23]. It is based on the fact that light electrons move much faster compared to the heavy nuclei. Thus, it can be assumed that the electrons adapt immediately to any changes of the potential induced by the motion of the nuclei. In this sense, the electronic wave function can be stationary solved, i.e., at a fixed internuclear separation. The decoupling of electronic and nuclear motion is described by the following product ansatz for the wave function:

$$\Psi(\mathbf{R}, \mathbf{r}) = \phi(\mathbf{r})\psi(\mathbf{R}). \tag{2.51}$$

Here, $\phi(\mathbf{r})$ are the electronic wave functions and $\psi(\mathbf{R})$ the nuclear wave functions.

[12]Here and in the following, $\mathbf{r}$ refers to the complete entirety of the electronic coordinates and $\mathbf{R}$ to all nuclear coordinates.

2.3.2 Molecular Orbitals

The electronic part of the total Hamiltonian (see Eq. 2.46) for fixed $\mathbf{R}$ is given by

$$\hat{H}_e = \hat{H} - \hat{T}_\mathrm{n}(\mathbf{R}) = \hat{T}_e + V(\mathbf{r}, \mathbf{R}). \tag{2.52}$$

All discussions so far hold for any number of nuclei. For a diatomic molecule, the relative coordinate $\mathbf{R} = \mathbf{R}_A - \mathbf{R}_B$ can be reduced to the internuclear distance $R = |\mathbf{R}|$ and the electronic Schrödinger equation in BO approximation reads [104, Ch. 3]:

$$\left(\hat{T}_e + V(\mathbf{r})\right) \phi_\gamma(\mathbf{r}) = V_\gamma(R)\phi_\gamma(\mathbf{r}). \tag{2.53}$$

The electronic wave functions $\phi_\gamma(\mathbf{r})$ and the eigenenergies $V_\gamma(R)$ are depending on a set of quantum numbers γ and the fixed parameter R. The ansatz to solve the electronic Schrödinger equation (see Eq. 2.53) is based on methods, which have already been introduced to built the wave functions of many-electron systems (see Sec. 2.2). The total molecular wave function is constructed as a product of single-electron wave functions. The single-electron wave functions for their part are built by a linear combination of atomic orbitals.

Two common methods to construct the molecular orbitals of hydrogen H_2 are the Heitler-London (HL) [98] and the molecular orbital (MO) approximation [45, Ch. 9]. In the HL approach, the total molecular wave function is approximated by the linear combination of two wave functions, which themselves are the product of two atomic $1s$ orbitals. In the MO approximation, first the wave function of ionic hydrogen H_2^+ is constructed by a linear combination of atomic $1s$ orbitals (LCAO). In the second step, the MO approach deviates conceptionally from the HL approximation in a sense that the total H_2 wave function is obtained by the product of the molecular orbitals of H_2^+. For both approximations, the Pauli principle requests the spatial wave function to be either symmetric or antisymmetric with respect to an exchange of the particles. This leads to symmetric *gerade* wave functions and anti-symmetric *ungerade* wave functions. The *gerade* wave functions are energetically favorable and have a bonding character.

Concerning precision, the dissociation energies obtained by both methods have a large deviation from the experimental value[13]. Both approximations are based on using atomic $1s$ orbitals to construct the molecular orbitals. However, a spherical $1s$ orbital, which is centered around one nucleus, does for example not account for the interaction between one electron and the other nucleus. Electron correlations are also neglected. In order to account for them, a basis set of non-spherical wave functions needs to be used.

Using elaborated quantum chemistry codes and state-of-the-art computer clusters, the wave functions and potentials of small molecules can be computed precisely [96].

[13] $E_\mathrm{diss}^\mathrm{HL} = 3.14\,\mathrm{eV}$, $E_\mathrm{diss}^\mathrm{MO} = 2.7\,\mathrm{eV}$, $E_\mathrm{diss}^\mathrm{exp} = (4.7470 \pm 0.0003)\,\mathrm{eV}$ [45, Ch. 9]

To achieve a high level of accuracy, large basis sets of atomic and molecular orbitals are combined with advanced Hartree-Fock methods, which include configuration interaction (CI) or higher-order ADC schemes (see Sec. 2.2.2). However, even with these sophisticated approaches, the calculations for large molecules, molecular ions or excited states are extensive and still very demanding (see Ch. 8).

Nomenclature

Due to the additional degrees of freedom, the symmetry properties of molecules are more complex compared to atoms or ions, which have a center symmetry around the nucleus. This entails a more elaborated nomenclature to characterize molecular orbitals. Within this thesis, only homonuclear diatomic molecules (H_2, Ch.7 and Ar_2, Ch.8) are discussed. They have the following state nomenclature[14]:

$$^{2S+1}\Lambda^{(+,-)}_{(g,u)}. \tag{2.54}$$

Here, Λ denotes the angular momentum and S is the total spin, which gives the multiplicity $2S+1$. Analogue to atoms, the angular momentum is characterized with $\Sigma, \Pi, \Delta, \Phi$ for $\Lambda = 0, 1, 2, 3$. The subscripts (g, u) and superscripts $(+, -)$ reflect symmetry properties of the total wave function Φ. $(+, -)$ are the eigenvalues of the reflection operator σ, i.e., $\sigma\Phi = \pm\Phi$. σ is a symmetry operator accounting for reflection on a virtual plane through the axis of the two nuclei. Applying the reflection operator twice results in the initial wave function:

$$\sigma(\sigma\Phi) = \sigma^2\Phi = \Phi. \tag{2.55}$$

The subscripts (g, u) are linked to the inversion operator I. It defines inversion with respect to the center of mass of the molecule. The inversion operator applied to states Φ_g of *gerade* (g) symmetry yields $I\Phi_g = +\Phi_g$. In case of states Φ_u of *ungerade* (u) symmetry, the identity $I\Phi_u = -\Phi_u$ exists. As for the reflection operator, applying the inversion operator twice results in the original wave function:

$$I^2\Phi = \Phi. \tag{2.56}$$

A detailed treatment of molecular symmetries, which is based on group theory, is given in Ref. [109].

2.3.3 Potential Energy Curves

Up to now, the focus of the discussion has been on the molecular orbitals, which are obtained by solving the electronic Schrödinger equation (see Eq. 2.53). However, also the electronic eigenenergies $V_\gamma(R)$, called potentials, are of great relevance for the

[14] This subsection is compiled from Ref. [236, Ch. 2.2.3].

analysis of the experimental results in Ch. 7 and 8[15]. With Eq. 2.49, the potentials derived from the electronic Schrödinger (see Eq. 2.53) have the form

$$V_\gamma(R) = U_\gamma(R) + \frac{Z_A Z_B}{R}. \tag{2.57}$$

The representation of Eq. 2.57 as a function of the internuclear separation R yields the so-called potential energy curves (PECs) (see Fig. 2.5). Each PEC represents an electronic state, which is labeled in accordance to the nomenclature of Eq. 2.54.
For small $R \to 0$, all PECs diverge due to the strong $(Z_A Z_B)/R$ Coulomb repulsion between the two approaching nuclei. For large $R \to \infty$, the PECs converge to the asymptotic limit of two separated atoms. The corresponding potential energy $V_\gamma(R \to \infty)$ is the so-called dissociation limit.
The electronic configuration of a state is reflected in the $U_\gamma(R)$ term of Eq. 2.57. For a binding state, $U_\gamma(R)$ accounts for an attraction and the corresponding PECs have a minimum. These states lead to a stable molecule. The minimum of the ground state PEC defines the equilibrium internuclear distance R_{eq}. For a molecule in the vibrational ground state, R_{eq} is usually in good agreement with the expectation value of the internuclear distance. In contrast to binding states, repulsive states are characterized by an $U_\gamma(R)$ term, which results in anti-bonding leading to the dissociation of the molecule. The dissociation energy D is the difference between the dissociation limit $V_\gamma(R \to \infty)$ and the potential energy of the ground state $V_\gamma(R_{\text{eq}})$.

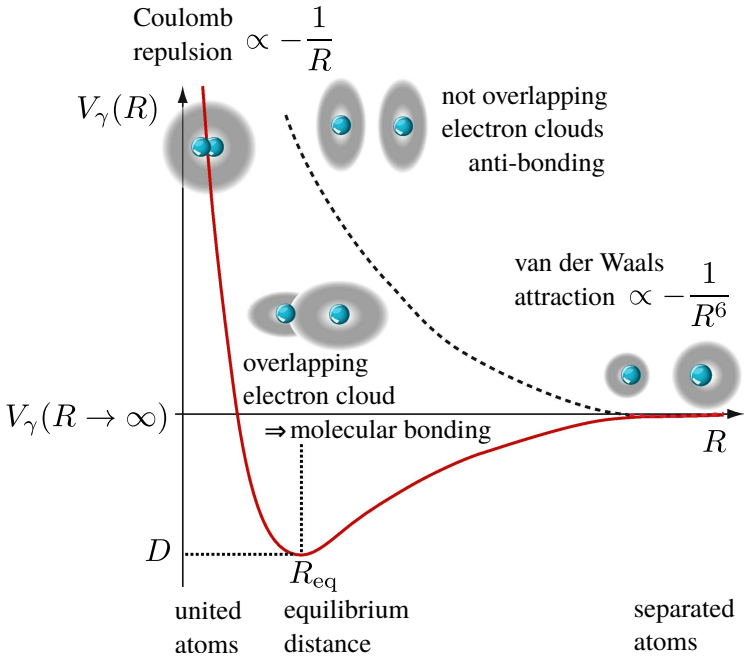

Figure 2.5: Overview of different types of potential energy curves (PECs). Explanations are given in the text. Taken and adapted from Ref. [41].

[15] This subsection is compiled from Ref. [41] and Ref. [104, Ch. 3.2.2].

2.3.4 Nuclear Wave Function

After having analyzed the electronic part of the molecular Schrödinger equation (see Eq. 2.50), the nuclear part is discussed in the following. In BO approximation, the nuclear Schrödinger equation is given by [104, Ch. 3]:

$$\left(-\frac{1}{2\mu}\nabla_R^2 + V_\gamma(R)\right)\psi(R) = E_{\gamma\nu}\psi(R). \tag{2.58}$$

The eigenenergies $E_{\gamma\nu}$ account for the total energy of the molecular state, which is denoted by a set of electronic γ and nuclear ν quantum numbers. $\psi(R)$ are the wave functions of the nuclear motion. In total, the energy $E_{\gamma\nu}$ has three contributions [26, Ch. 9.3]:

$$E_{\gamma\nu} = V_\gamma(R) + E_\nu(R) + E_{\mathrm{rot}}(R). \tag{2.59}$$

The characteristic energies and time scales of each contribution are very different. The energies of the electronic potentials $V_\gamma(R)$ are typically in the order of some ten eV and electron motion happens within 10 to 100 as. Vibrational energies $E_\nu(R)$ are in the order of 1/10 eV and characteristic vibrational periods are few to hundred fs. Rotational motion takes place on the ps time scale and typical rotational energies are in the meV range[16].
It will be shown that the temporal resolution of the experiment (see Sec. 6.2.3) allows to investigate processes, which take place on the vibrational time scale. For small vibrational amplitudes, i.e., for small displacements with respect to the equilibrium internuclear distance R_{eq}, the potential $V_\gamma(R)$ can be expanded in terms of a Taylor series [236, Ch. 2.2.3]:

$$V_\gamma(R) = V_\gamma(R_{\mathrm{eq}}) + (R - R_{\mathrm{eq}})\frac{\mathrm{d}V_\gamma}{\mathrm{d}R}\bigg|_{R=R_{\mathrm{eq}}} + \frac{1}{2}(R - R_{\mathrm{eq}})^2\frac{\mathrm{d}^2V_\gamma}{\mathrm{d}R^2}\bigg|_{R=R_{\mathrm{eq}}} + \mathrm{h.o.} \tag{2.60}$$

At the potential minimum R_{eq}, the first derivation $\frac{\mathrm{d}V_\gamma}{\mathrm{d}R}\big|_{R=R_{\mathrm{eq}}} = 0$ and one obtains a harmonic potential:

$$V_\gamma(R) \approx V_\gamma(R_{\mathrm{eq}}) + \frac{1}{2}k(R - R_{\mathrm{eq}})^2. \tag{2.61}$$

The coupling constant is $k = \frac{\mathrm{d}^2V_\gamma}{\mathrm{d}R^2}\big|_{R=R_{\mathrm{eq}}}$ and the classical vibrational frequency is given by $\omega = \sqrt{k/\mu}$. A harmonic potential is the lowest order approximation of a binding PEC. Using it to solve the nuclear Schrödinger equation (see Eq. 2.58) results in vibrational wave functions, which are given by Hermitian polynomials. The corresponding vibrational states with eigenenergies E_ν are described by the quantum number ν.

[16] Molecular rotations are not part of the experimental study and are therefore dropped in the further discussion.

The next higher level of approximation is the Morse potential which offers more tuning possibilities by means of three parameters [104, Ch. 3]. The anharmonicity of such type of potential causes the spacing between the vibrational levels to be not equidistant and to decrease towards the dissociation limit.

2.3.5 Franck-Condon Principle

The Franck-Condon (FC) principle is applied to describe the transitions between vibrational levels of different electronic states[17].
By using the BO approximation, the initial Ψ_i and final Ψ_f state wave functions can be decomposed in an electronic and nuclear part. The transition is induced by an electromagnetic wave polarized along x with amplitude E_0. The dipole-operator is given by $\hat{H}_\mathrm{d} = -xE_0e^{-\mathrm{i}\omega t}$ and the transition amplitude reads:

$$A_{if} = \left\langle \Psi_f \left| \hat{H}_\mathrm{d} \right| \Psi_i \right\rangle = \left\langle \phi_f\psi_f \left| \hat{H}_\mathrm{d} \right| \phi_i\psi_i \right\rangle \tag{2.62}$$

$$= \int \psi^*_{\gamma_f\nu_f}(R) \left(\int \phi^*_f(\mathbf{r};\mathbf{R})\hat{H}_\mathrm{d}\phi_i(\mathbf{r};\mathbf{R})\mathrm{d}\mathbf{r} \right) \psi_{\gamma_i\nu_i}(R)\mathrm{d}R \tag{2.63}$$

$$= \int \psi^*_{\gamma_f\nu_f}(R) M_{if}(R) \psi_{\gamma_i\nu_i}(R)\mathrm{d}R. \tag{2.64}$$

The dipole transition matrix element $M_{if}(R) = \int \phi^*_f(\mathbf{r};\mathbf{R})\hat{H}_\mathrm{d}\phi_i(\mathbf{r};\mathbf{R})\mathrm{d}\mathbf{r}$ is dependent on the internuclear distance R. Assuming that M_{if} changes little with R and that one of the vibrational wave functions (Ψ_i or Ψ_f) is localized to a small region of R, Eq. 2.64 can be approximated like

$$A_{if} \approx M_{if} \int \psi^*_{\gamma_f\nu_f}(R)\psi_{\gamma_i\nu_i}(R)\mathrm{d}R. \tag{2.65}$$

Now, the integration over the vibrational wave functions can be done straightforward. The Franck-Condon factors are defined as the absolute square of the integral over the vibrational wave functions:

$$c^\mathrm{FC}_{\gamma_i\nu_i\to\gamma_f\nu_f} = \left| \int \psi^*_{\gamma_f\nu_f}(R)\psi_{\gamma_i\nu_i}(R)\mathrm{d}R \right|^2. \tag{2.66}$$

The FC factors describe the integral overlap between the vibrational wave functions of two electronic states. For photon absorption, the transitions between the vibrational levels happen so fast that the internuclear separation can be regarded as frozen. Hence, the transitions occur on vertical lines at fixed R. Due to the large wave function overlap, the transition amplitude is usually largest at the classical

[17] This section is compiled from Ref. [41] and Ref. [26, Ch. 10.3]. For simplicity, the following derivations neglect changes in the rotational quantum number.

outer turning points. Photoionization can lead to the coherent excitation of several vibrational states, which launches a so-called nuclear wave packet. Within this thesis, the FC principle is applied to describe molecular photoexcitation and -ionization (see Ch. 7 and 8).

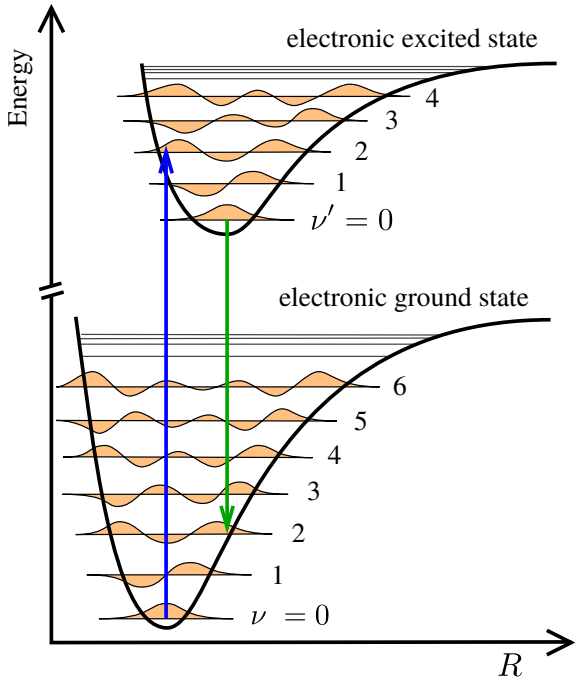

Figure 2.6: Franck-Condon principle. The excitation via a vertical transition (blue arrow) from the $\nu = 0$ vibrational state of the electronic ground state preferentially populates the $\nu' = 2$ vibrational state of the electronic excited state. The green arrow represents the relaxation of the molecule. Taken and adapted from Ref. [39].

2.3.6 Van-der-Waals Molecules

Chemical, covalent bonding is caused by "sharing" of valence electrons between the constituents of a molecule. Therefore, noble atoms with closed valence shells usually do not form molecules. However, other attractive forces besides covalent bonding do exist. An example is the Coulomb attraction between atoms and polar molecules. For atoms and molecules without a permanent dipole, the Van-der-Waals (VdW) interaction is present. It is induced by the mutual polarization of the electron clouds. VdW interaction is described by the polarizabilities α_A and α_B of constituent A and B and scales with the internuclear distance R like [104, Ch. 3]

$$V_{\mathrm{VdW}}(R) \propto \frac{\alpha_A \alpha_B}{R^6}. \tag{2.67}$$

Compared to chemical bonds, bindings induced by VdW interaction are a factor of 100 to 1000 weaker [236]. A VdW molecule consisting of two noble gas atoms is called a dimer. The binding PECs are shallow and contain only a small number of vibrational states. In first approximation, the binding PECs of dimers can be described by Lennard-Jones potentials [104, Ch. 3]. The magnitude of VdW interactions is typically in the order of thermal energies at room temperature, i.e., $k_B T = 1/40\,\mathrm{eV}$ [104, Ch. 3], Thus, dimers are preferentially formed in a cold environment. In the present experiment, these conditions are achieved by supersonic expansion (see Sec. 4.1). An introduction to the theory of dimer (and cluster) formation as well as empirical studies on optimal expansion conditions are given in Refs. [94, 95].

2.4 Interatomic Relaxation Mechanisms

In order to relax to its electronic ground state, an isolated excited atom or molecule[18] will release its excess energy in form of a photon or by the ejection of electrons. Depending on the state of excitation, different intra-atomic relaxation pathways are possible. Valence excitation is usually followed by fluorescence with picosecond lifetimes or by autoionization [38, 174] happening within femtoseconds. Inner- and core-shell excitation usually comes along with Auger decays [4, 168].
If the excited atom however is embedded in an environment, new interatomic relaxation pathways open up. In 1997, Cederbaum *et al.* [31] were the first to predict such a process, which became famous as interatomic or intermolecular Coulombic decay (ICD). In ICD, the excess energy of a de-exciting atom is transferred to a close-by atom via a virtual photon and the formally neutral neighbor is ionized. As both reaction partners are charged, the system typically undergoes Coulomb explosion.
ICD is a fast process taking place on the femtosecond time scale. The actual ICD lifetime depends amongst other things on the interatomic distance R [230] and the number of neighbors [12]. The first experimental evidence of ICD was given by Marburger *et al.* [156] in 2003 by an experiment on neon clusters. It was followed by a static experiment on neon dimers [119] and the first time-resolved experiment in 2013 [237]. Triggered by theory, a large variety of ICD-type relaxation mechanisms has been proposed and was experimentally confirmed. It is shown that ICD-type processes are omnipresent in weakly-bound systems such as noble gas or water dimers and clusters. Making the step from pure understanding to application, ICD is nowadays proposed as a tool for cancer treatment [81]. In this scenario, the slow electrons accompanying ICD destroy the tumour by breaking its DNA [24].
In the following, interatomic relaxation mechanisms, which are important for the interpretation of the relaxation dynamics of argon dimers (see Ch. 8), are presented.

[18] For simplicity, only the term "atom" is used in the following compilation. However, all the presented mechanisms are also existing for molecules.

In order to give a comprehensible and descriptive overview, it is renounced to present the phenomena in a detailed mathematical framework. A compact theory of ICD-type processes is given, e.g., in Ref. [193, Ch. 2].

2.4.1 Interatomic Coulombic Decay (ICD)

Different to the $2s^{-1}$-vacancy state of the neon dimer [119], the $Ar^+(3s^{-1}) - Ar$ state of the argon dimer is not subject to ICD, as it energetically lies below the $Ar^+(3p^{-1}) - Ar^+(3p^{-1})$ states.
However, one-site ionized and excited $Ar^+(3p^{-2}nl) - Ar$ states exist, which are above $Ar^+(3p^{-1}) - Ar^+(3p^{-1})$ and thus can decay via ICD [178]:

$$Ar^+(3p^{-2}nl) - Ar \xrightarrow{ICD} Ar^+(3p^{-1}) + Ar^+(3p^{-1}) + e^-_{ICD}. \tag{2.68}$$

The ICD described in Eq. 2.68 is schematically depicted in Fig. 2.7. The final products are two Coulomb-exploded $Ar^+(3p^{-1})$ fragments and an ICD electron. In the discussion of the experimental results (see Ch. 8), the kinetic energy release (KER) of Coulomb-exploded dimers is the main observable. For two fragments of charge q_1 and q_2, the KER is in first approximation given by the distance-dependent Coulomb repulsion of the fragments:

$$\mathrm{KER} \approx \frac{q_1 \cdot q_2}{R}. \tag{2.69}$$

In case of a dimer, R is the internuclear distance of the two nuclei. The KER allows to draw conclusions on the internuclear distance at the moment of the fragmentation. This makes it an optimal observable to study nuclear dynamics. The understanding of the KER with regard to PECs is emphasized in Sec. 4.6.

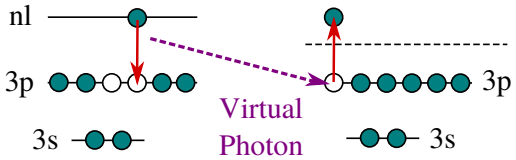

Figure 2.7: Illustration of the ICD of Eq. 2.68. The excited nl electron of the initial $Ar^+(3p^{-2}nl) - Ar$ state fills a $3p^{-1}$ hole and the excess energy is transferred via a virtual photon (dashed purple arrow) to the neutral site of the dimer which is ionized.

Depending on the initial $Ar^+(3p^{-2}nl) - Ar$ state, the ICD lifetimes can vary much and range from some ten femtoseconds up to one picosecond [178]. Nuclear dynamics on the $Ar^+(3p^{-2}nl) - Ar$ states has an influence on the internuclear distance R, where the decay happens. This dynamics prior to the decay is of importance in

the discussion of Ch. 8. The ICD from initial $Ar^+(3p^{-2}nl) - Ar$ states has been confirmed experimentally [212, 213, 216] and ab initio calculations are done by Miteva *et al.* [178].

2.4.2 Electron-Transfer Mediated Decay (ETMD)

Electron-transfer mediated decay (ETMD) was first predicted by Zobeley, *et al.* [297]. In contrast to ICD, it involves the migration of an electron. Thus, it requires a larger orbital overlap and typically happens at smaller internuclear distances.
For argon dimers, ETMD was observed for initial one-site triply ionized states of $Ar^{3+}(3s^{-1}3p^{-2}(+3p^{-4}3d)) - Ar$ character [227, 286]. The decay via electron transfer results in two $Ar^{2+}(3p^{-2})$ fragments and an ETMD electron (see Fig. 2.8):

$$Ar^{3+}(3s^{-1}3p^{-2}(+3p^{-4}3d)) - Ar \xrightarrow{\text{ETMD}} Ar^{2+}(3p^{-2}) + Ar^{2+}(3p^{-2}) + e^-_{\text{ETMD}}. \quad (2.70)$$

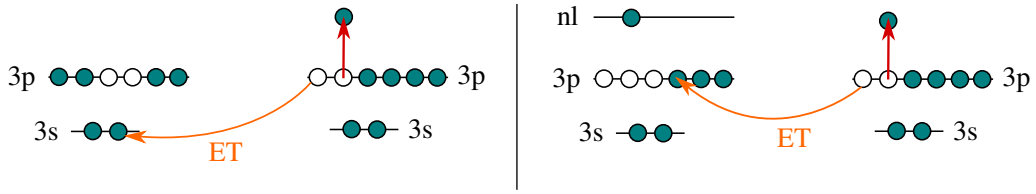

Figure 2.8: Illustration of the ETMD of Eq. 2.70. A vacancy, either $3s^{-1}$ or $3p^{-1}$, of the initially ionized site of the dimer is filled by an electron from the neutral site. An ETMD electron is emitted and the formally neutral site gets doubly charged.

2.4.3 Radiative Charge Transfer (RCT)

In a radiative charge transfer (RCT), the charged site of the dimer attracts an electron of the neutral site. The excess energy is released via a real photon [125]. For the argon dimer, RCT can happen for initial one-site doubly charged $Ar^{2+}(3p^{-2}) - Ar$ states (see Fig. 2.9) [212, 225]. They are of binding character and charge transfer is more favorable at small R, which includes a priori nuclear motion. The final products of the described RCT are two $Ar^+(3p^{-1})$ ions and a photon:

$$Ar^{2+}(3p^{-2}) - Ar \xrightarrow{\text{RCT}} Ar^+(3p^{-1}) + Ar^+(3p^{-1}) + \text{photon}. \quad (2.71)$$

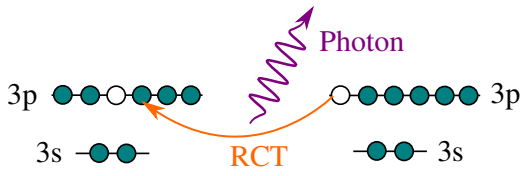

Figure 2.9: Illustration of the RCT of Eq. 2.71. One of the $3p^{-1}$ vacancies of the charged site is filled by an electron from the neutral site. The excess energy is released by emitting a photon.

2.4.4 Charge Transfer (CT) at Curve Crossings

For the $Ar^{2+}(3s^{-1}3p^{-1}(+3p^{-3}3d)) - Ar$ states, a relaxation channel via charge transfer to repulsive $Ar^{+}(3p^{-2}nl) - Ar^{+}(3p^{-1})$ states is possible. As the one-site doubly ionized $Ar^{2+}(3s^{-1}3p^{-1}(+3p^{-3}3d)) - Ar$ states are of shallow, but of binding character, a wave packet excited at the equilibrium internuclear distance R_{eq} will propagate towards smaller R. At each crossing point with an $Ar^{+}(3p^{-2}nl) - Ar^{+}(3p^{-1})$ state, population can be transferred due to non-adiabatic couplings [258]:

$$Ar^{2+}(3s^{-1}3p^{-1}(+3p^{-3}3d)) - Ar \xrightarrow{CT} Ar^{+}(3p^{-2}nl) + Ar^{+}(3p^{-1}). \tag{2.72}$$

The relevant PECs are displayed in Fig. 2.10. They are calculated by Ref. [177] using the ADC(2) method (see Sec. 2.2.2). From the computational side, the calculation of high-lying excited states is quite demanding, because the approximation of the two dimer sites as two separated atoms breaks down. A large basis set is needed to get the excited electron correctly. However, this increases the density of states which hampers the convergence of the calculations. Moreover, the PECs strongly interact with neighboring PECs and the assignment of the exact character of individual states is challenging. For this reason, the character of the violet, orange and yellow curve in Fig. 2.10 cannot been assigned.

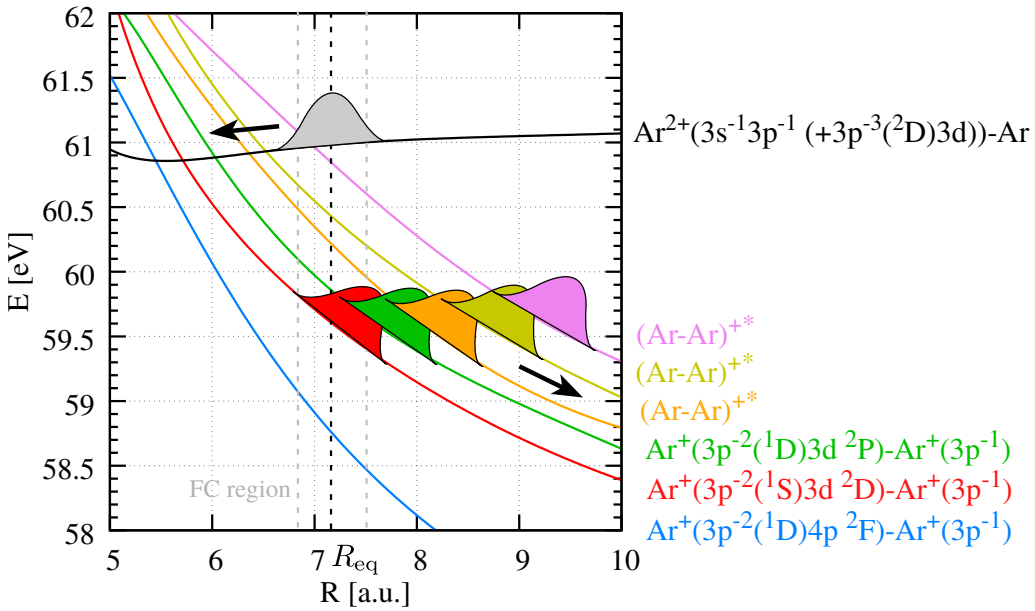

Figure 2.10: PECs of the argon dimer in the energy range of 58 – 62 eV. A wave packet (grey) on the initial $Ar^{2+}(3s^{-1}3p^{-1}\,^1P\,(+3p^{-3}(^2D)3d\,^1P)) - Ar$ state propagates from the Franck-Condon (FC) region towards smaller R. At the crossings with the dissociative $Ar^{+}(3p^{-2}nl) - Ar^{+}(3p^{-1})$ states, electronic coupling leads to population transfer. All PECs shown are calculated by Ref. [177].

2.4.5 Landau-Zener Transitions

In order to calculate the transition probabilities at crossing points of PECs, the Landau-Zener (LZ) formalism is a common approach[19]. It gives an analytic solution to the problem of calculating transitions between states of a two-level system[20].
As depicted in Fig. 2.10, the CT process is linked to nuclear motion, because the two nuclei move towards each other before the transition can happen. From a different point of view, the motion of the nuclei can be regarded in terms of the collision of two heavy particles and the transition can be described by inelastic scattering. In this regard, the relative motion of the nuclei is approximated by classical trajectories $\mathbf{R}(t)$. In the framework of this semi-classical treatment, transitions between the states can be described by non-adiabatic coupling elements or by off-diagonal elements of an interaction potential matrix (see Fig. 2.11).

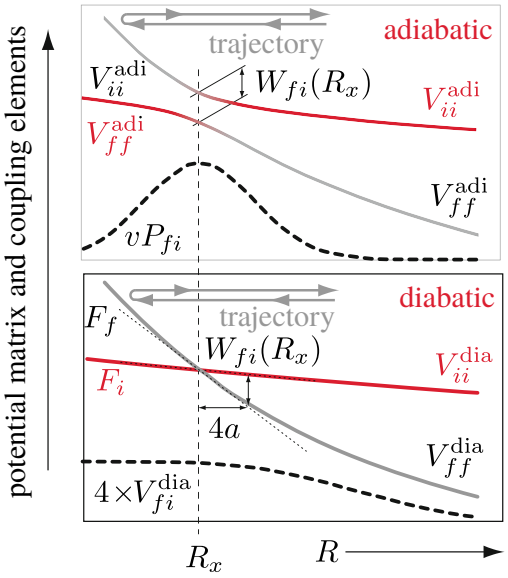

Figure 2.11: Adiabatic V_{kk}^{adi} (top) and diabatic V_{kk}^{dia} (bottom) representation of potentials to describe transitions at a crossing point R_x. $W_{if}(R_x)$ is the energy difference between the potentials. Taken and adapted from Ref. [104, Ch. 7].

If an adiabatic representation is used, the potential matrix will be diagonal, i.e., $V_{kk'} = \delta_{kk'}V_{kk}$, and transitions are induced by non-adiabatic coupling elements vP_{fi}. In a diabatic state representation, non-diagonal potential matrix elements account for the transition. Both representations are equivalent, but differ in terms of convergence and the proper choice depends on the specific problem. For diabatic states, the potentials are expanded linearly around the crossing point R_x. This linearization

[19] The theory was published independently by Landau [146], Zener [289], Stueckelberg [259] and Majorana [153].
[20] This section is compiled from Ref. [104, Ch. 7].

and the assumption of a constant potential matrix over the entire crossing region are basic approximations in the Landau-Zener model (see Eqs. 2.81 and 2.82).
In the semi-classical approximation, not only the trajectories $\mathbf{R}(t)$, but also the electronic Schrödinger equation is time-dependent:

$$\left(\hat{H}_e - \mathrm{i}\hbar\frac{\partial}{\partial t}\right)\Psi(t,\mathbf{r}) = 0. \tag{2.73}$$

An expansion ansatz can be applied and the wave function is expanded in a complete basis set of $\phi_k(\mathbf{r};\mathbf{R}(t))$ states

$$\Psi(t,\mathbf{r}) = \sum_k c_k(t)e^{-\mathrm{i}\varphi_k(t)}\phi_k(\mathbf{r};\mathbf{R}(t)). \tag{2.74}$$

The semi-classical phase $\varphi_k(t)$ is derived from

$$\varphi_k(t) = \frac{1}{\hbar}\int_{-\infty}^{t} V_{kk}(\mathbf{R}(t'))\mathrm{d}t' = \frac{1}{\hbar}\int_{\infty}^{R}\frac{V_{kk}(\mathbf{R}(t))}{v_R(\mathbf{R}(t))}\mathrm{d}R. \tag{2.75}$$

The potential $V_{kk}(\mathbf{R}(t))$ is either described in an adiabatic or diabatic representation, The relative radial velocity is denoted by $v_R(\mathbf{R}(t)) = \mathrm{d}R/\mathrm{d}t$. The variation of the Schrödinger equation (see Eq. 2.73) with respect to the expansion coefficients $c_k(t)$ results in solving a system of coupled differential equations

$$\frac{\partial c_k(t)}{\partial t} = -\frac{1}{\hbar}\sum_{k\neq k'} M_{kk'}(t)e^{-\mathrm{i}(\varphi_k-\varphi_{k'})}c_{k'}(t) \tag{2.76}$$

with the coupling element $M_{kk'}(t)$, which is equal to

$$M_{kk'}(R(t)) = V_{kk'}^{\mathrm{dia}}(R(t)) = \left\langle \phi_{k'}(\mathbf{r};\mathbf{R}(t)) \left| \hat{H}_e \right| \phi_k(\mathbf{r};\mathbf{R}(t)) \right\rangle \tag{2.77}$$

in the diabatic case[21].
Based on the so far generally formulated theory, the Landau-Zener approximation for diabatic transitions is emphasized in the following. It treats the transition between two diabatic states $|i\rangle$ and $|f\rangle$ at a crossing point R_x. In this problem, the coupled differential equations (see Eq. 2.76) have to be solved for the starting conditions $c_{ii}(t\to-\infty) = 1$ and $c_{fi}(t\to-\infty) = 0$, which yields:

$$\frac{\partial c_{ii}(t)}{\partial t} = -\frac{\mathrm{i}}{\hbar}V_{if}(t)\mathrm{e}^{-\mathrm{i}\Delta\varphi_{if}}c_{fi}(t), \tag{2.78}$$

$$\frac{\partial c_{fi}(t)}{\partial t} = -\frac{\mathrm{i}}{\hbar}V_{fi}(t)\mathrm{e}^{-\mathrm{i}\Delta\varphi_{if}}c_{ii}(t) \tag{2.79}$$

[21] In the adiabatic case, $M_{kk'}(t) = \left\langle \phi_{k'}(\mathbf{r};\mathbf{R}(t)) \left| \hbar\frac{\partial}{\partial t} \right| \phi_k(\mathbf{r};\mathbf{R}(t)) \right\rangle$.

$$\text{with } \Delta\varphi_{if}(t) = \frac{1}{\hbar}\int_0^t (V_{ii}(t') - V_{ff}(t'))\mathrm{d}t'. \tag{2.80}$$

At the crossing point R_x, $V_{ii}(R_x) = V_{ff}(R_x)$ and one can Taylor-expanded the potentials for small distances $\Delta R = R - R_x$:

$$V_{ff} - V_{ii} = \Delta R \frac{\partial}{\partial R}(V_{ff} - V_{ii})\big|_{R=R_x} = (F_i - F_f)\Delta R = F_{if}\Delta R. \tag{2.81}$$

Thus, the potentials are linearly approximated in the vicinity of R_x. The constant F_{if} is the difference in the slopes of potential V_{ii} and V_{ff} at the crossing point and can be interpreted as the force on the corresponding trajectories. The identity $\Delta R = v_R t$ holds for setting time zero to the moment in time when R_x is crossed.
The next approximation assumes a constant coupling element over the entire crossing:

$$|V_{if}| = |V_{fi}| = V_{if}. \tag{2.82}$$

With the approximations of Eqs. 2.81 and 2.82, the phase difference (see Eq. 2.80) is given by

$$\Delta\varphi_{if}(t) = \alpha\frac{\pi}{2}t \quad \text{with} \quad \alpha = \frac{F_{if}v_R}{\pi\hbar}. \tag{2.83}$$

Using Eq. 2.83, the coupled differential equations (see Eqs. 2.78 and 2.79) can be solved analytically. A solution using contour integration is presented by Wittig [282]. Herein, the transition probability from adiabatic state $|i\rangle$ to adiabatic state $|f\rangle$, which corresponds to staying on the diabatic state (see Fig. 2.11), is derived to

$$P_{fi} = e^{-2\pi\Gamma} \quad \text{with} \quad \Gamma = \frac{|V_{if}|^2}{\hbar F_{if} v_R}. \tag{2.84}$$

Correspondingly, the transition probability between diabatic states $|i\rangle$ and $|f\rangle$ is $P_{fi}^{\mathrm{dia}} = 1 - P_{fi}$. In case of the curve crossing described in Sec. 2.4.4, the transition may occur on the way towards the classical inner turning point of the binding potential or on the way back. Then, the total Landau-Zener probability is given by

$$P_{\mathrm{LZ}} = 2P_{fi}(1 - P_{fi}) \quad \text{with} \quad P_{fi} = e^{-2\pi\Gamma}. \tag{2.85}$$

By introducing the Landau-Zener length $l_{\mathrm{LZ}} = |V_{if}|/F_{if}$, Γ defined in Eq. 2.84 becomes $\Gamma = l_{\mathrm{LZ}}|V_{if}|/(\hbar v_R)$ [164, Ch. 7.3.1]. The Landau-Zener length defines the distance from the crossing point, where $V_{ii} - V_{ff}$, i.e., the difference of the potential energies becomes comparable to the electronic coupling $|V_{if}|$. Like this, l_{LZ} gives an estimate up to which distance the coupling $|V_{if}|$ has an influence on the transfer dynamics. A detailed mathematical discussion of transitions at curve crossings is given in Ref. [295].

Getting back to the motivation of calculating CT transitions at crossings of PECs of the argon dimer (see Sec. 2.4.4), the deviation from $1/R$ Coulomb potentials of the $Ar^+(3p^{-2}nl) - Ar^+(3p^{-1})$ states is displayed in Fig. 2.12.
In the LZ formalism, the potential matrix of the coupling is assumed to be time-independent. Hence, the transition is not induced by a time-dependent perturbation, but by the static deviation from a $1/R$ Coulomb potential. As depicted in Fig. 2.12, the repulsive $Ar^+(3p^{-2}nl) - Ar^+(3p^{-1})$ states strongly deviate from $1/R$. This justifies to calculate LZ probabilities for the corresponding transitions [177]. The results are listed in Tab. 2.1.

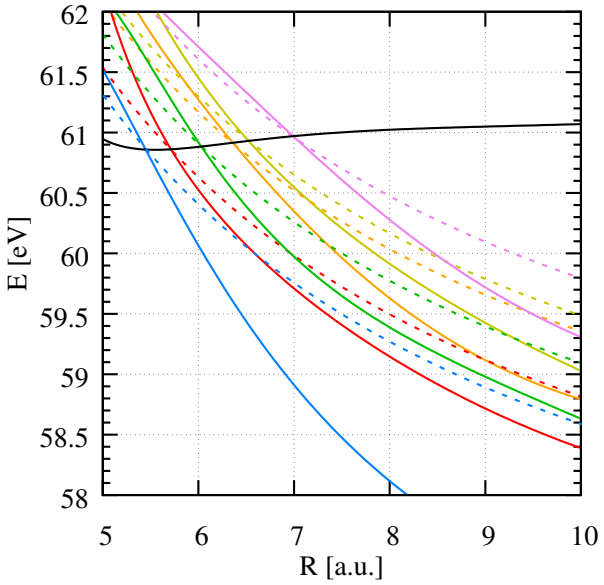

Figure 2.12: PECs of the argon dimer between $58 - 62\,\text{eV}$. The continuous curves are calculated [177], the dashed curves are $1/R$ Coulomb potentials shifted by a respective vertical energy offset to match the crossing points. The color code of the states is the same as in Fig. 2.10.

Table 2.1: Probabilities P_{fi} (Eq. 2.84) with corresponding rates Λ and lifetimes τ for transitions at R_x. The rate Λ is calculated like $\Lambda = 2P_{fi}(1 - P_{fi}))T$ with T being the vibrational period of the initial bound state. The last column shows the total rate and corresponding lifetime. The calculations are performed by Ref. [177].

R_x [a.u.]	Intermediate state	P_{fi}	T [fs]	Λ [fs^{-1}]	τ [ps]
5.73	$Ar^+(3p^{-2}(^1S)3d\,^2D) - Ar^+(3p^{-1})$	0.964	365.83	1.87×10^{-4}	5.32
6.03	$Ar^+(3p^{-2}(^1D)3d\,^2D) - Ar^+(3p^{-1})$	0.914	"	4.31×10^{-4}	2.32
6.39	$(Ar - Ar)^{2+}$	0.781	"	9.33×10^{-4}	1.07
6.52	$(Ar - Ar)^{2+}$	0.929	"	3.59×10^{-4}	2.79
6.98	$(Ar - Ar)^{2+}$	0.918	"	4.11×10^{-4}	2.44
				2.32×10^{-3}	0.43

2.5 Classical Simulation

As pointed out in the introduction (see Ch. 1), pump-probe spectroscopy is a commonly used method to follow the dynamics of a quantum system in real-time. For example, it can be applied to trace charge migration in a fragmenting molecule [238, 239] and to study ICD in neon dimers in a time-resolved manner [237, 240]. In the analysis of pump-probe experiments, an experimental observable, e.g., the kinetic energy release (KER) (see Sec. 4.6), is plotted as a function of the delay. The interpretation of such delay-dependent spectra is not straightforward, because usually many different channels contribute. In order to disentangle the different contributions, a simulation that models the experiment can be useful.
In the present case, the XUV-IR pump-probe experiment on charge transfer dynamics in Ar_2 is modeled by a classical simulation (see Sec. 8.2.1). The model accounts for molecular dynamics by propagating classical point-like particles on PECs (see Sec. 2.3.3). It uses the same basic code which has been developed in Ref. [236] and whereupon the following description is based on. In the first step of the simulation, a particle of reduced mass $\mu = (m_1 m_2)/(m_1 + m_2)$ is placed on a PEC $V(R)$ at time t_0 and internuclear distance $R(t_0)$. The particle has no initial velocity and $\frac{\mathrm{d}R}{\mathrm{d}t}|_{t_0=0} = 0$. Having set the starting conditions, the particle is propagated on $V(R)$ by stepwise solving Newton's classical equations of motion. Therefore, the simulation is conducted on an equidistant grid spanned by $(R_0, R_1, ..., R_i, ..., R_n)$ with a step size of $\Delta R = R_i - R_{i-1}$. For each step R_i the acceleration $a(R_i)$ is calculated:

$$a(R_i) = \frac{1}{\mu} \frac{V(R_i) - V(R_{i-1})}{\Delta R}. \tag{2.86}$$

The time interval $\Delta t(R_i - R_{i-1})$ to pass the distance ΔR with velocity $v(R_{i-1})$ is

$$\Delta t(R_i - R_{i-1}) = \frac{-v(R_{i-1}) + \sqrt{v^2(R_{i-1}) + 2a(R_i)\Delta R}}{\Delta R} \tag{2.87}$$

and the total time to pass n intervals ΔR is the sum $t_{\mathrm{tot}} = \sum_{i=1}^{n} \Delta t(R_i - R_{i-1})$. After each step, the present kinetic energy of the particle is calculated:

$$E_{\mathrm{kin}}(R_i) = V(R_i) - V(R_0). \tag{2.88}$$

Knowing the kinetic energy $E_{\mathrm{kin}}(R_i)$, the velocity input for the subsequent step is computed:

$$v(R_i) = \sqrt{\frac{2E_{\mathrm{kin}}(R_i)}{\mu}}. \tag{2.89}$$

The particle moves on $V(R)$ until the point in time t_{probe} when it is promoted to the final PEC $V'(R)$ (see Fig. 2.13). On this PEC, the particle starts with the velocity already gained on $V(R)$. It is propagated to asymptotic internuclear distances

$R_\infty = n\Delta R$ until the velocity change is negligible. The total kinetic energy gained on $V(R)$ and $V'(R)$ is summed up and can directly be compared to the measured kinetic energy (see Sec. 8.2.1).

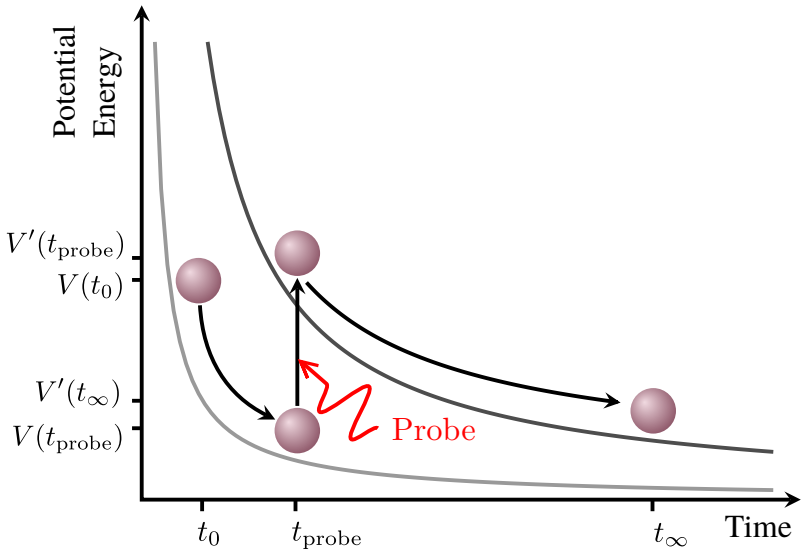

Figure 2.13: Illustration of the classical simulation. At time t_0, a point-like classical particle starts to propagate along the PEC $V(R)$. At a time t_{probe}, the particle is transferred to a different PEC $V'(R)$ and is propagated to asymptotic times t_∞. Taken and adapted from Ref. [236, Ch. 2.6].

3 Free-Electron Laser

Free-electron lasers (FELs) [22] operating in the XUV/X-ray photon energy regime represent a new generation of accelerator-based light sources and can be considered as the further development of third generation synchrotron sources [7]. The generation of XUV or X-ray light with synchrotrons is a well-established technique. Here, electrons are accelerated to relativistic velocities on a circular orbit. In order to generate light, the accelerated electrons are forced to traverse periodic structures of dipole magnets with alternating polarity, so-called undulators or wigglers. By this means, they are deflected perpendicular to their direction of motion by the magnetic fields and start to emit synchrotron radiation [281]. In this process, the emitted light power is proportional to the number of contributing electrons and the radiation is incoherent as the electrons radiate independently from each other.
Different to synchrotrons, FELs produce light with laser-like properties. Strictly speaking, the acronym *LASER* for *light amplification by stimulated emission of radiation* is not exactly appropriate with regard to FELs. However, the light produced by FELs features properties, which are also characteristic for conventional lasers: high photon density, low divergence, spatial and (partially) temporal coherence. In the 1970s, the first lasing of an FEL in the IR regime was demonstrated [44]. However, it took more than 25 years until the first operation in the XUV regime was achieved at the free-electron laser in Hamburg (FLASH) [13]. In 2009, the Linac Coherent Light Source (LCLS) in Stanford, California, expanded the wavelength range of FELs into the hard X-ray regime [52]. For the time being, there are several more XUV[22] and X-ray[23] FELs in operation and under construction.
Due to the lack of appropriate materials, XUV or X-ray FELs cannot be equipped with resonators in analogy to optical resonators known from conventional lasers[24]. Hence, for XUV or X-ray FELs saturation needs to be achieved within a single passage through the undulator. The interaction between the emitted radiation and the relativistic electron bunch results in the structuring into so-called microbunches (see Sec. 3.2). The micro-bunching effect is advantageous because each microbunch radiates coherently as if it was a single point-like particle (see Sec. 3.3). As a consequence, the emitted light power is proportional to the square of the number of

[22] FERMI (Italy) [5], SDUV-FEL (China) [294], SCSS (Japan) [250] (Now integrated into the SACLA facility).
[23] SACLA (Japan) [115], SwissFEL (Switzerland) [175], PAL-XFEL (South Korea) [135], European XFEL (Germany) [280], LCLS-II (USA) [257]. An overview of all FEL facilities worldwide is given on `http://sbfel3.ucsb.edu/www/vl_fel.html`, last request: 11/30/2017.
[24] FELs operating in the optical to THz regime can be equipped with resonators, e.g. FELIX [274].

radiating electrons within a bunch. Utilizing this mechanism, the peak brilliance[25] of XUV and X-ray FELs is up to eight orders of magnitude higher compared to third generation synchrotrons (see Fig. 3.1).

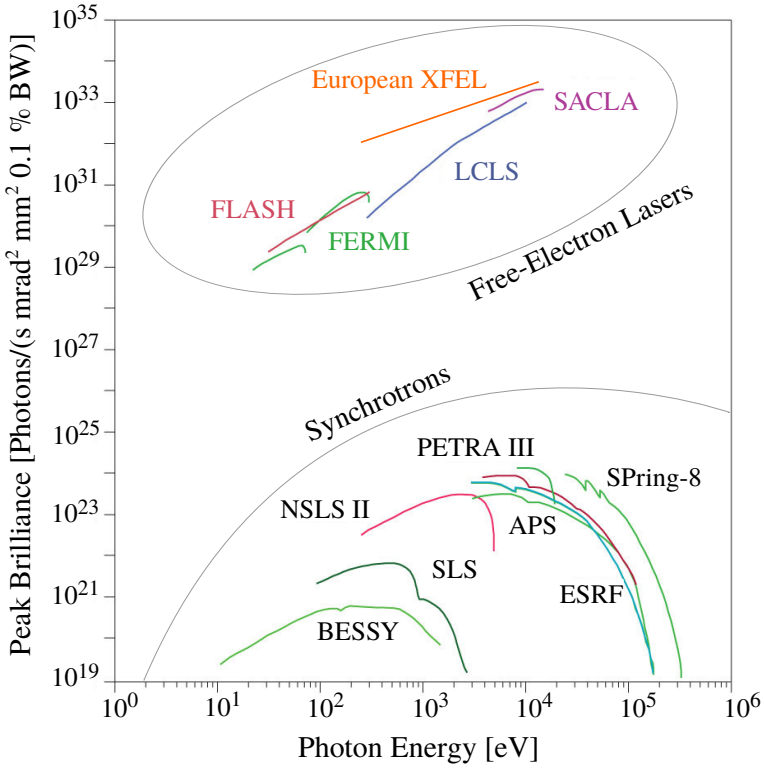

Figure 3.1: Peak brilliance of free-electron lasers compared to modern synchrotrons. Taken and adapted from Refs. [2, 68].

The achievable pulse durations of modern synchrotrons typically range from 10 to 100 picoseconds. With XUV or X-ray FELs, however, pulse durations in the order of few tens of femtoseconds are routinely reached [99] and the aim is to enter the attosecond regime [112, 224]. Using those short and brilliant pulses allows to study the dynamics of physical, chemical, biological and biochemical processes on their natural time scale. Furthermore, the unprecedented intensity of FEL radiation opens a new chapter in non-linear light-matter interactions [60].
The following sections describe the working principle and the basic theory of FELs[26]. A detailed review on FEL theory can be found for example in Refs. [199, 200].

[25] Brilliance: Photons/(s · mrad² · mm² · 0.1 % Bandwidth).
[26] The following compilations are based on Ref. [234].

3.1 Undulator Radiation

An XUV/X-ray FEL consists of three main components: a pulsed electron source, a linear accelerator and an undulator (see Fig. 3.2).

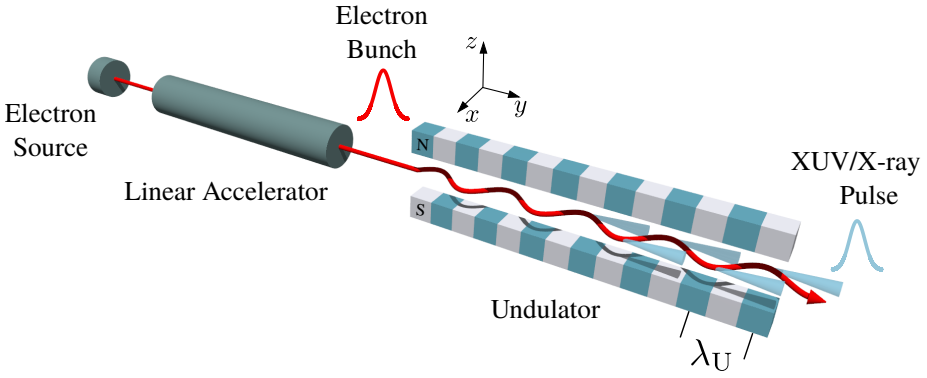

Figure 3.2: Basic components of an FEL: Electron source, linear accelerator and undulator. Adapted from Ref. [200].

The source provides bunches of electrons, which gain relativistic energies in the linear accelerator. After the acceleration, the electron bunches enter an undulator, i.e., a periodic structure of permanent magnets with alternating polarity. Due to the Lorentz force, the electrons are deflected perpendicular to their direction of motion in an oscillating manner and start to emit synchrotron radiation (see Fig. 3.2). Because of the relativistic velocities ($\beta = v/c \approx 1$) and the small amplitude of their trajectories, the electrons emit radiation in a narrow cone in forward direction. The maximum opening angle of this cone is given by $\theta \leq 1/\gamma$ (with $\gamma = 1/\sqrt{1-\beta^2}$) [107]. To give a first estimation of the fundamental wavelength λ_{xuv} of the emitted radiation, one has to take into account two relativistic effects. First, due to the relativistic length contraction, the undulator period λ_U (see Fig. 3.2) is reduced to $\lambda_U^* = \lambda_U/\gamma$ in the coordinate system of the moving electrons and the electrons oscillate with a frequency $\nu^* = c/\lambda_U^*$. Second, due to the relativistic Doppler shift, an observer in the laboratory frame sees the radiation blue-shifted, which additionally boosts the frequency to $\nu^{**} = \nu^*/\gamma(1-\beta)$. Both effects lead to an approximated fundamental wavelength of [235, Ch. 1]

$$\lambda_{xuv} \approx \frac{\lambda_U}{2\gamma^2}. \tag{3.1}$$

An attentive derivation accounts for the slowdown of the longitudinal electron velocity due to the transverse oscillatory motion. Hence, the velocity considered for the relativistic Doppler shift is different and Eq. 3.1 is corrected to [235, Ch. 1]:

$$\lambda_{xuv} = \frac{\lambda_U}{2\gamma^2}\left(1 + \frac{K^2}{2}\right). \tag{3.2}$$

Here, K is the so-called undulator parameter that is defined by $K = \frac{eB_0\lambda_U}{2\pi m_e c}$ with B_0 being the peak magnetic field on the undulator axis.
The undulator parameter sets a limit to the maximum opening of the light cone $\theta_{max} = K/\gamma$. For $K \leq 1$, the radiation is emitted in a narrow cone into forward direction, which is an important condition to maximize the energy transfer from the electrons to the light field (see Sec. 3.2) and to operate a single-pass FEL in the so-called "self-amplified spontaneous emission" (SASE) mode (see Sec. 3.3).
By considering Eq. 3.2, one recognizes that the wavelength λ_{xuv} can be tuned by varying either the electron energy or the undulator parameter K.

3.2 Interaction of Electrons and Radiation Field

In contrast to FELs in the optical, infrared or THz regime, XUV or X-ray FELs cannot be equipped with resonators as the reflectivity of metals or other mirror coatings drops dramatically for photon energies above 10 eV [235, Ch. 3]. Thus, continuous energy transfer

$$\mathrm{d}W = \mathrm{d}(\gamma m c^2) = \mathbf{F} \cdot \mathrm{d}\mathbf{s} = -e\mathbf{E} \cdot \mathrm{d}\mathbf{s} = -e\mathbf{E} \cdot \mathbf{v}\ \mathrm{d}t \tag{3.3}$$

from the electrons to the radiation field has to be achieved in one single passage through the undulator [130]. In Eq. 3.3, W is the total energy of the electrons, $\mathbf{F}$ is the force vector, $\mathbf{s}$ is the direction vector, $\mathbf{E}$ is the electric field vector and $\mathbf{v}$ is the velocity vector. Due to energy conservation, the radiation field gains energy if $\frac{\mathrm{d}W}{\mathrm{d}t} < 0$.
To deduce a condition for maximum energy transfer, the interaction between a single electron and the radiation field is considered. The field is written as a plane electromagnetic wave with wavenumber $k_{xuv} = 2\pi\lambda_{xuv} = \omega_{xuv}/c$, amplitude E_0 and phase φ_0, which is co-propagating with the electron [130],

$$E_x(y,t) = E_0\ \cos(k_{xuv}y + \omega_{xuv}t + \varphi_0). \tag{3.4}$$

The light wave travels along y and is polarized in x direction. The magnetic field of the undulator points in z direction. The underlying coordinate system is displayed in Fig. 3.2.
According to Eq. 3.3, energy is transferred steadily from the electron to the light wave, if the x-component of the electric field vector E_x and the electron velocity v_x point in the same direction. In Fig. 3.3 (a), this so-called FEL case is illustrated. The opposite case will be laser acceleration. Here, E_x and v_x are pointing in opposite directions and the electron gains energy from the light wave (see Fig. 3.3 (b)).

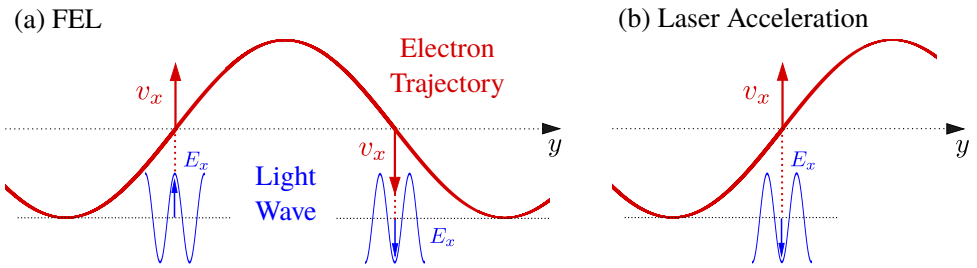

Figure 3.3: (a) FEL case. Energy is transferred from the electron to the light wave. The x-component of electric field vector E_x and of the electron velocity vector v_x point in the same direction. (b) Laser acceleration case. Energy is transferred from the light wave to the electron. E_x and v_x point in opposite directions. Taken and adapted from Ref. [235, Ch. 3].

The light wave travels straight along the y direction, but the electron travels on a longer sinusoidal trajectory. Therefore, its average velocity

$$\langle v_y \rangle = c \left(1 - \frac{1}{2\gamma^2} \left(1 + \frac{K^2}{2} \right) \right) \tag{3.5}$$

is smaller than the speed of light c and the light wave will always propagate ahead of the electron [235, Ch. 3].
To achieve maximum energy gain from the electron to the light wave, the light wave has to slip forward such that E_x and v_x remain parallel for all times. For this condition to be fulfilled, only light waves with wavelengths $\lambda_k = \lambda_{\mathrm{xuv}}/k$ that advance the electron by an integer number $k = 1, 2, 3, ...$ of wavelengths within a half undulator period λ_U will constructively interfere (see Fig. 3.3 (a)). To cross half an undulator period $\lambda_\mathrm{U}/2$, the electron needs the time $t_e = \lambda_\mathrm{U}/2 \langle v_y \rangle$. To travel the same distance, it takes $t_{lw} = \lambda_\mathrm{U}/2c$ for the light wave and the time difference is given by

$$\Delta t = t_e - t_{lw} = \frac{\lambda_\mathrm{U}}{2} \left(\frac{1}{\langle v_y \rangle} - \frac{1}{c} \right). \tag{3.6}$$

To obtain constructive interference, the time difference Δt has to equal $\lambda_k/2c$ (for $k = 1, 2, 3, ...$). Solving for λ_k and inserting the definition of $\langle v_y \rangle$ from Eq. 3.5 yields

$$\lambda_k = \frac{\lambda_\mathrm{U}}{2k\gamma^2} \left(1 + \frac{K^2}{2} \right) \text{ for } k = 1, 2, 3, ... \tag{3.7}$$

The fundamental wavelength is $\lambda_1 = \lambda_{\mathrm{xuv}}$, which is equal to the wavelength already derived in Eq. 3.2. A more accurate derivation shows that only odd harmonics $k = 1, 3, 5, ...$ are observed along the propagation axis y [35, Ch. 4]. However, due to the beam divergence and the long distances between undulator and experiment, also off-axis even harmonics can be present in the FEL spectrum. Typically the intensity of the 2$^{\mathrm{nd}}$ and 3$^{\mathrm{rd}}$ harmonic is some tenth of a percent of the fundamental and drops for higher harmonics [47].

3.3 Microbunching and SASE

In the previous section, an expression for the resonance wavelength was derived for the idealized case of a single electron interacting with the radiation field. However, the situation is more complicated in an actual FEL, because here all electrons within one bunch interact with the radiation field at once. To still fulfill the resonance condition for energy transfer from the electrons to the light wave, the electrons within one bunch need to be spatially modulated and compressed to so-called microbunches that are separated by the resonance wavelength λ_{xuv} (see Eq. 3.7). Only in this case, the electrons of one microbunch emit radiation coherently. The built-up of the microbunch structure is depicted in Fig. 3.4.

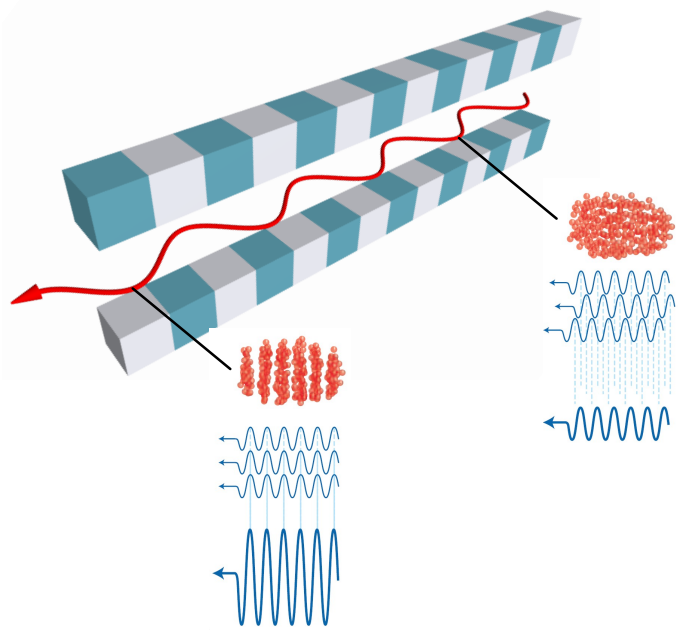

Figure 3.4: Schematic representation of microbunching in an undulator. At the entrance on the right, the electrons (red balls) are randomly phased and emit radiation incoherently (blue waves). The SASE mechanism leads to the bunching of the electrons at the resonance wavelength λ_{xuv} (see Eq. 3.7). At the end of the undulator on the left, the emitted radiation is coherent. After Ref. [165].

At the beginning of the undulator, the electrons are distributed uniformly within the bunch and each electron incoherently emits radiation. However, there is a chance that small fluctuations in the radiation field or variations in the spatial distribution of the electrons at the beginning of the undulator can serve as a seed to initiate the growth of a microbunch structure. Then, the electrons within one microbunch start to emit radiation coherently and the back action of the radiation field on the electrons further amplifies the modulation. Due to the stochastic nature and

the reinforcing characteristics, this process is referred to "self-amplified spontaneous emission" (SASE). At the end of the undulator, the SASE mechanism reaches saturation and the microbunches start to fall apart. In the following, microbunching and the SASE mechanism are described in a more detail.
In high-gain FEL theory [199], the SASE mechanism is accounted for by the so-called FEL equations, i.e., a system of coupled differential equations, which describe the electron trajectory and the generation of the radiation field in a self-consistent way [21]. On the one hand, the FEL equations are based on Maxwell's wave equations, which describe the radiation field induced by the electron current. On the other hand, the Lorentz force equation describes the forces on the electrons by the radiation and the undulator field [165].
For initially homogeneously distributed electrons, i.e., no phase relation, the FEL equations have a stable solution and no energy is transferred from the electrons to the radiation field. In contrast, the SASE mechanism is a special, because unstable, solution to the FEL equations for which perturbed initial conditions lead to an exponential energy gain of the radiation field [199]. In Ref. [165] a figurative description of the SASE gain mechanism is given and that is shown in Fig. 3.5.

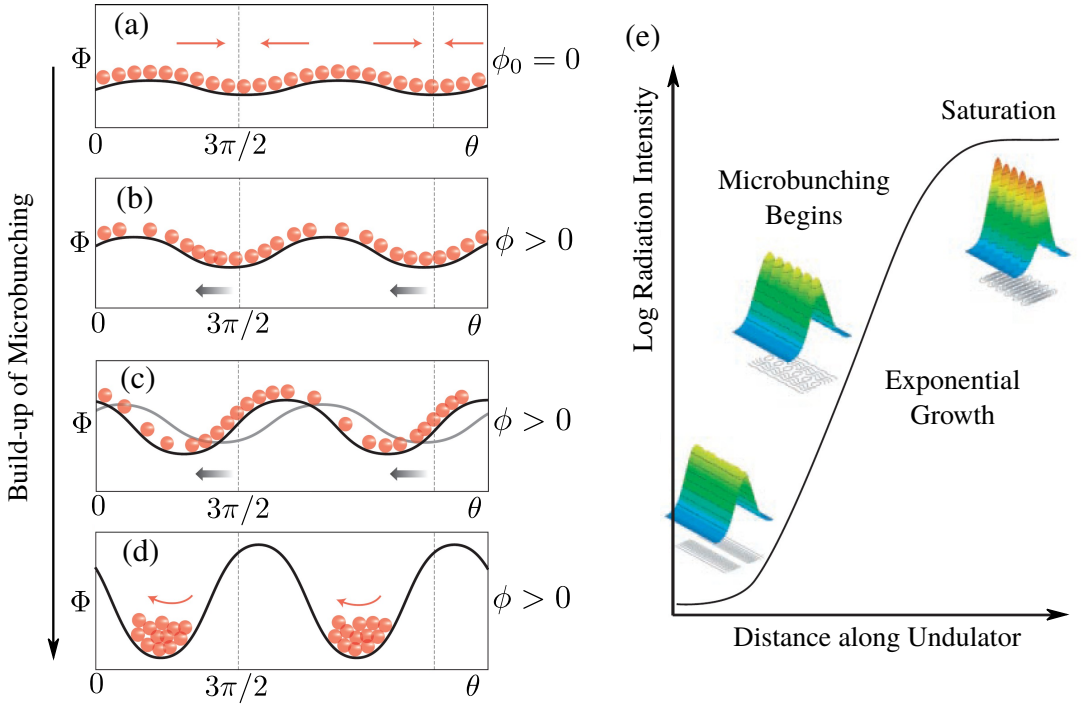

Figure 3.5: (a)-(d) Plots to illustrate the high-gain FEL mechanism. Explanations are given in the text. Taken from Ref. [165]. (e) Schematic illustration of the exponential growth of the FEL intensity (solid line) and the microbunching of the electrons (dark blue: low electron density; red: high electron density) in dependence on the distance along the undulator. Adapted from Ref. [176].

The high-gain FEL mechanism is illustrated for the case of a small initial field amplitude fluctuation that serves as an input seed. The initial light wave phase ϕ_0 is zero. The forces, which compress the electrons, are represented by periodic potential wells Φ that are traveling at the resonance velocity $\langle v_y \rangle$ (see Eq. 3.5) in the rest frame of the electrons from left to right. The initial seed field causes the electrons to get bunched around the phases $\theta = 3\pi/2$ and $\theta = 7\pi/2$ (red arrows in Fig. 3.5 (a)). In consequence of this small bunching, the light field phase ϕ increases ($\phi > 0$) and the potential wells are shifted to the left by $(\theta + \phi)$ (see Fig. 3.5 (b) and (c)). In doing so, the electrons are raised in the potential and transfer kinetic energy to the radiation field by "falling" into the potential wells. Accordingly, the depth of the potential wells is increased and the exponential instability is established. The SASE mechanism continues until the light field amplitude is so large that maximum bunching is achieved and the increase of ϕ declines (see Fig. 3.5 (d)). The process reaches saturation when the electrons begin to "surf" in the potential wells, i.e., the re-absorbed energy from the radiation field equals the kinetic energy gained from the potential. The exponential growth of the radiation intensity within one passage through the undulator gives rise to the term high-gain FELs. The evolution of microbunching and the accompanied growth in radiation intensity is depicted in Fig. 3.5 (e). The bunching of electrons results in spatially coherent emission of radiation. This directly affects the emitted light intensity, which now scales like $I \sim N^2$ with N being the number of electrons.
For high-gain FELs, the so-called gain length l_g is an important quantity that defines the distance along the undulator axis y after which the radiation intensity increased aobut a factor of e:

$$I(y) = I_0 \exp\left(\frac{y}{l_g}\right). \tag{3.8}$$

The gain length l_g depends critically on the electron beam parameters at the beginning of the undulator, e.g. the electron energy, the peak current and the beam diameter. The saturation regime is typically reached after a distance of about $20 \times l_g$ [176]. With increasing electron energies and correspondingly shorter output wavelengths, also the gain length increases. For this reason, XUV FELs like FLASH feature undulators of about 30 m length [241], whereas undulators of X-ray FELs need to in the order of 100 m [52].

3.4 Pulse Characteristics

As a consequence of the stochastic nature of the SASE mechanism (see Sec. 3.3), the emitted FEL pulses are subject to statistical fluctuations[27] as well. Fig. 3.6 shows shot-to-shot spectra taken at the SASE free-electron laser FLASH (see Sec. 3.5) at a central wavelength of $\lambda = 32.2\,\mathrm{nm}$. The spectral distribution is different for each shot and shows strong variations in amplitude and phase. Each pulse consists of a noisy background which is superimposed by narrow spikes.
Especially for time-resolved experiments, the irregularity of SASE pulses is challenging, because the knowledge of pulse duration and shape is crucial to determine the temporal resolution and to interpret the data.
In difference to the optical regime, methods to characterize XUV pulses are not experienced techniques and are still under development for FELs. Terahertz streaking using gas-phase targets [75, 85] and XUV/optical cross-correlation using solid-state targets [215] are two approaches to measure the pulse duration on a shot-to-shot level. These methods are technically demanding as they rely on a jitter-free synchronization between the FEL pulse and an external probe pulse.

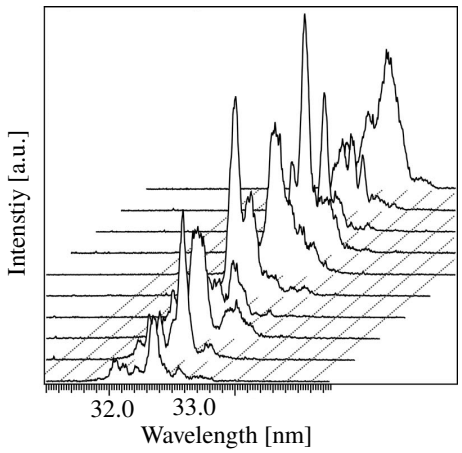

Figure 3.6: Shot-to-shot SASE FEL spectra at a central wavelength of $\lambda = 32.2\,\mathrm{nm}$ ($\hbar\omega = 38.5\,\mathrm{eV}$) recorded by a grazing incidence stigmatic spectrometer at the free-electron laser FLASH. From Ref. [47].

In order to eliminate the problems with regard to synchronization, intensity autocorrelation is a self-referencing method to measure pulse durations [181, 187]. The basic idea is to split the pulse into two parts. Afterwards, the two split pulses are send into a non-linear medium whose response is monitored as a function of the

[27] Higher-harmonics of an external laser can be used to actively initiate the emission of the FEL radiation. In contrast to SASE FELs, the pulses from these so-called seeded FELs feature a high shot-to-shot wavelength stability, low-intensity fluctuations and a close to transform-limited bandwidth [5].

delay between the pulses. In the present case, the non-linear signal is the yield of ions created by atomic photoionization. According to Eq. 2.16, the yield of ions created by direct photoionization depends to the n^{th}-power on the intensity I, $Y \propto I^n$. Thus, the n^{th}-order autocorrelation signal generated by two pulse replicas, which are delayed by τ, is given by [247]:

$$A^{(n)}(\tau) = \int_{-\infty}^{+\infty} \mathrm{d}t \left| (E(t) + E(t-\tau))^n \right|^2 . \tag{3.9}$$

Here, $E(t)$ and $E(t-\tau)$ are the time-dependent electric fields of the undelayed and delayed part of the pulse, respectively. $A^{(n)}(\tau)$ represents the optical-cycle interference between $E(t)$ and $E(t-\tau)$ and is therefore called interferometric autocorrelation signal. For XUV wavelengths, the uncertainty in the delay τ is usually larger than the optical period T and the interferences are washed out[28]. Hence, the cycle-averaged, or n^{th}-order, intensity autocorrelation signal reads [247]:

$$\bar{A}^{(n)}(\tau) = \int_{\tau-T}^{\tau} \mathrm{d}\tau' A(\tau') = \sum_{i=1}^{n-1} \binom{n}{i} \int_{-\infty}^{+\infty} \mathrm{d}t I(t)^i I(t-\tau)^{n-i} + \text{const.} \tag{3.10}$$

The intensity autocorrelation signals of Ne^{2+} and Ar^{4+} ions shown in Fig. 3.7 are recorded at the free-electron laser FLASH2 (see Sec. 3.5) using a reaction microscope (see Ch. 4) in combination with a back-reflecting split-mirror (see Ref. [102] and Sec. 9.1). Both spectra show two distinct features: a narrow peak and a broad hump. The spectra are fitted using a Bi-Gaussian function. The analysis of the hump structure yields the average pulse duration. At a photon energy of $\hbar\omega = 26.9\,\text{eV}$, two photons are necessary to ionize from Ne^+ to Ne^{2+} and the measured autocorrelation signal is of 2^{nd}-order (see Fig. 3.7 (a)). In order to get the temporal width of the pulse σ_{pulse}, the width σ_{fit} resulting from a Gaussian fit to the hump structure needs to be divided by $\sqrt{2}$. The average pulse duration expressed in terms of the full width at half maximum (FWHM) is thus given by $T^{(2)}_{\text{pulse}} = \sqrt{2\ln(2)}\sigma_{\text{fit}}$. The autocorrelation signal of Fig. 3.7 (a) returns a pulse duration of $T^{(2)}_{\text{pulse}} = (32 \pm 2)\,\text{fs}$ (FWHM).
Fig. 3.7 (b) shows a delay-dependent Ar^{4+} yield. The ionization from Ar^{3+} to Ar^{4+} is a 3^{rd}-order process, because three photons of $\hbar\omega = 23.7\,\text{eV}$ need to be absorbed. For the 3^{rd}-order, the pulse width is given by $\sigma_{\text{pulse}} = \sqrt{2/3}\sigma_{\text{fit}}$ and the pulse duration at FWHM is $T^{(3)}_{\text{pulse}} = 4/3\sqrt{2\ln(2)}\sigma_{\text{fit}}$. Thus, the autocorrelation signal of Fig. 3.7 (b) results in a pulse duration of $T^{(3)}_{\text{pulse}} = (71 \pm 3)\,\text{fs}$ (FWHM).
The narrow peak on top of the broad hump originates from the interference of the spikes within an FEL pulse and is related to the temporal coherence time [201]. Fits return coherence times of 4 fs (FWHM) (see) and 7 fs (FWHM) for Fig. 3.7 (a)

[28] Recently, the authors of Ref. [272] have successfully demonstrated interferometric autocorrelation in the XUV regime by using a high-precision split-delay optics,

and (b), respectively. This is in agreement with earlier experiments, where the coherence time is determined to ∼6 fs [180]. A more detailed analysis of intensity autocorrelations measured at FLASH2 can be found in Ref. [266].

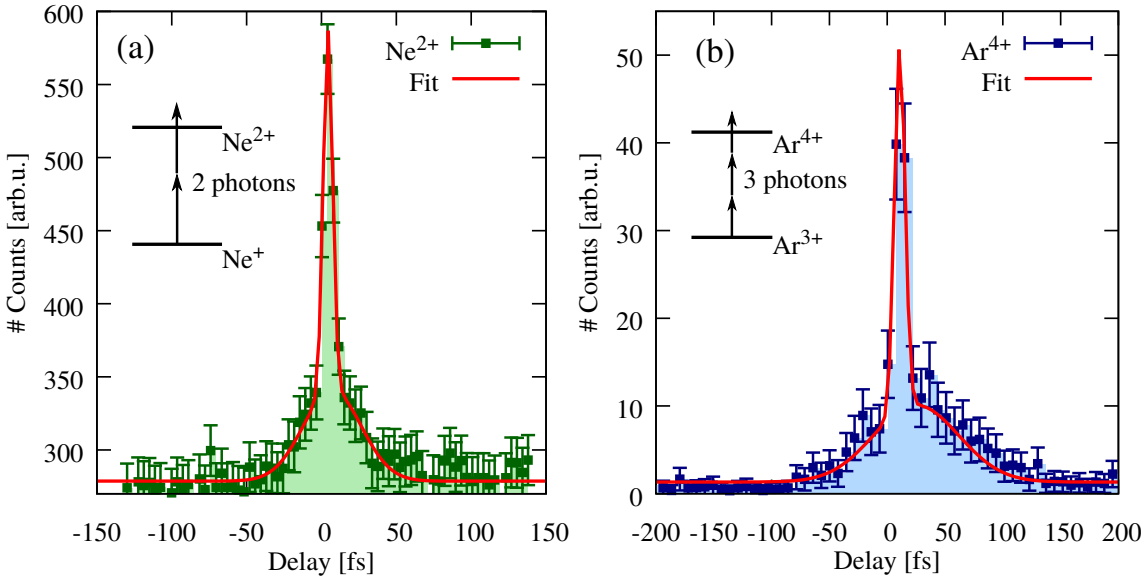

Figure 3.7: Intensity autocorrelation signals measured at FLASH2. (a) 2nd-order signal. Yield of Ne^{2+} ions recorded at $\hbar\omega = 26.9$ eV as a function of the delay between the two pulse replicas. Two photons are needed to ionize from Ne^{+} to Ne^{2+}. A Bi-Gaussian function is used to fit the data (red line). (b) 3rd-order signal. Yield of Ar^{4+} ions recorded at $\hbar\omega = 23.7$ eV as a function of the delay between the two pulse replicas. Three photons are needed to ionize from Ar^{3+} to Ar^{4+}. A Bi-Gaussian function is used to fit the data (red line).

3.5 Free-Electron Laser in Hamburg (FLASH)

The **F**ree-Electron **Las**er in **H**amburg (FLASH) originated from the TESLA test facility project [217]. It was the first FEL worldwide to lase at XUV wavelengths [2, 13]. Since its opening in 2005, the facility was extended and operates now two single-pass XUV FELs that are driven by the same superconducting linear accelerator [58]. First simultaneous operation of FLASH1 and FLASH2 was achieved in summer 2014. The most important parameters for FLASH1 and FLASH2 are listed in Tab. 3.1. An overview of the FLASH facility is given in Fig. 3.8 and the main components are briefly explained according to Ref. [241].

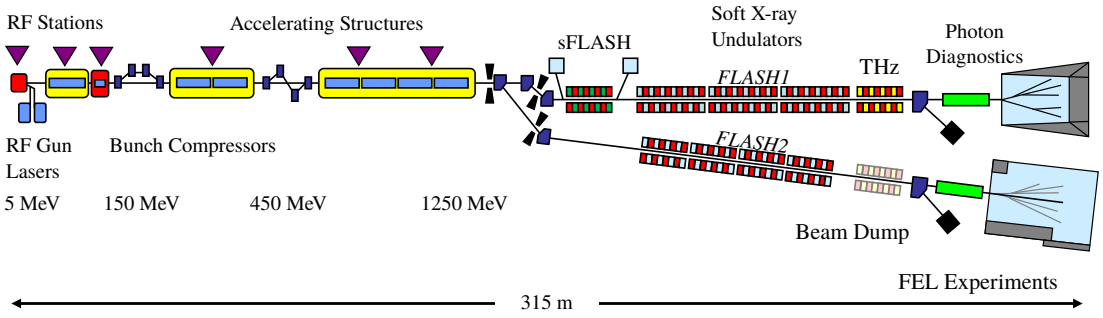

Figure 3.8: Overview of the FLASH facility. From Ref. [58].

3.5.1 Electron Source

The electron source is the first upstream component. It is based on laser ablation and pulses of a 262-nm-laser with 4 ps duration and 1 µJ pulse energy hit a Cs_2Te photo cathode [2]. Each laser shot releases one bunch of electrons with bunch charges in the order of 0.02 to 1.2 nC. The pulsed laser is synchronized to a superconducting 1.3 GHz radio-frequency (RF) cavity where a field gradient of 40 MV/m accelerates the electrons away from the photo cathode to energies up to 5 MeV [13]. FLASH has a special bunch train pattern. In this so-called burst-mode, a bunch train consisting of 1 to 750 bunches with an intra-bunch spacing of 1 µs (1 MHz) to 25 µs (40 kHz) is released with a repetition rate of 10 Hz [58]. As each individual electron bunch generates one XUV pulse, the electron bunch repetition rate is directly linked to the XUV pulse repetition rate. The two undulator lines have their own photo-injector laser, which allows to independently set bunch separation, number of bunches and the bunch charge for FLASH1 and FLASH2. More details about possible bunch train patterns are given in Sec. 4.7 and Ref. [58].

3.5.2 Acceleration Structures

In matters of high peak currents, small emittance, little momentum spread and short pulse lengths, the demands on the electron bunch are very high for the SASE process to take place. These high requirements are so far only fulfilled by linear accelerators. The superconducting RF linear accelerator of FLASH was developed within the TESLA[29] collaboration and consists of seven accelerating modules. Each module is assembled by eight niobium 1.3 GHz RF cavities which are powered by klystrons. In contrast to normal conducting accelerators, the TESLA technology allows to use RF pulses of several hundred microseconds up to continuous wave, which in principle can be completely filled with electron bunches [58]. As a consequence, the repetition rate of superconducting accelerators exceeds that of normal conducting ones. After having passed the accelerating structures, the electrons have a maximum energy of 1250 MeV (see Fig. 3.8). Two magnetic chicanes are used to compress the electron bunches to achieve peak currents in the order of kiloamperes. Further details about the accelerator can be found in Refs. [2, 242].

3.5.3 Undulators

A kicker-septum system splits the electron bunch train between the two undulator lines within $20 - 50\,\mu s$ switching time [58]. The bunch trains for FLASH2 are extracted at an angle of 12° with respect to FLASH1 (see Fig. 3.8). At FLASH1, the radiation is produced by six 4.5 m long fixed-gap undulators made of permanent NdFeB magnets with a period of $\lambda_U = 27.3\,mm$. The peak magnetic field of 0.48 T results in an undulator parameter of $K = 1.23$ [242]. The photon energy can only be varied by changing the kinetic energy of the electrons. In contrast to FLASH1, FLASH2 features variable-gap undulators with a period of $\lambda_U = 31.4\,mm$. Hence, by varying the gap, the undulator parameter can be changed from $K = 0.7 - 2.8$ [242]. This allows to change the photon energy within seconds. The FLASH2 undulator line consists of 12 segments with a segment length of 2.5 m.

[29] TeV-Energy Superconducting Linear Accelerator.

Table 3.1: Parameters for FLASH1 (delivered to users) and FLASH2 (achieved during commissioning). Taken from Ref. [58].

	FLASH1	FLASH2
Electron beam		
Energy range	$0.35 - 1.25\,\mathrm{GeV}$	$0.4 - 1.25\,\mathrm{GeV}$
Peak current	$2.5\,\mathrm{kA}$	$2.5\,\mathrm{kA}$
Bunch charge	$0.06 - 1.2\,\mathrm{nC}$	$0.02 - 1\,\mathrm{nC}$
Normalized emittance	$1.4\,\mathrm{mm\,mrad}$	$1.4\,\mathrm{mm\,mrad}$
Energy spread	$0.2\,\mathrm{MeV}$	$0.5\,\mathrm{MeV}$
Average β-function	$10\,\mathrm{m}$	$6\,\mathrm{m}$
Repetition rate	$10\,\mathrm{Hz}$	$10\,\mathrm{Hz}$
Number of bunches per second[a]	7500	7500
Bunch separation	$1 - 25\,\mu\mathrm{s}$	$1 - 25\,\mu\mathrm{s}$
Undulator		
Type	planar, fixed gap	planar, variable gap
Period	$27.3\,\mathrm{mm}$	$31.4\,\mathrm{mm}$
K_{rms}	0.9	$0.7 - 1.9$
Segment length	$4.5\,\mathrm{m}$	$2.5\,\mathrm{m}$
Number of segments	6	12
Photon beam SASE		
Wavelength range (fundamental)	$4.2 - 52\,\mathrm{nm}$	$4 - 90\,\mathrm{nm}$
Average single pulse energy	$1 - 500\,\mu\mathrm{J}$	$1 - 500\,\mu\mathrm{J}$
Pulse duration (FWHM)	$30 - 200\,\mathrm{fs}$	$10 - 200\,\mathrm{fs}$
Peak power	$1 - 5\,\mathrm{GW}$	$1 - 5\,\mathrm{GW}$
Spectral width (FWHM)	0.7 % - 2 %	0.5 % - 2 %
Peak brilliance[b]	$10^{28} - 10^{31}$	$10^{28} - 10^{31}$

[a] Shared between FLASH1 and FLASH2.
[b] Brilliance: Photons/(s · mrad^2 · mm^2 · 0.1 % Bandwidth).

4 Reaction Microscope

Reaction **mi**croscopes (REMIs) [185] are multi-particle coincidence spectrometers, which are widely used in atomic and molecular physics. They are versatile instruments to investigate the most fundamental reactions in atoms or molecules triggered upon absorption of photons, impact of electrons or bombardment with ions [269]. To do so, the charged reaction fragments, i.e., ions and electrons, are accelerated onto large-area time- and position-sensitive detectors. By measuring the time of flight (TOF) and the impact position of the particles on the detector, the complete initial 3-dimensional momentum vectors can be reconstructed (see Sec. 4.4). The combination of a homogeneous electric and magnetic field ensures a solid angle acceptance of 4π for ions and electrons, respectively. A benefit of this type of momentum spectroscopy is to detect associated reaction fragments in coincidence. This enables to perform so-called kinematically complete experiments [141]. The reaction microscope used at FLASH is schematically shown in Fig. 4.1. The FEL beam (purple) is focussed into a supersonic gas jet, which contains the target atoms or molecules (green balls). Created ions (red trajectory) and electrons (blue trajectory) are separated by their charge and guided onto opposing detectors by an electric field produced by the spectrometer. An additional magnetic field generated by the Helmholtz coils ensures 4π acceptance also for the electrons.

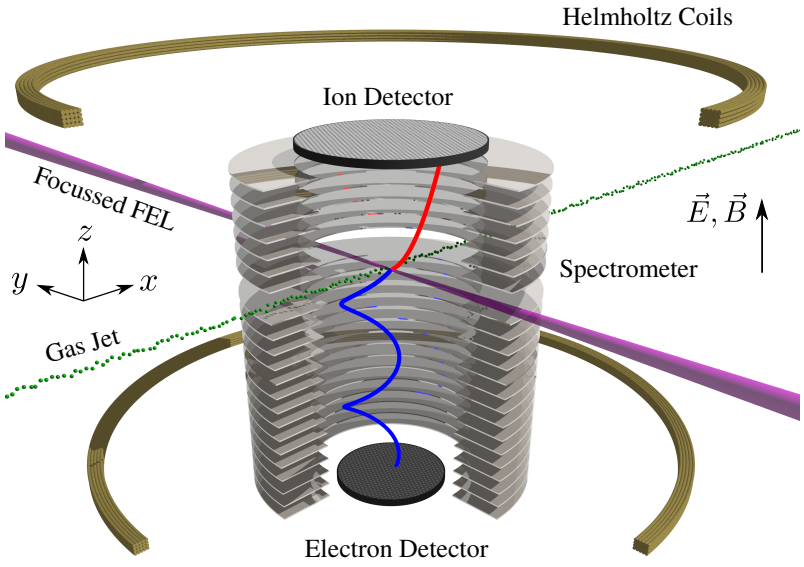

Figure 4.1: Illustration of the FLASH reaction microscope.

In Sec. 4.1 through 4.3, the main components of a REMI are introduced. The reconstruction of ion momenta, the assignment of coincidences and the kinetic energy release (KER) are discussed in Sec. 4.4, 4.5 and 4.6, respectively. In the last Sec. 4.7, the challenges of operating a REMI at an FEL are addressed.

4.1 Supersonic Gas Jet

Based on the concept of measurement, experiments done with a reaction microscope are usually in the gas phase. This prerequisite has some important consequences.
First, the thermal energy of the target atoms or molecules has to be smaller than the measured energy of the fragments after the reaction. The mean kinetic energy of gas particles at room temperature is $k_B T \approx 1/40\,\mathrm{eV}$. Therefore, it is necessary to cool the target atoms or molecules to achieve sufficient momentum and energy resolution.
Second, the interaction volume should be well localized, because the momentum that is gained in the electric field of the spectrometer depends on the starting position of the particle (see Sec. 4.2). According to this, the momentum resolution improves with the reduction in size of the interaction volume. In the present case, the interaction volume is limited by the focal spot size (diameter some µm) and not by the spatial extension of the gas jet (maximum diameter $\sim 2\,\mathrm{mm}$).
Third, the target density needs to low, i.e., in the order of $< 10^{10}$ particles/cm^3, to perform coincidence experiments. Otherwise, too many reaction fragments are created in the interaction volume. If this happens, it will become impossible to correctly sort the fragments belonging to one reaction.
In the present case, these requirements are fulfilled by exploiting the thermodynamic effect of supersonic expansion to create a cold target gas jet with typical temperatures of some Kelvin.
For supersonic expansion to happen, gas is expanded through a tiny nozzle[30] from a reservoir of high pressure into a low pressure region. A scheme of the process is depicted in Fig. 4.2 [244]. The reservoir in front of the nozzle has a backing pressure p_0 and a temperature T_0. In this region, gas flows slowly and the Mach number[31] M_a is much smaller than one ($M_a \ll 1$). The pressure p_e in the expansion region, however, is much smaller than the backing pressure p_0 and particles are accelerated along the pressure gradient, indicated by the dashed arrow. In first approximation, the process can be considered isentropic as heat conduction and friction are negligible due to the small thickness of the nozzle[32]. Consequently, entropy is conserved.

[30] Nozzle diameters are typically in the order of some tens of µm.
[31] The Mach number is defined as the ratio between the velocity of the gas particles v_{jet} and the local speed of sound v_{sound}, i.e., $M_a = v_{\mathrm{jet}}/v_{\mathrm{sound}}$.
[32] Typically thickness $100 - 200\,\mu\mathrm{m}$.

At a pressure ratio of $p_0/p_e = 2.1$, the Mach number equals one ($M_a = 1$) and all gas particles move exactly at the local sound velocity $v_{\text{jet}} = v_{\text{sound}}$ [244].

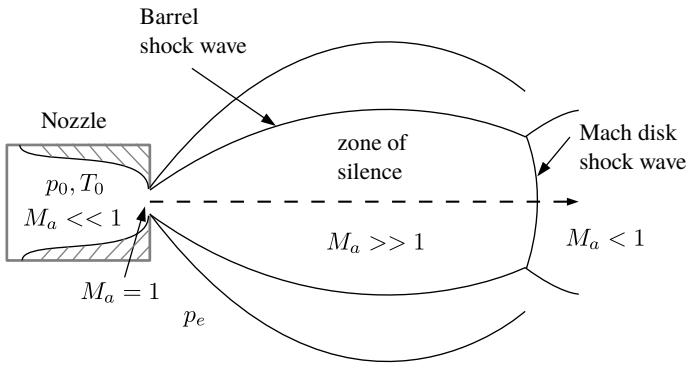

Figure 4.2: Supersonic expansion. Adapted from Ref. [244].

If the backing pressure p_0 increases continuously, the pressure at the end of the nozzle exceeds p_e and the gas is underexpanded. Then, the gas expands in shock waves for pressure balancing. The formation of the shock waves comes along with the creation of a so-called "zone of silence", i.e., a region where $M_a \gg 1$ and the jet velocity reaches supersonic speed (see Fig. 4.2). To compensate the reduction of spatial density, the density in momentum space increases which results in a decrease of temperature. For an ideal gas, the maximum velocity of the jet is given by [147]:

$$v_{\text{jet}} = \sqrt{\frac{2k_B T_0}{m} \frac{\gamma}{\gamma - 1}}. \tag{4.1}$$

Here, $k_B = 1.38 \cdot 10^{-23}\text{J/K}$ is the Boltzmann constant, T_0 the temperature before the expansion, m the particle mass and $\gamma = \frac{f+2}{f}$ the adiabatic index with f being the number of degrees of freedom of the particle.
Usually, shock waves travel at the speed of sound in a gas. In a supersonic expansion, however, informations about downstream boundary conditions, like residual gas pressure or the walls of the expansion reservoir, cannot be transported and the gas overexpands to pressures smaller than p_e. In the outer regions, the jet gets compressed by Barrel shock waves of high pressure and high temperature gradients. In this regions, the particle density is very high and the main part of the jet is reflected to form the Mach disk shock wave (see Fig. 4.2). Here, reflected shock waves add up to shock waves of high pressure and temperature gradient and the expansion cone closes up [198].
With growing ratio of $v_{\text{jet}}/v_{\text{sound}}$, the number density of particles decreases quickly and accordingly also the number of collisions between the gas particles. This means that properties of the gas jet like the velocity v_{jet} and the temperature component $T_{||}$ along the jet propagation direction get "frozen". The lowest longitudinal

target temperatures obtained by supersonic expansion are $T_{||} \leq 1\,\mathrm{K}$ for helium[33]. The transverse temperature component decreases with increasing distance from the transition region [147]. To obtain a cold jet, the gas particles need to be extracted before the breakdown of the expansion, i.e., within the zone of silence and in front of the Mach disk (see Fig. 4.2). In the experiment, a sharp-edged conical skimmer is coaxially opposing the nozzle to peel off cold gas particles from the zone of silence (see inset of Fig. 4.3). An empirical formula for the distance x_{Mach} from the nozzle to the Mach disk is given by[198]:

$$x_{\mathrm{Mach}} = 0.67 d \sqrt{\frac{p_0}{p_e}}, \tag{4.2}$$

with nozzle diameter d, backing pressure p_0 and pressure in the expansion region p_e. The so-called speed ratio S measures the degree of transformation of the free enthalpy of the gas into directed kinetic energy. It is defined by the ratio of the jet velocity v_{jet} and the thermal velocity of the gas particles $v_{\mathrm{thermal}} = \sqrt{2 k_B T_{||}/m}$.

$$S = \frac{v_{\mathrm{jet}}}{v_{\mathrm{thermal}}} = \sqrt{\frac{\gamma}{\gamma - 1} \frac{T_0}{T_{||}}} \tag{4.3}$$

The speed ratio S is reached after full expansion of the gas and depends, e.g., on the backing pressure p_0, the nozzle diameter and some gas-specific constants[34].

Experimental Implementation

The REMI at FLASH features six jet stages, which are separated by apertures and are differentially pumped. This ensures that in spite of backing pressures of up to 70 bar, ultra-high vacuum (UHV) conditions of $\leq 10^{-11}$ mbar are conserved in the main chamber (see Sec. 4.7.1). Fig. 4.3 shows a schematic lateral cut through the experimental setup along the jet direction. The gas expands from a reservoir through a tiny nozzle[35] into the first jet stage. As described above, a first skimmer, which extends into the zone of silence, selects only the cold gas particles with a narrow longitudinal momentum distribution. A second skimmer further limits the transverse momentum component of the jet (see inset of Fig. 4.3). The nozzle is

[33] Even lower target temperatures of < 2 mK are achieved in reaction microscopes that use Magneto-Optical-Traps (MOTs) for target preparation, e.g., Refs. [67, 113, 296].

[34] In case of supersonic expansion, an analytic expression for the speed ratio S is given by solving the classical Boltzmann equation [244]:

$$S = A \left(\sqrt{2} \frac{p_0 d}{k_B T_0} \left(\frac{5 3 C_6}{k_B T_0} \right)^{1/3} \right)^B$$

with backing pressure p_0, nozzle diameter d, Boltzmann constant k_B, temperature T_0 and gas-specific constants A, C_6, and B.

[35] Depending on the experiments, diameters between 5 to 50 µm are used.

mounted on a triaxial xyz-manipulator, which allows to adjust the distance to the first skimmer in x-direction as well as the position in the perpendicular (y, z)-plane. In this way and by varying the backing pressure, the target density can be regulated. The subsequent stages $(3, 4, 5, 6)$ are separated by small apertures of 2 mm inner diameter. Three pairs of slits (two vertical, one horizontal) in the jet stages 4, 5 and 6 allow to tune the jet divergence in the (y, z)-plane and thus the target density. Finally, a spatially well-confined (diameter ≤ 2 mm) and cold jet enters the main chamber.

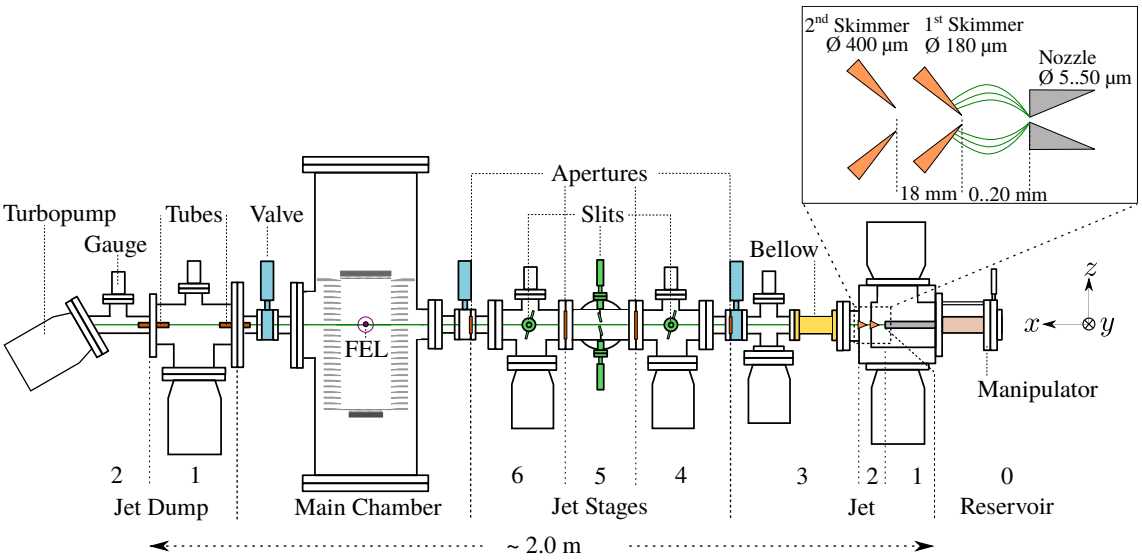

Figure 4.3: Schematic lateral cut through the FLASH reaction microscope along the jet direction. From right to left: Jet chamber, jet stages, main chamber and jet dump. Inset on the top right: Detailed view of the first and second jet stage.

Jet particles, which are not ionized, are collected in the jet dump in order to avoid an increase of the residual gas pressure in the main chamber by target gas particles. The main chamber, jet dump 1 and jet dump 2 are separated by small tubes of 4 mm inner-diameter for differential pumping. Tab. 4.1 lists typical pressures in the different stages during jet operation.

Table 4.1: Typical pressures during operation of an argon jet at a backing pressure of $p_0 \approx 3$ bar and a nozzle diameter of 30 µm. (mc: main chamber, d1: dump 1, d2: dump 2).

Stage	1	2	3	4	5	6	mc	d1	d2
Pressure [mbar]	10^{-3}	10^{-6}	10^{-7}	10^{-8}	10^{-9}	10^{-10}	10^{-11}	10^{-11}	10^{-10}

4.2 Spectrometer

The FEL beam is focussed into the supersonic gas jet in a perpendicular arrangement in the middle of the main chamber (see Fig. 4.1). Ions and electrons resulting from ionization events of atoms or molecules within the spectrometer volume are accelerated onto time- and position-sensitive detectors by means of a homogeneous electric field. The spectrometer is depicted in Fig. 4.4.

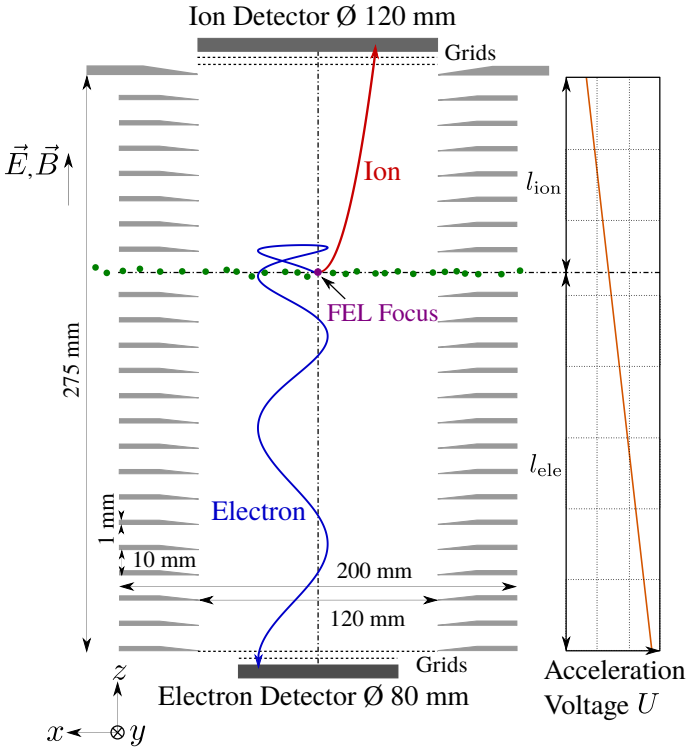

Figure 4.4: Drawing of the spectrometer. Adapted from Refs. [59, 236].

The spectrometer consists of 22 rings made of annealed stainless steal, which are coaxially separated by a distance of 10 mm along the spectrometer axis. The spectrometer rings are 1 mm thick and have an inner-diameter of 120 mm and an outer-diameter of 200 mm, respectively. The inner boundary of the rings is sharp-edged towards the center to generate well-defined equipotential planes to ensure a homogeneous electric field. The individual rings are electrically connected by a cascade of 1 kΩ resistors which allows to apply a constant potential over the entire spectrometer (see Fig. 4.4). At both ends of the spectrometer, fine-mashed metal grids[36] ensure a homogeneous termination of the electric field. Additional grids in front of the ion and electron detector are used to post-accelerate the particles in order to increase the detection efficiency.

[36] Wire diameter: 30 µm, mesh size: 224 µm, transmittance: ∼ 80 %.

In total, the spectrometer is 275 mm long. Compared to other reaction microscopes, the ion side is kept short ($l_{\text{ion}} = 94.5\,\text{mm}$) by purpose. Ions stemming from Coulomb explosions of molecules have large transversal momentum components, because very high ion charge states are reachable in the FEL focus [238]. Thus, the combination of a relatively short acceleration distance and electric field strengths in the order of some tens of V/cm ensures a high acceptance for Coulomb-exploded ions. The electron side l_{ele} is about a factor of two longer than the ion side. Hence, the electrons' time of flights (TOFs) are stretched, which results in a better momentum resolution along the spectrometer axis. Another feature of the present spectrometer is the absence of a field-free drift region after the acceleration distance, which is quite common in experiments using ions or electrons as projectiles. In such experiments, the drift region compensates for uncertainties in the TOF of the ions due to the relatively large interaction region caused by the finite size of the projectile beam [269]. In the present experiment, no drift region is needed, because the interaction region is well-defined by the small FEL focal spot diameter of $\leq 20\,\mu\text{m}$.
A particle of mass m and charge q with zero initial momentum $p_z = 0$ along the spectrometer axis z reaches the detector after a TOF[37]

$$t = l_a \sqrt{\frac{2m}{qU}} \propto \sqrt{\frac{m}{q}}. \tag{4.4}$$

Here, U is the applied voltage and l_a the acceleration length. The proportionality of the TOF to the square root of the mass-to-charge ratio allows to distinguish different ion species. For this to hold, the TOFs of different ion species have to differ significantly. In the usual case, the ions gain more kinetic energy in the electric field of the spectrometer than the initial kinetic energy released in the fragmentation reaction and the discrimination condition is well fulfilled.
Fig. 4.5 shows a typical ion TOF mass spectrum recorded at a photon energy of $\hbar\omega = 27\,\text{eV}$ and argon as target. All ions besides the Ar^{n+} ions ($n = 1, \ldots, 5$) are undesired background events, a problem that is discussed in more detail in Sec. 4.7.1. The Ar^{n+} ions arise from the cold supersonic jet and therefore have sharp TOF peaks. Like this, they can be distinguished from the broad ion background.
For the same momentum, light electrons move with much higher velocities compared to the heavier ions ($m_{\text{proton}}/m_e \approx 1800$). Therefore, a magnetic field is additionally applied parallel to the electric field. By the magnetic field, electrons are forced onto spiral orbits onto the detector (blue trajectory in Fig. 4.4) and a 4π acceptance is also achieved for the electrons. The magnetic field in the order of 10 Gauss is generated by a pair of Helmholtz coils.

[37] $l_a = \frac{1}{2}at^2 \rightarrow t = \sqrt{\frac{2l_a}{a}}$, where the acceleration a is given by $a = \frac{qU}{l_a m}$.

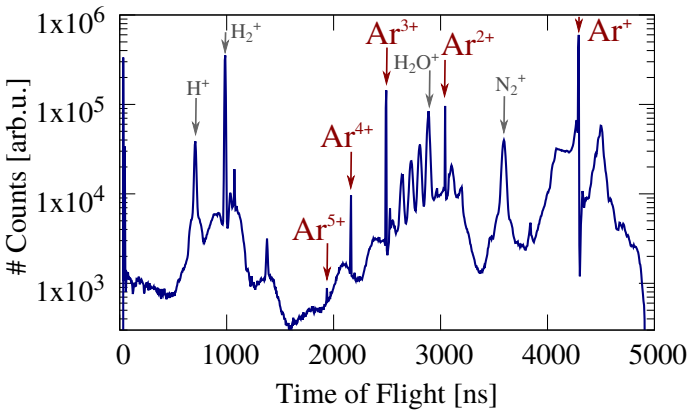

Figure 4.5: Typical ion TOF mass spectrum. Different ion species are identified by their characteristic TOF, which is proportional to $\sqrt{m/q}$.

4.3 Detectors

Large-area detectors measure the time of flight and the impact position of ions and electrons. The particles first hit a microchannel plate (MCP), which amplifies the signals and allows to extract the TOF information by referencing each induced signal to an external trigger. A delay-line anode located behind the MCP is used to obtain the position information. Fig. 4.6 gives an overview of the detector assembly and its working principle.

4.3.1 Microchannel Plates

Microchannel plates (MCPs) are composed of a matrix of parallel arranged small channels (typically diameter 10 - 100 µm), which is embedded in a material of high electric resistance, e.g., lead glass [283]. The channel walls are made from materials with a low electron work function, for example GaP or GaAsP. This allows an impinging primary particle to easily break off secondary electrons from the channel walls (see Fig. 4.6 (b)). The signal gets amplified along the channel as a high voltage of about 1 kV is applied between the front and the back of the MCP. This leads to a multiplication of the secondary electrons in an avalanche like manner and an electron shower is released at the channel exit. The formation of the electron avalanche causes a voltage drop between MCP front and back which is read out capacitively. These voltage drop signals are referenced to the FEL trigger and correspond to the ions' and electrons' TOFs:

$$\mathrm{TOF} = t_{\mathrm{MCP}} - t_{\mathrm{trigger}}. \tag{4.5}$$

The MCP channels are tilted by $\sim 8°$ with respect to the normal axis. This increases the active-area and the detection efficiency for particles hitting the MCP surface in normal direction. By stacking two or more MCPs on top of each other, the

amplification and the signal-to-noise ratio is improved [163]. Fig. 4.6 (b) shows a stack of two MCPs in a so-called Chevron arrangement. The idea is to prevent ion feedback along the channels in the opposite direction to the electron cascade. This arrangement is especially of advantage for coincidence experiments with opposing ion and electron detectors.

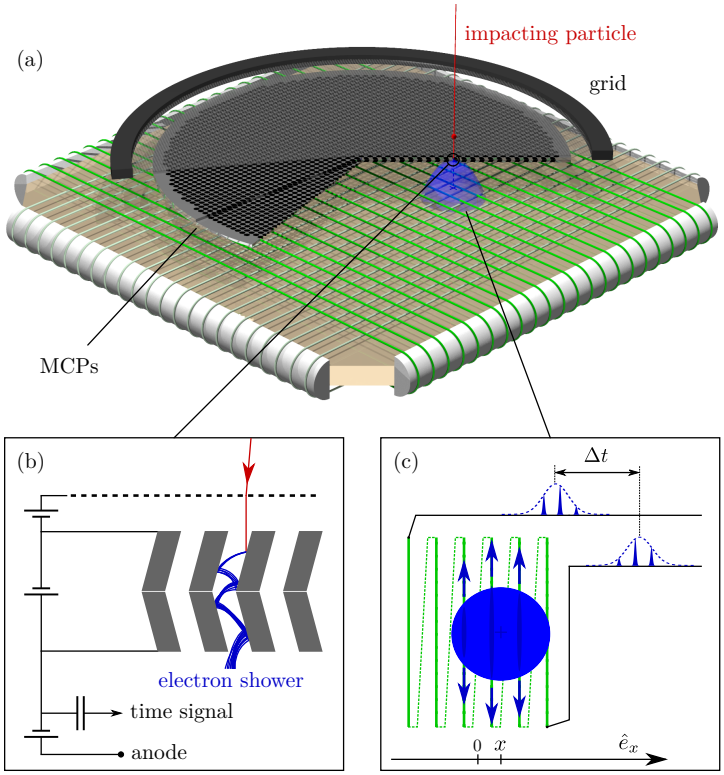

Figure 4.6: (a) Working principle of the time- and position-sensitive detector. (b) An impinging primary particle initiates an electron avalanche in a channel of the MCP. This leads to a drop in the voltage over the MCP stack which gives the time signal. The signal is read-out capacitively. (c) The electron cloud gets attracted by the delay-line anode. The induced position-sensitive runtime signal propagates to both ends of the delay-line wire. From Ref. [59].

In the FLASH reaction microscope, the ion detector is equipped with a Chevron-type stack of two MCPs (diameter 120 mm), whereas the electron detector features a stack of three MCPs (diameter 80 mm). A channel diameter of 25 µm and a center-to-center spacing of 32 µm results in an active-area of about 60 % for the MCPs of the ion detector.

The creation of secondary electrons within the channels strongly depends on the energy and the mass of the primary particle. The detection efficiency is highest for low-mass particles with high kinetic energies (keV range). However, the kinetic energy release that ions have after a fragmentation reaction plus the kinetic energy

they gain during acceleration in the spectrometer is far below 1 keV. Thus, to improve the detection efficiency, the primary particles are post-accelerated after the spectrometer by a high-voltage, which is applied between a fine metal grid and the front of the MCP.

4.3.2 Delay-Line Anode

For the position read-out, the electron cloud is detected by a delay-line anode located behind the MCP (see Fig. 4.6 (a)).
A delay-line anode consists of a long, thin wire made of a special copper-alloy, which is wound around two opposing extended ceramic insulators (see Fig. 4.6 (a)) [145]. In order to attract the negatively charged electron cloud, the delay-line anode is put onto a more positive potential compared to the backside of the MCP. The signals induced on the delay-line travel with constant velocity $v_\perp$ to both ends of the wire (see Fig. 4.6 (b)). At least two perpendicular aligned wire planes are needed to obtain 2-dimensional position information [252]. Such a delay-line anode is called quadanode and one of the two coordinates is given by [202]:

$$x = \frac{v_\perp}{2}(t_1 - t_2). \tag{4.6}$$

Here, $t_1 = t_1^* - t_{\mathrm{MCP}}$ and $t_2 = t_2^* - t_{\mathrm{MCP}}$ are the arrival times of the signal at the ends of the wire relative to the MCP timing signal t_{MCP}. The effective propagation velocity of the signal along the wire is denoted by $v_\perp$.
Usually, each anode layer is made of two parallel wound wires. The first wire is the so-called signal wire, which is put to a more positive potential ($\sim +50\,\mathrm{V}$) compared to the second reference wire. The signal wire attracts the electron cloud and at the same time the reference wire records the current noise. Signal and reference are subtracted electronically and a noise-reduced signal is obtained for further processing.
The TOF and the position read-out of two succeeding particles is only unproblematic, if the signal run-time to both ends of the wire is bigger than the time difference between the impact events. If this condition does not hold, signals of different impact events will mix up and the position information is lost.
To account for this problem, the so-called time sum condition, i.e., the condition that the sum of the run-times is constant for one wire, is used [117]:

$$t_{\mathrm{sum}} = t_1 + t_2 = \text{ const.} \tag{4.7}$$

Using three instead of two wire layers helps to further improve the multi-particle hit detection efficiency by introducing redundancy. In a so-called hexanode, three individual layers are rotated by 60° relative to each other. In this geometry, the position (x, y) can be determined by combining two of the three layers [117].

The FLASH reaction microscope operates with a quadanode at the ion detector and a hexanode for the electron detector. A manual how to calibrate a hexanode can be found for example in Refs. [29, 138].

4.4 Reconstruction of Ion Momenta

The detectors described in Sec. 4.3 measure the time of flight (TOF) along the z-axis[38] and the impact position in the perpendicular (x, y)-plane. Additionally, the applied potential over the spectrometer U and the magnetic field strength B as well as the acceleration length l_a need to be known in order to reconstruct the initial momentum vectors. In the next sections, the momentum reconstruction of ions and electrons is derived and follows Refs. [140, 234]. Generally speaking, the approach is based on Newton's fourth law, which allows to linearly decouple superimposed motions.

4.4.1 Longitudinal Ion Momentum

First, the reconstruction of the momentum along the time of flight axis is discussed. An ion of mass m and charge q exits the interaction volume with an initial momentum component p_z in longitudinal direction. Due to the electric field E, the ion is additionally accelerated over the distance l_a:

$$\ddot{z} = \frac{qE}{m} = \frac{qU}{ml_a}. \tag{4.8}$$

Here, the voltage U is applied over the acceleration length l_a. Hence, l_a can be written as a superposition of the two motions and is given by:

$$l_a = \frac{p_z}{m}t + \frac{1}{2}\ddot{z}t^2. \tag{4.9}$$

Here, t is the absolute time of flight of the ions from the interaction point to the detector. Inserting Eq. 4.8 and solving for p_z yields for the longitudinal ion momentum[39]:

$$p_z = \frac{l_a m}{t} - \frac{qUt}{2l_a}. \tag{4.10}$$

An expression for the total time an ion needs to travel the distance between the reaction volume and the detector is found by solving Eq. 4.9 for t:

$$t_\pm = \frac{2l_a m}{\sqrt{p_z^2 + 2mqU} \pm p_z}. \tag{4.11}$$

[38] Here and in the following, the coordinate system displayed in Fig. 4.1 is used.

[39] In atomic units: $p_z[\text{a.u.}] = \left(0.457 \ \frac{\text{a.u. ns}}{\text{mm amu}}\right)\frac{l_a m}{t} - \left(8.04 \cdot 10^{-3} \ \frac{\text{a.u. mm}}{\text{ns eV}}\right)\frac{qUt}{l_a}$ with $[t]$=ns, $[l_a]$=mm, $[qU]$=eV.

The "+" sign in Eq. 4.11[40] means that these ions initially fly towards the detector, whereas the "−" sign represents ions starting with negative momentum in opposite direction.
The momentum resolution of the ions is influenced by many parameters and is not equal for all directions. Along z, the momentum resolution is mainly affected by inhomogeneities of the electric, the finite focal size in z and the resolution of the detector. The field inhomogeneities can be corrected in the post-analysis. The intrinsic detector resolution is basically limited by the response time of the MCPs, which is in the order of some picoseconds. As discussed in Sec. 4.1, the jet temperature along z is small because the skimmers cut away the particles with high momenta in this direction. Compared to the finite focal size of $\sim 20\,\mu\text{m}$, the intrinsic detector resolution and the jet temperature along z are neglectable factors. Taking the mass of argon and applying the method of error propagation to Eq. 4.10, the momentum resolution in z can be estimated to $\Delta p_z \approx 0.1$ a.u.

4.4.2 Transverse Ion Momentum

Perpendicular to the spectrometer axis in the (x, y)-plane, the ion trajectories are not affected by the electric field. Furthermore, the influence of the magnetic field on the ion trajectory can be neglected in first approximation because of the high mass of the ion. The geometry and the parameters to reconstruct the transverse momenta p_x and p_y are defined in Fig. 4.7.
Besides a constant offset mv_{jet} due to the jet velocity along x, the impact position (x, y) depend linearly on the initial momenta p_x and p_y as well as the time of flight t:

$$x = \frac{t}{m}\left(p_x + mv_{\text{jet}}\right) \text{ and } y = \frac{t}{m}p_y. \tag{4.12}$$

Reorganizing Eq. 4.12 yields for the transverse momentum components:

$$p_x = m\left(\frac{x}{t} - v_{\text{jet}}\right) \text{ and } p_y = m\left(\frac{y}{t}\right). \tag{4.13}$$

Along the jet direction x, the longitudinal jet temperature, the finite focal size and the detector resolution need to be taken into account to estimate the momentum resolution. The focal spot along x is similar to the z-direction, i.e., $\sim 20\,\mu\text{m}$. In x-direction, the intrinsic detector resolution ($\sim 0.5\,\text{ns}$) is given by the width of the signals traveling along the wires of the delay-line anode, which themselves are broadened due to the spatial extension of the electron cloud emerging from the MCPs.

[40] In ns: $t_\pm(p_z)[\text{ns}] = \left(719.9\ \frac{\text{ns}}{\text{cm}}\sqrt{\frac{\text{eV}}{\text{amu}}}\right) t_\pm(p_z)$ with $[qU]$=eV, $[p_z]$=$\sqrt{\text{amu}\cdot\text{eV}}$, $[a]$=cm, $[m]$=amu.

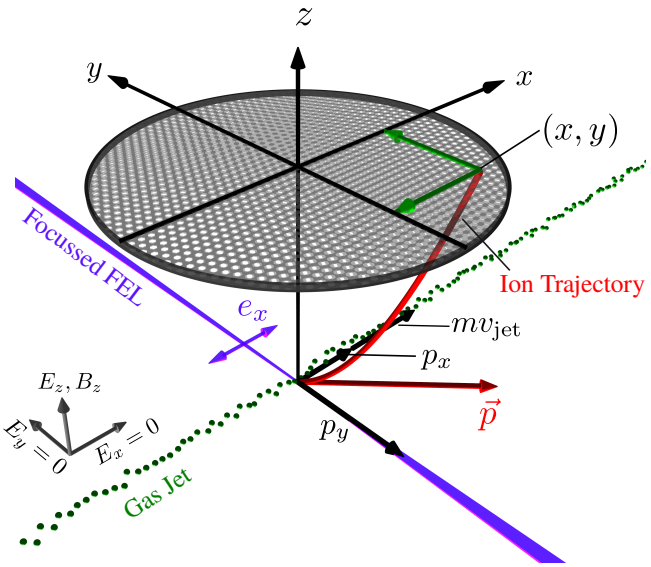

Figure 4.7: Determination of the transverse ion momenta p_x and p_y. Sketch of the ion trajectory (red) from the intersection point of the focussed FEL (purple) and the gas target (green balls) to the impinging point (x, y) on the detector.

For the argon dimer experiment, the longitudinal jet temperature is estimated to $\sim 2\,\mathrm{K}$, whereas it is $< 1\,\mathrm{K}$ for the H_2 experiment. In summary, using Eq. 4.13 with error propagation, this results in a resolution of $\Delta p_x \lesssim 0.5\,\mathrm{a.u.}$.
In y-direction, the FEL beam perpendicularly crosses the jet and ions from the target are created over a distance which equals the diameter of the jet of about 1 mm. As in z-direction, the jet temperature is negligible as the skimmers also cut in this direction. The intrinsic detector resolution of $\sim 0.5\,\mathrm{ns}$ is the same as in the y-direction. Summing up, this yields a momentum resolution of $\Delta p_y \approx 8\,\mathrm{a.u.}$ for argon and is smaller for the lighter hydrogen.

4.4.3 Electron Momenta

Electrons are not detected in the experiments discussed in Ch. 6, 7 and 8. In order to reach high ion charge states, the FEL intensity is kept high during these experiments ($I_{\mathrm{FEL}} \sim 10^{14}\mathrm{W/cm^2}$, see Sec. 6.1). Such high intensity settings come along with the drawback of not been able to measure electrons. For each FEL shot, too many electrons (> 10) are created and the detector gets saturated immediately (see also the discussion of Sec. 4.7). Consequently, electron momenta cannot be used for the interpretation of the experimental data and the reconstruction of their momentum is not presented within this section. However, for reasons of completeness, it is conducted in Appendix B.

4.5 Coincidences

An advantage of momentum spectroscopy with REMIs is the assignment of coincidences by applying momentum conservation. The following discussion is based on Ref. [236]. If the temperature of the molecular constituents is neglected, i.e., there is no relative momentum between them, the sum momentum of all fragments has to be zero in order to fulfill momentum conservation. Hence, in case of a diatomic molecule, the summed momentum components of the two ions have to equal zero in all directional components (x, y, z):

$$\mathbf{p}_{\text{sum}} = \mathbf{p}_{\text{ion1}} + \mathbf{p}_{\text{ion2}} = \mathbf{0}. \tag{4.14}$$

Due to the finite temperature of the molecules before the fragmentation, Eq. 4.14 cannot be fulfilled exactly under experimental conditions. Instead, a distinct window condition is applied to assign coincidences. The recoil momenta of the electrons is marginal compared to the large ion momenta after Coulomb explosions and can be neglected (see also Sec. 4.6). Exemplary, the momentum sums of the coincidence channel $Ar^+ + Ar^+$ are shown in Fig. 4.8. In accordance to the discussion of the previous section, the momentum sum $p_z$sum is smallest, because the momentum resolution is best in this direction.

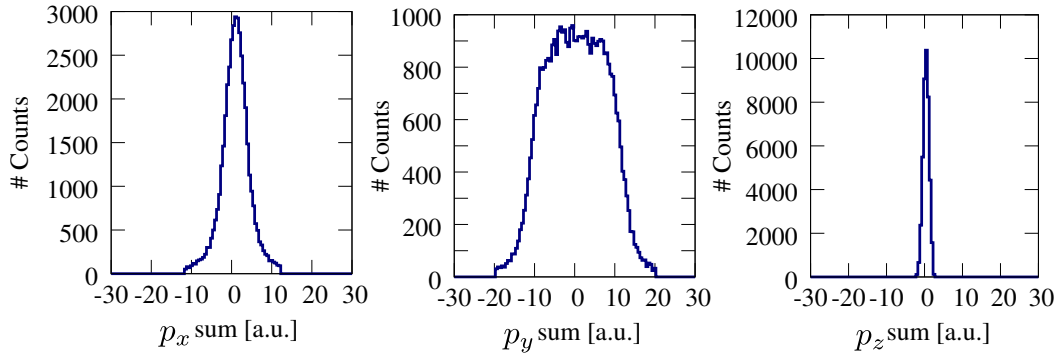

Figure 4.8: Momentum sum of the $Ar^+ + Ar^+$ coincidence channel in all three spatial directions (x, y, z).

4.6 Kinetic Energy Release (KER)

As emphasized in the introduction and in Ch 2, Coulomb-explosion imaging (CEI) is a widely used technique to investigate the fragmentation dynamics of molecules [20, 203]. In this regard, the kinetic energy release (KER) is an important quantity, because it gives insights into the geometry of the molecule at the point in time of the fragmentation[41]. It is defined as the sum kinetic energy of all particles of

[41] This section is compiled from Ref. [236]

the fragmentation. In general, the KER of coincident fragments is given by the difference between the potential energy E_i at the initial molecular geometry and the asymptotic energy E_∞ for all fragments being separated by infinite distances:

$$\mathrm{KER} = E_i - E_\infty. \tag{4.15}$$

In case of the most simple molecular geometry, i.e., a diatomic molecule, the fragmentation can be described in terms of potential energy curves (PECs) (see Sec. 2.3.3) and $\mathrm{KER} = E(R_{\mathrm{eq}}) - E(R = \infty)$ as depicted in Fig. 4.9.

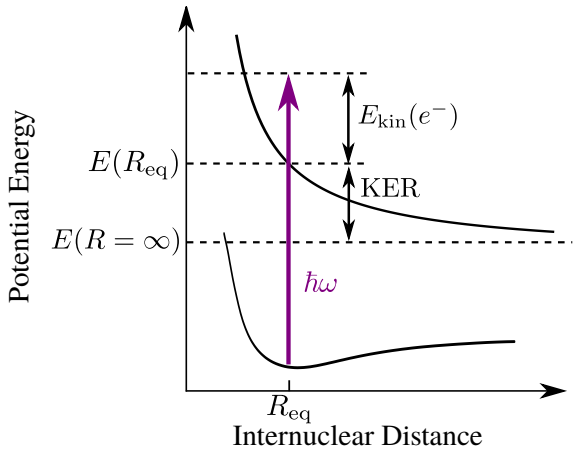

Figure 4.9: Kinetic energy release (KER) for the fragmentation of a diatomic molecule. The molecule is ionized by a photon $\hbar\omega$ at the equilibrium internuclear distance R_{eq} from its ground state to a repulsive PEC. The electron takes away the energy $E_{\mathrm{kin}}(e^-) = \hbar\omega - E(R_{\mathrm{eq}})$. $E(R = \infty)$ is the energy of the fragments at asymptotically far distances. The kinetic energy release is given by $\mathrm{KER} = E(R_{\mathrm{eq}}) - E(R = \infty)$. Taken from Ref. [236].

If the recoil momentum of the emitted electrons is negligible, the coincident fragments of a homonuclear molecule will always have the same kinetic energy. Hence, the KER is double the kinetic energy of one of the particles. Consider for example the low-charge-state channel $\mathrm{Ar}_2^{2+} \rightarrow \mathrm{Ar}^+ + \mathrm{Ar}^+$. In first approximation, the KER at the equilibrium internuclear distance R_{eq} is given by the Coulomb repulsion of two charges $q_1 = q_2 = +1$: $\mathrm{KER} = 1/R_{\mathrm{eq}} = 0.14$ a.u.. Accordingly, the recoil momentum of one at the fragments is $p_{\mathrm{ion}} = \sqrt{\mathrm{KER} \cdot m(^{40}\mathrm{Ar})} = 101$ a.u. Hence, the approximation to neglect the recoil momenta of the electrons $p_{e^-} \leq 1$ a.u.[42] is well appropriate.

[42] E.g. for $E_{\mathrm{kin}}(e^-) = 10$ eV: $p_{e^-} = \sqrt{2E_{\mathrm{kin}}(e^-)m_e} = 0.85$ a.u.

4.7 REMI customized for FEL Experiments

Due to the unprecedented high intensities (see Ch. 3) and large ionization cross sections for most residual gas atoms and molecules at XUV photon energies, a REMI operating at an FEL needs to fulfill high demands in terms of vacuum conditions. Furthermore, the high pulse repetition rate of FELs, which are based on superconducting LINACs (see Sec. 3.5), calls for a data acquisition system, which is fast and powerful enough to handle the high data rate.

4.7.1 Vacuum Requirements

Conditioned by the working principle of a REMI, each ion and electron, which is created inside the spectrometer, is accelerated towards the respective detector and is registered as an event (see Sec. 4.2). The detectors, however, do not discriminate between particles from the target and from the residual gas background. At photon energies above ∼15 eV, one photon is enough to ionize all relevant molecules of the residual gas (see Fig. 4.10 (a)). In addition, the photoabsorption cross sections of background molecules are in the same order as the cross sections of, e.g., noble gas target atoms (see Fig. 4.10 (b)). In combination with high FEL pulse energies in the order of some tens of µJ (see Sec. 3.5), this causes a non-negligible number of background events even out of the FEL focus.

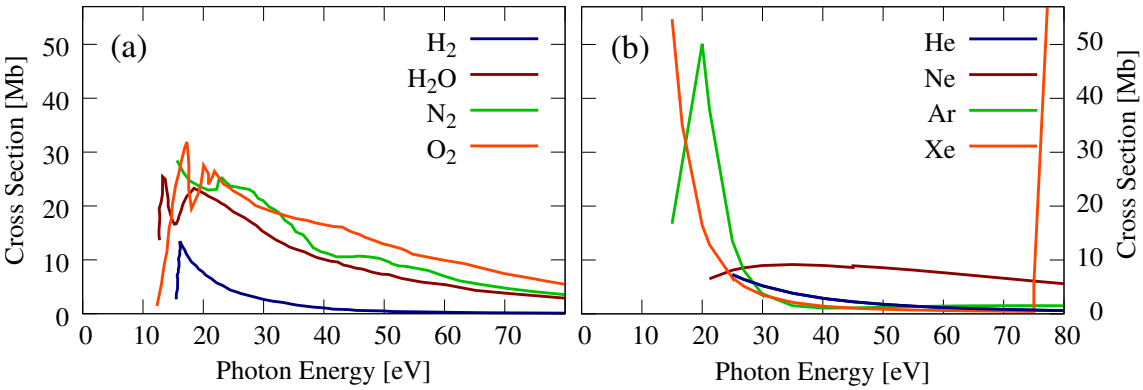

Figure 4.10: Total photoabsorption cross sections at XUV photon energies. (a) Residual gas molecules. Data taken from Ref. [79]. (b) Noble gases. Data taken from Ref. [287].

If the number of background events is too high, lots of MCP channels will be hit at once. This causes a drop in the voltage over the MCP, which leads to a reduced detection efficiency and the saturation of the detector. In the following, an exemple calculation of the expected number of background events for a given FEL diameter and residual gas pressure is performed. The FEL beam with a diameter of $d = 2\,\mathrm{mm}$ crosses the spectrometer with inner-diameter $l = 120\,\mathrm{mm}$. The background pressure

is assumed to be $p = 10^{-8}$ mbar. The photon energy is chosen to be $\hbar\omega = 27$ eV and a 1:3 mixture of water and hydrogen is assumed for the background gas. The corresponding total cross sections are taken from Fig. 4.10 (a). With these parameters and at a moderate pulse energy of $E_{\text{pulse}} = 5$ µJ the number of ionization events per FEL pulse[43] is about 20,000 and both detectors would immediately saturate. To avoid this, the residual gas pressure needs to be kept at a level of $\leq 10^{-11}$ mbar. With the same parameters as before, the number of background events per pulse is now estimated to ~ 20.
To reach pressures of $\leq 10^{-11}$ mbar in a large vacuum vessel like the REMI main chamber (CF DN250 tube)[44], pumping by just using conventional turbo molecular pumps is not sufficient. In the present case, the complete inner-walls of the main chamber are coated with a thin film (~ 1.5 µm) of so-called non-evaporable getter (NEG) material [16]. NEG is a special alloy, e.g., Ti-Zr-V, which has a huge surface area. Thereby the probability of residual gas molecules to stick to the chamber walls is increased. At extreme vacua, the thermal outgasing of hydrogen from the chamber walls is the major source of residual gas background. The outgasing rate of H_2 excites that of other molecular species like CO, CH_4 and CO_2 by more than two orders of magnitude [16]. However, turbo molecular pumps are not well-suited to pump light H_2 and the pumping speed is in the order of ~ 150 ℓ/s [91]. The authors of Ref. [16] report a NEG pumping speed of ~ 0.5 $\ell/(\text{s} \cdot \text{cm}^2)$ for H_2. If the REMI main chamber is approximated to be a cylinder of 25 cm diameter with a length of 80 cm, the pumping speed of the NEG coating is ~ 3600 ℓ/s. Hence, pumping by NEG is a method to decrease the amount of residual H_2 and thereby to reach very low final pressures. After venting the chamber, the NEG coating needs to be re-activated by heating to temperatures of ~ 200°C for at least 24 hours. However, each air venting significantly degenerates the NEG coating and after several activation-air-venting cycles higher bake-out temperatures are required to reach the same pumping performance as in the beginning [17]. In order to temper this aging effect, the vacuum vessel needs to be vented with an inert gas like nitrogen.

4.7.2 Data Acquisition System

The high pulse repetition of superconducting FELs such as FLASH requires a dedicated data acquisition system, which is capable of processing the incoming amount of data from REMI experiments.
The FLASH accelerator has an RF pulse of 800 µs duration to speed up electron bunches at a repetition rate of 10 Hz [58]. The bunch trains for FLASH1 and FLASH2 can be individually distributed within these 800 µs. Each bunch train is generated by its own injector laser and hence features its own charge, number of

[43] $N_{\text{events}} = \sigma_{\text{tot}}(N_{\text{particles}}/A)N_{\text{photons}}$ with $N_{\text{particles}} = pV/(k_B T)$ and $N_{\text{photons}} = E_{\text{pulse}}/(\hbar\omega)$
[44] CF stands for the ConFlat standard used for vacuum flanges, DN250 refers to a European size standard for vacuum components.

bunches and bunch separation [58]. The bunch pattern for simultaneous operation of both FELs in case of maximum possible number of bunches for REMI operation at FLASH2 is shown in Fig. 4.11. At 10 Hz repetition rate, FLASH1 gets 1 bunch and 148 bunches with a spacing of 5 µs (200 kHz) are delivered to FLASH2. In principle, FLASH can also operate at 1 µs bunch separation (1 MHz) (see Tab. 3.1 in Sec. 3.5), but as the time of flights for most ion species are larger than 1 µs (see, e.g., Fig. 4.5), a bunch separation < 5 µs is not usable for REMI experiments.

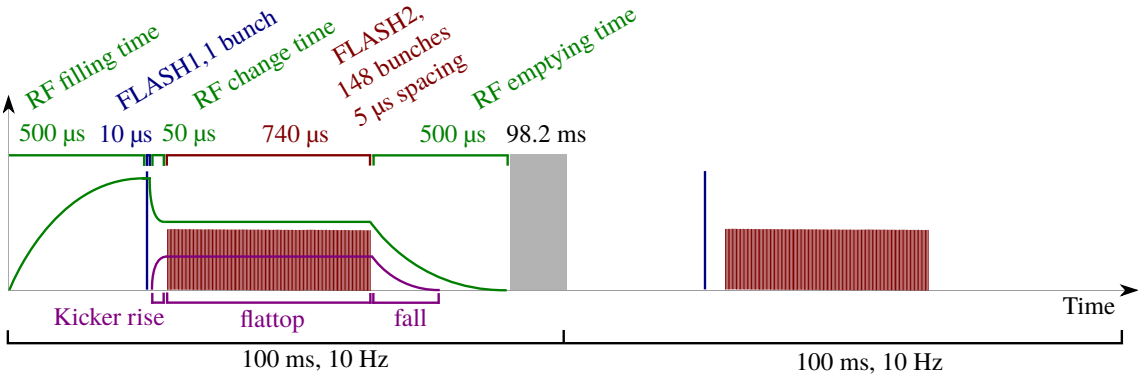

Figure 4.11: Timing for FLASH1 and FLASH2 for two-user operation and maximum number of pulses for a REMI experiment at FLASH2. Adapted from Ref. [58].

In contrast to other REMI experiments, which for example use optical laser pulses at repetition rates of 1 kHz [59], the processing of the data by electronic hardware is not an option at FLASH. It is not possible to electronically identify and digitize a signal by a constant-fraction-discriminator (CFD) and a time-to-digital converter (TDC), within the pulse separation of 5 µs. Furthermore, the beamtime at a user facility like FLASH is limited and sufficient statistics need to be accumulated within a fixed period of time.
Therefore, four Acqiris DC282 digitizer cards, each with four channels, are used to record the entire voltage signal of all detector channels[45]. The highest sampling rate of the digitizer cards is 2 GHz (0.5 ns between two samples) and the maximum voltage range for each channel is ±5 V [236]. The digitizer cards cannot be read-out each 5 µs, i.e., after each individual FEL spot, but the signal trace for each channel recorded during the entire pulse train is stored internally on the digitizer cards. Then, the 10 Hz FEL master trigger initiates the read-out of the channels after the end of each pulse train (i.e. within the 98.2 ms time window indicated in Fig. 4.11). The peak finding on the signals and the sorting of the data is done by computer algorithms in the online as well as the offline analysis. More details about the data acquisition system and the data processing can be found in Refs. [140, 236].

[45] 5 channels for the ion detector, 7 channels for the electron detector and additional channels for, e.g., delay and pulse energy read-out.

5 Setup of the XUV-IR Experiment

The XUV-IR pump-probe experiment is set-up at beamline BL2 at FLASH1 (see Sec. 3.5). FEL pulses of (27.0 ± 0.5) eV (FWHM) photon energy and pulse durations of ~ 50 fs (FWHM) are provided at a repetition rate of 10 Hz. They are spatially and temporally overlapped with IR-probe pulses from a synchronized Ti:Sa laser (see Sec. 5.1).
The FEL and the IR beam are focussed into a supersonic gas jet in a collinear arrangement in the middle of the REMI spectrometer (see Fig. 5.1). Argon is expanding through a 30 µm diameter nozzle with an injection pressure of 2 bar (see Sec. 4.1). By the supersonic expansion, argon dimers are formed and the ratio of dimers to monomers within the jet is about 1:20.
An extraction field of 55 V/cm along the spectrometer axis (see Sec. 4.2) is applied to accelerate the ions onto the detector (see Sec. 4.3). As no electrons are measured in this experiment, the magnetic field and the electron detector are switched off. The ions are recorded as a function of the delay between XUV and IR pulse.

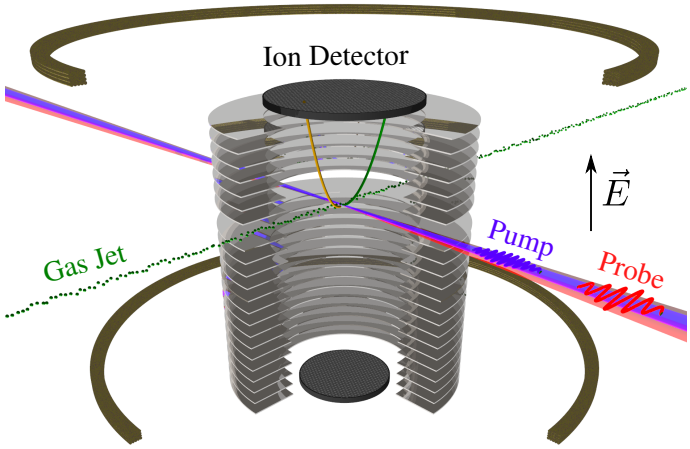

Figure 5.1: Illustration of the XUV-IR pump-probe setup using a REMI.

A schematic lateral cut through the experimental setup is shown in Fig. 5.2. The XUV and the IR beam are guided to the experiment in two different beamlines. The XUV radiation is focussed by an ellipsoidal mirror of 2 m focal length down to a diameter of approximately 20 µm [264], whereas the IR beam is brought into focus

by a lens ($f = 40\,\mathrm{cm}$) mounted outside of the vacuum system. To collinearly overlap the two beams, the IR beam is deflected by 90° with a holey 2" silver-coated mirror (Hole diameter: 4 mm). An IR focus of about 50 µm ensures spatially overlap of the two foci. Apertures with different diameters can be put into the FEL beam path to cut away the halo of the FEL and to reduce stray light in the main chamber. Transmission filters sitting on two motorized wheels in the upstream section of BL2 [264] are used to suppress higher harmonics of the FEL radiation (see Sec. 3.4) and also to adjust the overall FEL pulse energy. Apertures in the tunnel section as well as in the experimental hall can also be utilized to tune the pulse energy and to fix the FEL beam path.
A fluorescence screen ($1\times1\ \mathrm{cm}^2$) can be moved to the nominal focal point to check the spatial overlap of the two foci. The fluorescence induced by the XUV and the IR light is monitored by a CCD camera with magnification optics.
The position and the shape of the FEL beam after the focus is observed by the fluorescence of the XUV radiation on a thin Ce:YAG crystal, which can be put into the beam path if needed.

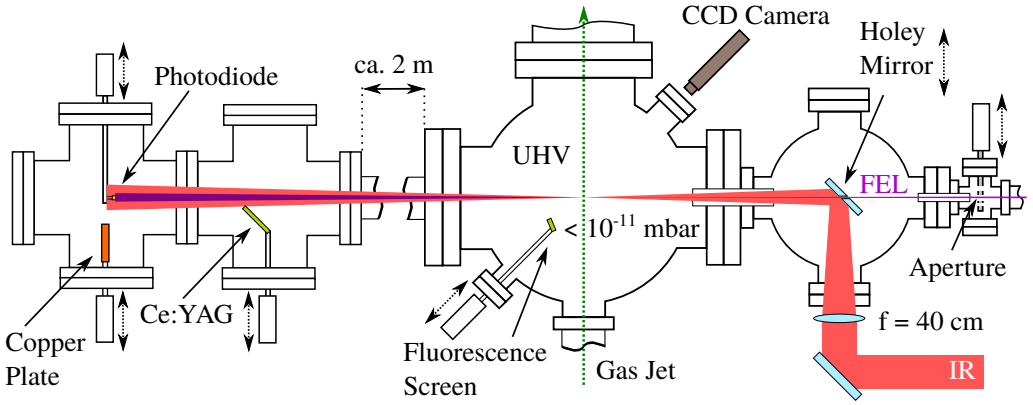

Figure 5.2: Schematic lateral cut through the XUV-IR pump-probe setup.

The temporal overlap of the pulses is an essential prerequisite for all pump-probe experiments. A fast switching photodiode at the end of the beamline is used to get a rough estimate ($\sim 1\,\mathrm{ns}$) of the temporal overlap of XUV and IR pulse. In order to further determine the temporal overlap, the delay-dependent signal of a physical process measured with the detectors of the REMI can be employed. It is shown that the ground state dissociation of H_2^+ can be used. The results of this new approach are presented in Sec. 7.2.
During the actual experiments, the photodiode is not utilized and replaced by a copper plate to dump the FEL beam. The copper plate is electrically connected and the voltage signals induced by XUV pulses due to the photoelectric effect can serve as a reference for the pulse energy (see Sec. 6.1.2).

Differential pumping stages between main chamber, FEL beamline and FEL dump, respectively, are essential to maintain ultra-high vacuum conditions in the main chamber (residual gas pressure $< 10^{-11}$ mbar).

5.1 Optical Laser System

The FLASH1 facility provides two IR[46] laser systems, which can be used for pump-probe experiments [211]. An overview of the FLASH1 pump-probe laser infrastructure is given in Fig. 5.3. Both laser systems are based on a Ti:Sa oscillator, which is locked to the 1.3 GHz master clock of the FEL accelerator. The pulses from the Ti:Sa serve as an input for two different amplifiers. The high power amplifier (Hidra) operates at a repetition rate of 10 Hz with pulse energies up to 20 mJ and minimum pulse lengths of 50 fs. Differently, the so-called burst mode amplifier is designed to replicate the bunch train structure of FLASH on a shot-by-shot basis [264]. This OPCPA-based[47] system delivers pulses with durations of 120 fs at a maximum energy per pulse train of 20 µJ. More informations on the FLASH1 pump-probe laser can be found in Ref [211].

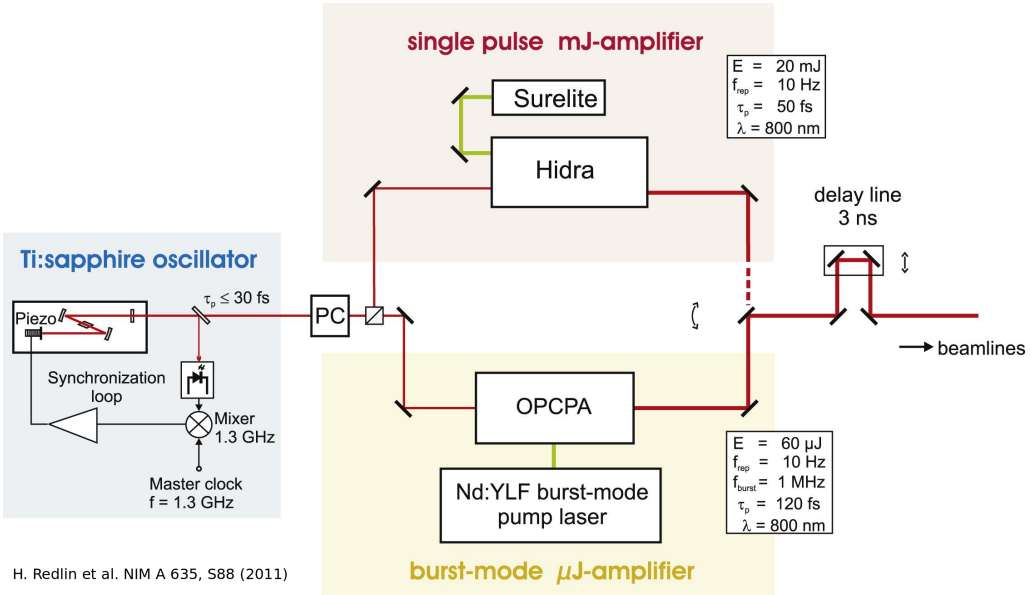

Figure 5.3: Optical laser system at FLASH1. Taken from Ref. [211].

The IR laser system is located in a separated, climate and temperature controlled laser hutch within the FLASH1 experimental hall. From there, the IR pulses are transported to the experiments in beamlines under vacuum.

[46] Central wavelength: $\lambda = 800$ nm.
[47] OPCPA: Optical parametric chirped-pulse amplification.

To do pump-probe experiments, the synchronization between the pulses is of crucial importance for the achievable temporal resolution. As IR and XUV pulses are generated by different sources, they are not intrinsically synchronized. Therefore, it is unalterable to precisely measure the timing between XUV and IR pulses. Long-term drifts caused by external sources such as temperature fluctuations can amount to several hundred femtoseconds up to picoseconds over a whole day.
In the experiments presented here, a streak camera is used to measure the long-term arrival time drifts between XUV and IR pulses [211]. The streak camera does not use the XUV pulses themselves as a time reference, but the electron bunches, which have generated the XUV pulses. To do so, the electron bunches are utilized to generate optical synchrotron radiation by deflection at a dipole magnet before being removed in the electron dump.
For the present studies, the high-power Hidra amplifier with a repetition rate of 10 Hz is used, because the burst-mode amplifier did not reach the specified pulse energy per shot at the time of the experiments. As sufficient statistics are crucial for REMI experiments, this is a considerable restriction.

6 Multi-Photon Ionization of Argon

In Sec. 2.1, basic theoretical concepts of atomic photoionization have been discussed. For multi-photon ionization at XUV photon energies and FEL intensities, the mechanisms of sequential and non-sequential ionization have been introduced (see Sec. 2.1.3).
Experimental studies on the multi-photon ionization of argon in the XUV regime are reported by Refs. [77, 88, 105, 106, 120, 182, 186, 188, 275]. In a pioneering study, Wabnitz *et al.* [275] measured the multi-photon ionization of argon at $\hbar\omega = 12.7\,\mathrm{eV}$ in the intensity regime $I \sim 10^{13}\,\mathrm{W/cm^2}$. By applying the scaling law, $Y \propto I^n$ (see Sec. 2.1.3), they found sequential ionization to be the dominant process to create Ar^{2+}. For Ar^{3+}, the error bar on the photon number n was too big and it could not undoubtedly been discriminated between the sequential and the non-sequential channel. A subsequent study by Moshammer *et al.* [186] looked into the multi-photon ionization of argon at $\hbar\omega = 38.8\,\mathrm{eV}$ in an intensity range of $I \sim 10^{12} - 10^{13}\,\mathrm{W/cm^2}$, i.e., comparable to Ref. [275]. Here, the intensity-dependent ion yield analysis revealed a combination of non-sequential and sequential ionization being the processes at work to create Ar^{2+} and Ar^{3+} ions. Extending the intensity range to lower values, $I \sim 10^{11} - 10^{12}\,\mathrm{W/cm^2}$, the same group could confirm that non-sequential ionization is the dominant mechanism [120]. At higher intensities $I \sim 10^{14}\,\mathrm{W/cm^2}$ and $\hbar\omega = 20\,\mathrm{eV}$, Motomura *et al.* [188] found sequential ionization being the major mechanism to create charge states up to Ar^{6+}.
In an experiment at $\hbar\omega = 21\,\mathrm{eV}$ and $I \sim 5 \times 10^{12}\,\mathrm{W/cm^2}$, Hikosaka *et al.* [105] investigated multi-photon double ionization of Ar. By measuring photoelectrons, they showed that Ar^{2+} is created via sequential ionization: $Ar + \hbar\omega \rightarrow Ar^{+} + e^{-}$ and $Ar^{+} + 2\hbar\omega \rightarrow Ar^{2+} + e^{-}$. Furthermore, an enhancement of the two-photon ionization by Ar^{+*} resonances is confirmed by experiment [77, 106, 182] and theory [88].

In the following chapter, the multi-photon ionization of argon at a photon energy of $\hbar\omega = 27\,\mathrm{eV}$ is studied in terms of identifying the dominant ionization channels been at work in the present intensity range $I \sim 10^{13} - 10^{14}\,\mathrm{W/cm^2}$ (see Eq. 6.1). The study comprises two parts. First, argon is exclusively irradiated by single XUV pulses (see Sec. 6.1) and the occurring ion yields are discussed as a function of the FEL intensity. Second, an IR laser pulse is used to identify intermediate resonances along the ionization pathway (see Sec. 6.2).

6.1 Interaction with a Single XUV Pulse

The data presented in the following section are recorded using single XUV pulses and the setup described in Ch. 5.
The FEL intensity I_{FEL} is estimated by taking the pulse energy $E_{\mathrm{pulse}} \approx 10 - 20\,\mu\mathrm{J}$, measured by a gas-monitor detector (GMD) [264], the focal spot size $A_{\mathrm{focus}} \approx \pi \cdot (d/2)^2$ with diameter $d \approx 20 - 30\,\mu\mathrm{m}$ [264] and the pulse duration $\tau_{\mathrm{FEL}} \approx 50\,\mathrm{fs}$:

$$I_{\mathrm{FEL}} = \frac{E_{\mathrm{pulse}}}{A_{\mathrm{focus}}\tau_{\mathrm{FEL}}} = 1 \times 10^{13} - 1 \times 10^{14}\,\frac{\mathrm{W}}{\mathrm{cm}^2}. \tag{6.1}$$

A 200 nm thick aluminium filter was used to fine tune the overall intensity. At the fundamental photon energy ($\hbar\omega = 27\,\mathrm{eV}$), the transmission[48] is $T_{1\mathrm{st}} = 0.62$. For the second and third harmonic, the transmission amounts to $T_{2\mathrm{nd}} = 0.71$ and $T_{3\mathrm{rd}} = 0.01$, respectively. The relative intensities of the second and third harmonic with respect to the fundamental are typically in the order of $\sim 0.5\,\%$ [47]. However, the second harmonic is usually not emitted along the beam propagation axis [35].

6.1.1 Time of Flight Mass Spectrum

The time of flight (TOF) mass spectrum of multiply charged argon ions recorded under the aforementioned photon parameters is depicted in Fig. 6.1. The momentum component p_z along the spectrometer axis (see Sec. 4.2) is contained in the width of the peaks. Ions originating from cold atoms of the gas jet result in sharp peaks in the TOF spectrum and therefore can be clearly separated from "hot" background ions (H^+, H_2^+, H_2O^+, N_2^+), which cause broad peaks. Argon ion charge states up to 5+ are measured. From experiments using synchrotron radiation, the single-photon cross sections for double ionization of argon are known [108, 157]. Based on this, one can estimate that by taking into account only single-photon absorption of the FEL's second and third harmonic, the relative intensity between Ar^{2+} and Ar^+ would be at least an order of magnitude lower compared to the present results. Hence, one can conclude that the recorded multiply charged Ar^{n+} ions result from multi-photon ionization. This finding has been already confirmed by Refs. [120, 186]. Jiang *et al.* [120] recorded ion charge states up to Ar^{4+} at $\hbar\omega = 28\,\mathrm{eV}$ and $I = 2 \times 10^{11} - 4 \times 10^{12}\,\mathrm{W/cm^2}$. In the present case, charge states up to Ar^{5+} are measured. This provides evidence that the estimated intensity range of $I = 1 \times 10^{13} - 1 \times 10^{14}\,\mathrm{W/cm^2}$ is reasonable (see Eq. 6.1). The report of Ar^{6+} at $I \sim 10^{14}\,\mathrm{W/cm^2}$ and $\hbar\omega = 20\,\mathrm{eV}$ by Motomura *et al.* [188] further confirms the determined intensity range.

[48] `http://henke.lbl.gov/optical_constants/filter2.html`, last request: 11/29/2017.

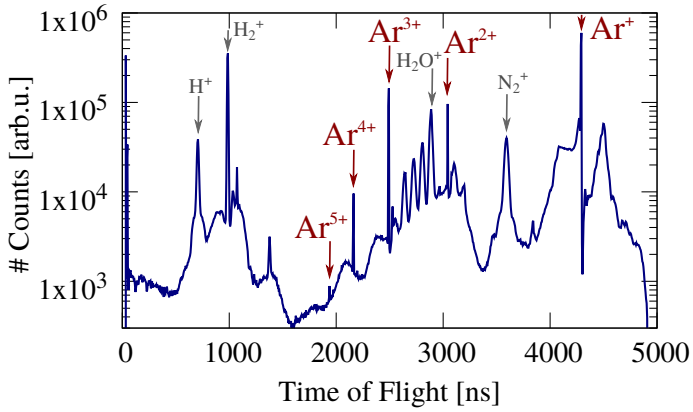

Figure 6.1: TOF mass spectrum of $Ar^{(1-5)+}$ ions (red arrows) at $\hbar\omega = 27\,\text{eV}$ and $I = 1 \times 10^{13} - 1 \times 10^{14}\,\text{W/cm}^2$. Background ions are marked by grey arrows.

6.1.2 Pulse Energy Calibration

The pulse energy of each FEL pulse E_{pulse} is measured by the photocurrent I_{ph} which is induced at the down-stream copper plate (see Ch. 5, Fig. 5.2). The photocurrent is not strictly linear to the number of photons in the pulse and it is therefore calibrated using background ions that arise from single-photon ionization events of the unfocussed FEL. This way, the photocurrent I_{ph} from the copper plate is referenced to a linear signal measured inside the spectrometer. In doing so, the pulse energy E_{pulse} is determined as close as possible with respect to the interaction point. For single-photon ionization, the yield of ion A^+ depends linearly on E_{pulse}:

$$Y_{A^+}(E_{\text{pulse}}, \hbar\omega) = \sigma_{A\to A^+}(\hbar\omega) \cdot n_A \cdot V \cdot E_{\text{pulse}}. \tag{6.2}$$

Here, $\sigma_{A\to A^+}(\hbar\omega)$ is the cross section to ionize the atom A to ion A^+, n_A is number density of atom A in the gas jet and V the interaction volume. In the present case, n_A and V are constant. Reorganizing Eq. 6.2 results in

$$E_{\text{pulse}} = c_A(\hbar\omega) \cdot Y_{A^+}, \tag{6.3}$$

with the pre-factor $c_A(\hbar\omega) = 1/(\sigma_{A\to A^+}(\hbar\omega) \cdot n_A \cdot V)$.
Background ions are selected by a position and TOF conditions (see Fig. 6.2 (a) and (b)). The position condition excludes ions out of the focus that are potentially produced by the absorption of multiple photons. The background ion species are marked by arrows in the TOF spectrum of Fig. 6.2 (b).

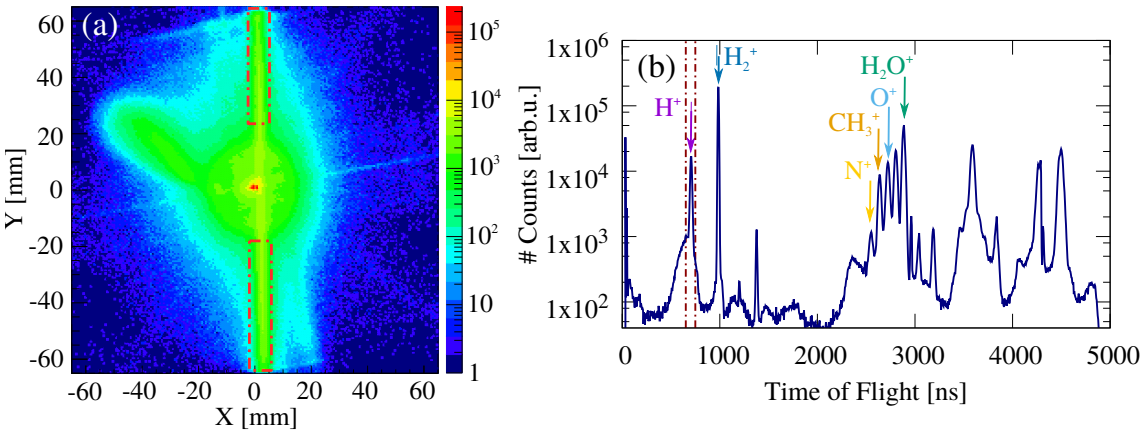

Figure 6.2: (a) Position condition (red dashed-dotted rectangles) to select background ions. (b) TOF mass spectrum of background ions selected by the position condition of (a). The TOF condition to select H^+ ions is confined within the vertical dashed-dotted red lines. Background ions are marked by arrows.

As listed in Tab. 6.1, the ionization potentials I_p of residual gas constituents are smaller than the present photon energy of $\hbar\omega = 27\,\text{eV}$ and all of the specified ions can arise from single-photon ionization.

Table 6.1: Ionization potentials I_p and cross sections σ of residual gas species at $\hbar\omega = 27\,\text{eV}$.

Channel	I_p [eV]	$\sigma(27\,\text{eV})$ [Mb] [79]
$H_2O \rightarrow H_2O^+$	12.6 [195]	10
$H_2 \rightarrow H_2^+$	15.4 [62]	3
$H_2 \rightarrow H^+ + H$	18.1 [62]	0.1
$O_2 \rightarrow O^+ + O$	18.8 [262]	5
$N_2 \rightarrow N^+ + N$	24.3 [191]	0.7
$CH_4 \rightarrow CH_3^+ + H$	14.8 [149]	7

The yield of background ions Y_{A^+} normalized to the photocurrent distribution is plotted as a function of the photocurrent I_{ph} in Fig. 6.3 (a) and fitted by a third-order polynomial function

$$Y_{A^+}(I_{\text{ph}}) = \sum_{i=0}^{3} a_i \cdot I_{\text{ph}}^i. \tag{6.4}$$

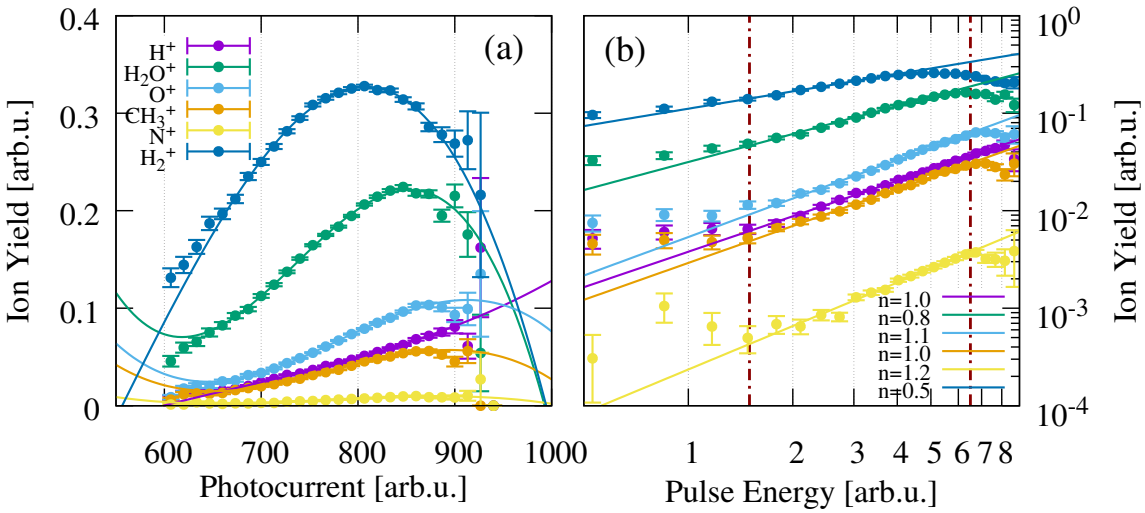

Figure 6.3: (a) Yield of background ions as a function of photocurrent measured by the down-stream copper plate. Also shown are polynomial fits according to Eq. 6.4. (b) Yield of background ions in dependence on the pulse energy calibrated on H^+ in a double-logarithmic plot. Same color assignment as in (a). Also shown are fits by the power law $Y = a \cdot I^n$. The two dashed-dotted lines mark the valid region of the calibration.

The yields of H_2^+ and H_2O^+ ions show a strong non-linear behavior at photocurrents above $I_{\mathrm{ph}} > 800$ arb.u. This is most likely due to saturation effects facilitated by large cross sections (see Tab. 6.1). The total yield of H_2^+ ions is higher compared to H_2O^+ ions, because the amount of residual H_2 in the experimental chamber after bake-out is higher compared to H_2O. The cross sections to create O^+ and CH_3^+ ions are also high (see Tab. 6.1). However, due to the lower abundance of O_2 and CH_4 in the residual gas, O^+ and CH_3^+ ions saturate at higher photocurrents compared to H_2O^+. The linear dependence on the pulse energy of the ions considered so far is restricted to a small photocurrent range and H_2^+, H_2O^+, O^+ as well as CH_3^+ ions are not considered as candidates for the calibration. The H^+ ion yield, however, shows a linear dependence over a large photocurrent range from $I_{\mathrm{ph}} = 600 - 900$ arb.u. An explanation of this behavior is the cross section of the $H_2 \rightarrow H^+$ channel, which is about an order of magnitude lower compared to all channels considered so far (see Tab. 6.1). The cross section of $N_2 \rightarrow N^+$ is also small, but also the total yield, which excludes N^+ ions to be a good reference out of statistical reasons. According to this discussion, H^+ ions are chosen to calibrate the pulse energy.
Combining Eq. 6.3 and 6.4, the pulse energy E_{pulse} in dependence on the photocurrent I_{ph} calibrated on a background ion reads:

$$E_{\mathrm{pulse}}(I_{\mathrm{ph}}) = c_A(\hbar\omega) \cdot \sum_{i=0}^{3} a_i \cdot I_{\mathrm{ph}}^i. \tag{6.5}$$

To test the calibration, the yields of background ions are plotted as a function of the H^+-calibrated pulse energy in a double-logarithmic plot in Fig. 6.3 (b) and are fitted according to the power law $Y = a \cdot I^n$. As expected, H^+ depends linearly on the pulse energy and the fit returns $n = 1.0$ in the range from $E_{\text{pulse}} = 1.5 - 6.5\,\text{arb.u.}$ Fit results of $n = 0.8$ and $n = 0.5$ for H_2O^+ and H_2^+, respectively, suggest that these ions are already starting to saturate at low pulse energies. O^+, CH_3^+ and N^+ show $n \approx 1$ in the fit range $E_{\text{pulse}} = 1.5 - 6.5\,\text{arb.u.}$ and constrain the validation of the H^+ calibration. For the further discussion, a constant pulse duration τ_{FEL} and a constant focal spot size A_{focus} is assumed and the pulse energy converted into intensity like $I = E_{\text{pulse}}/(\tau_{\text{FEL}} \cdot A_{\text{focus}})$.

6.1.3 Ion Yield vs. FEL Intensity

Like the already discussed background ions, the target $Ar^{(1-5)+}$ ions are selected by individual TOF conditions. However, in contrast to the background ions, an overall position condition includes only ions, which emerge from ionization events of atoms out of the focus. The yields Y of $Ar^{(1-5)+}$ ions are analyzed as a function of the FEL intensity I in a double-logarithmic plot in Fig. 6.4. Using this representation, the number of absorbed photons n is comprised in the slope n of a linear fit $Y = a \cdot I^n$ [218]. The fit on the H^+ calibration data returns a slope of $n = 1.0 \pm 0.0$ as expected. For the creation of Ar^+, one photon of $\hbar\omega = 27\,\text{eV}$ is required (see Fig. 6.4 (b)). For the low intensity region, i.e., between $I = 1.4 - 2.5\,\text{arb.u.}$, the fit shows a slope of $n = 0.8 \pm 0.0$, which is in accordance with single-photon absorption, but also shows the tendency for a starting saturation. For $I > 2.5\,\text{arb.u.}$, the Ar^+ yield is not longer linear with intensity and starts to decrease for higher intensities. This is a clear signature of saturation, i.e., almost all neutral atoms in the focus are ionized to Ar^+ and the power-scaling law is no longer valid to describe the yield of Ar^+ ions. The energy level scheme of Fig. 6.4 (b) shows that three photons need to be sequentially absorbed to ionize from the Ar ground state to Ar^{2+}. In the case of non-sequential ionization (NSI), however, only two photons are necessary. The fit of the Ar^{2+} data in Fig. 6.4 is restricted to the range between $I = 1.4 - 2.8\,\text{arb.u.}$ as for higher intensities the Ar^{2+} yield starts to saturate. In the low intensity region, the slope of $n = 3.0 \pm 0.1$ identifies that Ar^{2+} is created by the absorption of three photons from the Ar ground state by sequential ionization (SI) via the Ar^+ state. The yield of Ar^{3+} is linear over the entire intensity scale and the fit shows the number of absorbed photons to be $n = 3.4 \pm 0.1$. A non-integer number of photons indicates that at least two ionization pathways are superimposed to produce Ar^{3+}. Starting from the neutral Ar ground state, sequentially 5 photons and non-sequentially 4 photons, respectively, are required to produce Ar^{3+} (see Fig. 6.4 (b)). The observed slope of $n = 3.4 \pm 0.1$ is not in accordance with the number of photons of both ionization channels. However, starting from saturated Ar^+, 4 photons are needed for SI and 3 photons for NSI to ionize to Ar^{3+}. The superposition of both

ionization channels results in an average number of absorbed photons equal to 3.5. Moshammer *et al.* [186] also used the transition from NSI and SI to explain a slope of $n = 2.6 \pm 0.2$ to produce Ne^{2+} at $\hbar\omega = 38.8\,\text{eV}$.

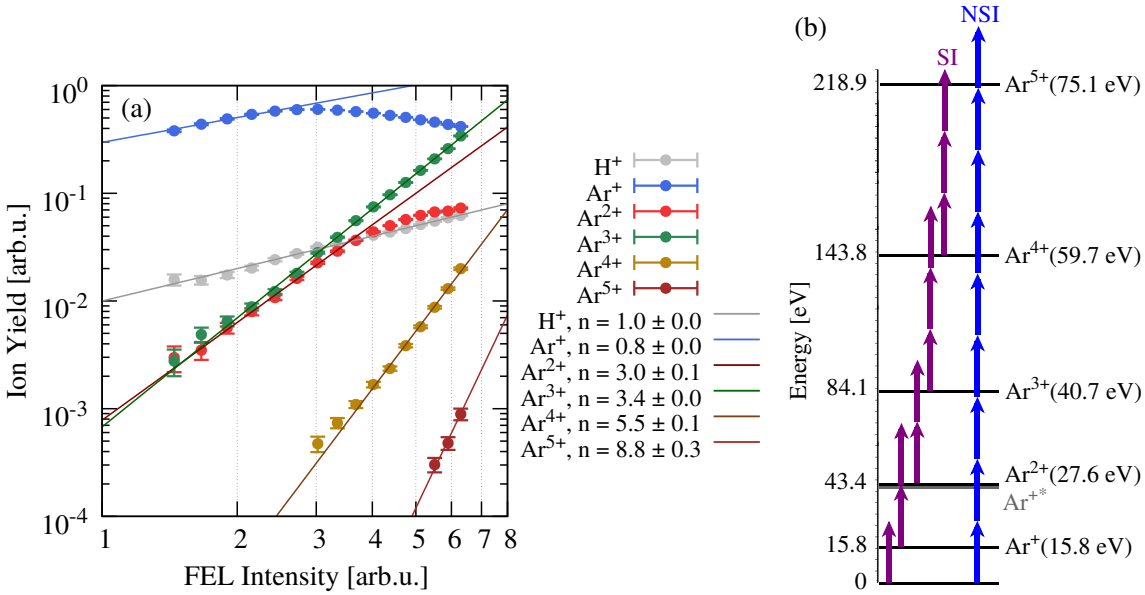

Figure 6.4: (a) Ion yield of $Ar^{(1-5)+}$ and H^+ as a function of FEL intensity in a double-logarithmic representation. Solid symbols and lines represent the data and fits according to $Y = a \cdot I^n$, respectively. (b) Energy level scheme up to Ar^{5+}. The length of the vertical arrows corresponds to a photon energy of $\hbar\omega = 27\,\text{eV}$. The purple arrows indicate sequential ionization (SI), the blue arrows non-sequential ionization (NSI). Level energies are taken from Ref. [137].

Another interpretation of the measured $n = 3.4 \pm 0.1$ takes into account intermediate Ar^{+*} states just below the Ar^{2+} threshold[49]. From $I > 4\,\text{arb.u.}$ onwards, the Ar^{2+} yield follows the yield of H^+, which has a slope of $n = 1$. This can be interpreted as single-photon ionization from saturated Ar^{+*}. Following this interpretation, Ar^{3+} is produced by the absorption of three sequential photons from saturated Ar^{+*} and four photons from the Ar^+ ground state. It is very likely that Ar^{+*} is saturated, because sequentially only two photons are required to access these states.
An interesting behavior is also found when comparing the absolute yield of Ar^{3+} to Ar^{2+}. Up to $I \sim 2.7\,\text{arb.u.}$, Ar^{3+} is equal to the Ar^{2+} yield and exceeds it for higher intensities. This means that Ar^{3+} is created more efficiently compared to Ar^{2+}. An interpretation of this phenomena is the "trapping" of population in the excited Ar^{+*} states. These states are just below the Ar^{2+} threshold and have large quantum numbers and angular momenta. Generally, the XUV ionization cross section for

[49] A detailed energy level scheme and electron configurations of the involved Ar^{+*} states is given in Sec. 6.2, especially in Fig. 6.10.

such states is small. Hence, the production of Ar^{2+} ions is retarded. However, as soon as an Ar^{2+} is created, the photon intensity is high enough to ionize to Ar^{3+}.
Ar^{4+} is produced at intensities $I > 3$ arb.u., i.e., at intensities where Ar^{2+} starts to saturate. Taking Ar^{+*} as initial state, 6 photons are required, whereas 5 photons are needed when starting from Ar^{2+}. The fit returns $n = 5.5 \pm 0.1$, which provides evidence that the assumption of taking an admixture of Ar^{+*} and Ar^{2+} as initial states is justified.
At the highest intensities, Ar^{5+} is produced and the fit results in $n = 8.8 \pm 0.3$. If Ar^{+*} and Ar^{2+} are taken as initial states, 9 and 8 photons, respectively, need to be absorbed to reach Ar^{5+}.

In summary, the analysis of the intensity dependent yield of $Ar^{(1-5)+}$ ions provides evidence that sequential ionization is the dominant mechanism at work. Furthermore, the yield of Ar^{2+} and Ar^{3+} identifies the importance of intermediate Ar^{+*} states to interpret the further ionization steps. In the following Sec. 6.2, the role of these intermediate states in the multi-photon ionization of argon is further investigated by an XUV-IR experiment.

6.2 IR-Assisted Multi-Photon Ionization of Argon

In the preceding section, it has been discussed that the multi-photon ionization of argon at a photon energy of $\hbar\omega = 27\,\mathrm{eV}$ is retarded by population trapping in highly excited Ar^{+*} states, which are lying just below the Ar^{2+} threshold. Within the FEL bandwidth of 0.5 eV (FWHM), three dipole-allowed transitions from the Ar^{+} $3p^5(^2P_{1/2,3/2})$ ground state to the following states are reported [137][50]:

1. Ar^{+*} $3p^4(^1D)5d(^2D_{5/2})$ at 26.62 eV.
2. Ar^{+*} $3p^4(^1S)5s(^2S_{1/2})$ at 26.66 eV.
3. Ar^{+*} $3p^4(^1D)5d(^2S_{1/2})$ at 26.89 eV.

The third state has the highest oscillator strength and also the highest cross section for IR ionization [69]. Hence, in order to transfer the "trapped" population into the Ar^{2+} continuum, a strong optical laser pulse is an adequate experimental tool. Two XUV photons are sequentially absorbed to populate these Ar^{+*} states and a superimposed IR laser ($\hbar\omega_{\mathrm{IR}} = 1.55\,\mathrm{eV}$) ionizes them to Ar^{2+}:

$$\mathrm{Ar} \xrightarrow{\mathrm{XUV}} \mathrm{Ar}^{+} + e^{-} \xrightarrow{\mathrm{XUV}} \mathrm{Ar}^{+*}, \tag{6.6}$$

$$\mathrm{Ar}^{+*} \xrightarrow{\mathrm{IR}} \mathrm{Ar}^{2+} + e^{-}. \tag{6.7}$$

In order to systematically investigate the effects of an additional IR laser pulse to the XUV multi-photon ionization pathway, the yield of produced argon ions is measured for three different IR intensities and as a function of the delay between XUV and IR pulse. The FEL intensity is on the same level as for the data recorded just with XUV radiation, i.e., $I_{\mathrm{FEL}} \approx 1 \times 10^{13} - 10^{14}\,\mathrm{W/cm^2}$ (see Eq. 6.1). Furthermore, the intensity of the IR laser needs to be known. Therefore, Sec. 6.2.1 is dedicated to two different methods to estimate the intensity of the IR laser.

6.2.1 Estimation of IR Laser Intensity

Measuring the absolute intensity of a laser at the focal spot is quite challenging, because the intensity itself is a quantity, which depends on pulse energy, pulse duration and focal spot size. The determination of those parameters is demanding itself and often comes along with big uncertainties. For example, in the experiment presented here, the focal spot size cannot be measured due to the lack of accessibility and suitable experimental tools. Therefore, two different methods are used to estimate the IR intensity: the ratio of Ar^{2+} to Ar^{+} ions and ADK-theory (see Sec. 2.1.2) applied to the momentum distribution of Ar^{+}.

[50] A detailed energy level scheme showing the states is depicted in Fig. 6.10.

The methods are especially advantageous, because they take into account ions, which are created directly in the focus. Hence, the intensity is estimated directly at the focal spot and does not need to rely on individual measurements or estimations of focus size, pulse duration, pulse energy or losses in the beam transport.

Ratio of Ar^{2+}/Ar^{+} Ions

The first method is based on comparing the ratio of Ar^{2+}/Ar^{+} ratio to a reference [278]. For this purpose, the number of Ar^{2+} and Ar^{+} ions is counted for different transmissions and pulse durations of the IR laser. The transmission is adjusted by a power throttle. The pulse durations are tuned by changing the compressor settings of the laser. Note that the given values for the pulse duration are only nominal values. The actual values can be off by a factor of $\sim 50\,\%$ due to many uncertainties. Fig. 6.5 (a) and (b) display TOF spectra, which are recorded by ionizing the target using only the IR laser pulses. On the basis of these TOF spectra, the number of Ar^{2+} and Ar^{+} ions is determined and the resulting ratios compared to Ref. [278] in Fig. 6.5 (c). According to this, the IR intensity is $I \approx 2.5 \times 10^{14}\,\mathrm{W/cm^2}$ for both laser settings. As already mentioned, this number should be understood as a rough estimate to get the order of magnitude of the IR intensity rather than a precision measurement.

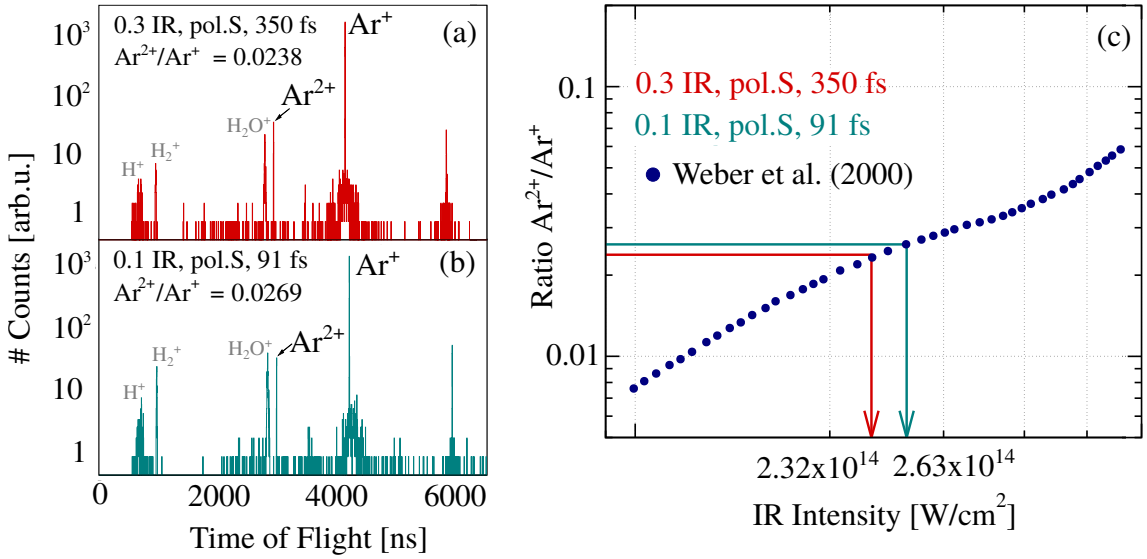

Figure 6.5: (a) TOF mass spectrum for 0.3 IR transmission, S-polarized (in TOF direction), 350 fs pulse duration. (b) TOF spectrum for 0.1 IR transmission, S-polarized (in TOF direction), 91 fs pulse duration. (c) Ratio Ar^{2+}/Ar^{+} determined from (a) and (b) compared to Weber *et al.* [278].

ADK-Theory

The second approach is based on measuring the width of the recoil-ion momentum distribution after strong-field induced tunnel ionization[51]. Recalling Eq. 2.27 of Sec. 2.1.2, the width along the laser polarization is given by:

$$\Gamma_{\mathrm{ADK}}(p_{||}) = A \ \cdot \exp\left(-(p_{||}-p_0)^2 \frac{\omega^2 (2I_p)^{3/2}}{3I^{3/2}}\right), \tag{6.8}$$

with amplitude A, momentum along laser polarization $p_{||}$, central momentum p_0, laser frequency ω, ionization potential I_p and laser intensity I.

The measured width $\Gamma_{||\mathrm{IR}}(p_{||})$ is a convolution of $\Gamma_{\mathrm{ADK}}(p_{||})$ and $\Gamma_{\mathrm{noIR}}(p_{||})$, which can be obtained from a measurement where the polarization is perpendicular to $p_{||}$, i.e., $\Gamma_{\mathrm{noIR}}(p_{||}) = \Gamma_{\perp\mathrm{IR}}(p_{||})$:

$$\Gamma_{||\mathrm{IR}}(p_{||}) = \Gamma_{\mathrm{ADK}}(p_{||}) * \Gamma_{\perp\mathrm{IR}}(p_{||}), \tag{6.9}$$

with $\Gamma_{\perp\mathrm{IR}}(p_{||}) = A \cdot \exp\left(-(p_{||}-p_0)^2 \frac{1}{w^2}\right)$ and the width w.
The convolution of two Gaussians yields $\sigma^2_{\mathrm{conv}} = \sigma_1^2 + \sigma_2^2$ and thus

$$\sigma^2_{||\mathrm{IR}} = \sigma^2_{\mathrm{ADK}} + \sigma^2_{\perp\mathrm{IR}} = \frac{1}{2}\left(\frac{3I^{3/2}}{2\omega^2(2E_i)^{3/2}} + w^2\right). \tag{6.10}$$

Accordingly, the width of the convoluted distribution reads:

$$\Gamma_{||\mathrm{IR}}(p_{||}) = A \cdot \exp\left(-(p_{||}-p_0)^2 \left(\frac{3I^{3/2}}{\omega^2(2E_i)^{3/2}} + w^2\right)^{-1}\right). \tag{6.11}$$

Eq. 6.11 is used as a fit function to determine the laser intensity I. The width w for the "no IR" case is measured by the experiment. The photon energy is $\hbar\omega_{\mathrm{IR}} = 1.55\,\mathrm{eV}$ and the ionization potential from Ar to Ar^+ is $I_p = 15.8\,\mathrm{eV}$ [137]. In order to validate the ADK-approach, the method is tested with a known momentum distribution for Ar^+ ions taken from Ref. [59] in Fig. 6.6 (a). A fit according to Eq. 6.11 yields an IR laser intensity of $5.4 \times 10^{14}\,\mathrm{W/cm^2}$, which is very close to the input value of $5.2 \times 10^{14}\mathrm{W/cm^2}$. Therefore, the ADK method is approved to give a substantiated estimation of the laser intensity. Fig. 6.6 (b) and (c) show the $p_{||}$ momentum distribution of Ar^+ ions for two laser settings. The laser is polarized along $p_{||}$. Fits by Eq. 6.11 result in intensities of $I = (2.2 \pm 0.1) \times 10^{14}\,\mathrm{W/cm^2}$ and $I = (2.0 \pm 0.1) \times 10^{14}\,\mathrm{W/cm^2}$ for 0.3 IR transmission at 350 fs and 0.1 IR transmission at 90 fs, respectively.

[51] At the present wavelength $\lambda = 800\,\mathrm{nm}$ and referring to the result of the first approach ($I \approx 2.5 \times 10^{14}\,\mathrm{W/cm^2}$), the Keldysh parameter is $\gamma \approx 1$, i.e., in the transition region between the multi-photon and the strong-field regime (see Sec. 2.1.2) and the ADK-theory is applicable.

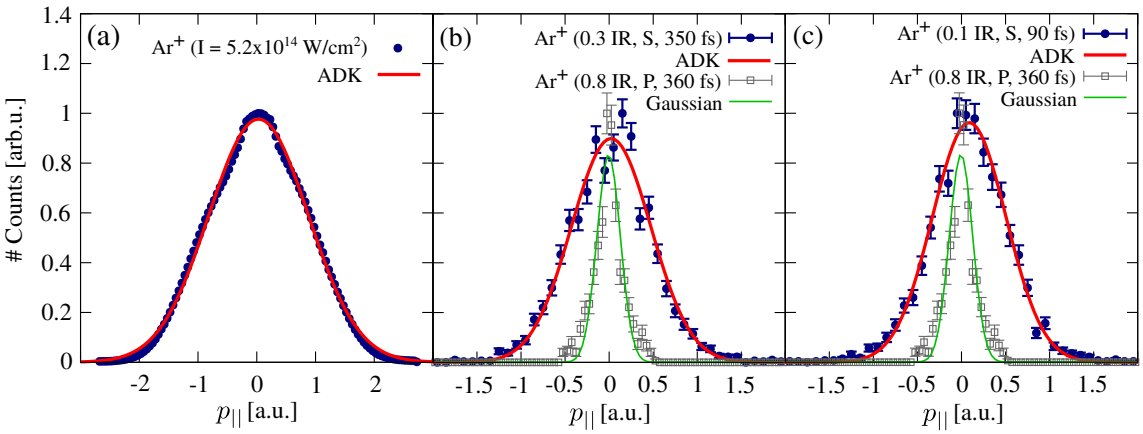

Figure 6.6: Momentum distribution $p_{||}$ of Ar^+ ions. The laser is S-polarized along $p_{||}$. The red ADK fits are according to Eq. 6.11 and assume an unfolded width of $w = 0.188$ a.u., which is determined by a Gaussian fit (green line) to the longitudinal momentum in case of P polarization, i.e., perpendicular to $p_{||}$. (a) $p_{||}$ measured in Ref. [59] at a laser intensity of 5.2×10^{14} W/cm^2. (b) 0.3 IR transmission, 350 fs, S-polarized. (c) 0.1 IR transmission, 90 fs, S-polarized.

Comparison of the Methods

The intensity of the laser is adjusted by the transmission through a power throttle. Fig. 6.7 shows the estimated intensity by the Ar^{2+}/Ar^+ ratio and the ADK approach in dependence on the transmission. For the 350 fs setting, the values obtained by the ratio and ADK method agree well. In the case of 90 fs, the two methods are off by ∼25 %. A linear dependence is visible for both cases. During the experiments, the transmission is varied from 0.05 to 0.3, which means $I_{IR} \approx 1 - 2 \times 10^{14}$ W/cm^2.

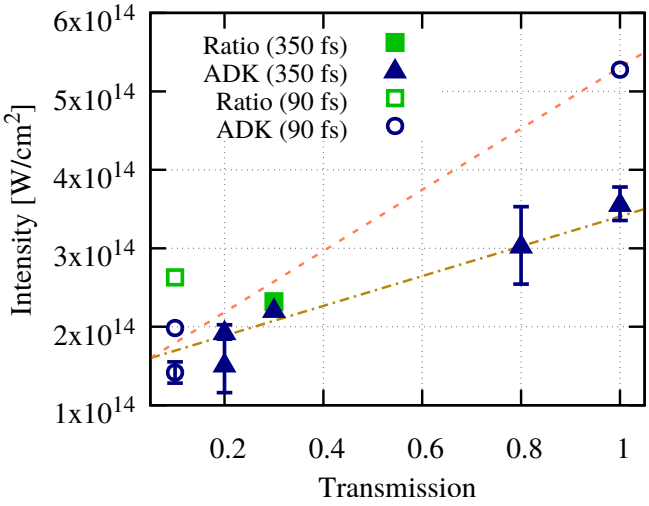

Figure 6.7: IR laser intensities estimated by the Ar^{2+}/Ar^+ ratio and the ADK approach.

6.2.2 Time of Flight Mass Spectrum with FEL and IR Laser

The time of flight (TOF) mass spectrum of $Ar^{(1-4)+}$ ions shown in Fig. 6.8 (a) is recorded with FEL and IR laser being present at the same time. As for the experiment using only FEL pulses (see Sec. 6.1), the XUV photon energy is $\hbar\omega = 27\,\text{eV}$ at an intensity of $I_{\text{FEL}} = 10^{13} - 10^{14}\,\text{W/cm}^2$. The intensity of the IR laser is estimated to $I_{\text{IR}} \approx 1 - 2 \times 10^{14}\,\text{W/cm}^2$ (see Sec. 6.2.1). Compared to the TOF spectrum with XUV only (see Fig. 6.8 (b)), a drastic difference is observed for Ar^{2+}. With IR laser, Ar^{2+} is the most prominent peak in the spectrum and even exceeds Ar^{+}. Fig. 6.8 (c) shows a difference plot of Fig. 6.8 (a) minus (b). The excess of Ar^{2+} with IR laser is clearly visible. A zoom into the TOF region of Ar^{3+} and Ar^{4+} also shows an excess these ion species with IR being present. For Ar^{+}, a small decrease is noticeable. The Ar^{+} peak popping up in the positive range is due to saturation of the detector. High FEL intensities, however, are needed to reach high ionic charge states.

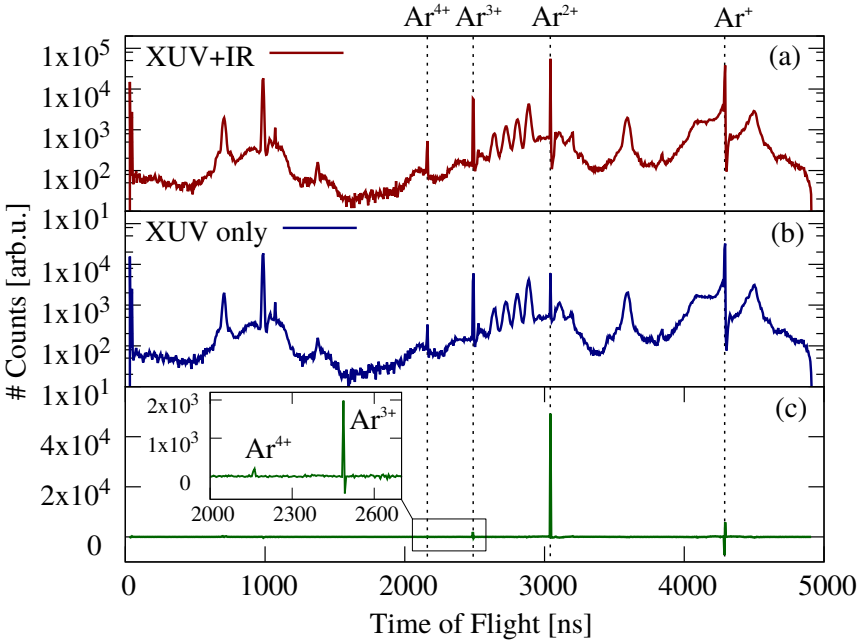

Figure 6.8: (a) TOF mass spectrum of $Ar^{(1-4)+}$ ions (dashed lines) at $\hbar\omega = 27\,\text{eV}$, $I_{\text{FEL}} = 10^{13} - 10^{14}\ \text{W/cm}^2$ and IR laser at 0.05 IR transmission. According to Sec. 6.2.1, this corresponds to an IR intensity of $I_{\text{IR}} \approx 1 \times 10^{14}\ \text{W/cm}^2$. The pulse length of the IR laser is set to 350 fs to guarantee temporal overlap. (b) TOF mass spectrum of $Ar^{(1-4)+}$ ions (dashed lines) at $\hbar\omega = 27\,\text{eV}$, $I_{\text{FEL}} = 10^{13} - 10^{14}\ \text{W/cm}^2$ without IR. (c) Difference plot of (a) minus (b).

The analysis of Fig. 6.8 demonstrates a strong influence of the IR laser on the total number of produced ions. In the next step, the $Ar^{(1-4)+}$ yields are analyzed as a function of the delay between IR and XUV pulse and as a function of the FEL intensity.

6.2.3 Ar^{2+} Ions

Delay-Dependent Ar^{2+} Yield

At first, the number of Ar^{2+} ions is examined as a function of the pump-probe delay for three transmission settings of the IR laser (see Fig. 6.9). The entire delay range is $t_d = \pm 2$ ps. For negative delays ($t_d < 0$), the IR precedes the XUV pulse, for positive delays ($t_d > 0$) the IR arrives late with respect to the XUV pulse. Fig. 6.9 (a) shows the delay-dependent Ar^{2+} yield for a IR laser transmission of $T = 0.3$. The yield distribution is normalized to the averaged number of counts for negative delays. Accordingly, for $\Delta t < 0$, the yield equals $Y = 1$ over a broad delay range (-2 ps to ~ -0.5 ps). For $t_d > 0$, the yield increases step-like to $Y = 4.9$ and stays constant over the entire positive delay range. For lower IR laser transmissions of $T = 0.1$ and $T = 0.05$ (see Fig. 6.9 (b) and (c)), the yield increases to $Y = 9.0$ and $Y = 11.8$, respectively, and is even more pronounced.

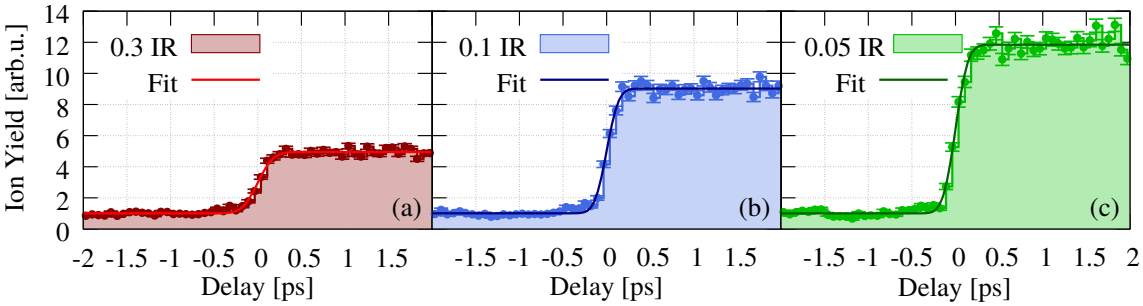

Figure 6.9: Yield of Ar^{2+} ions as function of the delay between IR and XUV pulse. Here and in the following, for negative delays, the IR pulse arrives early with respect to the XUV pulse, for positive delays vice versa. Continuous lines are fits according to Eq. 6.17. (a) 0.3 IR laser transmission. (b) 0.1 IR laser transmission. (c) 0.05 IR laser transmission.

Excitation and Ionization Scheme

As already touched in the beginning of Sec. 6.2, the delay-dependent change in the Ar^{2+} yield is explained by the XUV excitation of Ar^{+*} states, which are efficiently probed to Ar^{2+} by a subsequent IR pulse:

$$\text{Pump}: \quad \text{Ar} \xrightarrow{\text{XUV}} \text{Ar}^{+} + e^{-} \xrightarrow{\text{XUV}} \text{Ar}^{+*}, \tag{6.12}$$

$$\text{Probe}: \quad \text{Ar}^{+*} \xrightarrow{\text{IR}} \text{Ar}^{2+} + e^{-}. \tag{6.13}$$

If the IR precedes the XUV pulse, it cannot ionize excited Ar^{+*} states, because they have not been populated yet by the XUV absorption. Only if Ar^{+*} states have been excited by the XUV beforehand (see Eqs. 6.12 and 6.13), a succeeding IR-probe

pulse can ionize them to the Ar^{2+} continuum. A detailed energy level scheme of the involved states is depicted in Fig. 6.10. At first, neutral Ar atoms are ionized to the $Ar^{+}3p^5(^2P_{1/2,3/2})$ ground state by the absorption of one XUV photon. Sequentially, within the same FEL pulse, a second XUV photon is absorbed that excites to Ar^{+*} states (Fig. 6.10 (a)). Three dipole-allowed transitions from the $Ar^{+}3p^5(^2P_{1/2,3/2})$ ground state to Ar^{+*} states are reported in literature [137][52]:

$$Ar^{+}3p^5(^2P_{3/2,1/2}) + \hbar\omega \rightarrow Ar^{+}3p^4(^1D)5d(^2D_{5/2})\ (26.62\,\text{eV}), \tag{6.14}$$

$$Ar^{+}3p^5(^2P_{3/2,1/2}) + \hbar\omega \rightarrow Ar^{+}3p^4(^1S)5s(^2S_{1/2})\ (26.66\,\text{eV}), \tag{6.15}$$

$$Ar^{+}3p^5(^2P_{3/2,1/2}) + \hbar\omega \rightarrow Ar^{+}3p^4(^1D)5d(^2S_{1/2})\ (26.89\,\text{eV}). \tag{6.16}$$

The last transition (Eq. 6.16) is the strongest with an oscillator strength two to four times higher than for the others (Eqs. 6.14 and 6.15) [69].

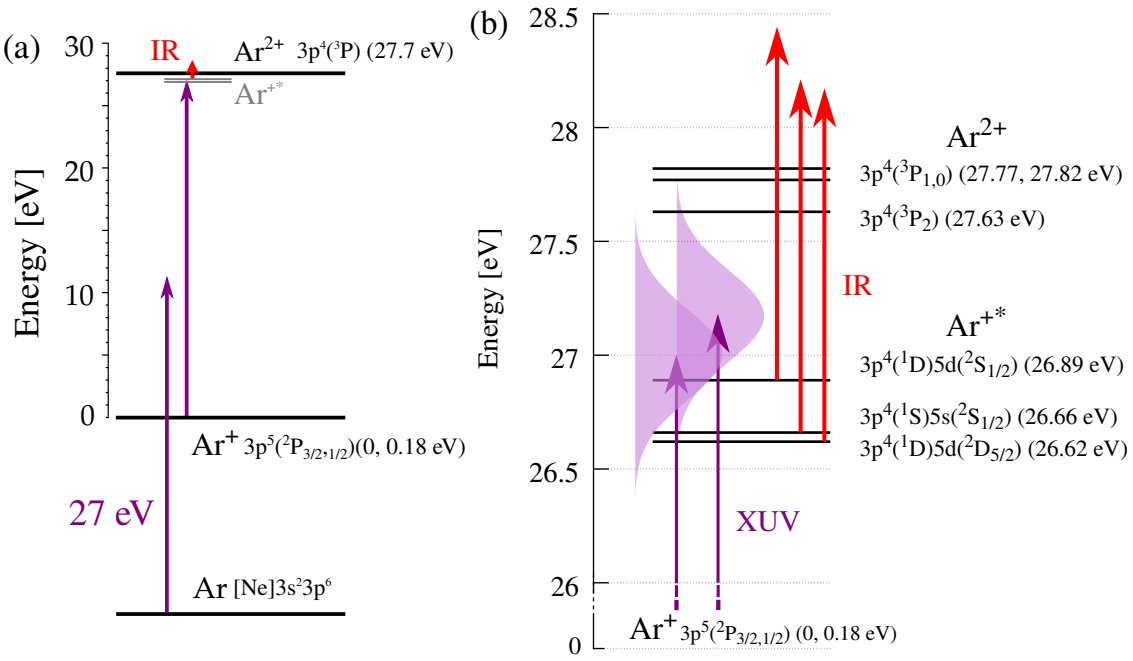

Figure 6.10: Energy level scheme up to Ar^{2+} [137]. (a) Two photons of $\hbar\omega = 27\,\text{eV}$ (purple arrows) are sequentially absorbed to excite singly-charged Ar^{+*} states just below the Ar^{2+} threshold. (b) Zoom into the Ar^{2+} threshold region. One IR photon (red arrow) of $\hbar\omega_{IR} = 1.55\,\text{eV}$ is sufficient to ionize, e.g., from Ar^{+} $3p^4(^1D)5d(^2S_{1/2})$, to the Ar^{2+} continuum. The purple Gaussians represent the FEL bandwidth of 0.5 eV (FWHM).

[52]The energy of the excited states (value in brackets) is given with respect to Ar^{+} $3p^5(^2P_{3/2})$.

Fig. 6.10 (b) shows that the XUV photon energy of $\hbar\omega = 27\,\text{eV}$ favors the strong transition to the Ar^+ $3p^4(^1D)5d(^2S_{1/2})$ state within the FEL bandwidth of 0.5 eV (FWHM). For all three Ar^{+*} states (Eqs. 6.14, 6.15 and 6.16), the energy of one IR photon (1.55 eV) is sufficient to ionize to the Ar^{2+} continuum. Generally, the IR cross section for highly excited states is large. In addition, excitations to states with larger quantum number n, e.g., Rydberg states, above Ar^+ $3p^4(^1D)5d(^2S_{1/2})$ is also possible within the FEL bandwidth.
In Fig. 6.10, the IR ionization is demonstrated using a vertical multi-photon picture. However, as already touched in Sec. 6.2.1, at the present IR intensities of $I_{\text{IR}} \approx 1 \times 10^{14}\,\text{W/cm}^2$, one is within the transition region between the multi-photon and the strong-field picture to describe the ionization. However, in contrast to dedicated studies looking explicitly into this transition region (e.g. Ref. [59]), in the present study the IR laser should be regarded just as a "tool", which allows to probe and control the XUV multi-photon ionization.
The highest yield ratio is observed for the lowest IR transmission of $T = 0.05$ (see Fig. 6.9). This is counter-intuitive to the expectations of a stronger IR pulse enabling the production of more Ar^{2+} and points to a saturation effect being the cause of this behavior. With higher IR intensity, more Ar^{2+} is produced and the detector is saturated more quickly. It may not count the number of ions correctly any more, which directly affects the yield ratio. However, as this experiment also aims to look at higher ion charge states, a saturation of the low ion charge states is unavoidable.

Temporal Resolution

The slope of the yield increase at zero delay is an intrinsic measure of the temporal resolution of the experiment, which itself depends on the pulse durations of pump and probe pulse (see Fig. 6.11). The step-like delay-dependent ion yield (see Fig. 6.9) allows to use an error function

$$f(t_d) = a \cdot \text{erf}((t_d - t_0)/\sqrt{2}\sigma) + c, \tag{6.17}$$

with amplitude a, delay value t_d, delay offset t_0, standard deviation σ and offset c, to describe the increase of Ar^{2+}.
For all three IR settings, the offset t_0 is centered at $t_0 = 0\,\text{ps}$ within the error values of the fit. In the present case, the XUV pulses of $\sim 50\,\text{fs}$ (FWHM) are shorter than the $\sim 300\,\text{fs}$ (FWHM) IR pulses. Thus, the temporal resolution is mostly limited by the IR pulse duration (see Fig. 6.11). Assuming Gaussian pulse profiles for XUV and IR pulse, the width of the fitted error function represents the temporal resolution of the experiment. The full width at full maximum (FWHM) depends on the standard deviation σ like $\text{FWHM} = 2\sqrt{2\ln(2)}\sigma$. Taking the mean value of the three fits shown in Fig. 6.9 results in $(280 \pm 20)\,\text{fs}$ FWHM for the instrument response function.

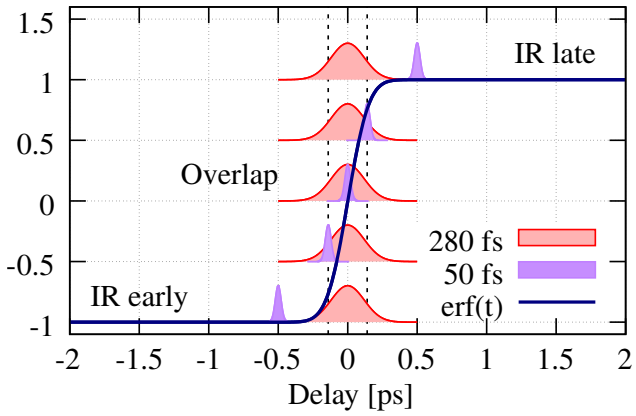

Figure 6.11: Illustration of the analogy between Ar^{2+} yield and temporal resolution. The red colored Gaussian profiles represent IR pulses of 280 fs (FWHM), the purple ones XUV pulses of 50 fs (FWHM).

Lifetime of Excited States

The excitation and ionization pathway introduced in Eqs. 6.12 and 6.13 is fulfilled, when XUV and IR pulse temporally overlap for the first time. However, from $t_d \sim +270\,\text{fs}$ onwards, the yield increase lasts until the end of the positive delay range $t_d = +2\,\text{ps}$, i.e., at points in time when the IR pulse arrives long after the XUV excitation. This is in contrast to, e.g., two-color above threshold ionization of noble gases. Here, the formation of photoelectron sidebands only occurs for temporal overlapping XUV and IR pulses and thereby gives a measure for the synchronization [172, 209, 210]. In the present case, the constant ion yield for $t_d > +270\,\text{fs}$ implies long lifetimes of the Ar^{+*} states, i.e., longer than 2 ps.
In a comparable experiment, Flögel *et al.* [69] observed Rabi oscillations in XUV ionization of atomic argon using HHG radiation. Similar to the present experiment, the 17$^{\text{th}}$ harmonic ($\hbar\omega = 26.78\,\text{eV}$) excites intermediate Ar^{+*} states and the Ar^{2+} yield is observed as a function of the delay between HHG-pump and IR-probe. In contrast to the present experiment, the intensities in Ref. [69] were lower: $I_{\text{XUV}} = 3.5 \times 10^{12}\,\text{W/cm}^2$ and $I_{\text{IR}}^{\text{max}} = 2 \times 10^{12}\,\text{W/cm}^2$. Furthermore, shorter pulses were used, i.e., $T_{\text{XUV}} = (20 \pm 3)\,\text{fs}$ and $T_{\text{IR}} = (71 \pm 3)\,\text{fs}$, which results in a better temporal resolution. Thus, modulations in the delay-dependent Ar^{2+} yield, which are due to an AC stark shift and Rabi oscillations between the Ar^{+} ground state and the excited Ar^{+*} state, were resolved. In the present study, however, the IR intensity is higher and the temporal resolution not sufficient to observe these effects.

Ar^{2+} Yield vs. FEL Intensity

In analogy to Sec. 6.1.3, this section analyzes the Ar^{2+} ion yield as a function of the FEL intensity for the cases of the IR pulse arriving early ($t_d < 0$) and late ($t_d > 0$).

The respective ions are selected by conditions for the negative ($-2\,\mathrm{ps} < t_d < -0.5\,\mathrm{ps}$) and positive ($+0.5\,\mathrm{ps} < t_d < +2\,\mathrm{ps}$) delay range (see Fig. 6.9). As already discussed in the delay-dependent analysis, a succeeding IR laser pulse has the potential of "steering" distinct XUV multi-photon ionization pathways by, e.g., reducing the number of XUV photons needed to reach a specific charge state. Thus, the ion yield is plotted as a function of the FEL intensity and the power law $Y \propto I^n$ [218] is applied. Fig. 6.12 (a), (b) and (c) display the Ar^{2+} ion yield as a function of FEL intensity for $t_d > 0$ and $t_d < 0$ as well as 0.3, 0.1 and 0.05 IR transmission, respectively.
For all three IR transmissions, the ion yields created by a late IR pulse, i.e., $t_d > 0$, clearly exceed those of $t_d < 0$ over the entire FEL intensity range. Furthermore, the ion production sets in at lower FEL intensities and the saturation region is reached at lower intensities. Before the onset of saturation, e.g., $I < 2.5$ arb.u., the ion yields for $t_d > 0$ are fitted according to $Y = a \cdot I^n$. For all IR settings, the fit results in a number of absorbed photons $n = 2$ within the error bars. For $t_d < 0$, all fits return $n = 3$ in the unsaturated region. Hence, in case of a late IR pulse, the number of photons needed to reach Ar^{2+} is reduced by one. The underlying energy level scheme (see Fig. 6.10) is recapitulated in a compact form in Fig. 6.13. Ionization channel (a) proceeds via the sequential absorption of three XUV photons:

$$\text{(a)}\ \mathrm{Ar} \xrightarrow{\mathrm{XUV}} \mathrm{Ar}^{+} + e^{-} \xrightarrow{\mathrm{XUV}} \mathrm{Ar}^{+*} \xrightarrow{\mathrm{XUV}} \mathrm{Ar}^{2+} + e^{-}. \tag{6.18}$$

The number of photons $n = 3$ for $t_d < 0$ agrees with the single pulse experiment. Thus, for $t_d < 0$, the IR pulse has little influence on the Ar^{2+} yield.

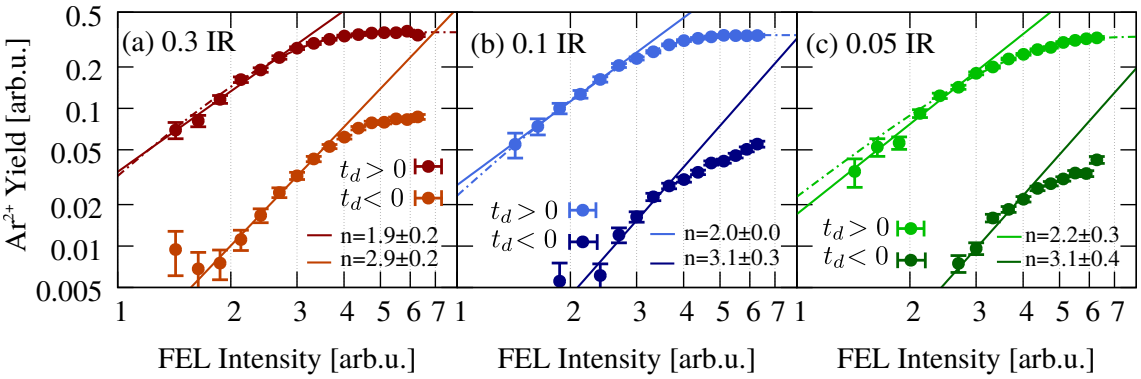

Figure 6.12: (a) Ar^{2+} yield as function of the FEL intensity. (a) With 0.3 IR transmission, for $t_d > 0$ (red) and $t_d < 0$ (orange). The respective ions are selected by conditions for the negative ($-2\,\mathrm{ps} < t_d < -0.5\,\mathrm{ps}$) and the positive ($+0.5\,\mathrm{ps} < t_d < +2\,\mathrm{ps}$) delay range (see Fig. 6.9). Also shown are fits according to $Y = a \cdot I^n$ (full line) in the unsaturated region and saturation fits (only for $t_d > 0$) according to $Y = b \cdot (1 - \exp(-c \cdot I^n))$ (dashed-dotted lines). (b) Same as (a), but for $T = 0.1$ ($t_d > 0$: blue, $t_d < 0$: dark-blue). (c) Same as (a), but for $T = 0.05$ ($t_d > 0$: green, $t_d < 0$: dark-green).

However, with the IR pulse arriving late, ionization channel (b) is open and the number of absorbed XUV photons required to ionize to Ar^{2+} is reduced to $n = 2$:

$$\text{(b) Ar} \xrightarrow{\text{XUV}} \text{Ar}^{+} + e^{-} \xrightarrow{\text{XUV}} \text{Ar}^{+*} \xrightarrow{\text{IR}} \text{Ar}^{2+} + e^{-}. \tag{6.19}$$

The fit results of $n = 2$ obtained for $t_d > 0$ (see Fig. 6.12 (a), (b) and (c)) show that channel (b) clearly dominates channel (a).

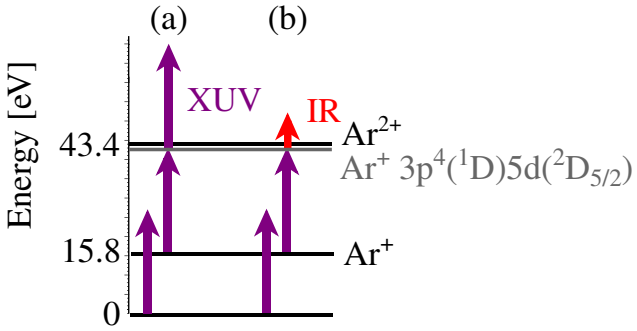

Figure 6.13: Energy level scheme up to Ar^{2+}. The purple arrows mark XUV photons of $\hbar\omega = 27\,\text{eV}$, while the red arrow indicates an IR photon of $\hbar\omega_{\text{IR}} = 1.55\,\text{eV}$. In the ionization pathway (a) three XUV photons are absorbed to ionize to Ar^{2+}, whereas two are required in channel (b).

6.2.4 Ar^{+} Ions

Delay-Dependent Ar^{+} Yield

The plots to analyze the Ar^{+} yield as a function of the delay for the three IR transmissions are shown in Fig. 6.14.

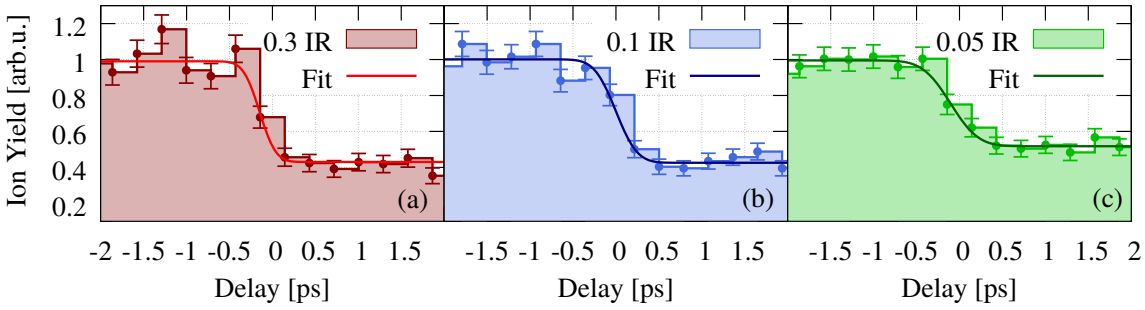

Figure 6.14: Yield of Ar^{+} ions as function of the delay between IR and XUV pulse. For negative delays, the IR pulse arrives early with respect to the XUV pulse, for positive delays vice versa. Continuous lines are fits according to Eq. 6.17. (a) 0.3 IR laser transmission. (b) 0.1 IR laser transmission. (c) 0.05 IR laser transmission.

The ion yield decreases for positive delays, because Ar^{+*} ions are ionized to Ar^{2+} by the succeeding IR pulse (see Eq. 6.13). However, the difference in the yield ratio $Y_{t_d<0}/Y_{t_d>0} \approx 0.45$ is not as pronounced as for Ar^{2+} ions and does not vary significantly for the three IR settings. A reason for this is the saturation of the Ar^+ signal already in case of just using XUV pulses. This is for example seen in the TOF spectrum shown in Fig. 6.8 (b). Here, a dip after the Ar^+ main peak is a signature for loss of ion count rate due to a saturated detector. Thus, the influence of the IR laser is not as strongly visible as for Ar^{2+} ions.
Since the Ar^+ signal is already saturated at low FEL intensities in the single XUV pulse measurement (see Fig. 6.4), it is set aside to discuss the Ar^+ yield as a function of the FEL intensity.

6.2.5 Ar^{3+} Ions

Delay-Dependent Ar^{3+} Yield

Next, the yield of Ar^{3+} is analyzed as a function of the delay in Fig. 6.15. Only a slight increase of the yield ratio $Y_{t_d<0}/Y_{t_d>0} \approx 15\,\%$ is observed for all three IR settings. The error function fits return delay offsets of $t_0 = (430 \pm 180)$ ps, $t_0 = (650 \pm 220)$ ps and $t_0 = (560 \pm 160)$ ps for 0.3, 0.1 and 0.05 IR transmission, respectively. This implies that the IR pulse affects the creation of Ar^{3+} ions delayed with respect to the temporal overlap of XUV and IR at $t_d = 0$ ps, which is marked by also plotting the fits to the Ar^{2+} yield of Fig. 6.15. To explain the temporal offset, the energy level scheme shown in Fig. 6.16 needs to be considered.

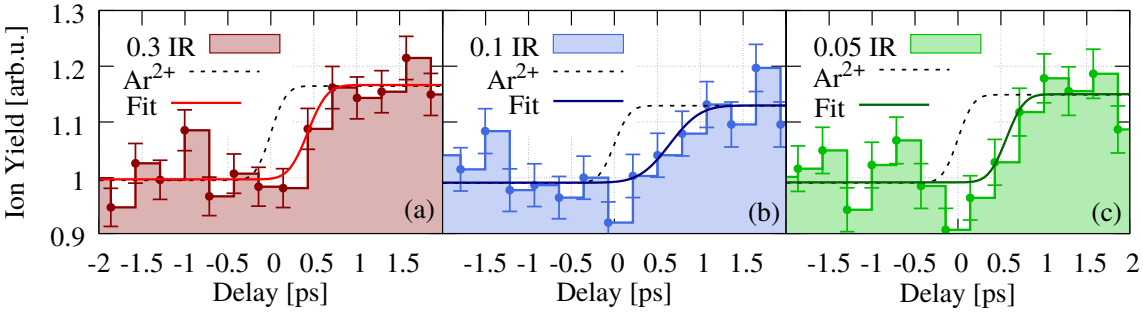

Figure 6.15: Yield of Ar^{3+} ions as function of the delay between IR and XUV pulse. For negative delays, the IR pulse arrives early with respect to the XUV pulse, for positive delays vice versa. Continuous lines are fits according to Eq. 6.17. Dashed lines represent the fits to Ar^{2+} (see Fig. 6.9) scaled to the Ar^{3+} yields. (a) 0.3 IR laser transmission. (b) 0.1 IR laser transmission. (c) 0.05 IR laser transmission.

From the Ar^{2+} $3p^4(^3P_{2,1,0})$ state, one dipole-allowed transition at $\hbar\omega = (27.0 \pm 0.5)$ eV (FWHM) to excited Ar^{2+*} is listed in literature [137][53]:

$$Ar^{2+}\ 3p^4(^3P_{2,1,0}) + \hbar\omega \rightarrow\ Ar^{2+}\ 3p^3(^2D)3d(^3P_{2,1,0})\ (26.53, 26.58, 26.60\,\text{eV}). \quad (6.20)$$

Yet, the bandwidth overlap with the Ar^{2+} $3p^3(^2D)3d(^3P_{2,1,0})$ state is little and transitions to the singlet Ar^{2+} $3p^3(^2D)3d(^1D_2,^1P_1,^1F_3)$ states at 27.27, 27.31 and 27.81 eV, respectively, are not dipole-allowed. This means that different to Ar^{+*}, only little population is transferred to excited Ar^{2+*} states. Furthermore, up to 10 IR photons need to be absorbed to ionize from Ar^{2+} $3p^3(^2D)3d(^3P_{2,1,0})$ to the Ar^{3+} continuum (see Fig. 6.16), which is 10 times more compared to the $Ar^{+*} \rightarrow Ar^{2+}$ case. The probability to simultaneously absorb the sufficient number of IR photons is highest at the maximum peak intensity of the IR pulse and not already at the rising edge of the pulse.

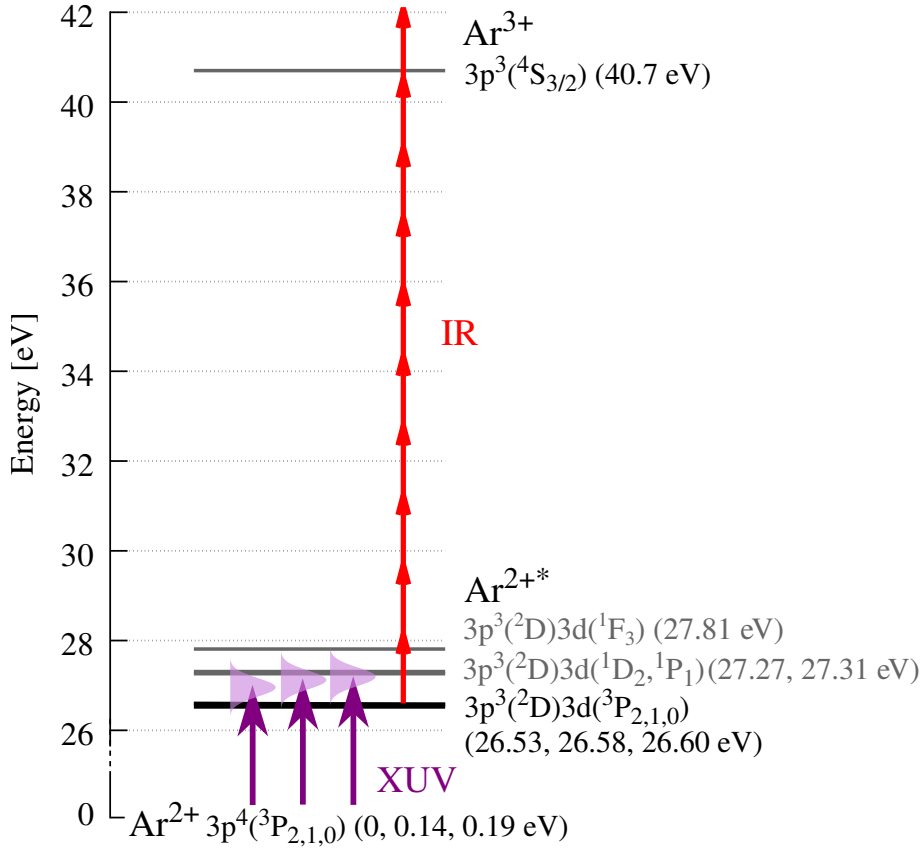

Figure 6.16: Energy level scheme between Ar^{2+} and Ar^{3+} [137]. (a) One photon of 27 eV is absorbed from the Ar^{2+} ground state. Within the bandwidth, the transition to $Ar^{2+}3p^3(^2D)3d(^3P_{2,1,0})$ is dipole-allowed.

[53]The energy of the excited states (value in brackets) is given with respect to Ar^{2+} $3p^4(^3P_2)$.

The weak energetic overlap of the XUV photons with the Ar^{2+} $3p^3(^2D)3d(^3P_{2,1,0})$ intermediate state gives rise to the following interpretation of the delayed rise of the Ar^{3+} yield. The data recorded using only the IR laser (see Sec. 6.2.1) have shown that with all three transmission settings, the IR laser is strong enough to autonomously double-ionize atomic Ar. To achieve this, a potential difference of $\Delta E = 43.39\,\text{eV}$ needs to be overcome, or in different words, 28 IR photons need to be absorbed simultaneously. The ionization potential from the Ar^{2+} ground state to Ar^{3+} is 40.7 eV and from the intermediate Ar^{2+*} state to Ar^{3+} 14.2 eV. Thus, the IR intensity should be high enough to overcome both potential differences. The optimum conditions for this to happen are a high density of Ar^{2+} ions and high peak intensities of the IR laser. The first condition is fulfilled when the Ar^{2+} yield reaches saturation. In Fig. 6.15 it is shown that this point in time coincides with the start of the increase of the Ar^{3+} yield for all three IR intensities. Hence, the large energy gap, either between the Ar^{2+} ground state or the intermediate Ar^{2+*} state, explains the low relative increase of the Ar^{3+} yield of $\sim 15\,\%$ with IR being present. Unfortunately, within the error bars, no evidence for a dependence on the IR transmission is found.

Ar^{3+} Yield vs. FEL Intensity

In Fig. 6.17, the yield of Ar^{3+} ions is plotted as a function of the FEL intensity for the positive ($t_d > 0$) and the negative ($t_d < 0$) delay range. There is no obvious difference between the Ar^{3+} yield for $t_d > 0$ and $t_d < 0$ for all three IR transmissions. The yield ratio $Y_{t_d>0}/Y_{t_d<0}$ is plotted in Fig. 6.17 (d)-(f). As already seen in the delay-dependent analysis (see Fig. 6.15), a late arriving IR pulse has only little influence on the yield ratio and the increase amounts only to $\sim 15\,\%$ independent on the IR transmission.
Also the number of absorbed photons $n = 3.5$ is the same within the errors of the fit and matches the result for Ar^{3+} of the data recorded using only XUV pulses (see Fig. 6.4 in Sec. 6.1.3). Possible XUV multi-photon ionization channels are shown in Fig. 6.21. Channel (a) proceeds via absorption of either 4 photons from the saturated Ar^+ ground state or 3 photons from the also saturated $Ar^+3p^3(^1D)5d(^2D_{5/2})$ state. Channel (b) is IR-assisted and by overcoming the step from $Ar^+3p^3(^2D)3d(^3P)$ to Ar^{2+} with the IR laser, the number of XUV photons needed is reduced to $n = 2$ and $n = 3$, respectively. However, for channel (a) or (b), 2 XUV photons need to be absorbed to ionize from Ar^{2+} to Ar^{3+}. In Fig. 6.17 (a)-(c) and in the delay-dependent analysis (see Fig. 6.15) it is seen that the Ar^{3+} yield is only little affected by the IR pulse. Thus, one can conclude that not the number of available Ar^{2+} ions, which massively is affected by the IR pulse, is the limiting factor to reach Ar^{3+}, but the number of available XUV photons. This is also confirmed by the fit results of $n = 3.5$ (see Fig. 6.17). For reasons of completeness, the channels (c)-(f) are illustrated in Fig. 6.21. These channels, however, proceed via IR ionization from the Ar^{2+} ground

state or the Ar^{2+} $3p^3(^2D)3d(^3P_{2,1,0})$ state to Ar^{3+}, which has already been discussed in the delay-dependent analysis to be very rare. The measured number of absorbed photons $n = 3.5$ for $t_d > 0$ confirms that they do not contribute much to the absolute ion yield.

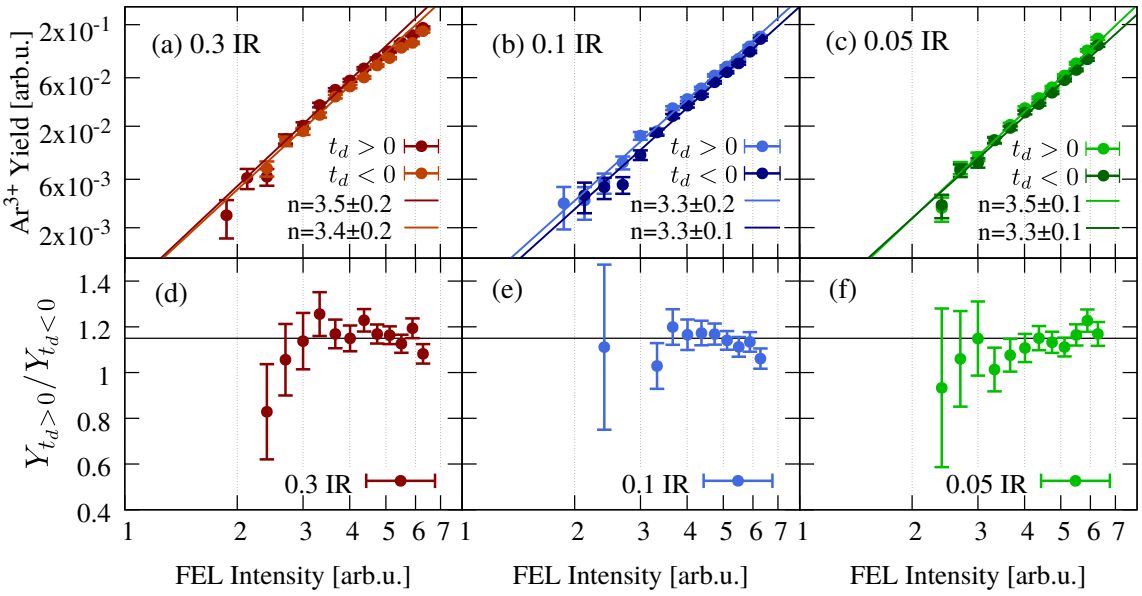

Figure 6.17: (a)-(c) Ar^{3+} yield as function of FEL intensity. (a) With 0.3 IR transmission, for $t_d > 0$ (dark-red) and $t_d < 0$ (dark-orange). The respective ions are selected by conditions for the negative ($-2\,\text{ps} < t_d < -0.5\,\text{ps}$) and the positive ($+0.5\,\text{ps} < t_d < +2\,\text{ps}$) delay range (see Fig. 6.15). Also shown are fits according to $Y = a \cdot I^n$ (full lines). (b) Same as (a), but for $T = 0.1$ ($t_d > 0$: blue, $t_d < 0$: navy). (c) Same as (a), but for $T = 0.1$ ($t_d > 0$: green, $t_d < 0$: dark-green). (d)-(f) Yield ratio $Y_{t_d>0}/Y_{t_d<0}$ for the cases of IR arriving late ($t_d > 0$) and early ($t_d < 0$) with respect to the FEL pulse. (d) IR transmission $T = 0.3$. (e) IR transmission $T = 0.1$. (f) IR transmission $T = 0.05$.

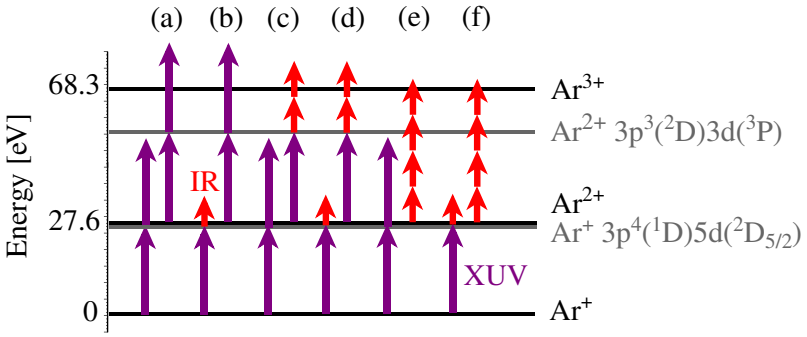

Figure 6.18: Energy level scheme up to Ar^{3+}. The purple arrows mark XUV photons of $\hbar\omega = 27\,\text{eV}$, while the red arrows indicate ionization by IR photons. Shown are six possible ionization pathways (a)-(f).

6.2.6 Ar^{4+} Ions

Delay-Dependent Ar^{4+} Yield

The delay-dependent yield of Ar^{4+} is plotted in Fig. 6.19. The relative yield ratio $Y_{t_d<0}/Y_{t_d>0} \approx 2$ is more pronounced compared to Ar^{3+}. The error function fits show no delayed rise of the yield increase with respect to time zero. In regard of the analysis of the Ar^{3+} yield, both observations imply that the IR-assisted ionization from $Ar^{3+} \rightarrow Ar^{4+}$ is eased compared to $Ar^{2+} \rightarrow Ar^{3+}$.

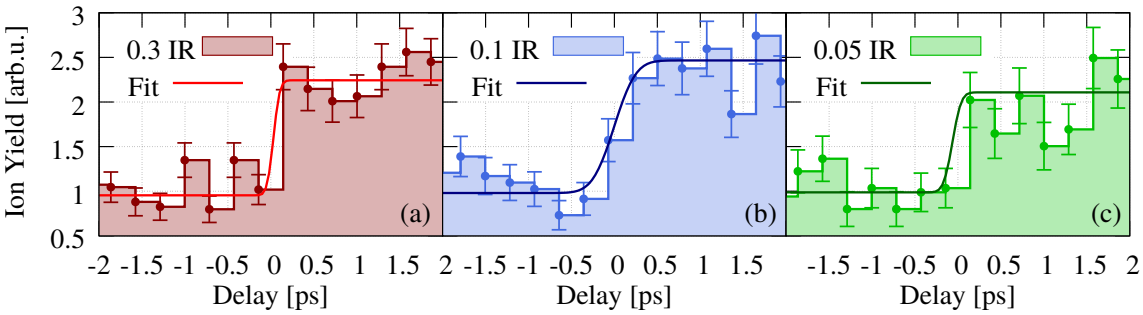

Figure 6.19: Yield of Ar^{4+} ions as function of the delay between IR and XUV pulse. For negative delays the IR pulse arrives early with respect to the XUV pulse, for positive delays vice versa. Continuous lines are fits according to Eq. 6.17. (a) 0.3 IR laser transmission. (b) 0.1 IR laser transmission. (c) 0.05 IR laser transmission.

The ionization potential of the Ar^{3+} $3p^3(^4S_{3/2},^2D_{3/2,5/2},^2P_{1/2,3/2})$ ground states is 59.58 eV, 56.96 eV and 55.26 eV, respectively [137]. Thus, the direct absorption of two XUV photons can excite Ar^{3+*} states very close to the Ar^{4+} ionization threshold. Unfortunately, no states are listed in the corresponding energy range [137]. However, if such high-lying Ar^{3+*} states are excited, the absorption of 3-4 IR photons will be sufficient to reach the Ar^{4+} continuum. The observed ion yields and the similarities to Ar^{2+} suggest the following ionization pathway:

$$Ar^{3+} \xrightarrow{2\times XUV} Ar^{3+*} \xrightarrow{IR} Ar^{4+} + e^- . \tag{6.21}$$

The yield increase up to $t_d = +2$ ps implies long lifetimes of the Ar^{3+*} states. Looking into literature [137], an alternative ionization pathway via a lower lying intermediate Ar^{3+*} state, which is reachable by a one-photon dipole-allowed transition, is also possible:

$$Ar^{3+}\ 3p^3(^2D_{3/2,5/2})\ (2.62\,\text{eV}) + \hbar\omega \rightarrow\ Ar^{3+}\ 3p^2(^1D)3d(^2D_{5/2})\ (29.59\,\text{eV}). \tag{6.22}$$

Compared to the ionization pathway suggested in Eq. 6.21, the ionization to Ar^{4+} requires the absorption of 20 IR photons. In analogy to Ar^{3+}, this should result

in a delayed rise of the Ar^{4+} yield with respect to time zero. However such a behavior is not observed in the data (see Fig. 6.19), which minimizes the probability for ionization via the Ar^{3+} $3p^2(^1D)3d(^2D_{5/2})$ state to be the dominant channel.

Ar^{4+} Yield vs. FEL Intensity

The yield of Ar^{4+} ions is studied as a function of the FEL intensity in Fig. 6.20 (a)-(c). The number of absorbed photons is in average $n = 5.5$ and agrees with the result for Ar^{4+} of the XUV only data (see Fig. 6.4, Sec. 6.1.3). However, for all IR transmissions, the absolute yield for $t_d > 0$ is higher compared to $t_d < 0$, which is also seen in the yield ratio that is $Y_{t_d>0}/Y_{t_d<0} \approx 2.5, 2$ and 1.7 for $T = 0.3, 0.1$ and 0.05, respectively (see Fig. 6.20 (d)-(f)).

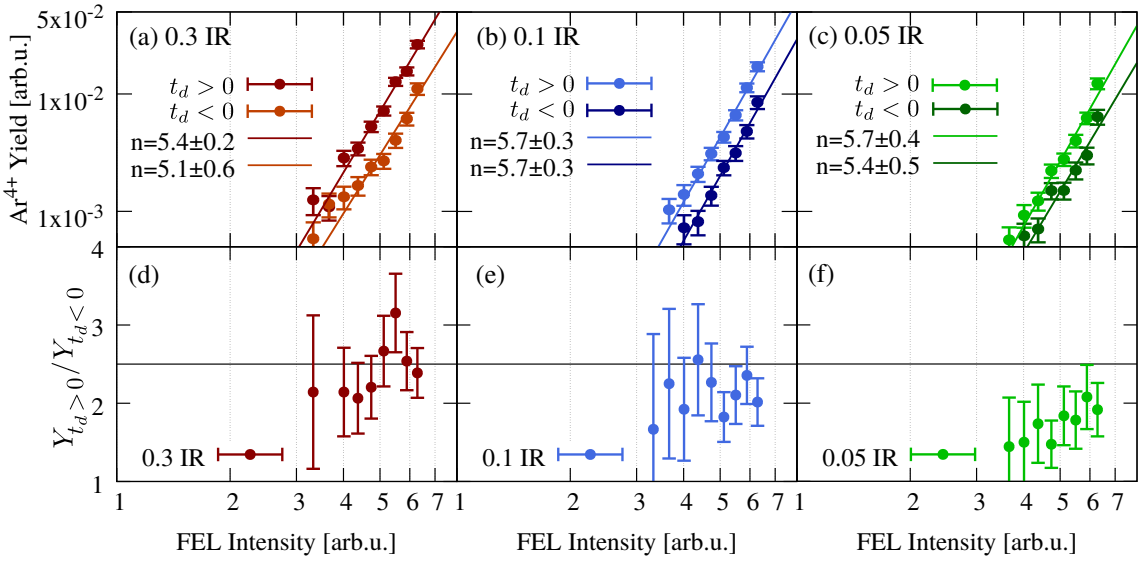

Figure 6.20: (a)-(c) Ar^{4+} yield as function of the FEL intensity. (a) With 0.3 IR transmission, for $t_d > 0$ (dark-red) and $t_d < 0$ (dark-orange). The respective ions are selected by conditions for the negative ($-2\,\text{ps} < t_d < -0.5\,\text{ps}$) and positive ($+0.5\,\text{ps} < t_d < +2\,\text{ps}$) delay range (see Fig. 6.19). Also shown are fits according to $Y = a \cdot I^n$ (full line). (b) Same as (a), but for $T = 0.1$ ($t_d > 0$: blue, $t_d < 0$: dark-blue). (c) Same as (a), but for $T = 0.1$ ($t_d > 0$: green, $t_d < 0$: dark-green). (d)-(f) Yield ratio $Y_{t_d>0}/Y_{t_d<0}$ for the cases of IR arriving late ($t_d > 0$) and early ($t_d < 0$) with respect to the FEL pulse. (d) IR transmission $T = 0.3$. (e) IR transmission $T = 0.1$. (f) IR transmission $T = 0.05$.

The dependence of the yield ratio on the IR transmission is a further indication that the suggested pathway via a Ar^{3+*} resonant state (see Eq. 6.21) is present. Regarding the energy difference, 3 or 2 IR photons are needed to overcome the energy difference between these Ar^{3+*} states and the Ar^{4+} continuum. The IR absorption probability scales with the number of available photons and is therefore enhanced for higher IR

intensities. Possible ionization channels are illustrated in Fig. 6.21. As discussed in Sec. 6.1.3, Ar^{3+} is reached by either 3 or 2 XUV photons from saturated Ar^{+*} and Ar^{2+}, respectively. Hence, channel (a) and (b) cannot be clearly distinguished by "counting" the number of absorbed XUV photons.
However, the determined number $n = 5.5$ allows to suggest that the total yields for $t_d > 0$ and $t_d < 0$ are mostly dominated by the absorption of 3 XUV photons from Ar^{3+}, which means in total 6 or 5 photons from Ar^{+*} and Ar^{2+}, respectively. Otherwise, the number of absorbed photons should change more dramatically towards $n \approx 5$ in analogy to Ar^{2+}. The same argument is true for channel (c), which consequently has only little influence on the number of absorbed photons.

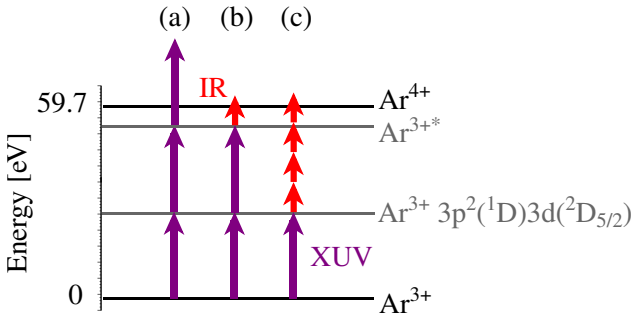

Figure 6.21: Energy level scheme up to Ar^{4+}. The purple arrows mark XUV photons of $\hbar\omega = 27\,\text{eV}$, while the red arrows indicate ionization by IR photons.

7 Dissociation and Fragmentation Dynamics of Hydrogen Molecules

Hydrogen (H_2) is the smallest molecule. However, despite its simple composition of just two protons and two electrons, it is a system, which is still widely studied as it gives a perfect playground to test quantum mechanics on its fundamental level and to benchmark state-of-the-art calculations. A whole "zoo" of experiments dealing with the light-induced dissociation and fragmentation of H_2 is reported in literature. First experiments used XUV synchrotron radiation to extract information about the dissociation dynamics by measuring the kinetic energies and angular distributions of the ejected protons and electrons [116, 148, 228]. Synchrotron radiation in combination with advanced multi-particle detection techniques like REMIs (see Ch. 4) allows to measure protons and electrons in coincidence, which improves the state sensitivity and helps to identify specific ionization mechanisms [279]. Amongst other things, general physical principles like symmetry breaking in molecules have been discovered [159]. Another type of experiments uses strong and ultrashort optical laser pulses in order to ionize, dissociate and fragment the molecule [18, 173, 206, 219, 277] as well as to follow the dynamics of the H_2^+ nuclear wave packet in real-time [53, 54, 66][54]. Furthermore, HHG-pump IR-probe schemes are exploited to observe and control wave packet dynamics [65]. Besides these experimental efforts, a rich and powerful time-dependent theory has been developed to describe H_2 and its dynamical response after excitation and ionization by photons, e.g., Refs. [14, 61–63].
However, a search through literature reveals only little reports on photoionization and -excitation using FEL radiation, i.e., in an intensity regime where more than one high energetic photon can be absorbed within one pulse. At FLASH (see Sec. 3.5), Jiang *et al.* [123] measured the KER distribution of coincident $D^+ + D^+$ fragments after two-photon double-ionization of D_2 at 38 eV. A comparison to theory allowed to distinguish the direct from the sequential ionization channel. In a second experiment, a XUV-pump XUV-probe scheme was used to map the nuclear wave packet motion of D_2^+ onto the repulsive $H^+ + H^+$ potential curve [121].
In order to improve the understanding of photoionization of H_2, the following section discusses dissociation and fragmentation channels present at $\hbar\omega = 28.2\,\text{eV}$ and an FEL intensity of $I_{\text{FEL}} \sim 10^{13}$ W/cm^2, i.e., about a factor of 3 less compared to the estimated FEL intensity of Sec. 6.1. The experimental observable is the kinetic energy of the H^+ fragments.

[54] Also the wave packet dynamics of the ionic deuterium molecule D_2^+ is studied.

Furthermore, it is shown how the ground-state dissociation of H_2^+ can be used as an intrinsic tool to find and quantify the temporal overlap between an XUV and IR laser pulse (see Sec. 7.2). The applied scheme is general and suitable to determine the temporal overlap for any gas-phase XUV-IR pump-probe experiment in a photon energy range between 20 to 30 eV.

7.1 Interaction with a Single XUV Pulse

The results on dissociation and fragmentation of H_2 obtained in a single XUV pulse measurement are discussed in the following sections.

7.1.1 Ground-State Dissociation

The ionization of H_2 to H_2^+ by a single XUV photon has been studied using synchrotron radiation, e.g., Refs. [116, 148, 228], and calculations [245] could confirm the measured cross sections to a high level of accuracy. At photon energies above $\hbar\omega \approx 20\,\text{eV}$, two ionization channels are open. The first is the non-resonant non-dissociative ionization to vibrational levels ν of the bound ionic H_2^+ $^2\Sigma_g^+(1s\sigma_g)$ state,

$$H_2 + \hbar\omega \rightarrow H_2^+\ {}^2\Sigma_g^+(1s\sigma_g, \nu) + e^-. \tag{7.1}$$

The second is non-resonant dissociative photoionization [62]:

$$H_2 + \hbar\omega \rightarrow H_2^+\ {}^2\Sigma_g^+(1s\sigma_g) + e^- \rightarrow H^+ + H(nl) + e^-. \tag{7.2}$$

Despite a cross section, which is just 5 % of that of the non-resonant non-dissociative channel (see Eq. 7.1) [158], especially dissociative photoionization of H_2 (and D_2) (see Eq. 7.2) has been extensively studied from the experimental side, because the kinetic energy of the ejected proton is a profound observable. Based on this, a rich portfolio of theoretical studies has emerged over the years. A comprehensive theoretical study is presented in Ref. [62] and includes, e.g., doubly excited H_2^{**} states.
In the dissociation reaction of Eq. 7.2, only the charged H^+, but not the neutral H, can be measured in a REMI experiment (see Ch. 4). However, the KER (see Sec. 4.6) is given by the sum of the kinetic energies of the H^+ and the neutral H fragment:

$$\text{KER} = E_{\text{kin}}(H^+) + E_{\text{kin}}(H). \tag{7.3}$$

If it is assumed that the KER is equally distributed between the fragments, the KER of the reaction is given by twice the kinetic energy of the measured H^+ and Eq. 7.3 reduces to

$$\text{KER} = 2 \cdot E_{\text{kin}}(H^+). \tag{7.4}$$

In the present experiment, a single photon of $\hbar\omega = 28.2\,\text{eV}$ ionizes the neutral H_2 $X^1\Sigma_g^+$ ground state to the bound ionic H_2^+ $^2\Sigma_g^+(1s\sigma_g)$ state (see Fig. 7.1 (a)). Thereby, not only a wave packet is launched in the bound vibrational states, but also continuum vibrational states above the H^++H(1s) dissociation limit of $E_\infty = 18.1\,\text{eV}$ are excited [14].

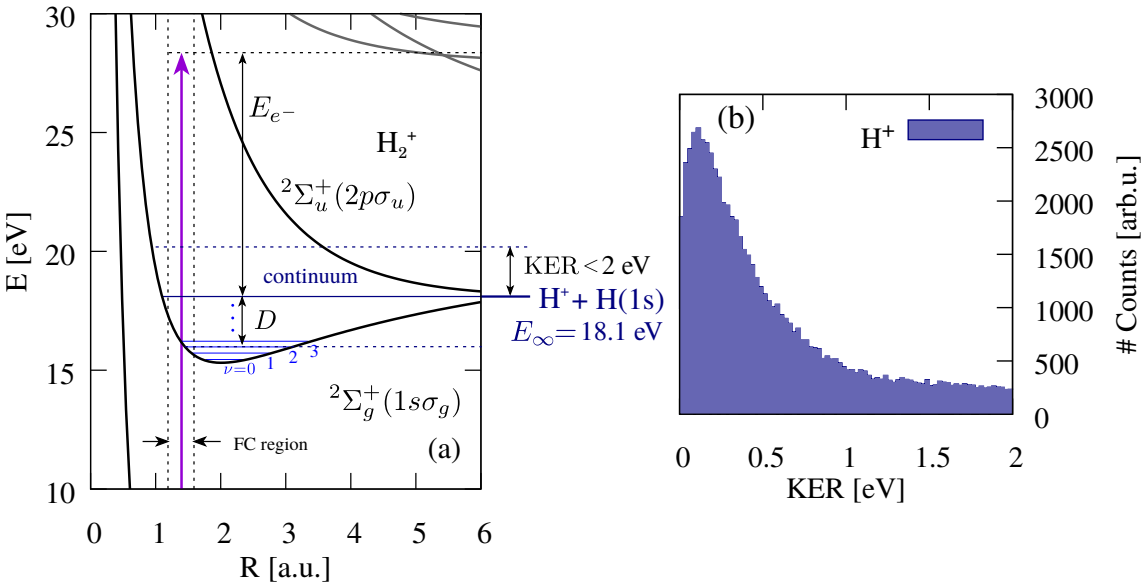

Figure 7.1: (a) PECs of H_2^+ taken from Ref. [62]. The Franck-Condon (FC) region lies within the vertical dashed lines. The purple arrow represents a photon of $\hbar\omega = 28.2\,\text{eV}$. The potential energy E is given relative to the H_2 vibrational ground state. The $H^+ + H(1s)$ dissociation limit is $E_\infty = 18.1\,\text{eV}$. The double-headed vertical black arrows indicate energy differences discussed in the text. Blue horizontal lines mark vibrational levels $\nu = 0, 1, 2, 3$ and $\nu = 19$ and are taken from Ref. [64]. (b) KER distribution of H^+ up to 2 eV recorded at a photon energy of $\hbar\omega = 28.2\,\text{eV}$ and an FEL intensity of $I \approx 10^{13}\,\text{W/cm}^2$.

In Ref. [64], the Franck-Condon (FC) factors (see Sec. 2.3.5) are calculated for the continuum states and a population up to 2 eV above the dissociation limit is found. Based on this, the dissociation of the continuum vibrational states results in maximum KERs of $< 2\,\text{eV}$, which is in agreement with the measured KER distribution shown in Fig. 7.1 (b). The low-energy region of KER $\approx 0\,\text{eV}$ must be attributed to the dissociation via bound H_2^+ $^2\Sigma_g^+(1s\sigma_g)$ states (see Eq. 7.2). For dissociation via bound states, the external photon energy $\hbar\omega$ is exactly shared between the kinetic energy of the photoelectron E_{e^-}, the energy D needed to overcome the potential energy of vibrational state ν plus the dissociation limit E_∞ and no energy is left for the KER of the final $H^+ + H(1s)$ fragments. Contributions of excited states, especially of autoionizing doubly excited H_2^{**} states, to the KER of H^+ ions are reported [9, 159] and will be discussed in Sec. 7.1.2 for the present experiment.

7.1.2 Dissociation via Excited States

In the intensity range of XUV multi-photon absorption, dissociation via excited H_2^{+*} states is possible [151]. A first XUV photon ionizes H_2 to the bound ionic H_2^+ $^2\Sigma_g^+(1s\sigma_g)$ state. Within the same pulse, a second photon is absorbed and resonantly excites the system to the H_2^+ $^2\Sigma_u^+(3p\sigma_u)$ state. The excitation and dissociation scheme is the following:

$$H_2 + \hbar\omega \rightarrow H_2^+ \ ^2\Sigma_g^+(1s\sigma_g) + e^-, \tag{7.5}$$

$$H_2^+ \ ^2\Sigma_g^+(1s\sigma_g) + \hbar\omega \rightarrow H_2^+ \ ^2\Sigma_u^+(3p\sigma_u) \rightarrow H^+ + H^*. \tag{7.6}$$

A look at the corresponding PEC in Fig. 7.2 (a) entails that the dissociation via this channel results in higher KERs compared to ground-state dissociation (see Sec. 7.1.1). At the present photon energy and within the FEL bandwidth of 0.5 eV (FWHM), the excitation to H_2^+ $^2\Sigma_u^+(3p\sigma_u)$ is the only resonant one-photon transition, which is dipole-allowed [10][55]. The state has a dissociation limit of $E_\infty = 28.3\,\text{eV}$ [231] and resonant excitation from the $\nu = 2$ vibrational level[56] of H_2^+ $^2\Sigma_g^+(1s\sigma_g)$ results in KERs of $\sim 14\,\text{eV}$. The respective peak in the KER distribution is shown in Fig. 7.2 (b). Outside of the FC region, i.e., for $R > 1.6$ a.u. and for higher vibrational states $\nu > 2$, the H_2^+ $^2\Sigma_u^+(3p\sigma_u)$ state cannot be resonantly excited, which decreases the cross section of this channel substantially.
Another dissociation channel involves a doubly excited H_2^{**} state that is embedded in the H_2^+ continuum and thus is subject to autoionization. The role of doubly excited states in dissociative photoionization of H_2 has triggered a great amount of experimental and theoretical work and is well understood [9, 159]. At $\hbar\omega = 28.2\,\text{eV}$, the lowest of the Q_1 doubly excited states with $^1\Pi_u$ and $^1\Sigma_u$ symmetry can be excited [62]. The cross section to excite $^1\Sigma_u$ is much higher and therefore the state with this symmetry is predominately populated [229]. The lifetime of doubly excited H_2^{**} states is known to be in the order of $\sim 1\,\text{fs}$ [64] and the decay into the bound ionic H_2^+ $^2\Sigma_g^+(1s\sigma_g)$ state happens via the ejection of an electron [62]:

$$H_2 + \hbar\omega \rightarrow H_2^{**} \ Q_1 \ ^1\Sigma_u^+ \rightarrow H_2^+ \ ^2\Sigma_g^+(1s\sigma_g) + e^- \rightarrow H^+ + H(1s) + e^-. \tag{7.7}$$

The KER of the $H^+ + H$ fragments is given by the difference between the kinetic energy K_{Q_1} gained on the Q_1 curve minus the energy D needed to dissociate the H_2^+ molecule (see Fig. 7.2 (a)). The energy K_{Q_1} depends on the moment in time when the autoionization takes place, i.e., is $R-$dependent. If the autoionization happens directly after the excitation of the Q_1 state, i.e., at $R \sim 1.5$ a.u., K_{Q_1} will be small

[55] The $^2\Pi_u^+(3p\pi_u)$ state is only accessible via a perpendicular transition, which is much weaker compared to a parallel dipole transition [64]. $^2\Sigma_g^+(2s\sigma_g)$ and $^2\Sigma_g^+(3d\sigma_g)$ are only excited via direct two-photon transitions [10, 71].

[56] In Sec. 7.2, it is shown that the $\nu = 2$ vibrational level is predominantly populated.

and the kinetic energy of the emitted electron E_{e^-} will be large. If the decay happens at larger R, K_{Q_1} will be larger and E_{e^-} is accordingly smaller. Fig. 7.2 (a) shows that the maximum possible KER $\approx 9\,\text{eV}$ is attained by an excitation within the FC region and autoionization at $R \sim 3\,\text{a.u.}$ into high-lying vibrational states of H_2^+ $^2\Sigma_g^+(1s\sigma_g)$ so that $D \approx 0\,\text{eV}$.

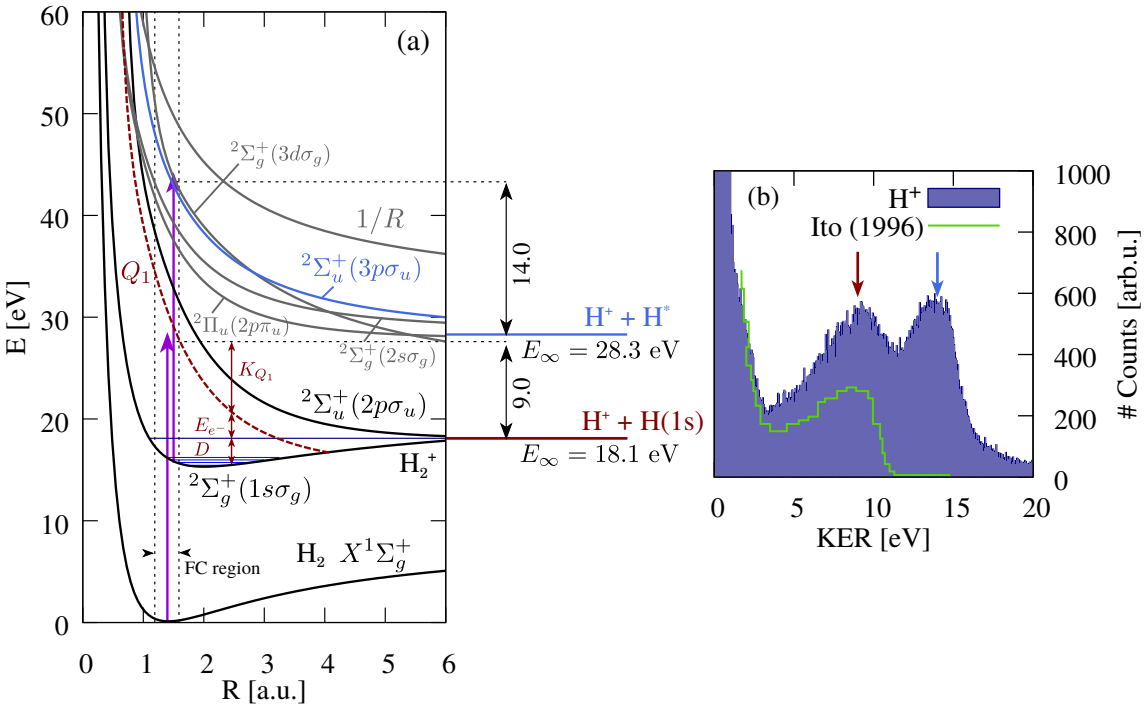

Figure 7.2: (a) PECs of H_2, H_2^+ [62] and the $1/R$ Coulomb potential curve. The purple arrows represent photons of $\hbar\omega = 28.2\,\text{eV}$. The potential energy E is given relative to the H_2 vibrational ground state. The first dissociation limit $H^+ + H(1s)$ is $E_\infty = 18.1\,\text{eV}$, the second $H^+ + H^*$ is $E_\infty = 28.3\,\text{eV}$ [231]. Vertical double-headed arrows (black and dark-red) indicate specific energies discussed in the text. Blue horizontal lines mark vibrational levels $\nu = 0, 1, 2, 3$ and $\nu = 19$, which are taken from Ref. [64]. (b) KER distribution of H^+ recorded at a photon energy of $\hbar\omega = 28.2\,\text{eV}$ (filled steps). Results of Ito *et al.* [116] are overlayed (green line). Arrows (dark-red and light-blue) mark KERs discussed in the text.

However, it is expected that in accordance to the findings of Sec. 7.2, not the most high-lying vibrational states are predominantly populated, but rather states $\nu \leq 3$. Consequently, $D > 0\,\text{eV}$ and KER $< 9\,\text{eV}$ for the Q_1 channel are expected. The KER distribution shown in Fig. 7.2 (b), however, shows a peak at KER $\approx 9\,\text{eV}$. Following the argumentation from above, it cannot exclusively stem from the Q_1 autoionizing channel. Therefore, it is assumed that also the H_2^+ $^2\Sigma_u^+(2p\sigma_u)$ state contributes.

Energetically, a reaction like

$$H_2 + \hbar\omega \rightarrow H_2^+ \, ^2\Sigma_u^+(2p\sigma_u) + e^- \rightarrow H^+ + H(1s) + e^- \tag{7.8}$$

is possible, if the excitation happens outside the FC region at $R > R_{eq}$. Ito *et al.* [116] measured the KER of H^+ ions as a function of the photon energy using synchrotron radiation. The corresponding distribution for $\hbar\omega = 28\,\text{eV}$ is plotted in Fig. 7.2 (b). It shows a maximum at KER $\approx 9\,\text{eV}$, which the authors assign to partly come from the $H_2^+ \, ^2\Sigma_u^+(2p\sigma_u)$ channel (see Eq. 7.8). Similar to the present experiment, the distribution of Ref. [116] features a shoulder towards lower KERs. The authors interpret this to be a signature of the autoionizing Q_1 channel (see Eq. 7.7).
Hoshina *et al.* [110] suggest a two-photon channel, which they referred to as dissociative two-photon above-threshold-ionization (ATI). In this channel, two photons are directly absorbed from the H_2 ground state and the molecule is excited to H_2^{+*} states below the $H^+ + H^+$ threshold. The authors of Ref. [110] conclude a predominant population of the $H_2^+ \, ^2\Pi_u(2p\pi_u)$ state leading to a final KER of $H^+ + H^*$ of $\sim 10\,\text{eV}$, i.e., close to the 9 eV peak of the present data (see Fig. 7.2 (b). The suggested ATI channel requires the non-sequential absorption of two photons. This will also lead to the fragmentation into $H^+ + H^+$ [123]. In Sec. 7.1.3, the $H^+ + H^+$ fragmentation channel is discussed and the KER distribution does not show a contribution of non-sequential two-photon double ionization. Hence, the contribution from two-photon ATI to the KER distribution shown in Fig. 7.2 (b) is very unlikely.

7.1.3 Fragmentation into $H^+ + H^+$ Ions

Besides the dissociative photoionization discussed in Sec. 7.1.1 and 7.1.2, also two-photon double-ionization of H_2 followed by Coulomb explosion is possible at $\hbar\omega = 28.2\,\text{eV}$. The KER of $H^+ + H^+$ fragments allows to distinguish contributions from the direct non-sequential

$$H_2 \; X^1\Sigma_g^+ + 2\hbar\omega \rightarrow H^+ + H^+ + 2e^- \tag{7.9}$$

and the sequential channel via the intermediate ionic bound $H_2^+ \, ^2\Sigma_g^+(1s\sigma_g)$ state

$$H_2 \; X^1\Sigma_g^+ + \hbar\omega \rightarrow H_2^+ \, ^2\Sigma_g^+(1s\sigma_g) + e^-, \tag{7.10}$$

$$H_2^+ \, ^2\Sigma_g^+(1s\sigma_g) + \hbar\omega \rightarrow H^+ + H^+ + e^-. \tag{7.11}$$

For the fragmentations described in Eqs. 7.9 and 7.11, the R-dependent KER reads

$$\text{KER}(R) = \frac{1}{R} - E_\infty = E_{\text{kin}}(H^+) + E_{\text{kin}}(H^+) \tag{7.12}$$

with the $H^+ + H^+$ dissociation limit of $E_\infty = 31.6\,\text{eV}$ and the kinetic energy of the final fragments $E_{\text{kin}}(H^+)$.

A similar experiment looking into the two-photon double ionization of D_2 has been performed at a photon energy of 38 eV and intensities of $I \approx 10^{13} - 10^{14}\,\mathrm{W/cm^2}$ [123]. The measured KER distribution of $D^+ + D^+$ ions showed contributions of the sequential as well as the non-sequential channel. From the theoretical side, cross sections are calculated for the non-sequential channel [251] and ionization schemes involving excited H_2^{+*} states are discussed for the sequential channel [10, 71].
The PECs relevant for the present experiment are depicted in Fig. 7.3 (a). By directly absorbing two photons at the equilibrium internuclear distance, the $1/R$ Coulomb potential curve is directly reachable, which would yield high KERs of the $H^+ + H^+$ fragments. In the sequential channel, however, the wave packet launched in the intermediate ionic H_2^+ $^2\Sigma_g^+(1s\sigma_g)$ state is promoted to the $1/R$ curve at larger R, which results in lower KERs of the fragments.

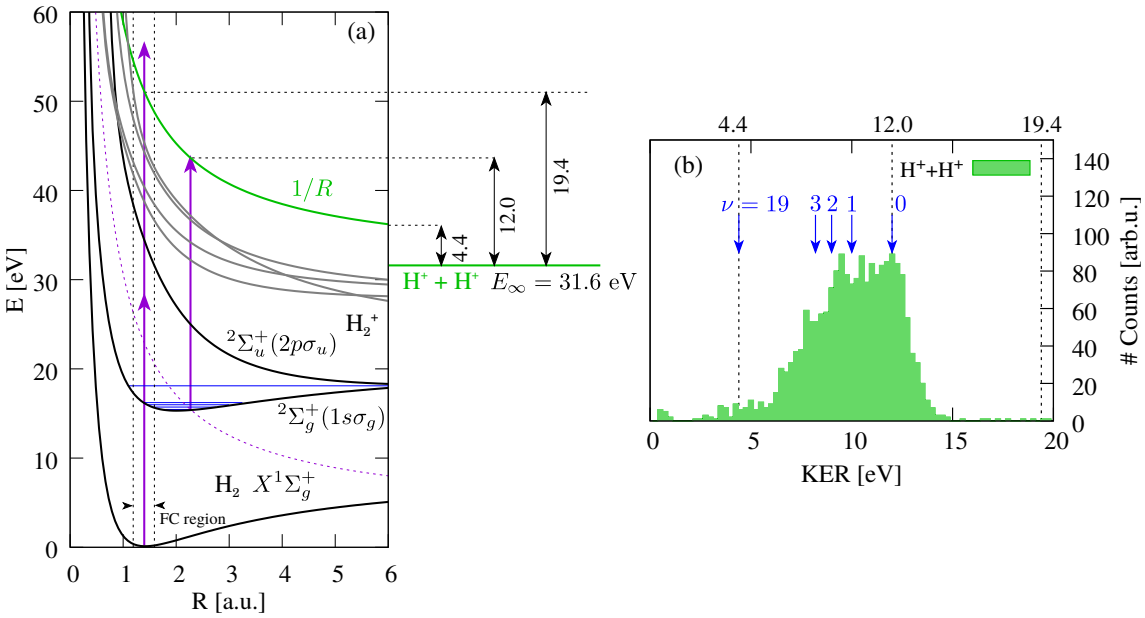

Figure 7.3: PECs of H_2 (black), H_2^+ (black) and the $1/R$ Coulomb curve (green). The PECs are taken from Ref. [62]. The purple arrows represent photons of $\hbar\omega = 28.2\,\mathrm{eV}$. The potential energy E is given relative to the H_2 vibrational ground state. The $H^+ + H^+$ dissociation limit is $E_\infty = 31.6\,\mathrm{eV}$. The numbers besides the vertical double-headed arrows indicate some specific KERs discussed in the text. Blue horizontal lines mark vibrational levels $\nu = 0, 1, 2, 3$ and $\nu = 19$ and are taken from Ref. [64]. (b) KER distribution of $H^+ + H^+$ ions recorded at a photon energy of $\hbar\omega = 28.2\,\mathrm{eV}$ and an FEL intensity of $I \sim 10^{13}\,\mathrm{W/cm^2}$. Vertical dashed lines mark KERs discussed in the text.

The measured KER distribution of $H^+ + H^+$ ions is plotted in Fig. 7.3 (b). No KERs above $\sim 15\,\mathrm{eV}$ are observed, which rules out the direct, non-sequential channel. In the first step of the sequential channel, a wave packet is launched in the bound

vibrational states of the ionic H_2^+ $^2\Sigma_g^+(1s\sigma_g)$ state as well as continuum vibrational states above the dissociation threshold of $E_\infty = 18.1\,\text{eV}$ [14].
The dashed violet curve in Fig. 7.3 (a) is the $1/R$ curve displaced by a vertical offset of minus 28.2 eV, i.e., the present photon energy. It intersects the curve of the H_2^+ $^2\Sigma_g^+(1s\sigma_g)$ state at $R \approx 2.3\,\text{a.u.}$ and at a potential energy of $E \sim 15.4\,\text{eV}$, which is close to the energy $E_{\nu=0} = 15.45\,\text{eV}$ of the vibrational ground state [64]. At $R = 2.3\,\text{a.u.}$, $\nu = 0$ is the lowest vibrational state from which the $1/R$ curve can be reached by a 28.2-eV-photon. Furthermore, the time-averaged density distribution of the vibrational states is largest at the classical outer turning point[57], which favors the population of the $1/R$ curve at $R \approx 2.3\,\text{a.u.}$ This corresponds to the peak at $\sim 12\,\text{eV}$ in the KER distribution of Fig. 7.3 (b). At $R \approx 2.3\,\text{a.u.}$, also higher vibrational states $\nu > 0$ can contribute to the KER peak at $\sim 12\,\text{eV}$, but for these states the population transfer to the $1/R$ curve is less likely as the time-integrated density distribution is small away from the classical turning points. For $R > 2.3\,\text{a.u.}$, the $1/R$ curve is reachable from all vibrational states $\nu > 0$ at their classical outer turning points and the KER distribution reflects the population of the respective vibrational states. It is found that the $\nu = 1, 2\,\text{and}\,3$ states contribute most (see Fig. 7.3 (b)). This is in agreement with the D_2 experiment reported by Ref. [123].

7.2 Ground-State Dissociation by IR Pulse

In this section, it is shown how the manipulation of a physical process, i.e., the ground-state dissociation of H_2^+ (see Sec. 7.1.1), can be used as an intrinsic measure to find and quantify the temporal overlap between an XUV and an IR laser pulse. The experimental observable is the KER of H^+ ions in the energy range below 2 eV as a function of the delay between the pulses. First, the case of the IR pulse arriving late with respect to the XUV excitation is discussed. The corresponding KER distribution is shown in Fig. 7.4 (b). The KER distribution measured using a single XUV pulse is plotted for comparison. The center of the XUV+IR distribution is shifted from zero towards higher KERs and peaks at a KER of 0.85 eV. The origin of this shift is explained in Fig. 7.4 (a), which shows the lowest ionic bound H_2^+ $^2\Sigma_g^+(1s\sigma_g)$ state and associated bound vibrational levels. IR photons transfer population from the bound vibrational H_2^+ $^2\Sigma_g^+(1s\sigma_g)$ states into the continuum, which results in higher KERs compared to the XUV only case. The two horizontal red lines mark the 1-IR-photon and 2-IR-photon limit with respect to the central KER of 0.85 eV. The 2-IR-photon limit coincides with the $\nu = 2$ vibrational level. This implies that this vibrational state is mostly populated after XUV excitation. The observation is in agreement with Ref. [123], where a predominant population of the $\nu = 2$ level, followed by $\nu = 1$ and $\nu = 3$, is reported.

[57] Also at the inner turning point, but at the present photon energy of 28.2 eV, the $1/R$ curve is not reachable from the inner turning point.

The preceding interpretation treats the states in an unperturbed manner within the multi-photon picture (see Sec. 2.1.2). However, at the present IR intensity of $I_{\mathrm{IR}} \approx 1 \times 10^{14}$ W/cm^2, one is in the transition region between the multi-photon and strong-field picture to describe the ionization process. For the strong-field case, the modification of the PECs by the laser field is taken into account and the entire system is described in the so-called Floquet picture. This representation accounts for the dressing of the states by the laser field [249]. For the present study, the IR ionization should be regarded as a "tool" to probe distinct XUV-induced fragmentation pathways and not as the main subject of investigation itself.

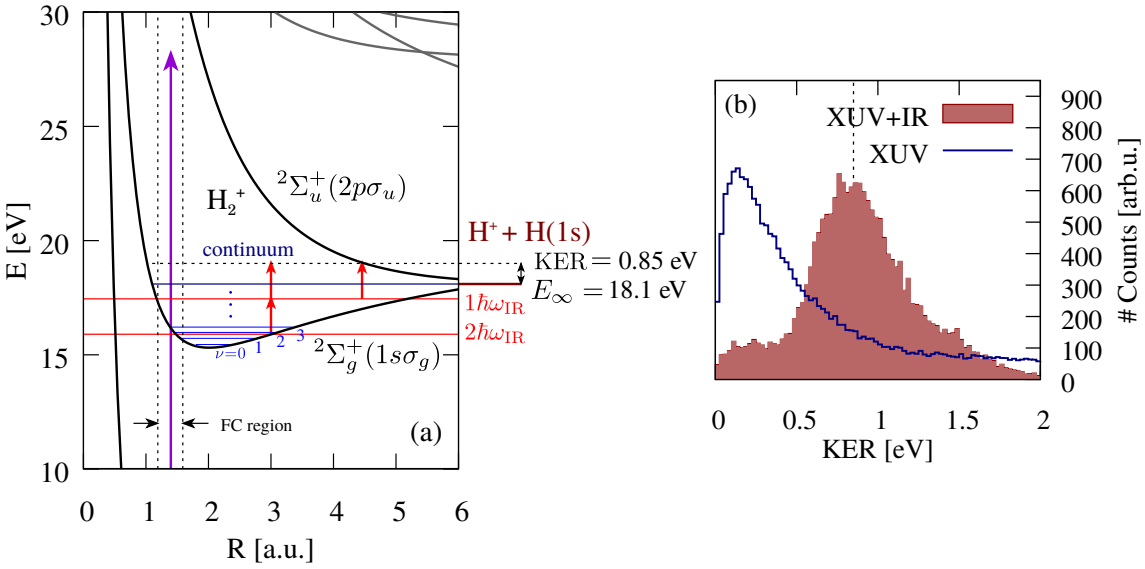

Figure 7.4: PECs of H_2^+ taken from Ref. [62]. The purple arrow represents a photon of $\hbar\omega = 28.2\,\mathrm{eV}$. The potential energy E is given relative to the H_2 vibrational ground state. The $H^+ + H(1s)$ dissociation limit is $E_\infty = 18.1\,\mathrm{eV}$. The double-headed black arrow indicates a KER of 0.85 eV. Blue horizontal lines mark vibrational levels $\nu = 0, 1, 2, 3$ and $\nu = 19$ and are taken from Ref. [64]. Vertical red arrows indicate IR photons of $\hbar\omega = 1.55\,\mathrm{eV}$. The two horizontal lines mark the 1-IR-photon and 2-IR-photon limited to reach a KER of 0.85 eV, respectively. (b) KER distribution of H^+ recorded with the IR pulse arriving late with respect to the XUV excitation.

The emergence of high energetic H^+ fragments as a function of the delay t_d between IR and XUV pulse gives an intrinsic signal of the temporal overlap of the pulses. Fig. 7.5 shows the KER between 0 and 2 eV over a delay range of -4 ps to +4 ps. For negative delays $t_d < 0$, the IR pulse is early with respect to the XUV pulse, for positive delays $t_d > 0$ vice versa. At a delay of $t_d \approx 0$ ps, the KER distribution rapidly changes to higher KERs of ~ 0.8 eV and stays constant until the end of the positive delay. This becomes obvious in the comparison of Fig. 7.5 (b)

and Fig. 7.5 (c). Here, the KER is integrated over the negative and positive delay range, respectively. A projection of Fig. 7.5 (a) onto the delay axis is depicted in Fig. 7.5 (d). It shows a step-like increase of the count rate at $t_d \approx 0\,\mathrm{ps}$. An error function is used to quantitatively describe the temporal overlap. The fit yields a step width of FWHM $= (580 \pm 110)\,\mathrm{fs}$ to be the measure of the temporal overlap. The resolution of the experiment is further investigated and benchmarked in Sec. 6.2.3. The long-lasting increase of the count rate to the end of the positive delay range allows to conclude that population transfer from long-lived bound vibrational states of H_2^+ $^2\Sigma_g^+(1s\sigma_g)$ is the origin of the signal increase.

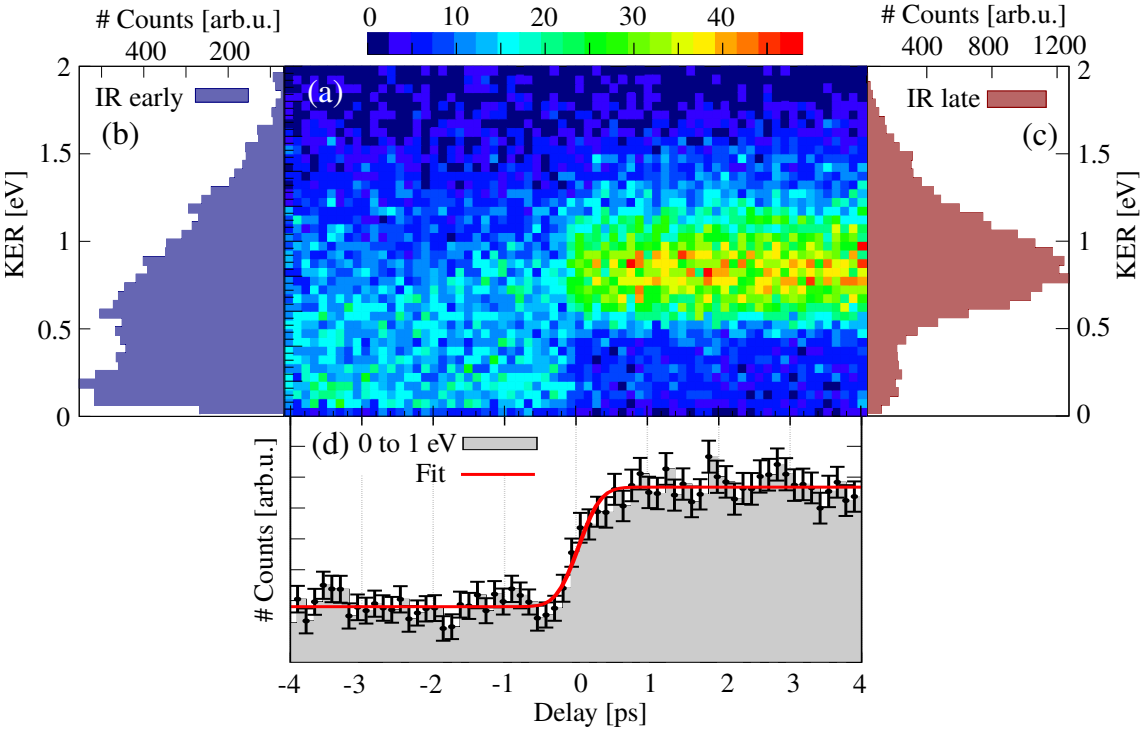

Figure 7.5: Temporal overlap determination. (a) KER of H^+ vs. the delay between IR and XUV pulse. For negative delays, the IR is early with respect to the XUV pulse, for positive delays vice versa. (b) Projection of all KERs within the negative delay range. (c) Same as (b) but for the positive delay range. (d) Projection of (a) onto the delay axis. The red curve shows a fit according to an error function (see Sec. 6.2.3, Eq. 6.17).

The discussed scheme can be employed to find the temporal overlap for any XUV-IR pump-probe in the gas phase in the range between $\hbar\omega_{\mathrm{XUV}} = 20 - 30\,\mathrm{eV}$. This is in particular interesting, because commonly used schemes based on the dissociation of N_2 or O_2 cannot be applied in this photon energy range [270].

8 Relaxation Dynamics of Argon Dimers

In the argon dimer, various interatomic relaxation processes such as interatomic coulombic decay (ICD), electron transfer mediated decay (ETMD) and radiative charge transfer (RCT) have been experimentally observed and examined by theoretical studies (see Sec. 2.4).

Most of the experimental schemes are based on the creation of an innershell vacancy upon absorption of a single XUV synchrotron photon. Morishita *et al.* [184] were the first to report experimental evidence of ICD in Ar_2. In their experiment, a $2p$ hole created by photoionization is replaced with $3s$ and $3p$ vacancies by intraatomic Auger decay, thereby exciting ICD-active states. Electron-ion-ion coincidence spectroscopy was used to measure the kinetic energy of the ICD electron and the KER of the final $ArAr^{2+} + Ar^{+}$ ions. Subsequent studies, also utilizing synchrotron radiation in combination with multi-particle coincidence spectroscopy, revealed more aspects of the process and undoubtedly proved ICD to be an important relaxation mechanism in Ar_2 [132, 133, 143, 268]. Especially the theoretical work by Stoychev *et al.* [258] and Miteva *et al.* [178] on the topic helped a lot to gain a wide understanding of ICD in Ar_2.

Electron transfer mediated decay (ETMD), was observed by Sakai *et al.* [227] using synchrotron radiation to populate triply ionized states with an inner-valence $3s$ vacancy $Ar^{3+}(3s3p^4)-Ar$. In this case, ETMD results in population of $Ar^{2+}(3p^{-2})-Ar^{2+}(3p^{-2})$ states, whereas ICD populates $Ar^{3+}(3p^{-3}) - Ar^{+}(3p^{-1})$ states. Both channels were distinguished by measuring the respective Coulomb-exploded ions and electrons in coincidence along with their KER.

In another synchrotron experiment, Saito *et al.* [225] found evidence of radiative charge transfer (RCT) to happen in the Argon dimer after excitation of one-site two-hole states of $Ar^{2+}(3p^{-2})-Ar$ character, which decay radiatively to $Ar^{+}(3p^{-1})-Ar^{+}(3p^{-1})$ by emission of a photon.

A different class of experiments uses electrons as projectiles to prepare ICD-, ETMD-, and RCT-active states. In doing so, Yan *et al.* [286] inferred information on ICD and ETMD by measuring KERs for the $Ar^{3+} + Ar^{+}$ and $Ar^{2+} + Ar^{2+}$ channels from quadruply charged Ar_2^{4+} states, which were excited by high-energy electron impact-ionization. In experiments using low-energy electrons, Ren *et al.* [212, 213] demonstrated that ICD and RCT can be switch on and off by tuning the excitation electron energy.

In most synchrotron and electron-impact studies, ICD-active states are populated by fast Auger decay. Consequently, a whole bundle of intra-/interatomic relaxation

and fragmentation pathways opens up. In an experiment, it is often quite challenging to unambiguously disentangle these different pathways. A more comprehensive approach, however, is to directly populate specific dimer states via direct dipole transitions from the Ar_2 ground state by absorption of few high energetic photons. In order to reach the lowest lying doubly and triply valence-ionized dimer states at the equilibrium internuclear distance $R_{eq} = 7.18$ a.u. [258], energies of ~ 36 eV and ~ 68 eV, respectively, are required [258] (see Fig. 8.4). Hence, to access states which relax via interatomic mechanisms in this energy range, XUV photons are well-suited. In order to study the relaxation dynamics of Ar_2, the present study takes advantage of the uniquely high photon intensities of FEL radiation (see Ch. 3), which allows the absorption of multiple photons within a single pulse (see Sec. 6.1). By adjusting the FEL intensity, the number of absorbed photons can be controlled. Like this, multi-photon absorption provides a well-defined handle to switch on and off different relaxation pathways and thus provides clean experimental conditions.
In this section, the relaxation and fragmentation pathways of argon dimers upon absorption of few XUV photons of 27 eV within a single pulse are studied. In Sec. 8.1.1, the KER distribution of $Ar^+ + Ar^+$ ions measured in coincidence is presented. Different channels are identified and discussed using the associated potential energy curves (PECs). In Sec. 8.1.2, new fragmentation pathways that open up with increasing FEL intensity are introduced.

8.1 Interaction with a Single XUV Pulse

8.1.1 Low FEL Intensity

As already discussed in Sec. 6.1, the absolute FEL intensity is estimated to be in the order of $I = 10^{13} - 10^{14}\,\mathrm{W/cm^2}$. In the following section, results are presented for an intensity I_{low}, which is a factor of ~ 2 smaller than the intensity I_{high} discussed in Sec. 8.1.2. The respective KER distribution is plotted in Fig. 8.1. It features a sharp peak at 3.8 eV and a broader peak at ~ 5.3 eV. The broadening of the KER peak at ~ 5.3 eV already gives a hint that nuclear motion plays a role in the corresponding relaxation channel. The emergence of the two peaks is discussed in the following in terms of the PECs depicted in Fig. 8.2.

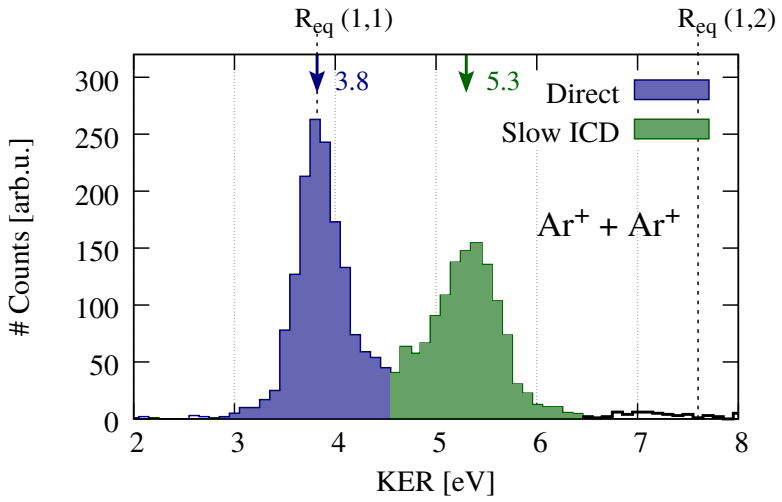

Figure 8.1: KER of Ar^++Ar^+ ions measured in coincidence at low FEL intensity. Contributions from different channels are color-coded. Vertical dashed lines mark the expected KER for fragmentation into $Ar^+ + Ar^+$ and $Ar^{2+} + Ar^+$ at R_{eq}. The arrows mark peaks as discussed in the text.

The absorption of one photon of $\hbar\omega = 27\,\text{eV}$ at the equilibrium internuclear distance $R_{eq} = 7.18\,\text{a.u.}$ of neutral Ar_2 is sufficient to ionize a $3p$ electron of the dimer resulting in an $Ar^+(3p^{-1}) - Ar$ state (see Fig. 8.2):

$$Ar - Ar + \hbar\omega \rightarrow Ar^+(3p^{-1}) - Ar + e^-. \tag{8.1}$$

The corresponding PECs[58] are very shallow in the Franck-Condon (FC) region and lie closely together. Thus, a wave packet does not move much on the PECs within the FEL pulse duration of 50 fs. At the present FEL intensity, the yield of singly charged dimers $Ar^+(3p^{-1}) - Ar$ is saturated. This assumption is justified as a strong saturation behavior of the yield of singly ionized Argon monomers Ar^+ is observed. The second photon is either absorbed at the still neutral or the already ionized site of the dimer. In the first case, the dimer is excited to the repulsive two-site doubly ionized $Ar^+(3p^{-1}) - Ar^+(3p^{-1})$ state[59] and fragments directly into $Ar^+(3p^{-1}) + Ar^+(3p^{-1})$ (see Fig. 8.2). The corresponding reaction reads:

$$Ar^+(3p^{-1}) - Ar + \hbar\omega \rightarrow Ar^+(3p^{-1}) + Ar^+(3p^{-1}) + e^-. \tag{8.2}$$

[58] Symmetries: $^2\Sigma_u^+$, $^2\Pi_{1/2u}$, $^2\Pi_{1/2g}$ and $^2\Pi_{3/2g}$ [178].

[59] In total 12 two-site final dicationic $Ar^+(3p^{-1}) - Ar^+(3p^{-1})$ states with the following symmetries are known: $^1\Sigma_g^+(2)$, $^3\Sigma_u^+(3)$, $^1\Sigma_u^-$, $^3\Sigma_g^-$, $^1\Pi_g$, $^3\Pi_g$, $^1\Pi_u$, $^3\Pi_u$, $^1\Delta_g$ and $^3\Delta_u$ [178]. For simplification, only one PEC is plotted in Fig. 8.2 to represent these states.

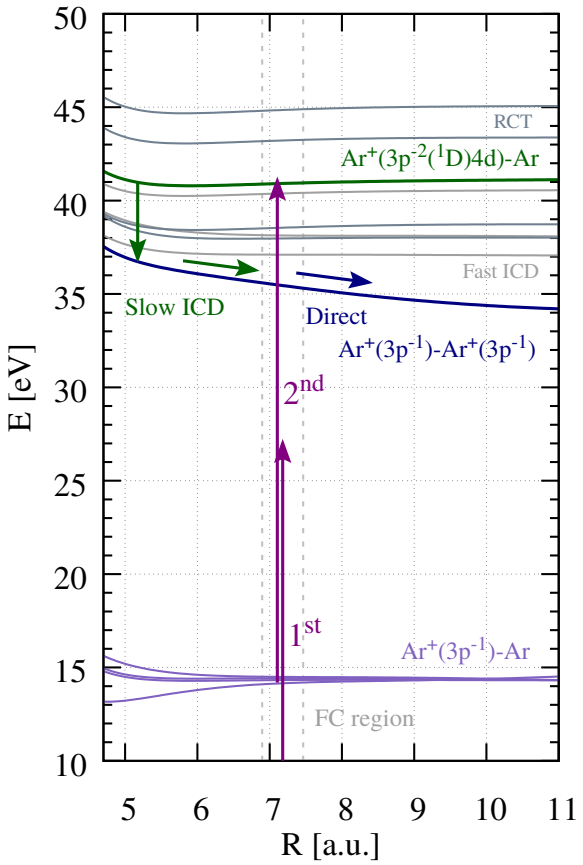

Figure 8.2: PECs of the argon dimer between $10 - 50\,\mathrm{eV}$. The potential energy E is given with respect to the $\mathrm{Ar} - \mathrm{Ar}$ ground state. States relevant for the discussion in the text are colored. For simplification, only a single PEC is plotted to represent $\mathrm{Ar}^+(3p^{-2}(^1D)4d) - \mathrm{Ar}$ (dark-green) and $\mathrm{Ar}^+(3p^{-1}) - \mathrm{Ar}^+(3p^{-1})$ states (blue). All curves are taken from Refs. [178, 258]. The purple vertical arrows indicate photons of $\hbar\omega = 27\,\mathrm{eV}$. The FC region lies in the two vertical dashed grey lines.

This direct channels gives rise to the peak at 3.8 eV in the KER distribution of $\mathrm{Ar}^+ + \mathrm{Ar}^+$ ions in Fig. 8.1. The measured value of 3.8 eV matches the computed KER of a Coulomb explosion of two point charges $q_1 = q_2 = 1$ at $R_{\mathrm{eq}} = 7.18\,\mathrm{a.u.}$, i.e., $\mathrm{KER} = (q_1 \cdot q_2)/R_{\mathrm{eq}} = 3.79\,\mathrm{eV}$. This finding allows to draw the conclusion that the absorption of the second photon takes place within the Franck-Condon-region around R_{eq}, i.e., takes place faster than the time needed for nuclear motion to set in. Assuming a stepwise absorption via an intermediate state is justified as it was shown that for high FEL intensity the sequential channel dominates over the non-sequential channel, if the sequential channel is energetically allowed [186, 275, 288]. A simplified argument is the following: If a real intermediate state is involved, the absorption of the second photon can happen at any later time within the FEL pulse with respect to the instant of absorption of the first photon. A high photon intensity

within the whole FEL pulse is the only prerequisite in this scenario. In the non-sequential case, both photons need to be absorbed at the same moment in time, which is less likely. As one can see in Fig. 8.2, the sequential channel to ionize from the neutral Ar − Ar ground state to the doubly ionized $Ar^+(3p^{-1}) - Ar^+(3p^{-1})$ via the intermediate $Ar^+(3p^{-1}) - Ar$ state is energetically possible with the present photon energy and hence dominates. The dominance of the sequential channel at the present FEL intensity is also demonstrated for multi-photon ionization of atomic argon in Sec. 6.1.
In case of absorbing the second photon at the already ionized site, the dimer is excited to a one-site singly ionized and excited state. At $\hbar\omega = 27\,\text{eV}$ and within the FEL bandwidth of 0.5 eV (FWHM), the $Ar^+(3p^{-2}(^1D)4d\ ^2S) - Ar$ state can be resonantly excited by a dipole-allowed transition [178] (see Fig. 8.2)[60]:

$$Ar^+(3p^{-1}) - Ar + \hbar\omega \rightarrow Ar^+(3p^{-2}(^1D)4d\ ^2S) - Ar. \tag{8.3}$$

The $Ar^+(3p^{-2}(^1D)4d\ ^2S) - Ar$ state is of binding character and located above the repulsive $Ar^+(3p^{-1}) - Ar^+(3p^{-1})$ state. As a consequence, ICD is energetically allowed:

$$Ar^+(3p^{-2}(^1D)4d\ ^2S) - Ar \xrightarrow{\text{ICD}} Ar^+(3p^{-1}) + Ar^+(3p^{-1}) + e^-_{\text{ICD}}. \tag{8.4}$$

The occurrence of ICD for this type of states was already observed experimentally by, e.g., Refs. [132, 133, 212, 213, 216] and is also investigated in great detail by ab initio calculations in Ref. [178], on which the following discussion is based on. In contrast to the shallow $Ar^+(3p^{-2}nl) - Ar$ states[61] in the energy range between 36.5 − 38 eV, (see Fig. 8.2, labeled "Fast ICD"), which are known to decay fast via ICD (lifetimes between 28 − 130 fs [178]) in the vicinity of R_{eq}, the resonantly excited $Ar^+(3p^{-2}(^1D)4d\ ^2S) - Ar$ state belongs to a class of higher excited Rydberg states with feature a deeper potential well. The formation of the deeper potential well can be explained by less repulsion between the electron of a high-lying Rydberg orbital and the neutral Ar neighbor [179]. As a consequence, the characteristic vibrational period of these states is small (between 180 − 250 fs [178]). This is an order of magnitude shorter than the ICD lifetimes of these states at R_{eq} and the decay is influenced by the nuclear motion. After being excited at R_{eq}, the wave packet broadens and moves towards smaller internuclear distances. In the vicinity of the left classical turning point, the wave packet gets "squeezed" and its localization probability is high. At the same time, the ICD rate increases with smaller $R < R_{\text{eq}}$ and is ∼20 times larger than at R_{eq}. For the state of interest (see Eq. 8.3), the left turning point is located at $R \approx 5.1$ a.u. [178]. Hence, the two repelling nuclei gain a higher KER compared to the direct channel (see Eq. 8.2), because the repulsive

[60] For simplification, only one PEC of the $Ar^+(3p^{-2}(^1D)4d\ ^2S) - Ar$ states is plotted in Fig. 8.2.
[61] After Ref. [178]: $Ar^+(3p^{-2}(^1S)4s\ ^2S)-Ar$, $Ar^+(3p^{-2}(^1D)3d\ ^2D)-Ar$, $Ar^+(3p^{-2}(^1D)3d\ ^2P)-Ar$.

$Ar^+(3p^{-1}) - Ar^+(3p^{-1})$ curve is accessed at $R < R_{eq}$. This results in the second KER peak at $\sim 5.3\,\text{eV}$ of the $Ar^+ + Ar^+$ channel (see Fig. 8.1).
In comparison to the narrow KER peak of the direct channel, the KER peak of the slow ICD channel shows a broad shoulder towards smaller KERs. This feature can be explained by nuclear motion during the decay. The wave packet moves towards smaller internuclear distances after the excitation at R_{eq}. However, the ICD decay rate is a function of R [230]. Hence, the $Ar^+(3p^{-1}) - Ar^+(3p^{-1})$ curve can be accessed at internuclear distances between R_{eq} and the left turning point according to the R-dependent decay rate. Thus, the decay rate is imprinted in the KER distribution and shows up as a shoulder towards lower KERs.
In a recent experiment, Rist *et al.* [216] studied ICD from $Ar^+(3p^{-2}(^1D)4d\ ^2S) - Ar$ by extracting the internuclear-distance dependent ICD decay width $\Gamma(R)$ from the measured KER and found significant deviations from predictions of ab initio calculations. In this regard, the KER distribution measured in the present experiment is closer to the experimental results of Ref. [216] and not to the theoretical model presented therein. In an electron-impact experiment by Ren *et al.* [213], slow ICD after excitation to $Ar^+(3p^{-2}(^1D)4d\ ^2S) - Ar$ has been observed and the results confirm the data presented here.
Concerning further channels, one can exclude contributions from RCT [162, 212, 225] in the KER distribution of the $Ar^+ + Ar^+$ channel, because the RCT-active $Ar^{2+}(3p^{-2}) - Ar$ states[62] are not accessible by sequentially absorbing two photons of 27 eV from the Ar_2 ground state (see Fig. 8.2, labeled "RCT"). $Ar^{2+} + Ar^+$ fragments are not detected at the present low FEL intensity, which allows to draw the conclusion that mostly not more than two photons are absorbed as the ionization to $Ar^{2+} + Ar^+$ requires at least three photons (see Fig. 8.4).
$Ar^+(3p^{-2}nl) - Ar$ states between $36.5 - 38.0\,\text{eV}$ are known to decay fast via ICD onto $Ar^+(3p^{-1}) + Ar^+(3p^{-1})$ around R_{eq} [178], which would also result in KERs $\sim 3.8\,\text{eV}$. Thus, this is not distinguishable from the direct fragmentation channel (Eq. 8.2). However, at the present photon energy of $\hbar\omega = 27\,\text{eV}$, these states cannot be resonantly excited from the intermediate $Ar^+(3p^{-1}) - Ar$ state and also not by direct two-photon absorption from the $Ar - Ar$ ground state.

8.1.2 High FEL Intensity

The following section shows results that are recorded at an FEL intensity I_{high}, which is a factor of 2 higher compared to Sec. 8.1.1. The new relaxation pathways, which open up by populating energetically higher-lying states, are discussed by the measured KER distributions (see Fig. 8.3). Compared to the distribution at low FEL intensity (see Fig. 8.1), two new prominent features arise in the KER of $Ar^+ + Ar^+$ ions. Firstly, a new peak shows up at 7.2 eV (see Fig. 8.3 (a)). Secondly,

[62] The first RCT-active state $Ar^{2+}(3p^{-2}\ ^3P) - Ar$ is located at $\sim 43.5\,\text{eV}$, the second at $\sim 45\,\text{eV}$.

the peak at 5.3 eV is now more pronounced compared to the direct peak at 3.8 eV (see Fig. 8.3 (a)). The origins of these new features are explained in the following taking into account the PECs displayed in Fig. 8.4. At high FEL intensity settings, dimer fragments of charge state $q > 1$ are detected. The KER of $Ar^{2+} + Ar^{+}$ ions is plotted in Fig. 8.3 (b). It shows a peak at ~ 7.5 eV with a broad shoulder towards higher KERs. However, also coincidence channels with product charges of $q_1 \cdot q_2 > 2$ are detected and discussed in Sec. 8.3.

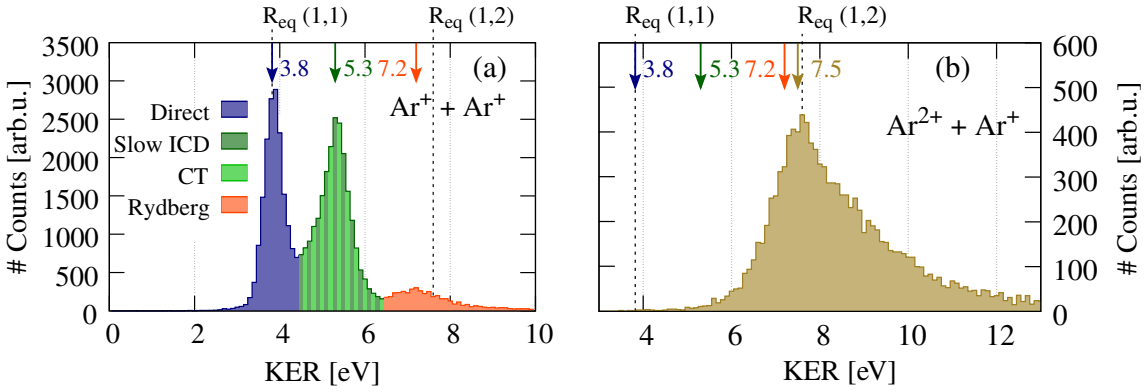

Figure 8.3: KER of (a) Ar^{+}+Ar^{+} and (b) Ar^{2+}+Ar^{+} ions measured in coincidence at high FEL intensity. Contributions from different channels are color-coded. Vertical dashed lines mark the expected KER for fragmentation into $Ar^{+} + Ar^{+}$ and $Ar^{2+} + Ar^{+}$ at R_{eq}, respectively. The arrows mark peak positions discussed in the text.

In the following, possible excitations starting from the one-site singly ionized and excited $Ar^{+}(3p^{-2}4d) - Ar$ state (see Eq. 8.3) are considered. In this regard, the third photon can either be absorbed at the still neutral or the already ionized and excited site of the dimer. It is plausible to assume that the absorption of the third photon, which needs to happen within the FEL pulse duration of 50 fs, takes place in the Franck-Condon region. The characteristic vibrational period of the wave packet in the potential of the $Ar^{+}(3p^{-2}4d) - Ar$ state is on the order of 200 fs [178] and the absorption of the third photon needs to happen close to R_{eq} in order to further excite/ionize the wave packet. Energetically, this means that excited states just below the triple ionization threshold are reachable (see Fig. 8.4).
First, the absorption of the third photon at the already ionized site is discussed. Calculations show that the highest one-site doubly ionized state beneath the triply ionized state is in the energy range between $60 - 62$ eV and is an admixture of $Ar^{2+}(3s^{-1}3p^{-1}\,{}^{1}P) - Ar$ (43 %) and $Ar^{2+}(3p^{-3}({}^{2}D)3d\,{}^{1}P) - Ar$ (50 %) states[63] [258].

[63] The triplet one-site doubly ionized state $Ar^{2+}(3s^{-1}3p^{-1}\,{}^{3}P(+3p^{-3}({}^{2}D)3d\,{}^{3}P))$ is located in the energy range between $57 - 58$ eV and may partly contribute [258]. However, for the discussion of the XUV-pump IR-probe results in Sec. 8.2.1, the triplet state plays a less important role as the IR ionization probability to triply ionized final states is larger for states closer to the respective ionization threshold.

This state can be accessed for the ionization by the third photon being accompanied by electron shake-down [80]:

$$\mathrm{Ar}^+(3p^{-2}(^1D)4d\,^2S) - \mathrm{Ar} + \hbar\omega \rightarrow \mathrm{Ar}^{2+}(3s^{-1}3p^{-1}\,^1P(+3p^{-3}(^2D)3d\,^1P)) - \mathrm{Ar} + e^-. \tag{8.5}$$

The $\mathrm{Ar}^{2+}(3s^{-1}3p^{-1}\,^1P(+3p^{-3}(^2D)3d\,^1P))$ state is represented in Fig. 8.4 by the black curve. It is of binding character with a potential minimum at $R \approx 5.5\,\mathrm{a.u.} < R_{\mathrm{eq}}$ and is crossed by repulsive states of $\mathrm{Ar}^+(3p^{-2}nl) - \mathrm{Ar}^+(3p^{-1})$ character (see Fig. 8.4, light-green curves). At the curve crossings, a new relaxation mechanism is possible: charge can be transferred non-adiabatically (see Sec. 2.4.4):

$$\mathrm{Ar}^{2+}(3s^{-1}3p^{-1}\,^1P(+3p^{-3}(^2D)3d\,^1P)) \xrightarrow{\mathrm{CT}} \mathrm{Ar}^+(3p^{-2}nl) - \mathrm{Ar}^+(3p^{-1}). \tag{8.6}$$

The repulsive $\mathrm{Ar}^+(3p^{-2}nl) - \mathrm{Ar}^+(3p^{-1})$ states are populated for $R < R_{\mathrm{eq}}$ and the KER is higher compared to fragmentation at R_{eq}. According to the internuclear distance at the crossing points between $R = 6 - 7\,\mathrm{a.u.}$, the expected KER for $\mathrm{Ar}^+(3p^{-1}) + \mathrm{Ar}^+(3p^{-1})$ fragments is $3.9 - 4.5\,\mathrm{eV}$. However, it will be shown that the actual shape of the $\mathrm{Ar}^+(3p^{-2}nl) - \mathrm{Ar}^+(3p^{-1})$ states is important as it especially for small R deviates from $\mathrm{Ar}^+(3p^{-1}) - \mathrm{Ar}^+(3p^{-1})$, which leads to KERs of $\sim 5\,\mathrm{eV}$ (see Sec. 8.2.1). In the KER distribution of $\mathrm{Ar}^+ + \mathrm{Ar}^+$ ions (see Fig. 8.3), the increase in the green contribution is attributed to the charge transfer (CT) channel (see Eq. 8.6). This non-ICD-like relaxation channel is studied in more detail in an XUV-pump IR-probe experiment, which is discussed in Sec. 8.2.1.
Next, the absorption of the third photon at the still neutral site of $\mathrm{Ar}^+(3p^{-2}4d) - \mathrm{Ar}$ is discussed. Assuming no electron correlation, the $4d$-electron remains in its configuration and two-site doubly ionized Rydberg states are excited:

$$\mathrm{Ar}^+(3p^{-2}(^1D)4d\,^2S) - \mathrm{Ar} + \hbar\omega \rightarrow \mathrm{Ar}^+(3p^{-2}(^1D)4d\,^2S) - \mathrm{Ar}^+(3p^{-1}) + e^-. \tag{8.7}$$

In earlier work [258], states of $3d$ and $4p$-type in the energy range between $52 - 62\,\mathrm{eV}$ are reported, but unfortunately states of $4d$-type or other Rydberg states closer to the triple ionization threshold are not listed. In order to estimate a possible location of the $\mathrm{Ar}^+(3p^{-2}(^1D)4d\,^2S) - \mathrm{Ar}^+(3p^{-1})$ state, the following is considered: Ref. [178] reports the energy of the $\mathrm{Ar}^+(3p^{-2}(^1D)4d\,^2S) - \mathrm{Ar}$ and $\mathrm{Ar}^+(3p^{-2}(^1D)3d\,^2P) - \mathrm{Ar}$ state at $R = 12\,\mathrm{a.u.}$ to $E(R = 12\,\mathrm{a.u.}) = 41.1\,\mathrm{eV}$ and $E(R = 12\,\mathrm{a.u.}) = 37.4\,\mathrm{eV}$, respectively. The energy of $\mathrm{Ar}^+(3p^{-2}(^1D)3d\,^2P) - \mathrm{Ar}^+(3p^{-1})$ at $R = 12\,\mathrm{a.u.}$ is calculated by Ref. [258] to $E(R = 12\,\mathrm{a.u.}) = 56.9\,\mathrm{eV}$. Along this simple estimate, the sites of the dimer are treated independently and the energy of the $\mathrm{Ar}^+(3p^{-2}(^1D)4d\,^2S) - \mathrm{Ar}^+(3p^{-1})$ state at $R = 12\,\mathrm{a.u.}$ is approximated to $E(R = 12\,\mathrm{a.u.}) \approx (56.9 + (41.1 - 37.4))\,\mathrm{eV} = 60.6\,\mathrm{eV}$. Thus, in Fig. 8.4, the curves illustrating the $\mathrm{Ar}^+(3p^{-2}(^1D)4d\,^2S) - \mathrm{Ar}^+(3p^{-1})$ state (dashed orange curves) are just the $\mathrm{Ar}^+(3p^{-2}(^1D)3d\,^2P) - \mathrm{Ar}^+(3p^{-1})$ curve of Ref. [258] shifted up by 3.7 eV and

4.7 eV, respectively. The energy difference of $\Delta E = 1\,\text{eV}$ represents the uncertainty in the location of the state within this simple approach. It should be noted that the slope of the actual $\text{Ar}^+(3p^{-2}(^1D)4d\ ^2S) - \text{Ar}^+(3p^{-1})$ state is expected to be different from that of $\text{Ar}^+(3p^{-2}(^1D)3d\ ^2P) - \text{Ar}^+(3p^{-1})$ due to the different electronic configuration.

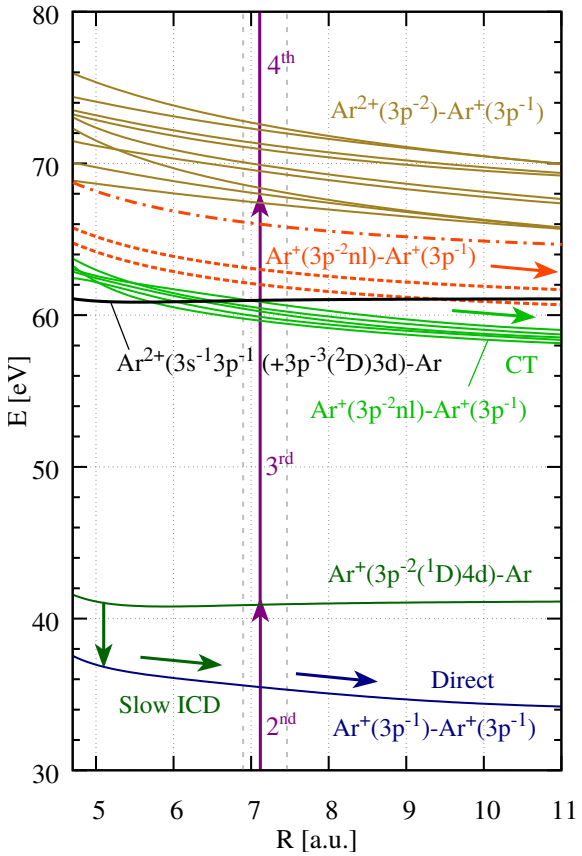

Figure 8.4: PECs of the argon dimer between $30 - 80\,\text{eV}$. The potential energy E is given with respect to the $\text{Ar} - \text{Ar}$ ground state. States relevant for the discussion in the text are color-coded. The $\text{Ar}^{2+}(3s^{-1}3p^{-1}(+3p^{-3}(^2D)3d)\,^1P)$ (black curve) and $\text{Ar}^+(3p^{-2}nl) - \text{Ar}^+(3p^{-1})$ states (light-green curves) are calculated by Ref. [177]. The orange curves representing $\text{Ar}^+(3p^{-2}(^1D)4d\ ^2S) - \text{Ar}^+(3p^{-1})$ are just estimated and therefore dashed. Higher lying Rydberg $\text{Ar}^+(3p^{-2}nl) - \text{Ar}^+(3p^{-1})$ states are symbolized by the orange dashed-dotted line. All other curves are taken from Refs. [178, 258]. The purple vertical arrows indicate photons of $\hbar\omega$ =27 eV. The FC region lies in the two vertical dashed grey lines.

However, treating the two sites independently oversimplifies the actual electronic configuration of the dimer. Especially states of high principal quantum number n do have a large overlap with the localized orbitals of the other argon atom [258]. Thus, when taking into account electron correlation, the ionization process at the

neutral site of the dimer can also be accompanied by electron shake-up [1, 37] into higher nl Rydberg states (dashed-dotted orange curve in Fig. 8.4):

$$\mathrm{Ar}^+(3p^{-2}(^1D)4d\ ^2S) - \mathrm{Ar} + \hbar\omega \rightarrow \mathrm{Ar}^+(3p^{-2}nl) - \mathrm{Ar}^+(3p^{-1}) + e^-. \tag{8.8}$$

In order to understand the high-KER contribution (see Fig. 8.3 (a), orange) intuitively, a classical orbit picture of the Rydberg electron is appropriate. It is presumed that the repulsion between a singly charged Rydberg-excited $\mathrm{Ar}^+(3p^{-2}nl)$ ion and a singly charged $\mathrm{Ar}^+(3p^{-1})$ ion in the ground state is higher compared to two $\mathrm{Ar}^+(3p^{-1})$ ground state ions, because the nl Rydberg electron truncates the electron shielding of the nuclear charges. Fig. 8.5 illustrates this schematically.

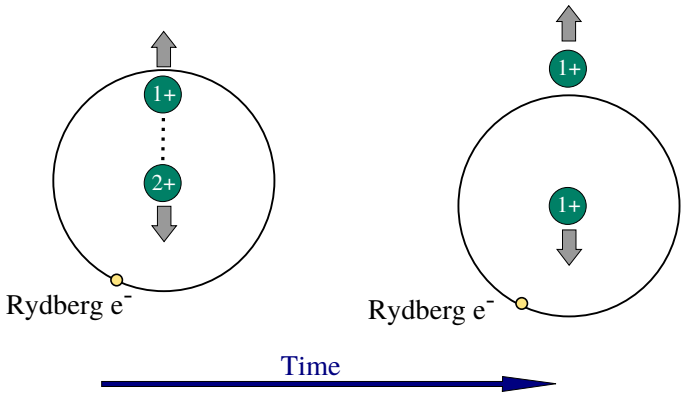

Figure 8.5: Frustrated triple ionization of an argon dimer.

As long as the radius of the Rydberg orbit r_{Ryd} is larger compared to the equilibrium internuclear distance R_{eq}, the electron is not localized at one of the two dimer sites and the nuclei "feel" the repulsion of $\mathrm{Ar}^{2+} + \mathrm{Ar}^+$. However, at the point in time when $r_{\mathrm{Ryd}} < R_{\mathrm{eq}}$, the Rydberg electron gets localized and $\mathrm{Ar}^+ + \mathrm{Ar}^+$ fragments with a KER comparable to $\mathrm{Ar}^{2+} + \mathrm{Ar}^+$ are measured. In literature, this phenomenon is referred to so-called frustrated triple ionization, which has been observed in strong field ionization experiments on Ar_2, where rescattered electrons can be trapped in Rydberg states [155, 271, 284]. Concerning the present experiment, a high-KER component at $\sim 7.2\,\mathrm{eV}$ for $\mathrm{Ar}^+ + \mathrm{Ar}^+$ is measured (Fig. 8.3 (a)). The value fits to the KER of the $\mathrm{Ar}^{2+} + \mathrm{Ar}^+$ channel, which peaks at $\sim 7.5\,\mathrm{eV}$ (see Fig. 8.3 (b)), and the findings of Refs. [155, 271, 284]. This similarity supports the hypothesis of frustrated triple ionization being the reason for the high-KER peak at $\sim 7.2\,\mathrm{eV}$ in the $\mathrm{Ar}^+ + \mathrm{Ar}^+$ channel. Using a delayed IR pulse, this fragmentation channel is further investigated and the results are discussed in Sec. 8.2.2.
In Eq. 8.8, the notation for the Rydberg state, i.e., $\mathrm{Ar}^+(3p^{-2}nl) - \mathrm{Ar}^+(3p^{-1})$, and the picture drawn in Fig. 8.5, describes the localization of the Rydberg electron at the doubly charged site. Alternatively, the Rydberg electron can also localize at the singly charged site. Then, the Rydberg state is better written as $\mathrm{Ar}^{2+}(3p^{-2}) - \mathrm{Ar}(3p^{-1}nl)$. This channel is further discussed in Sec. 8.2.3.

8.2 XUV-Pump IR-Probe

The presentation of the XUV-pump IR-probe results in this section is based on already having identified the relevant relaxation channels being at work in Sec. 8.1. The FEL intensity is kept at the same level as in the high-intensity single-pulse measurement (see Sec. 8.1.2). This ensures the population of highly excited dimer states (see Fig. 8.4), which can be efficiently probed by a delayed IR pulse[64]. The following Sec. 8.2.1 is dedicated to present the analysis and the results obtained for tracing the charge transfer (CT) process at curve crossings in a time-resolved manner. Afterwards, in Sec. 8.2.2 it is shown that a delayed IR pulse also enables to verify the relaxation pathway via frustrated triple ionization proposed in Sec. 8.1.2. Further channels probed by the IR pulse are discussed in Sec. 8.2.3.

8.2.1 Tracing Charge Transfer at Curve Crossings

In this section, the discussion of the applied pump-probe scheme is followed by the analysis of the corresponding delay-dependent KER distributions. Afterwards, a simulation modeling the experiment illustrates how the CT lifetime can be extracted from the experimental data. Finally, the determination of the CT lifetime is presented and compared to theoretical predictions.

Pump-Probe Scheme

The relevant PECs involved in the CT process are plotted in Fig. 8.6. It is the role of the XUV-pump[65] to populate $\mathrm{Ar}^{2+}(3s^{-1}3p^{-1}\,{}^1P\,(+3p^{-3}({}^2D)3d\,{}^1P)) - \mathrm{Ar}$ states within the Franck-Condon region:

$$\mathrm{Pump}: \mathrm{Ar} - \mathrm{Ar} \xrightarrow{3\times\mathrm{XUV}} \mathrm{Ar}^{2+}(3s^{-1}3p^{-1}\,{}^1P\,(+3p^{-3}({}^2D)3d\,{}^1P)) - \mathrm{Ar} + 2e^-. \quad (8.9)$$

As this state is of shallow, but binding character, the wave packet starts to move to $R < R_{\mathrm{eq}}$. The state is crossed by several repulsive states (yellow, green, red and blue curve) in a internuclear distance range between $R = 5.7 - 7.0\,\mathrm{a.u.}$ The states have been calculated by Ref. [177] (see Sec. 2.4.4). At the crossing points, population can be transferred to the repulsive states due to non-adiabatic couplings [258]:

$$\mathrm{Ar}^{2+}(3s^{-1}3p^{-1}(+3p^{-3}({}^2D)3d)\,{}^1P) - \mathrm{Ar} \xrightarrow{\mathrm{CT}} \mathrm{Ar}^{+}(3p^{-2}nl) - \mathrm{Ar}^{+}(3p^{-1}). \quad (8.10)$$

The intermediate repulsive states are of $\mathrm{Ar}^{+}(3p^{-2}nl) - \mathrm{Ar}^{+}(3p^{-1})$ character. The IR probe may only ionize the excited electrons of these states, if the charge transfer has

[64] Intensity $I \sim 10^{14}\ \mathrm{W/cm^2}$ (see Sec. 6.2.1), photon energy $\hbar\omega_{\mathrm{IR}} = 1.55\,\mathrm{eV}$, repetition rate 10 Hz (see Sec. 5.1), temporal resolution pump-probe experiment $\sim 280\,\mathrm{fs}$ (FWHM) (see Sec. 6.2.3).

[65] From the $\mathrm{Ar} - \mathrm{Ar}$ ground state, 3 photons of $\hbar\omega = 27\,\mathrm{eV}$ are absorbed sequentially, see Fig. 8.4.

already occurred. Then, it transfers population from the intermediate $Ar^+(3p^{-2}nl)-Ar^+(3p^{-1})$ states to the final $Ar^{2+}(3p^{-2}) - Ar^+(3p^{-1})$ states:

$$\text{Probe}: Ar^+(3p^{-2}nl) - Ar^+(3p^{-1}) \xrightarrow{\text{IR}} Ar^{2+}(3p^{-2}) + Ar^+(3p^{-1}) + e^-_{nl}. \tag{8.11}$$

This allows to observe the CT in a time-resolved manner by observing the KER of $Ar^{2+} + Ar^+$ ions as a function of the delay between XUV-pump and IR-probe.

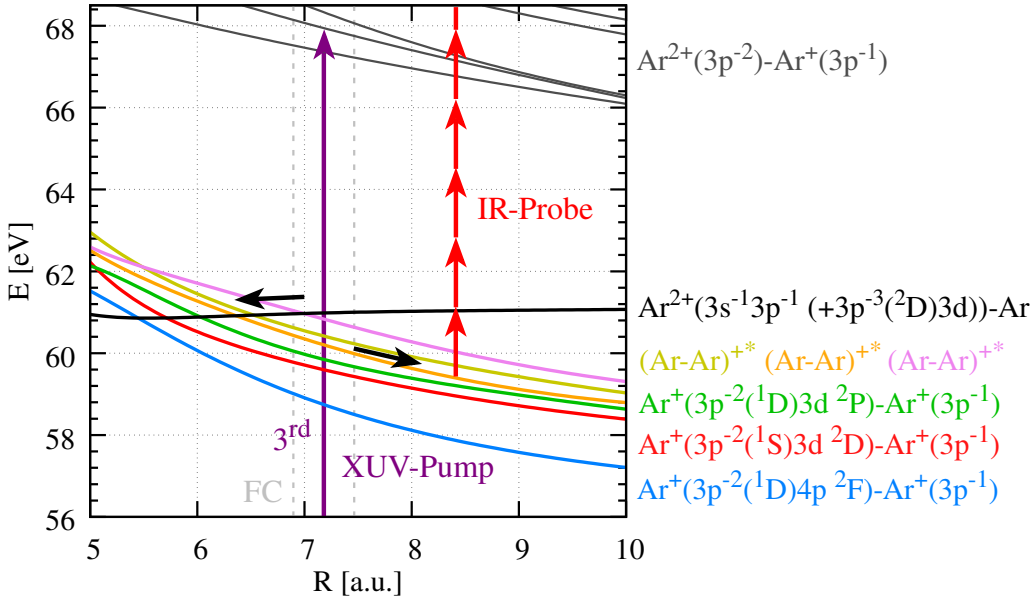

Figure 8.6: PECs of the argon dimer in the energy range 56 – 68.5 eV relevant for the discussed CT process at curve crossings. The XUV-pump (purple arrow) populates the initial $Ar^{2+}(3s^{-1}3p^{-1}\,{}^1P\,(+3p^{-3}({}^2D)3d\,{}^1P)) - Ar$ state within the FC region (area between dashed grey lines) and the wave packet starts to evolve to smaller R. At the crossings with the colored $Ar^+(3p^{-2}nl)-Ar^+(3p^{-1})$ states, population is non-adiabatically transferred. Afterwards, the IR-pulse (red arrows) probes the population of the intermediate states by ionization to the final $Ar^{2+}(3p^{-2}) - Ar^+(3p^{-1})$ states (dark-grey curves). All PECs shown are calculated by Refs. [177, 258].

In this scheme, the KER of the final $Ar^{2+}+Ar^+$ ions is given in good approximation by

$$\text{KER} = E_i(R_{\text{eq}}) - E_{\text{inter}}(R(t_d)) + E_f(R(t_d)) - E_f(R \to \infty). \tag{8.12}$$

Here, $E_i(R_{\text{eq}})$ is the potential energy on the $Ar^{2+}(3s^{-1}3p^{-1}\,{}^1P\,(+3p^{-3}({}^2D)3d\,{}^1P)) - Ar$ state at R_{eq}, $E_{\text{inter}}(R(t_d))$ is the potential energy on the intermediate $Ar^+(3p^{-2}nl)-Ar^+(3p^{-1})$ state at the instant of the IR probe at $R(t_d)$, $E_f(R(t_d))$ is the potential energy on the final $Ar^{2+}(3p^{-2}) - Ar^+(3p^{-1})$ state at $R(t_d)$ and $E_f(R \to \infty)$ is the energy in the asymptotic limit $R \to \infty$. The explicit delay dependence of Eq. 8.12 by means of the internuclear distance $R(t_d)$ makes the KER an ideal observable to trace the charge transfer process in time.

KER vs. Delay of Ar^{2+}+Ar^{+} Ions

The delay-dependent KER of Ar^{2+}+Ar^{+} ions is shown in Fig. 8.7. The delay is scanned over a range of ± 4 ps. For negative delays, the IR arrives early with respect to the XUV pulse, for positive vice versa.

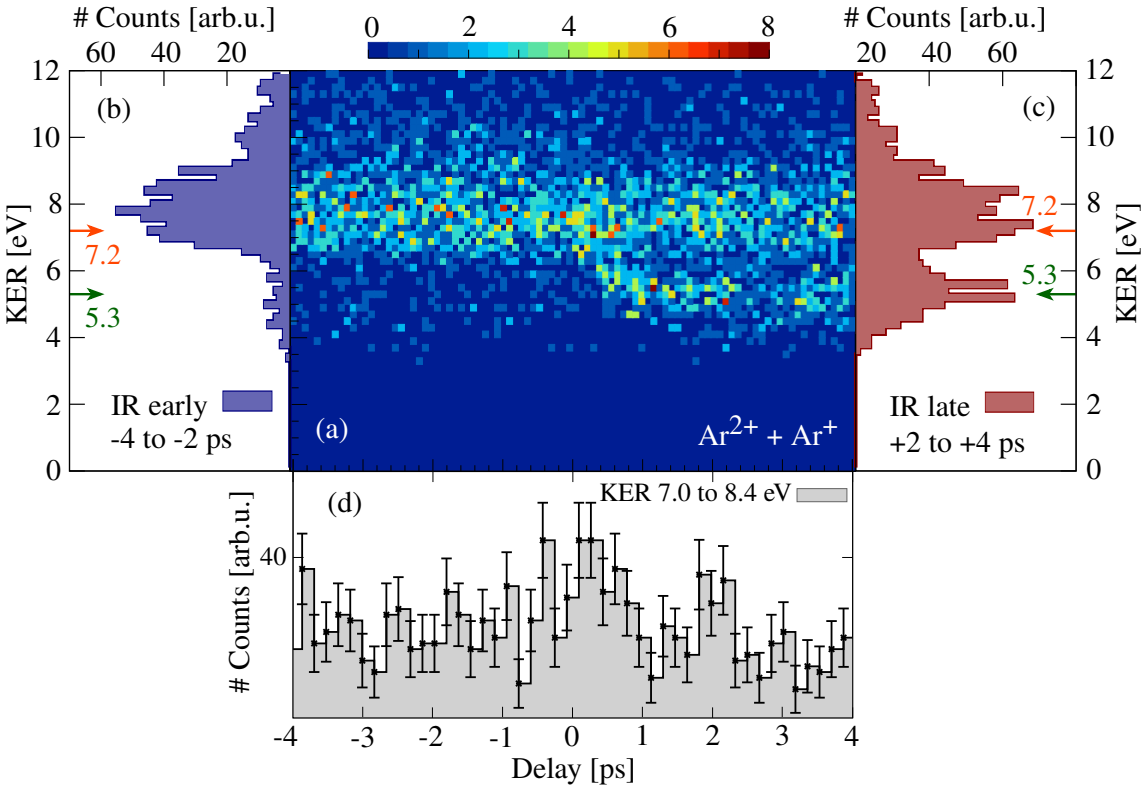

Figure 8.7: Ar^{2+} + Ar^{+} coincidence channel. (a) KER vs. delay. For negative delays, the IR is early with respect to the XUV pulse, for positive delays vice versa. (b) Projection of all KERs within -4 to -2 ps onto the KER axis. (c) Same as (b), but for +2 to +4 ps. (d) Projection of all KERs between 7.0 to 8.4 eV onto the delay axis.

For negative and positive delays, the plot shows a delay-independent KER contribution at ∼ 7.5 eV (see also the projections (b) and (c)). According to Sec. 8.1.2, this constant background originates from ionization with a single XUV pulse to $Ar^{2+}(3p^{-2})$−$Ar^{+}(3p^{-1})$ within the Franck-Condon region. More interestingly, Fig. 8.7 shows a delay-dependent feature starting from KER ∼ 7.5 eV at time delay zero and asymptotically reaching KERs between 4 − 6 eV at +4 ps. The asymptotic KER (see Fig. 8.7 (c)) matches that of the CT channel (see Fig. 8.3 (a)) and thus the delay-dependent KER behaves as described in Eq. 8.12.
The facts that the Ar^{2+} + Ar^{+} coincidence channel is not observed in the low intensity single XUV pulse measurement (see Sec. 8.1.1) and that there are less high-KER contributions in the respective Ar^{+} + Ar^{+} channel (see Fig. 8.1) implies that

the observed delay-dependent signal stems from probing the high-lying intermediate $Ar^+(3p^{-2}nl) - Ar^+(3p^{-1})$ CT states and is not caused, e.g., by probing the slow ICD channel. The IR ionization probability of the excited nl electron of the $Ar^+(3p^{-2}nl) - Ar^+(3p^{-1})$ states is higher compared to the ionization of a $3p$ electron from the energetically lower-lying $Ar^+(3p^{-1}) - Ar^+(3p^{-1})$ state, i.e., the final state after slow ICD.

Coming back to Fig. 8.7, a projection of the KERs in the range of $7.0 - 8.4\,\mathrm{eV}$ onto the delay axis (d) reveals a weak peak in the range 0 to $+1\,\mathrm{ps}$. In order to improve the statistics that is limited by the 10 Hz repetition rate of the IR laser (see Sec. 5.1), the restrictions on the sum momenta (see Sec. 4.5) to assign coincidences are diminished. Based on this, the KERs of all Ar^{2+} ions resulting from Coulomb explosions, i.e., those that have non-zero kinetic energy, are plotted in Fig. 8.8.

These ions are not measured in coincidence, i.e., they also include contributions from channels different than Ar^{2+}+Ar^+, e.g., Ar^{2+}+Ar or Ar^{2+}+Ar^{2+}. By processing non-coincident data, the statistics is increased by a factor of ~ 10. Moreover, different contributions can be attributed by means of channel-specific KERs, which have been already identified in the coincident data presented in Sec. 8.1 and Fig. 8.7. In this regard, the non-coincident data of Fig. 8.8 resembles the coincident data of Fig. 8.7 in large part, however with higher statistics.

This being said, an increase of KERs within $7.0 - 8.4\,\mathrm{eV}$ for delays between 0 to $+1\,\mathrm{ps}$ is clearly visible in Fig. 8.8 (a) and also in the corresponding projection onto the delay axis (d). The yield increases step-like at zero time delay and shows a shallow falling slope towards higher KERs. In Sec. 8.2.1, a simulation illustrates that this delay-dependent yield is a measure of the CT lifetime.

Over the entire negative delay range, i.e., the IR being early relative to the XUV pulse, a channel with KERs of $\sim 4.5\,\mathrm{eV}$, which is not observed in the coincident data (see Fig. 8.7), shows up. Its origin is discussed in Sec. 8.2.3.

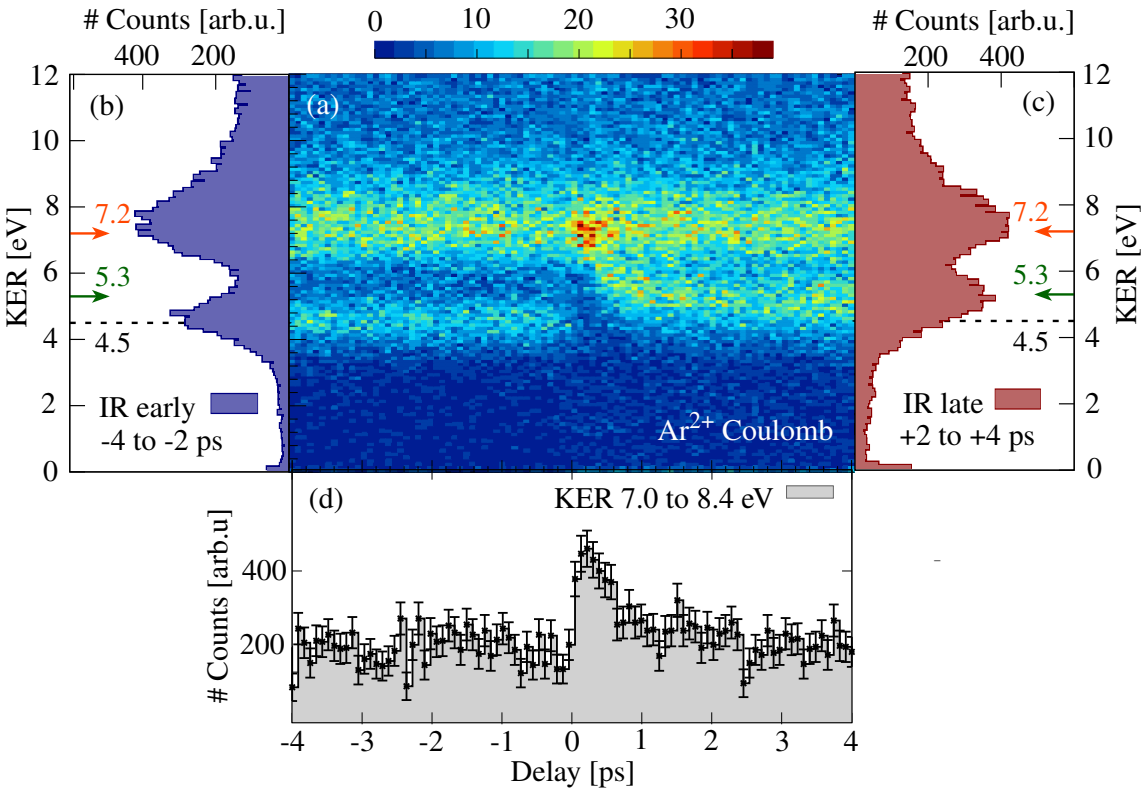

Figure 8.8: Coulomb-exploded Ar^{2+} ions (non-coincident). (a) KER vs. delay. For negative delays, the IR is early with respect to the XUV pulse, for positive delays vice versa. (b) Projection of all KERs within -4 to -2 ps onto the KER axis. (c) Same as (b), but for +2 to +4 ps. (d) Projection of all KERs between 7.0 to 8.4 eV onto the delay axis.

KER vs. Delay of Ar^++Ar^+ Ions

For the same statistical reasons already discussed for the $Ar^{2+} + Ar^+$ channel, all KERs of Ar^+ fragments stemming from Coulomb-explosions, but not measured in coincidence, are included in Fig. 8.9. According to Eq. 8.11, the IR-probe simultaneously increases the yield of $Ar^{2+} + Ar^+$ ions and at the same time depletes the yield of $Ar^+ + Ar^+$ ions with KERs between $\sim 4.5 - 6$ eV.
The KER region of interest for the CT channel ($4.8 - 5.8$ eV) is projected onto the delay axis in Fig. 8.9 (d). It shows a step-like decrease at time zero followed by a slow rise towards longer delays. As expected, this delay dependence represents the inverse image of the Ar^{2+} yield shown in Fig. 8.8 (d) and thus is a further evidence of the CT process (see Eq. 8.11).
The contribution at ~ 3.8 eV (see projections (b) and (c)) is attributed to the direct fragmentation channel into $Ar^+ + Ar^+$ at R_{eq} (see Sec. 8.1.1, Eq. 8.2). This channel shows no delay dependence and is constant over the entire delay range, which means

that it is not influenced by the relative timing between XUV and IR pulse. The ionization threshold $Ar^+(3p^{-1}) - Ar^+(3p^{-1}) \rightarrow Ar^{2+}(3p^{-2}) - Ar^+(3p^{-1})$ at R_{eq} is 35.5 eV (see Fig. 8.2), which is 7.9 eV higher compared to the $Ar^+ \rightarrow Ar^{2+}$ ionization threshold of 27.6 eV. In Sec. 6.2.1, it is shown that the ratio Ar^{2+}/Ar^+ using only the IR laser is $\sim 2\,\%$. Thus, regarding the even higher ionization threshold of $Ar^+(3p^{-1})-Ar^+(3p^{-1}) \rightarrow Ar^{2+}(3p^{-2})-Ar^+(3p^{-1})$, it can be concluded that the main part of the delay-independent KER contribution at ~ 3.8 eV stems from ionization by just the XUV pulse.
The KER contribution at ~ 7.2 eV is attributed to frustrated triple ionization whose delay-dependence is discussed in Sec. 8.2.2. Furthermore, Fig. 8.9 reveals a new channel with KERs of ~ 1.2 eV, which is not observed in the single XUV pulse experiment (see Sec. 8.1) and which is only present for positive delays, e.g., for the IR pulse arriving late with respect to the XUV pulse. The low KER suggests this channel to originate from a dissociation including a neutral Ar atom, i.e., $Ar^+ + Ar$. This channel is further discussed in Sec. 8.2.3.

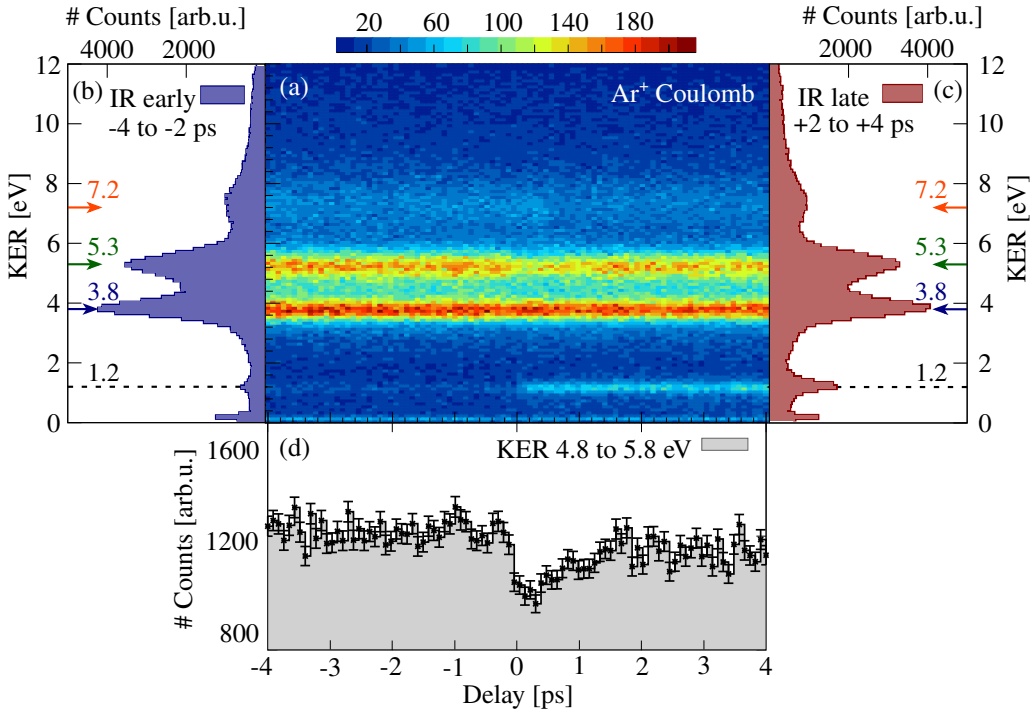

Figure 8.9: Coulomb-exploded Ar^+ ions (non-coincident). (a) KER vs. delay. For negative delays, the IR is early with respect to the XUV pulse, for positive delays vice versa. (b) Projection of all KERs within -4 to -2 ps onto the KER axis. (c) Same as (b), but for +2 to +4 ps. (d) Projection of all KERs between 4.8 to 5.8 eV onto the delay axis.

Simulation

In order to clarify the assigned KER contributions of Figs. 8.7 and 8.8 and to obtain more information on the CT process, the experiment is modeled by a classical simulation. It is based on propagating classical point-like particles on PECs (see Sec. 2.5). The simulation is similar to that described in Refs. [183, 236]. The CT is modeled as an exponential decay onto the $Ar^+(3p^{-2}nl) - Ar^+(3p^{-1})$ states at the corresponding crossings with $Ar^{2+}(3s^{-1}3p^{-1}\,{}^1P\,(+3p^{-3}({}^2D)3d\,{}^1P)) - Ar$ between 5.7 to 7.0 a.u. (see Fig. 8.6). The $Ar^+(3p^{-2}({}^1D)4p\,{}^2F) - Ar^+(3p^{-1})$ state is not included in the model as its crossing cannot be reached by the wave packet [80]. The experimental KER resolution does not allow to distinguish decay contributions of individual crossings and a common lifetime τ is assumed for all channels. The probability distribution of the curves' population follows the Landau-Zener probabilities for each crossing as calculated by Ref. [177] (see Sec. 2.4.5). For each event of the simulation, the value of τ is drawn from an exponential distribution. It determines the start of the fragmentation, i.e., the instant in time for the charge transfer onto the repulsive curves. In doing so, the simulation neglects the wave packet motion on the initial binding PEC. This approximation is well justified as the wave packet needs ~ 120 fs to reach the left most crossing[66], which is below the temporal resolution of the experiment of 280 fs (Sec. 6.2.3). On the $Ar^+(3p^{-2}nl) - Ar^+(3p^{-1})$ PECs, the particles are propagated following Newton's equations of motion. After a variable time t_{probe}, the particles are promoted to the final $Ar^{2+}(3p^{-2}) - Ar^+(3p^{-1})$ state, which is modeled by a $2/R$ Coulomb potential curve. Having reached this curve, the particles are propagated to a large internuclear distance ($R = 200$ a.u.) to determine the final KER (see Eq. 8.12). In order to match the experimental conditions, a constant background of events generated by directly populating the $2/R$ Coulomb potential curve at R_{eq} is included in the simulation.

The results of the simulation for an input lifetime of $\tau = 700$ fs and $\tau = 400$ fs are shown in Fig. 8.10 (a) and (b), respectively. The KER of the $Ar^{2+} + Ar^+$ channel is plotted versus the delay $t_d = \tau + t_{\mathrm{probe}}$.

The qualitative agreement with the experimental results (see Fig. 8.8) is convincing. For the projection onto the delay axis (c) and (d), the same KER range as used for the experimental data (see Fig. 8.8 (d)) is applied. In both cases, an exponential fit returns the respective input lifetime τ. Hence, the simulation shows that using the delay-dependent KER of the $Ar^{2+} + Ar^+$ channel is an appropriate tool to determine the lifetime of the CT process.

In order to further assess the quality of the simulation, Fig. 8.11 shows an overlay of the simulated asymptotic KER distribution, i.e., KERs within +2 to +4 ps, with the measured KERs.

[66] The vibrational period on the $Ar^{2+}(3s^{-1}3p^{-1}\,{}^1P\,(+3p^{-3}({}^2D)3d\,{}^1P)) - Ar$ PEC is 365 fs [177].

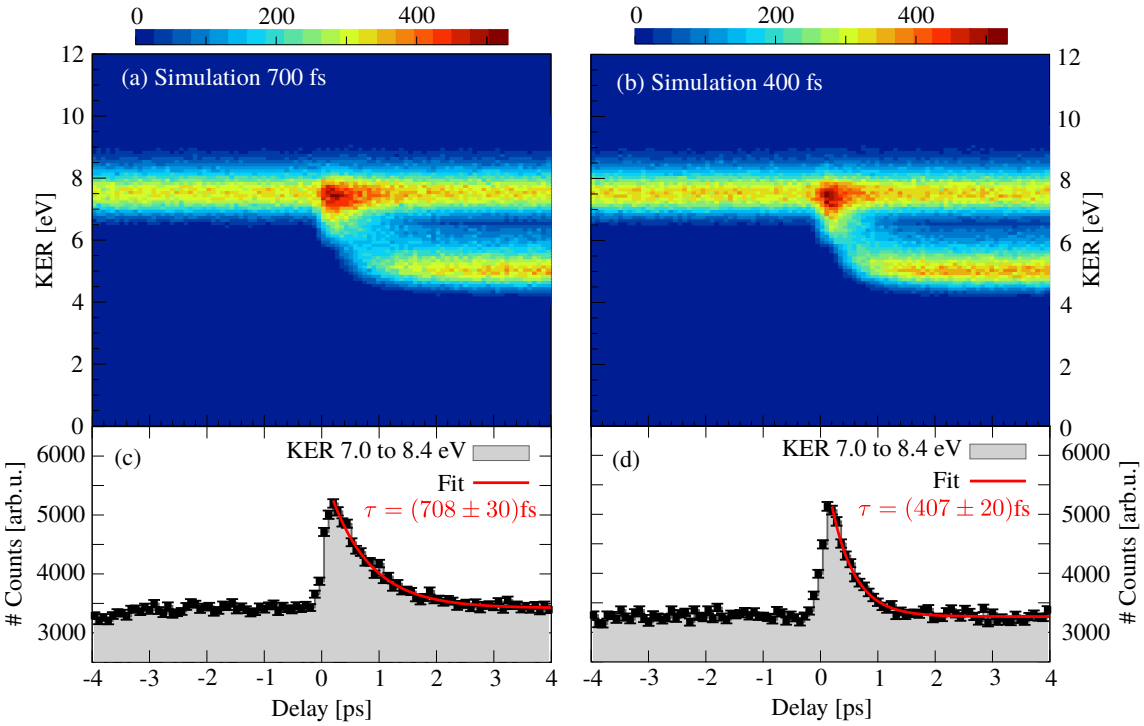

Figure 8.10: Simulation of the $Ar^{2+}+Ar^{+}$ channel. KER vs. delay for an input CT lifetime of (a) $\tau = 700$ fs and (b) $\tau = 400$ fs. (c) and (d) Projection of all KERs within 7.0 to 8.4 eV of (a) and (b), respectively, onto the delay axis. The red curve shows the result of an exponential fit.

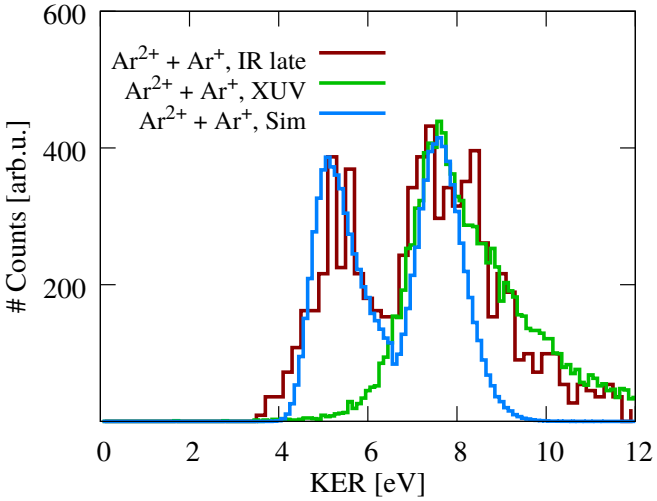

Figure 8.11: Overlay of different KER distributions. The blue line is the asymptotic $Ar^{2+}+Ar^{+}$ (+2 to +4 ps) KER distribution of the simulation, the red line is the corresponding one of the experiment (see Fig. 8.7). The green line shows the KER distribution of the $Ar^{2+}+Ar^{+}$ channel recorded in the single XUV pulse measurement (see Sec. 8.1.2, Fig. 8.3 (b)).

Besides for KERs > 8 eV, the overall agreement with the asymptotic KER measured in the Ar^{2+}+Ar^{+} channel is fairly good. The disagreement for the delay-independent high KER background (KER > 8 eV) is due to an approximation of the simulation, which uses a single $2/R$ Coulomb potential curve to represent the final $Ar^{2+}(3p^{-2}) - Ar^{+}(3p^{-1})$ states. However, the peak position of the high KER contribution also agrees with the Ar^{2+}+Ar^{+} distribution measured in the single XUV pulse experiment (see Fig. 8.3 (b)).
In the following, the importance of knowing the exact R-dependence of the intermediate $Ar^{+}(3p^{-2}nl) - Ar^{+}(3p^{-1})$ states used for the simulation is pointed out. In Fig. 8.12, the asymptotic KER is shown in case of using the calculated curves by Ref. [177] and $1/R$ Coulomb potential curves to represent the intermediate states. It is shown that taking intermediate $1/R$ curves leads to lower asymptotic KERs, which is not in agreement with the experimental KER distributions (see Fig. 8.11).

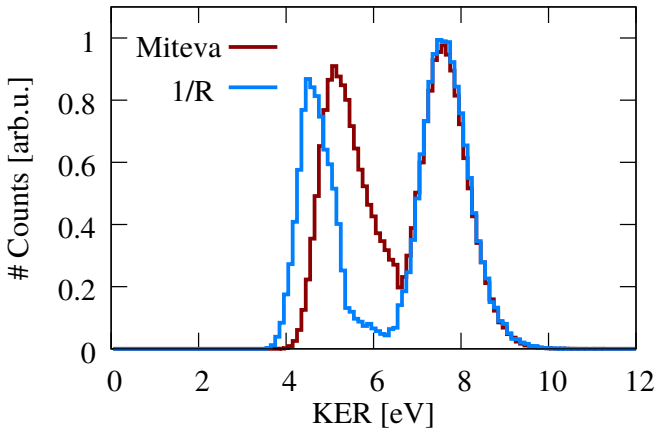

Figure 8.12: Simulated asymptotic KER of Ar^{2+} + Ar^{+} using the curves calculated by Ref. [177] (red line) and a $1/R$ Coulomb potential (blue line) to represent the intermediate $Ar^{+}(3p^{-2}nl) - Ar^{+}(3p^{-1})$ states.

Lifetime Determination of the Charge Transfer

With the CT lifetime determination successfully tested on the simulated data, it can now be applied to the experimental data.
First, it is discussed up to which internuclear distance R_{probe} the IR-probe can test the population of the intermediate repulsive states in order to obtain final KERs within the window 7.0 − 8.4 eV that is used to select the relevant Coulomb-exploded Ar^{2+} ions. Of all intermediate states, the $Ar^{+}(3p^{-2}(^1S)3d\,^2D) - Ar^{+}(3p^{-1})$ state (red curve in Fig. 2.12) crosses the bound state (black curve in Fig. 2.12) at the smallest internuclear separation, $R_{\mathrm{cross}} = 5.7$ a.u.. Consequently, the KER gained on this intermediate state is the highest of all intermediate states considered. In order to reach a final Ar^{2+} + Ar^{+} KER of 7.0 eV, i.e., the lower edge of the KER condition, the KER gained on the intermediate state $\mathrm{KER}_{\mathrm{inter}} = E_{\mathrm{inter}}(R_{\mathrm{cross}}) - E_{\mathrm{inter}}(R_{\mathrm{probe}})$,

has to be equal to the KER, which would be gained by directly accessing the $Ar^{2+}(3p^{-2}) - Ar^{+}(3p^{-1})$ state at R_{eq}, i.e, $KER_f = E_f(R_{eq}) - E_f(R_{probe})$. As can be seen in Fig. 8.13, this is the case for an internuclear distance $R_{probe} \approx 14$ a.u. As less KER_{inter} is gained for all other intermediate states, this is the upper limit of R_{probe} for which the KER condition 7.0 to 8.4 eV is still fulfilled.
Final $Ar^{2+} + Ar^{+}$ KERs of $>$ 8.4 eV are expected for probing to $Ar^{2+}(3p^{-2}) - Ar^{+}(3p^{-1})$ at $R < R_{eq}$. In the delay-dependent KER plots (see Fig. 8.7 and 8.8), however, no enhancement of KERs > 8.4 eV is visible. This implies that the population of the intermediate states is in most cases probed for $R_{probe} > R_{eq}$.
The selection of the KER condition for $Ar^{+} + Ar^{+}$ is more straightforward and has been discussed in detail in the analysis of the simulation (see e.g. Fig. 8.12).
Fig. 8.13 also shows that the IR ionization probability, i.e., depending on the internuclear separation R, different numbers of IR photons need to be absorbed to reach $Ar^{2+}(3p^{-2}) - Ar^{+}(3p^{-1})$, does not dependent on R. For all R, 4 IR photons are enough to reach the lowest lying $Ar^{2+}(3p^{-2}) - Ar^{+}(3p^{-1})$ states. Moreover, in Sec. 6.2.1, it is shown that the IR intensity of $I = 1 - 2 \times 10^{14}$ W/cm^2 is sufficient to create Ar^{+}, which implies the absorption of at least 10 IR photons. Hence, the overall high IR intensity further excludes an R-dependent IR ionization probability.

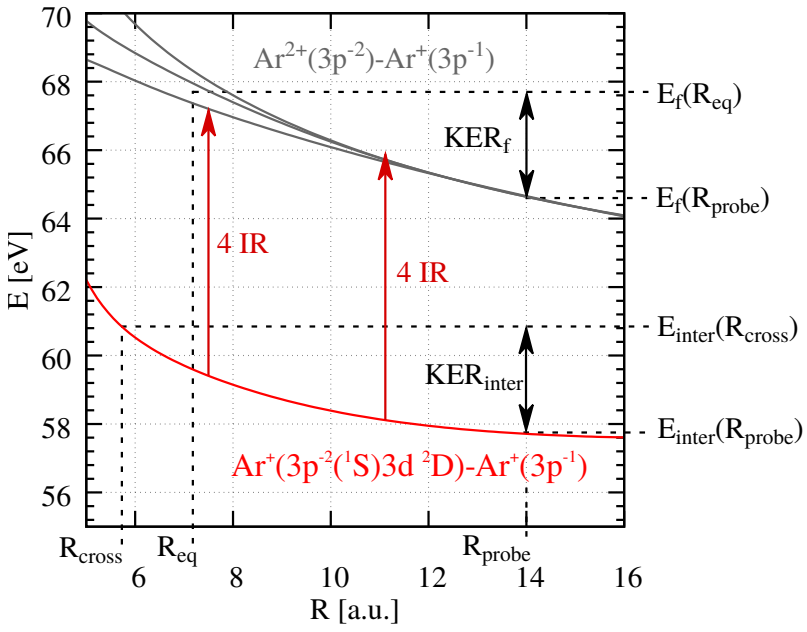

Figure 8.13: PECs of the argon dimer between 55 – 70 eV to demonstrate different contributions to the KER. The intermediate $Ar^{+}(3p^{-2}(^1S)3d\,^2D) - Ar^{+}(3p^{-1})$ state is plotted in red [177]. The $Ar^{2+}(3p^{-2}) - Ar^{+}(3p^{-1})$ states are taken from Ref. [258]. The double-headed vertical black arrows represent specific KERs discussed in the text. The two vertical dark-red arrows represent 4 IR photons with a sum energy of $\hbar\omega = 4 \cdot 1.55$ eV $= 6.2$ eV.

For the KER window 7.0 − 8.4 eV, Fig. 8.14 shows the projections of Coulomb-exploded Ar^{2+} and Ar^{+} ions onto the delay axis. As pointed out by Eq. 8.11, the increase in the Ar^{2+} channel coincides with a respective decrease in the Ar^{+} channel. This interplay between gain and loss is evident in Fig. 8.14.

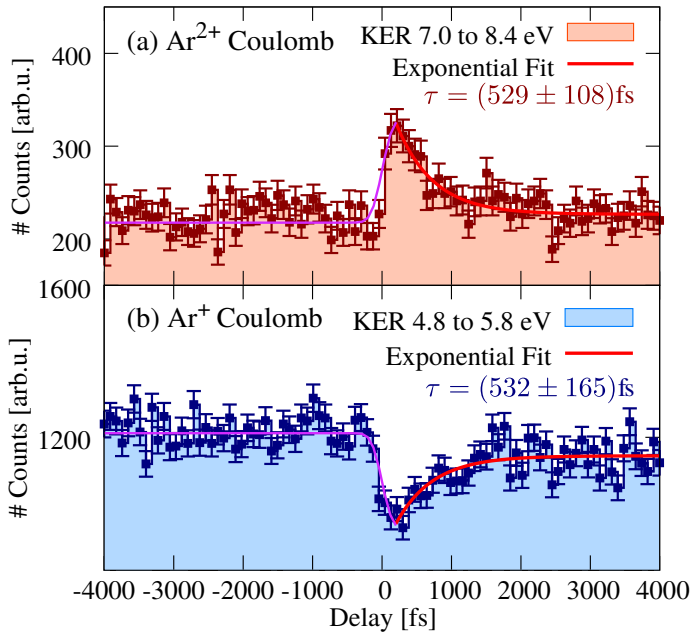

Figure 8.14: (a) Yield of Coulomb-exploded Ar^{2+} ions within the KER window 7.0 to 8.4 eV as a function of delay. (b) Yield of Coulomb-exploded Ar^{+} ions within the KER window 4.8 to 5.8 eV as a function of delay. The red lines are exponential fits to the data. The magenta line depicts the error function whose width marks the temporal resolution of the experiment (see Sec. 6.2.3).

In the yield of Coulomb-exploded Ar^{2+} ions (a), a step increase at ~ 200 fs is followed by a slow exponential decrease towards longer delays. The yield of Coulomb-exploded Ar^{+} ions (b) behaves exactly opposite and a step decrease at time zero is followed by a slow exponential increase. The step increase/decrease at time zero is in agreement with the error function (see Sec. 6.2.3), whose width marks the temporal resolution of the experiment (purple curve). As discussed in Eq. 8.11, the IR probe will only ionize the $Ar^{+}(3p^{-2}nl) - Ar^{+}(3p^{-1})$ states to $Ar^{2+}(3p^{-2}) - Ar^{+}(3p^{-1})$, if the CT has already occurred. This explains the sharp increase/decrease in the count rate and the following slow decay/rise, which contains the CT lifetime.
The complete CT relaxation cascade involves three states:

1. The initial state: $Ar^{2+}(3s^{-1}3p^{-1}\,{}^1P\,(+3p^{-3}({}^2D)3d\,{}^1P)) - Ar$,
2. The intermediate state(s) up to $R \leq 14$ a.u.: $Ar^{+}(3p^{-2}nl) - Ar^{+}(3p^{-1})$,
3. The final fragments at large $R \to \infty$: $Ar^{+}(3p^{-2}nl) + Ar^{+}(3p^{-1})$.

In analogy to Ref. [183], the population of these states can be described by the following rate equations:

$$\frac{\mathrm{d}N_i}{\mathrm{d}t} = -\lambda_i N_i, \tag{8.13}$$

$$\frac{\mathrm{d}N_{\mathrm{inter}}}{\mathrm{d}t} = \lambda_i N_i - \lambda_{\mathrm{diss}} N_{\mathrm{inter}}, \tag{8.14}$$

$$\frac{\mathrm{d}N_f}{\mathrm{d}t} = \lambda_{\mathrm{diss}} N_{\mathrm{inter}}. \tag{8.15}$$

Here, N_i, N_{inter} and N_f are the populations of the initial, intermediate and final states. $\lambda_i = 1/\tau_i$ indicates the decay constant with the CT lifetime τ_i. $\lambda_{\mathrm{diss}} = 1/\tau_{\mathrm{diss}}$ is the analogon for the dissociation time, i.e. the time the wave packets need to travel from the crossing points to the maximum allowed probe distance $R_{\mathrm{probe}} \approx 14\,\mathrm{a.u.}$ in order to still be within the $Ar^{2+} + Ar^{+}$ KER condition $7.0 - 8.4\,\mathrm{eV}$.
The experimental observables are the delay-dependent yields within the KER conditions ($7.0 - 8.4\,\mathrm{eV}$ for Ar^{2+}, $4.8 - 5.8\,\mathrm{eV}$ for Ar^{+}, see Fig. 8.14), because they represent the population N_{inter} of the intermediate states. The solution to Eqs. 8.13, 8.14 and 8.15 is given by:

$$N_i = \exp(-\lambda_i t), \tag{8.16}$$

$$N_{\mathrm{inter}} = \frac{\lambda_i}{\lambda_{\mathrm{diss}} - \lambda_i} \left(\exp(-\lambda_i t) - \exp(-\lambda_{\mathrm{diss}} t)\right). \tag{8.17}$$

In order to understand the experimental observables, two cases of Eq. 8.17 need to be considered. In the first case, the lifetime of the initial state is much shorter than the dissociation time, i.e., $\tau_i < \tau_{\mathrm{diss}}$ ($\lambda_i > \lambda_{\mathrm{diss}}$). Then, the rising edge of the yield distribution represents the lifetime of the initial state (see Fig. 8.15 (a)). In the opposite case, i.e., $\tau_i > \tau_{\mathrm{diss}}$ ($\lambda_i < \lambda_{\mathrm{diss}}$), the lifetime of the initial state is imprinted in the falling edge of the yield distribution (see Fig. 8.15 (b)) [183].
By employing the simulation, the dissociation time, i.e., the time the wave packet needs to travel from the crossing points to the maximum allowed probe distance $R_{\mathrm{probe}} \approx 14\,\mathrm{a.u.}$, is calculated to be $\tau_{\mathrm{diss}} = 110 - 120\,\mathrm{fs}$. The dissociation time defines the time interval, after which the population of the intermediate states can be probed after CT has occurred. In the following it is shown, that the CT lifetime τ_i is larger than τ_{diss} and the picture drawn in Fig. 8.15 is the appropriate one for the present case.

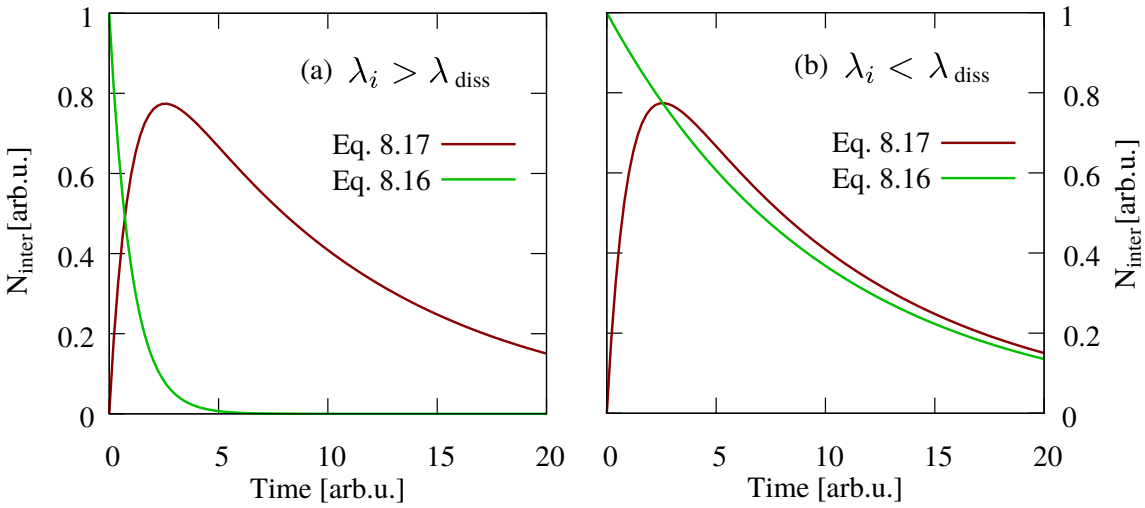

Figure 8.15: Plots illustrating two cases of Eq. 8.17. (a) The lifetime of the initial state τ_i is shorter than the dissociation time τ_{diss}, i.e., $\lambda_i > \lambda_{\text{diss}}$. (b) The lifetime of the initial state τ_i is larger compared to the dissociation time τ_{diss}, i.e., $\lambda_i < \lambda_{\text{diss}}$.

Returning to Fig. 8.14, the exponential fits to the slow falling/rising slope result in lifetimes of $\tau = (529 \pm 108)$ fs and $\tau = (532 \pm 165)$ fs, respectively. Following the discussion from above, i.e., $\tau_i > \tau_{\text{diss}}$, and the results of the simulation (see Fig. 8.10), this lifetime can be understood as the total lifetime of all CT processes from the initial $\text{Ar}^{2+}(3s^{-1}3p^{-1}\,{}^1P\,(+3p^{-3}({}^2D)3d\,{}^1P)) - \text{Ar}$ state onto the intermediate $\text{Ar}^{+}(3p^{-2}nl) - \text{Ar}^{+}(3p^{-1})$ states[67].
The comparison of the experimental findings, the results of the simulation and the calculation by Ref. [177] is shown in Fig. 8.16. The red curve represents the experimentally determined mean total lifetime $\tau_{\text{exp}} = (531 \pm 136)$ fs from the exponential fits to the Ar^{2+} and Ar^{+} yield, respectively (Fig. 8.14). The red-shaded area defines the corresponding error region. The simulation results (green curve) are based on an input lifetime of $\tau_{\text{sim}} = 530$ fs, i.e., the lifetime determined in the experiment. The agreement between simulation and experiment is rather good. The lifetime of $\tau_{\text{LZ}} = 430$ fs resulting from calculations using Landau-Zener probabilities is depicted by the blue curve [177]. It underestimates the lifetime determined from the experimental data, however agrees within the error bars of the fit. The width of the error function (magenta curve) marks the resolution of the experiment (see Sec. 6.2.3).

[67] Violet, yellow, orange, green and red curve of Fig. 2.12. As already mentioned, the crossing with the blue curve ($\text{Ar}^{+}(3p^{-2}({}^1D)4p\,{}^2F) - \text{Ar}^{+}(3p^{-1})$) is not reached [80].

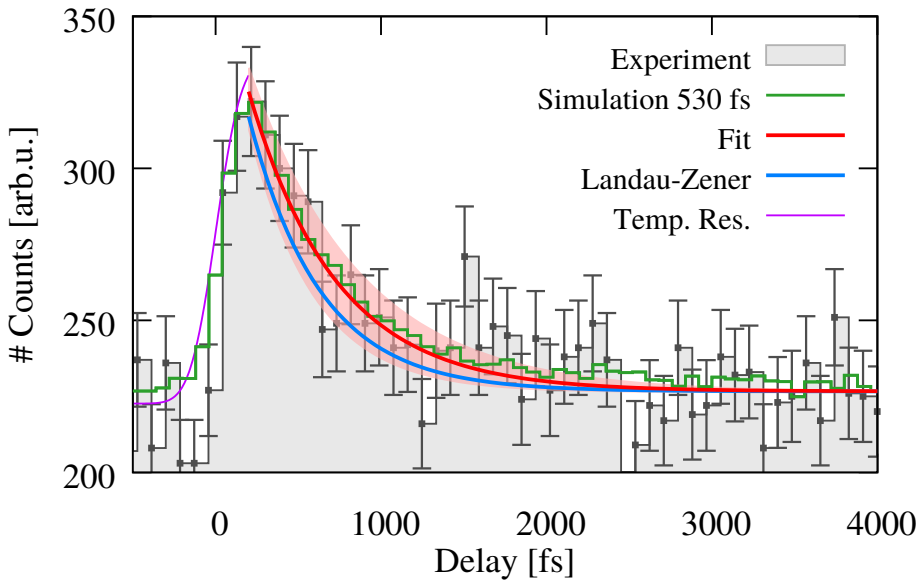

Figure 8.16: Delay-dependent yield of Coulomb-exploded Ar^{2+} ions measured in the experiment (grey) (same as Fig. 8.14 (a)). The plotted fit curve (red) shows the mean total lifetime $\tau_{exp} = (531 \pm 136)$ fs obtained by averaging the fit results of the Ar^{2+} and Ar^{+} channel (see Fig. 8.14). The yield obtained by employing the simulation with an input of $\tau_{sim} = 530$ fs is given by the green line. The total lifetime $\tau_{LZ} = 430$ fs calculated with Landau-Zener probabilities is depicted by the blue curve. The magenta curve shows an error function whose width marks the temporal resolution of the experiment (see Sec. 6.2.3).

The underestimation by the theoretical value could have several reasons. According to Ref. [80] and as already pointed out in Sec.2.4, the calculation of the intermediate $Ar^{+} - Ar^{+*}$ states is challenging. Therefore, the number, the positions and the coupling strengths of the crossings might change if one would go to a higher level computational method.

8.2.2 Probe of Frustrated Triple Ionization

In the single XUV pulse measurement at high FEL intensity (see Sec. 8.1.2), it is proposed that the relaxation channel of frustrated triple ionization causes a high-KER contribution (~ 7.2 eV) in the $Ar^{+} + Ar^{+}$ coincidence channel. By making use of a delayed IR-pulse, this relaxation channel can be probed.

Pump-Probe Scheme

First, the XUV-pump (see Fig. 8.18, purple arrow) prepares $Ar^+(3p^{-2}nl)-Ar^+(3p^{-1})$ Rydberg states, which are located just below the triple ionization threshold[68]:

$$\text{Pump}: Ar - Ar \xrightarrow{3\times XUV} Ar^+(3p^{-2}nl) - Ar^+(3p^{-1}). \tag{8.18}$$

After the excitation, the IR-probe pulse (see Fig. 8.18, red arrows) ionizes the nl Rydberg electron and the final triply ionized $Ar^{2+}(3p^{-2}) + Ar^+(3p^{-1})$ states are reached:

$$\text{Probe}: Ar^+(3p^{-2}nl) - Ar^+(3p^{-1}) \xrightarrow{IR} Ar^{2+}(3p^{-2}) - Ar^+(3p^{-1}) + e^-_{nl}. \tag{8.19}$$

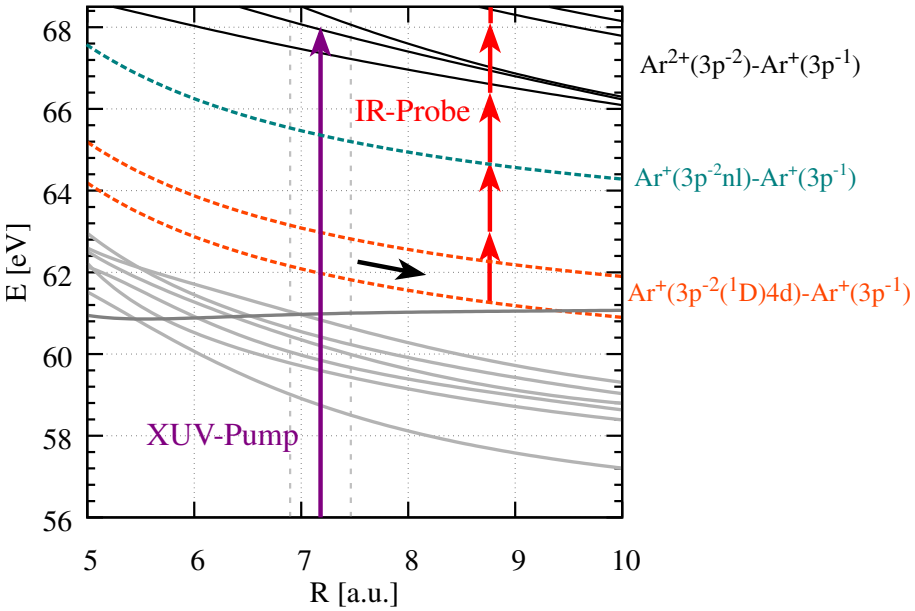

Figure 8.17: PECs of the argon dimer in the energy range $56 - 68.5$ eV. The dashed curves representing the Rydberg states (turquois: $Ar^+(3p^{-2}nl) - Ar^+(3p^{-1})$, orange: $Ar^+(3p^{-2}(^1D)4d\,^2S) - Ar^+(3p^{-1})$) are not calculated ones and should be understood as place holders to demonstrate the pump-probe scheme. The vertical purple arrow depicts the XUV excitation within the FC region. The IR-probe is depicted by the vertical red arrows. The final $Ar^{2+}(3p^{-2}) - Ar^+(3p^{-1})$ states are drawn in black. The grey curves are the $Ar^+(3p^{-2}nl) - Ar^+(3p^{-1})$ states [177], which are relevant for the discussed CT process (see Sec. 8.2.1).

As the final KER ~ 7.2 eV of the dissociating $Ar^+(3p^{-2}nl) - Ar^+(3p^{-1})$ states (see Fig. 8.3 (a)) is within the KER of the $Ar^{2+} + Ar^+$ channel (see Fig. 8.3 (b)), the IR-probe does not measurably change the final $Ar^{2+} + Ar^+$ KER in the pump-probe

[68] The step-by-step XUV multi-photon ionization/excitation pathway is discussed in detail in Sec. 8.1.2.

experiment. However, the yield of $Ar^+ + Ar^+$ ions with KERs $> 6\,eV$ will drop with the IR pulse being present.

KER vs. Delay of Ar^++Ar^+ Ions

Fig. 8.18 shows the KER of $Ar^+ + Ar^+$ ions as a function of the delay in the range $6.4 - 10.0\,eV$. For negative delays, i.e., the IR pulse is early with respect to the XUV pulse, the KER component of the frustrated triple ionization ($\sim 7.2\,eV$) is present. For positive delays, however, this contribution vanishes. The projection onto the delay axis (d) confirms this finding. The yield drop persists over the entire positive delay range and thereby reflects lifetimes of $> 4\,ps$ for the $Ar^+(3p^{-2}nl) - Ar^+(3p^{-1})$ Rydberg states.

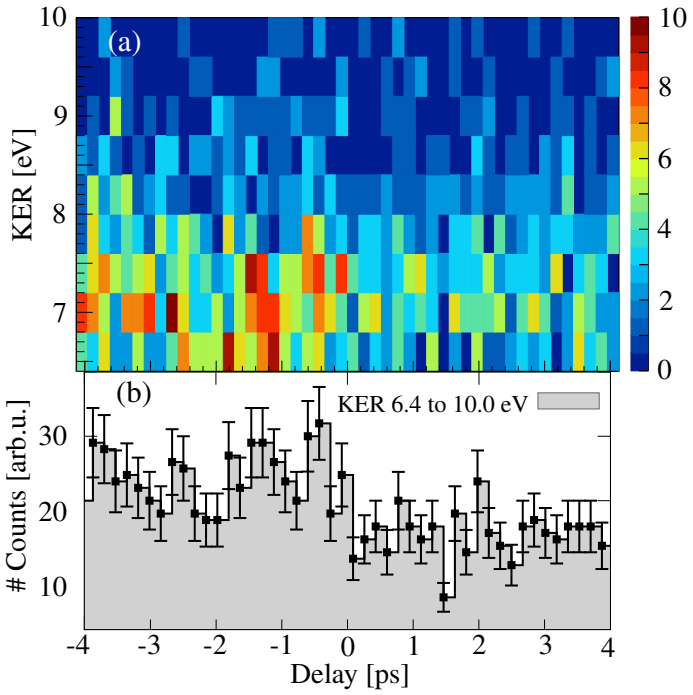

Figure 8.18: (a) KER vs. delay of Ar^++Ar^+ ions in the range 6.4 to 10.0 eV. (b) Projection of (a) onto the delay axis.

8.2.3 Further Channels

The delay-dependent analysis of the KER of Coulomb-exploded Ar^{2+} ions (see Fig. 8.8) reveals a constant KER contribution of $\sim 4.5\,eV$ for the entire negative delay range, i.e., the IR pulse arrives early with respect to the XUV pulse. For positive delays, this contribution vanishes. It also shows up in the KER of Coulomb-exploded Ar^{2+} ions in the single XUV pulse data (not shown). Hence, it can be concluded that it stems from a fragmentation into $Ar^{2+} + Ar$, which is induced by XUV excitation.

As briefly mentioned in Sec. 8.1.2, alternatively to $Ar^+(3p^{-2}nl) - Ar^+(3p^{-1})$, also Rydberg states with an $Ar^{2+}(3p^{-2}) - Ar(3p^{-1}nl)$ character can be excited:

$$\text{Pump} : \text{Ar} - \text{Ar} \xrightarrow{3\times\text{XUV}} \text{Ar}^{2+}(3p^{-2}) - \text{Ar}(3p^{-1}nl). \tag{8.20}$$

Assuming an excitation near R_{eq}, the KER of the dissociated $Ar^{2+}(3p^{-2})$+$Ar(3p^{-1}nl)$ fragments is expected to be close to KER = 3.8 eV of $Ar^+(3p^{-1}) + Ar^+(3p^{-1})$ ions as the fragments have the same sum charge. However, the highly-excited nl Rydberg electron alters the shielding of the nuclear charges (see Fig. 8.5), which can lead to higher KERs of the $Ar^{2+}(3p^{-2}) + Ar(3p^{-1}nl)$ fragments.
The $Ar^{2+}(3p^{-2}) - Ar(3p^{-1}nl)$ states are located just below the triple ionization threshold and the IR-probe ionizes the nl electron of the neutral site:

$$\text{Probe} : \text{Ar}^{2+}(3p^{-2}) - \text{Ar}(3p^{-1}nl) \xrightarrow{\text{IR}} \text{Ar}^{2+}(3p^{-2}) + \text{Ar}^+(3p^{-1}) + e^-_{nl}. \tag{8.21}$$

In the following, it is discussed, if this channel has an influence on the determination of the CT lifetime. In order to contribute to the $Ar^{2+} + Ar^+$ yield in the KER range $7.0 - 8.4$ eV, which is used to determine the CT lifetime (see Sec. 8.2.1), the probing of the $Ar^{2+}(3p^{-2}) - Ar(3p^{-1}nl)$ states must occur in the vicinity of the FC region. However, the dissociation time is fast ($100 - 150$ fs) and the wave packets on the $Ar^{2+}(3p^{-2}) - Ar(3p^{-1}nl)$ states quickly leave the FC region after excitation. For larger $R > R_{\text{eq}}$, the IR pulse already probes dissociating $Ar^{2+}(3p^{-2}) - Ar(3p^{-1}nl)$ ions, which consequently results in KERs outside the critical KER condition ($7.0 - 8.4$ eV). Hence, this channel does not influence the extraction of the CT lifetime via the $Ar^{2+} + Ar^+$ channel.
Another channel appears in the delay-dependent KER of Coulomb-exploded Ar^+ ions at a KER of ~ 1.2 eV (see Fig. 8.9). The signal is weak for the negative delay range, but is more pronounced for the positive delay range. The signal does not show a delay-dependence and it is not present in the single XUV pulse measurement. Hence, it must be induced exclusively by the IR pulse. The low KER of just ~ 1.2. eV suggests a pathway via a dissociation where one site of the dimer stays neutral:

$$\text{Ar} - \text{Ar} \xrightarrow{\text{IR}} \text{Ar}^+(3p^{-1}) + \text{Ar} + e^-. \tag{8.22}$$

For the negative delay range, the signal is weaker since late-arriving XUV pulse further ionizes the dissociating dimer to higher charge states. For the positive delay range, the XUV precedes the IR pulse and thus cannot post-ionize, which leads to an enhancement of the signal. PECs of $Ar^+ - Ar$ and $Ar^+ - Ar^*$ character, start at a potential energy of ~ 14 eV and are reachable at the present IR laser intensity $I_{\text{IR}} = 1 - 2 \times 10^{14}\,\text{W/cm}^2$ (see Sec. 6.2.1). The KER of this channel is too low to have an influence on the CT lifetime determination via the $Ar^+ + Ar^+$ yield.

8.3 Higher Charge States

Up to now, final fragments of multiple charge $q_1 \cdot q_2 \leq 2$ are discussed. However, at the high FEL intensity setting (see Sec. 8.1.2), also coincidences including higher multiple charges $q_1 \cdot q_2 \leq 9$ are measured in a single XUV pulse experiment.

KER Distribution of $Ar^{3+} + Ar^{+}$ Ions

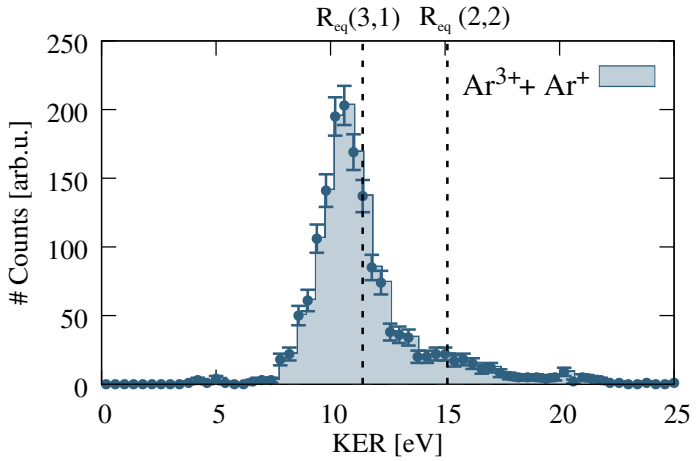

Figure 8.19: KER of $Ar^{3+} + Ar^{+}$ ions. The vertical dashed lines mark the KERs expected for fragmentation into $Ar^{3+} + Ar^{+}$ and $Ar^{2+} + Ar^{2+}$ ions at R_{eq}, respectively.

The KER distribution of $Ar^{3+} + Ar^{+}$ is discussed in Fig. 8.19. It shows a sharp peak at KER $\sim$10.5 eV, which is smaller than the expected KER for a Coulomb explosion of $Ar^{3+} + Ar^{+}$ at R_{eq}, i.e., KER $= (3 \cdot 1)/R_{eq} = 11.4$ eV. The KER difference of ΔKER $= 0.9$ eV towards lower KERs translates into a mean internuclear distance $R = R_{eq} + 0.6$ a.u. $= 7.8$ a.u. at the instant of the fragmentation. This implies nuclear motion, during the multiple steps of the ionization. Assuming a sequential ionization[69] gives the following multi-photon ionization cascade:

$$Ar - Ar \xrightarrow{1\times XUV} Ar^{+}(3p^{-1}) - Ar + e^{-}, \tag{8.23}$$

$$Ar^{+}(3p^{-1}) - Ar \xrightarrow{1\times XUV} Ar^{+}(3p^{-1}) - Ar^{+}(3p^{-1}) + e^{-}, \tag{8.24}$$

$$Ar^{+}(3p^{-1}) - Ar^{+}(3p^{-1}) \xrightarrow{2\times XUV} Ar^{2+}(3p^{-2}) - Ar^{+}(3p^{-1}) + e^{-}, \tag{8.25}$$

$$Ar^{2+}(3p^{-2}) - Ar^{+}(3p^{-1}) \xrightarrow{2\times XUV} Ar^{3+}(3p^{-3}) - Ar^{+}(3p^{-1}) + e^{-}. \tag{8.26}$$

Hence, within the FEL pulse duration of 50 fs, 6 photons need to be absorbed. All intermediate states listed above are of repulsive character and nuclear motion, i.e., dissociation to $R > R_{eq}$, can happen along the ionization path.

[69] The analysis of the atomic Ar^{n+} ion yields in Sec. 6.1.3 showed sequential multi-photon ionization to be dominant at the present FEL intensities.

In Sec. 8.1 and 8.2 it is shown that intermediate excited states play an important role in the relaxation dynamics of the dimer. Therefore, an ionization path starting from the $Ar^{2+}(3s^{-1}3p^{-1}\,(+3p^{-3}(^2D)3d)\,^1P) - Ar$ state is considered in the following. The direct absorption of 2 photons at the already ionized site results in one-site triply ionized states:

$$Ar^{2+}(3s^{-1}3p^{-1}\,(+3p^{-3}(^2D)3d)\,^1P) - Ar \xrightarrow{2\times XUV} Ar^{3+}(3s^{-1}3p^{-2}\,(+3p^{-4}3d)) - Ar + e^-. \tag{8.27}$$

These states are lying in the energy range $98-117\,\mathrm{eV}$ and are known to be subject to ICD and ETMD (see Sec. 2.4) [227, 286][70]. The decay via ICD results in $Ar^{3+} + Ar^+$ fragments:

$$Ar^{3+}(3s^{-1}3p^{-2}\,(+3p^{-4}3d)) - Ar \xrightarrow{ICD} Ar^{3+}(3p^{-3}) + Ar^+(3p^{-1}) + e^-_{ICD}. \tag{8.28}$$

Assuming ICD being fast, i.e. taking place in the vicinity of R_{eq}, and without measuring the ICD electron in coincidence to $Ar^{3+} + Ar^+$, one cannot undoubtedly discriminate the ICD from the direct channel by just the KER. In Ref. [227], the ICD electron is measured in coincidence and the authors conclude that ICD contributes strongly to the $Ar^{3+} + Ar^+$ channel. In contrast to the present experiment, however, the $Ar^{3+}(3s^{-1}3p^{-2}\,(+3p^{-4}3d)) - Ar$ states are populated after inner-valence ionization followed by a fast Auger cascade [227]. Therefore, the direct multi-photon ionization channel is not existing. Yet, in the present experiment, the shift of the center of the KER distribution towards lower KERs (see Fig. 8.19) suggests direct multi-photon ionization to be the dominant channel.
Besides the peak at $\sim 10.5\,\mathrm{eV}$, the KER distribution of $Ar^{3+} + Ar^+$ ions shows an extension towards higher KERs with a maximum at $\sim 15\,\mathrm{eV}$. It matches the KER of $Ar^{2+} + Ar^{2+}$ at R_{eq}, i.e., $\mathrm{KER} = (2\cdot 2)/R_{eq} = 15.1\,\mathrm{eV}$. This suspects this contribution to arise an $Ar^{2+} + Ar^{2+}$ precursor state. The origin of this channel is unclear.

KER Distribution of $Ar^{2+} + Ar^{2+}$ Ions

The KER distribution of $Ar^{2+} + Ar^{2+}$ ions is plotted in Fig. 8.20. It peaks at $\sim 13.8\,\mathrm{eV}$, which means a shift of $\Delta E = 1.3\,\mathrm{eV}$ towards lower KERs compared to the fragmentation at R_{eq}. In the sequential multi-photon ionization picture, the shift is explained by nuclear dynamics accompanying the ionization path. The first three ionization steps are the same as in the $Ar^{3+} + Ar^+$ channel (see Eqs. 8.23, 8.24 and 8.25). However, the fourth ionization step is different (see Eq. 8.26):

$$Ar^{2+}(3p^{-2}) - Ar^+(3p^{-1}) \xrightarrow{2\times XUV} Ar^{2+}(3p^{-2}) - Ar^{2+}(3p^{-2}) + e^-. \tag{8.29}$$

[70] A comprehensive summary and discussion of all relevant states for ICD and ETMD in the energy range $98 - 117\,\mathrm{eV}$ can be found in Ref. [227].

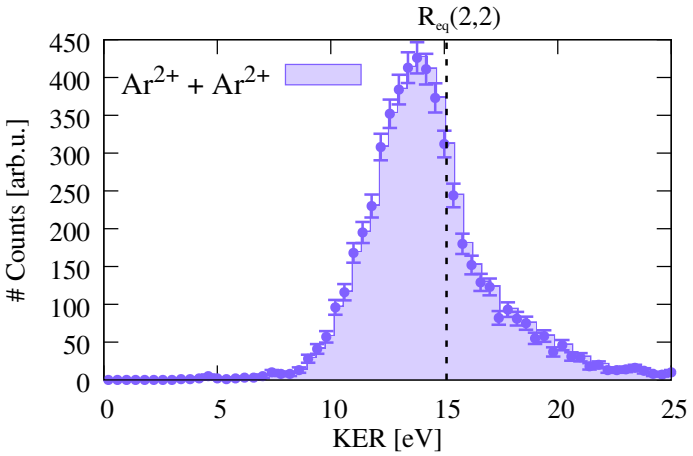

Figure 8.20: KER of $Ar^{2+} + Ar^{2+}$ ions. The vertical dashed line marks the KER expected for fragmentation into $Ar^{2+} + Ar^{2+}$ ions at R_{eq}.

The KER of $Ar^{2+} + Ar^{2+}$ ions will also include contributions from ETMD, because in contrast to ICD, the decay of respective $Ar^{3+}(3s^{-1}3p^{-2}\,(+3p^{-4}3d)) - Ar$ states via ETMD produces $Ar^{2+} + Ar^{2+}$ fragments [227]:

$$Ar^{3+}(3s^{-1}3p^{-2}\,(+3p^{-4}3d)) - Ar \xrightarrow{\text{ETMD}} Ar^{2+}(3p^{-2}) + Ar^{2+}(3p^{-2}) + e^{-}_{\text{ETMD}}. \quad (8.30)$$

The energetically allowed $Ar^{3+}(3s^{-1}3p^{-2}\,(+3p^{-4}3d)) - Ar$ states being subject to ETMD are within the energy region $98 - 112\,\text{eV}$ [227].
The KER distribution of $Ar^{2+} + Ar^{2+}$ ions shows a shoulder towards higher KERs, which could be a signature of an ETMD contribution peaking at $\sim 15\,\text{eV}$, i.e., the KER being expected for fragmentation at R_{eq}.
The total number of $Ar^{2+}+Ar^{2+}$ coincidences is higher than that of $Ar^{3+}+Ar^{+}$. This is in contrast to experiments, which study the dimer using inner-valence ionization followed by Auger decay [227] or electron-impact ionization [286], where the $Ar^{3+} + Ar^{+}$ dominates over the $Ar^{2+} + Ar^{2+}$. Due to the different ionization and excitation scheme compared to the present experiment, both studies claim to be exclusively sensitive to ICD and ETMD. The different branching ratios of the two channels in the present experiment constrains the existences of an ionization and relaxation pathway different to ICD and ETMD, namely direct multi-photon ionization.

KER Distribution of $Ar^{3+} + Ar^{2+}$ Ions

The KER of the $Ar^{3+} + Ar^{2+}$ channel is depicted in Fig. 8.21. Similar to $Ar^{3+} + Ar^{+}$ and $Ar^{2+} + Ar^{2+}$, the center of the distribution is shifted towards lower KERs, indicating dissociation during the sequential multi-photon ionization. However, the shift of $\Delta\text{KER} \approx 3.5\,\text{eV}$ with respect to the expected KER for fragmentation at R_{eq} is more pronounced. The increasing deviation from a simple Coulomb explosion model with increasing charge is further discussed in Fig. 8.23.

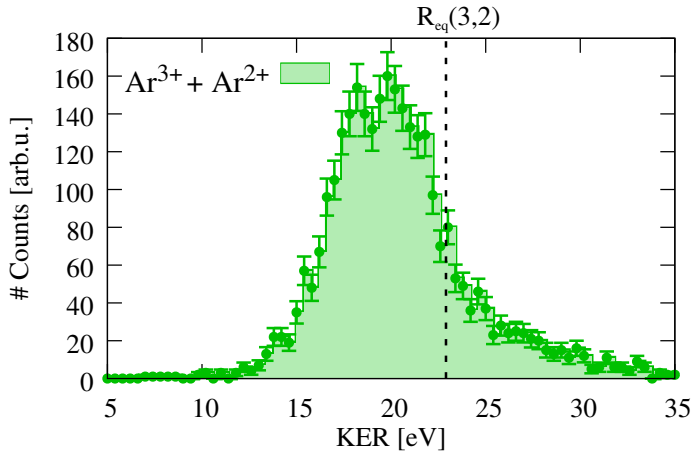

Figure 8.21: KER of $Ar^{3+} + Ar^{2+}$ ions. The vertical dashed line marks the KER expected for fragmentation into $Ar^{3+} + Ar^{2+}$ ions at R_{eq}.

In addition to the 6 photons needed to produce $Ar^{3+} + Ar^{+}$ (see Eqs. 8.23 through 8.26) and $Ar^{2+} + Ar^{2+}$ (see Eq. 8.29), 2 more photons need to be absorbed to obtain the charge state of $Ar^{3+} + Ar^{2+}$:

$$Ar^{3+}(3p^{-3}) - Ar^{+}(3p^{-1}) \xrightarrow{2\times XUV} Ar^{3+}(3p^{-3}) - Ar^{2+}(3p^{-2}) + e^{-}, \tag{8.31}$$

$$Ar^{2+}(3p^{-2}) - Ar^{2+}(3p^{-2}) \xrightarrow{2\times XUV} Ar^{3+}(3p^{-3}) - Ar^{2+}(3p^{-2}) + e^{-}. \tag{8.32}$$

On closer examination, the $Ar^{3+} + Ar^{2+}$ KER distribution reveals two peaks: one at $\sim 20.2\,eV$ and another at $\sim 18.4\,eV$. This observation can be explained by the two different precursor states (Eq. 8.31 and Eq. 8.32, respectively) whose PECs have different slopes. The peak at higher KER ($\sim 20.2\,eV$) is attributed to the $Ar^{2+}(3p^{-2}) - Ar^{2+}(3p^{-2})$ precursor as the slope of the $Ar^{2+}(3p^{-2}) - Ar^{2+}(3p^{-2})$ PECs is steeper [227] and more KER is gained during the dissociation of this intermediate step. Accordingly, the lower KER peak ($\sim 18.4\,eV$) is assigned to the flatter PECs of $Ar^{3+}(3p^{-3}) - Ar^{+}(3p^{-1})$ precursor states.

KER Distribution of $Ar^{3+} + Ar^{3+}$ Ions

The KER of the highest charged channel $Ar^{3+} + Ar^{3+}$ is shown in Fig. 8.22. The distribution is broader compared to the channels with lower sum charge. This is explained by the spatial width of the initial ground-state wave packet, which by the ionization is projected onto the final PEC. The ground state width is directly reflected by the measured KER distribution and the steeper the final potential curve, the broader will be the finally measured KER [236]. The center of the distribution peaks at $\sim 27\,eV$ and deviates about 7 eV from the KER predicted for fragmentation at R_{eq}. This is further discussed in Fig. 8.23.

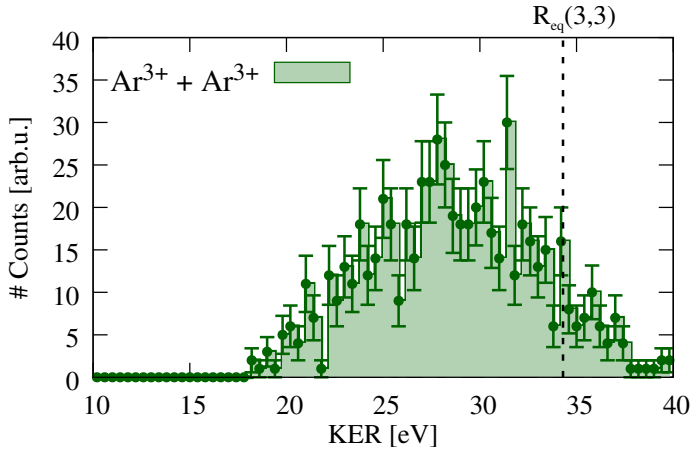

Figure 8.22: KER of $Ar^{3+} + Ar^{3+}$ ions. The vertical dashed line marks the KER expected for fragmentation into $Ar^{3+} + Ar^{3+}$ ions at R_{eq}.

Coulomb Explosion Model

In analogy to Ref. [236], a comparison between the measured KER and that expected from a Coulomb explosion at the equilibrium internuclear distance R_{eq}, i.e. KER = $(q_1 \cdot q_2)/R_{eq}$, is summarized in Fig. 8.23. Notably, the deviation gets worse with increasing charge state. To reach higher charge states, more and more photons need to be absorbed and more intermediate states are involved. Moreover, with higher multiple charge $q_1 \cdot q_2$, also the PECs get steeper and the Coulomb repulsion between highly-charged fragments is stronger. Thus, they will move further apart before being ionized by the next photon(s). Consequently, the deviation from the model is more pronounced for higher charged fragments.

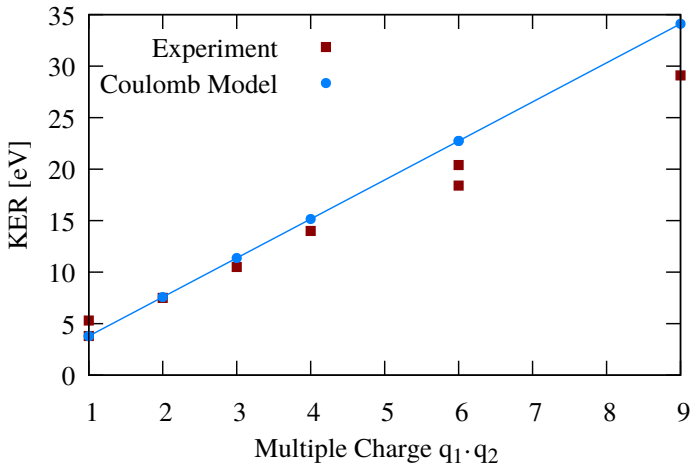

Figure 8.23: Comparison between the measured KERs (red squares) and the KERs predicted by Coulomb explosion at R_{eq} (blue dots and line). The x-axis is in units of multiple charge $q_1 \cdot q_2$ of the fragments.

9 In-Line XUV Split-Delay Optics for the REMI at FLASH2

In order to study the light-induced dynamics of atomic and molecular systems, XUV-pump XUV-probe experiments can be advantageous compared to pump-probe schemes using strong optical laser pulses. In the pump step, the absorption of a single XUV photon is typically sufficient to excite or ionize valence and inner-valence electronic states. The temporal evolution of the system is then probed by a delayed pulse of the same photon energy. The absorption of a single photon in the pump and in the probe step means only a small perturbation to the system under investigation. For XUV radiation and nowadays available intensities, the ponderomotive potential is small compared to the excitation and ionization energies (see Sec. 2.1.2), which is not the case in pump-probe experiments using strong optical laser pulses. Here, the system is strongly influenced and modified by the measurement itself. This leads to field-induced shifts of atomic levels [73] or dressed states in molecules [206]. Amongst other things, this implies a more complex interpretation of the experimental results and a more elaborated theoretical treatment [152].
In the last decades, the developement of lab-based high-harmonic XUV and soft X-ray light-sources [3] results in great progress in various scientific fields [40, 92, 194, 273]. To date, however, high harmonic sources suffer from pulse energies, which are in the order of less than 5 % of the average pulse energies delivered by FELs. The authors of Ref. [223] for example report a pulse energy of $E_{\text{pulse}} \approx 2\,\mu\text{J}$ of their HHG-source, whereas the XUV FELs FERMI and FLASH routinely deliver pulses of $E_{\text{pulse}} = 10 - 200\,\mu\text{J}$ [5] and $E_{\text{pulse}} = 1 - 500\,\mu\text{J}$ (see Tab. 3.1), respectively. Up to now, this discrepancy excludes HHG-sources from being well-suited for XUV-pump XUV-probe experiments. In contrast, the high pulse energies of FELs allow to use simple geometrical schemes to create two separated XUV pulses. For example, a pulse can be split into two replicas by a mirror which is cut into two halves. By moving one mirror half with respect to the other, a path difference can be established between the two pulses.
In the course of setting up a REMI endstation at FLASH2 and to overcome drawbacks of a previous setup, an in-line XUV split-delay and focussing optics is designed (see Sec. 9.2 and 9.3), implemented (see Sec. 9.4) and commissioned (see Sec. 9.6) in the framework of this thesis.

9.1 Previous Design

A simple way to divide a pulse by means of a split-mirror is to use a back-reflecting geometry under normal incidence. A relative displacement Δx of the mirror halves results in a time delay of $t_d = 2\Delta x/c$ with c being the speed of light. Following this back-reflecting approach, a collaboration between the Max-Planck-Institute for Nuclear Physics Heidelberg and the Max-Planck-Institute for Quantum Optics Garching developed a dedicated XUV split-delay optics for pump-probe experiments at FELs, which can be combined with a REMI (see Ch. 4) [102]. Using this setup, several high-ranked time-resolved studies were conducted at FLASH [121, 122, 124, 237]. The back-reflecting setup uses an one inch concave multilayer mirror, which is horizontally cut into two equal halves. The FEL beam hits the mirror halves at normal incidence, is back-reflected and focussed into the gas jet of the REMI. A top view of the geometry is schematically shown in Fig. 9.1 (a). By moving the lower mirror half with respect to the upper, a temporal delay between the split pulses can be introduced. The mirror has a focal length of 50 cm and the focal diameter at the interaction spot is estimated to $\sim 30\,\mu$m.

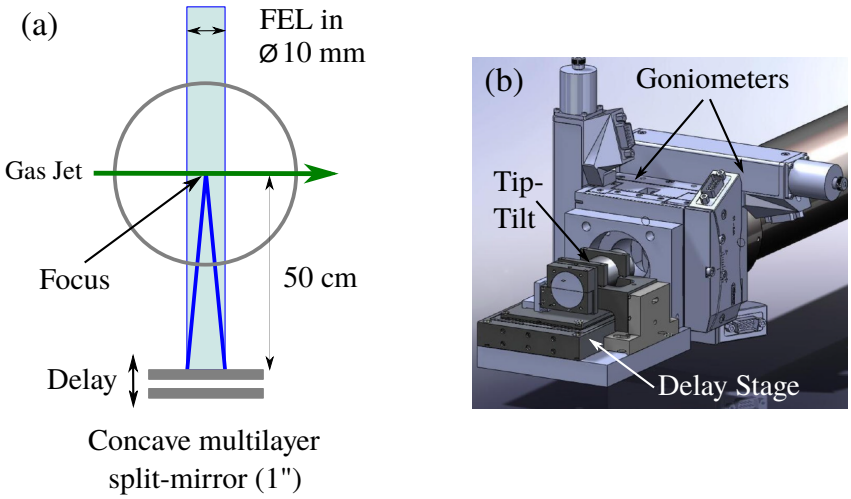

Figure 9.1: (a) Sketch of the old back-reflecting setup viewed from the top. (b) 3D CAD technical drawing of the old setup. Taken from Ref. [102].

Multilayer mirrors are made up of a stack of alternating nanometer layers of materials with different refractive indexes, e.g., Mo/Si [255]. They work as follows: beams, which are partly reflected from each interface, interfere constructively with each other in the outgoing path. This implies that layer materials and thicknesses have to be matched to the specific wavelength and appropriate reflectivity is only assured for a small bandwidth. Due to the high absorption of most materials in the XUV spectral range under normal incidence, the reflectivity of multilayer mirrors is usually not more than 70 %.

In the old back-reflecting setup, the lower mirror half is mounted on a nanometer-precision linear piezo stage[71] (see Fig. 9.1 (b)), which is movable in beam direction over a range of $\pm 400\,\mu m$. This corresponds to $\pm 1300\,fs$ in time delay and the manufacturer states the step precision to be better than 1 fs. The upper mirror is mounted on a tip-tilt piezo platform[72] (see Fig. 9.1 (b)) with 0.1 µrad angular resolution to spatially overlap the foci of the two mirror halves at the interaction point. The piezo stage and the tip-tilt platform are attached to two goniometers[73] (see Fig. 9.1 (b)), which allow rotations around the horizontal and vertical axis to hit the REMI gas jet in the center. To tune the focal distance and to hit the mirror centrally, the goniometers are supported by a triaxial xyz-manipulator. The geometry under 180° back-reflection angle makes this setup robust in terms of alignment and operation. However, since the back-reflecting split-delay optics was put into operation in 2009, a couple of drawbacks were recognized.
An important advantage of FELs is their tunable wavelength (see Ch. 3). As already mentioned, multilayer mirrors can only be manufactured for a very narrow wavelength range. Consequently, the corresponding mirror has to be newly manufactured for each experiment as XUV multilayer mirrors cannot be bought off the shelf. This is costly and also time-consuming. Furthermore, one has to install and precisely align the mirror halves for each experiment. This is a delicate and time-consuming operation. The vacuum chamber containing the split-delay optics has to be vented and after re-installation of the optics baked-out to 100 °C for at least 24 hours in order to reach UHV vacuum conditions of 10^{-10} mbar.
High vacuum demands for the mirror chamber are required, because the split-mirror has to be put as close as possible to the interaction region to most tightly focus the incoming FEL beam. To maintain vacuum conditions of $\leq 10^{-11}$ mbar in the REMI main chamber, a differential pumping tube between the mirror and the REMI main chamber is needed. In order to reach highest intensities in the foci, the diameter of the incoming FEL beam has to be large to fully illuminate the split-mirror. A large diameter (maximum 10 mm) conflicts with the need for small diameters of the differential pumping tube. Scattering of the incoming and back-reflected FEL beam at the pumping tube as well as at the horizontal edges of the split-mirror are major sources of stray light photons, which are measured as background by the REMI detectors (see Fig. 9.2). Especially for high pulse energies, the detectors run into saturation just due to stray light photons. This limits the possible intensity range for pump-probe experiments to low values.

[71] Physik Instrumente (PI) P-628 piezo linear stage.
[72] Physik Instrumente (PI) S-325 piezo Z/tip/tilt platform.
[73] PI miCos WT-85 and WT-100 motorized precision goniometers.

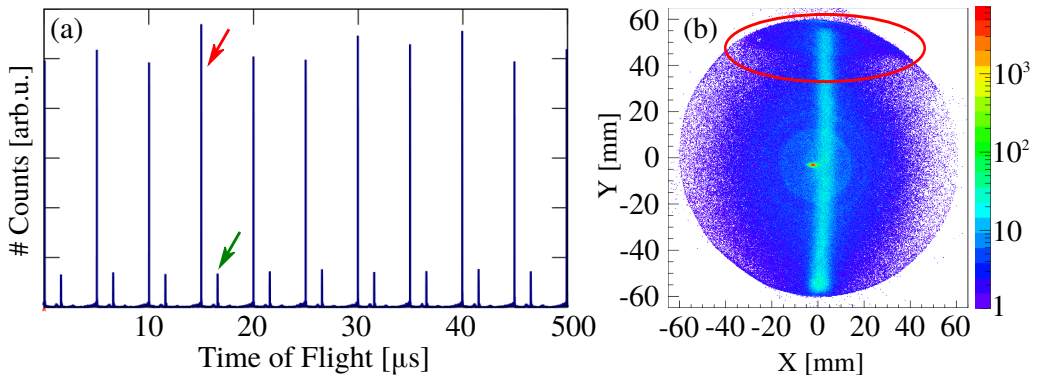

Figure 9.2: (a) Example of an ion TOF raw spectrum recorded for 10 minibunches with the previous back-reflecting split-delay setup. The minibunch distance is 5 µs. The highest peaks in the spectrum (red arrow) are due to stray light, which instantaneously arrives at the detector at the beginning of each minibunch. The green arrow marks a ~ 6 times smaller ion peak from the target. (b) Exemplary raw position image of the ion detector recorded with the old setup. The red ellipse at the top marks background events arising from scattering at the differential pumping tube. The trace of background events formed by the incoming and back-reflected FEL is also visible as a strong vertical line.

Due to the lack of space, the entrance hole and part of the differential pumping tube are located within the spectrometer rings (see Sec. 4.4). If photons hit the tube walls, the apertures, the spectrometer rings, the chamber walls or the split-mirror, they are not just scattered, but also absorbed by the material, This causes the emittance of photoelectrons[74]. As soon as these secondary electrons enter the field region of the spectrometer, they are directed onto the electron detector and shows up as a further source of background.
Due to the normal incidence geometry, the FEL beam has to pass the spectrometer volume twice. This is a disadvantage, because at usual XUV photon energies, each photon has enough energy to ionize any atom or molecule of the residual gas (see Sec. 4.7). This means that the ion and electron background further increases due to ionization of the residual gas. Electrons originating from different atoms or molecules have very similar time of flights due to their unique mass. Because of this, the sorting of events gets worse for multi-hit operation and the information to reconstruct momenta and coincidences get lost.
As a consequence of the pulse energy dependent increase of scattered photons and the correspondingly increased number of direct and secondary photoelectrons, it was not possible to record time-dependent electron spectra with the back-reflecting

[74] Average work functions of some materials present in the experimental setup. Iron: $W_e = 4.7\,\text{eV}$, copper $W_e = 4.8\,\text{eV}$, silicon $W_e = 4.8\,\text{eV}$, molybdenum $W_e = 4.6\,\text{eV}$ [222]. Work functions depend on the specific crystal structure.

split-delay optics. The measurement of electrons in coincidence with ions is however important to assign electronic states.
A further drawback of a back-reflecting geometry is the exclusion of reusing the FEL beam in a parasitic experiment located downstream of the REMI.

9.2 New Design

The basic concept of the new setup is to split and focus the beam already before it enters the REMI. This in-line configuration has several advantages, but comes along with technical challenges. The underlying geometry and the major components of the setup are depicted in Fig. 9.3.

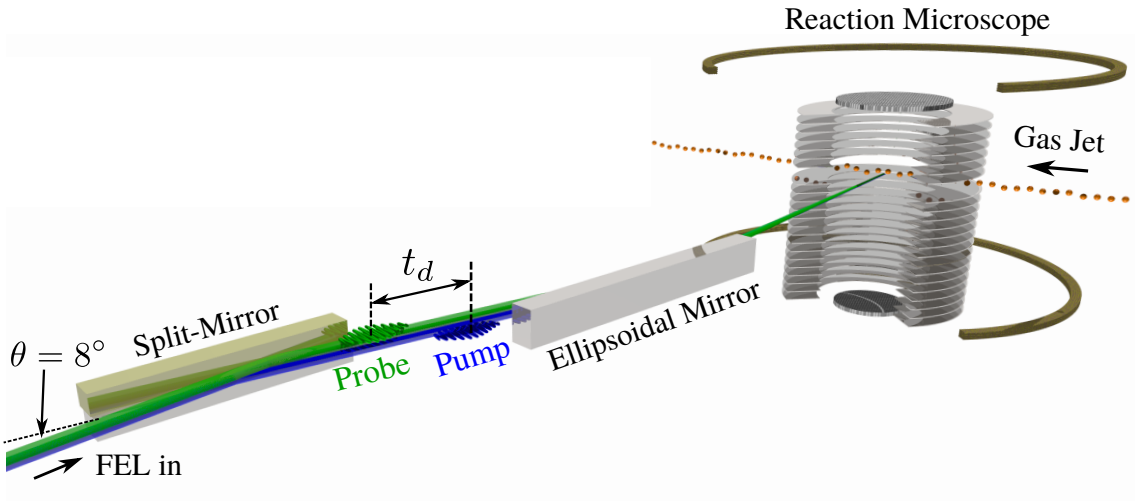

Figure 9.3: Design of the in-line XUV split-delay optics. Explanations in the text.

The FEL beam approaches from the left and first hits the split-mirror under a grazing angle of $\theta = 8°$. The split-mirror is a plane mirror, which is horizontally cut into two coextensive halves. The upper half is movable and can be translated along the mirror normal axis back and forth. Thus, a path difference can be introduced between the upper beam (green) and the lower beam (blue). In terms of pulses, an incoming FEL pulse is split into two replicas and the path difference translates into a temporal delay t_d between the pump (blue) and the probe (green) pulse. After splitting, the two beams are focussed by an ellipsoidal mirror into the gas jet of the REMI and the FEL beam passes the spectrometer only once.
In order to deflect the FEL beam in a broad range of photon energies, the use of total external reflection is an established method in X-ray and XUV optics. It occurs when mirrors are operated under grazing incidence angles [11, Ch. 3.4]. The critical incidence angle α_{crit}, below which total external reflection happens, is calculated according to Snell's law $\frac{\sin(\alpha_1)}{\sin(\alpha_2)} = \frac{n_2}{n_1}$. The angles α_1 and α_2 are the angles between

the incoming and outgoing beam with the mirror normal, respectively. The refractive indices n_1 and n_2 refer to the medium the beam enters from and the mirror material, respectively. The index n_1 is equal to one because the beam propagates in vacuum. In the present case, the mirror is coated with carbon, which has a refractive index of $n_2 = 0.9175$ [93] for a typical wavelength of $\lambda = 20.6\,\mathrm{nm}$ ($\hbar\omega = 60\,\mathrm{eV}$). Total external reflection happens for $\alpha_2 \leq 90°$ and the critical incidence angle of the example is $\alpha_2 = \alpha_{\mathrm{crit}} = \arcsin(n_2) = 67°$, which is equal to a critical grazing angle of $\theta_{\mathrm{crit}} = 90° - \alpha_{\mathrm{crit}} = 33°$. The grazing angle of $\theta = 8°$ in the present setup is chosen well below the limit of total external reflection and guarantees high reflectivity over a broad photon energy range from $30 - 150\,\mathrm{eV}$ (see Fig. 9.15).
At a grazing angle of $\theta = 8°$, the incoming FEL beam of diameter $d = 10\,\mathrm{mm}$ illuminates an ellipse with a horizontal extension of $l = d/\sin(8°) = 71.9\,\mathrm{mm}$. To account for this enlargement, the mirrors have to be elongated in the horizontal dimension. One half of the split mirror is 120 mm long and 10.5 mm high. The ellipsoidal mirror has a length of 180 mm and a height of 30 mm.
The source point of the FEL radiation is located within the first undulator, which is $\sim 85\,\mathrm{m}$ away from the interaction point of the experiment. To achieve tight focussing, the focal length is set to $f = 1\,\mathrm{m}$, i.e., much smaller compared to source distance. In this case, an ellipsoidal mirror is well-suited, because it images a point-like source directly into a point-like focus (see Fig. 9.14). Optimal focussing will be only obtained, if the ellipsoidal mirror is hit under the correct angle. Therefore, µm-precise kinematics are required to position the ellipsoidal as well as the split-mirror. In Sec. 9.4.1 and 9.4.3, information about the mirror kinematics and the quality of the mirrors are given.
Concerning the pump-probe capability of the new setup, the delay is scanned by moving the upper mirror half along the mirror normal axis with respect to the lower mirror half. The distance covered is called hub h and the path difference Δx can be computed geometrically (see Fig. 9.4):

$$\Delta x = a - b = a(1 - \cos(2\theta)) = \frac{h}{\sin(\theta)}(1 - \cos(2\theta)) = 2h\,\sin(\theta). \tag{9.1}$$

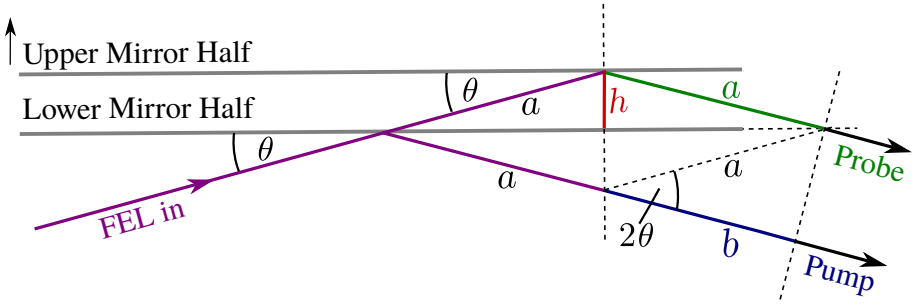

Figure 9.4: Top view sketch to illustrate the calculation of the path difference $\Delta x = b - a$.

The setup allows hub values of $h = \pm 3\,\mathrm{mm}$, which translate into a maximum delay range of $t_d = \pm 2.7\,\mathrm{ps}$ for a grazing angle of $\theta = 8°$. The minimum hub step $\Delta h = 1\,\mathrm{nm}$ is defined by the minimum step of the piezo kinematics which drives the upper mirror half. In order to spatially overlap the foci to a precision $\leq 1\,\mu\mathrm{m}$ at the focal distance of 1 m for all delay values, the upper mirror half is rotatable around the vertical (tilt) and horizontal (tip) axis[75]. To account for the translational and rotational degrees of freedom, a custom-made mirror kinematics based on piezo actuators is deployed (see Sec. 9.4.2).

9.3 Simulations

After having fixed the conceptual design, the beam path is simulated using ray tracing [260]. For this purpose, the open source software *POV-Ray*[76] is used. The simulation relies on ray optics and is a tool to check the general functionality and dimensioning of the new split-delay optics. An overview of the optical setup used in the simulation is shown in Fig. 9.5. The simulation takes a point source at a distance of 60 m in front of the ellipsoidal mirror. At a distance of 2 m before the split mirror, an aperture[77] cuts the beam diameter to the design value of 10 mm. The incidence angle on the split and the ellipsoidal mirror is 8°. The ellipsoidal mirror of the simulation is designed for 60 m source distance and a focal length of 1 m. The actual ellipsoidal mirror also has a focal length of 1 m, but is made for a source distance of 85 m. At the point in time when the simulation was performed, the source distance was still unclear and set to 60 m by purpose. However, this does not change the quality of the simulation, which assumes perfect optical imaging. The focal spot can be observed on a target screen, which is movable along the beam direction.

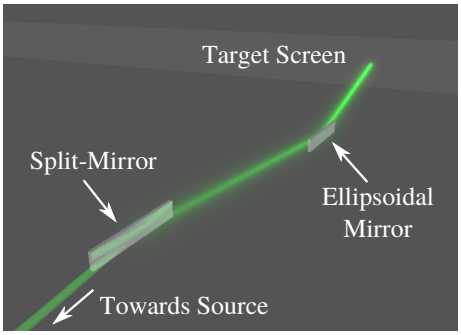

Figure 9.5: Overview of the optical setup used in the ray tracing simulation. The FEL beam (green) first hits the split-mirror and is afterwards focussed by the ellipsoidal mirror onto a target screen.

[75] The rotation axes are defined along the mirror surface.
[76] `http://www.povray.org/`, last request: 11/13/2017.
[77] Not shown in Fig. 9.5.

9.3.1 Mirror Dimensioning

The simulation is used to check the dimensioning of the mirrors. The upper row of Fig. 9.6 shows the footprint of a 10 mm diameter beam on the split-mirror for maximum negative, zero and maximum positive hub. The beam does not clip for any hub position for a mirror length of 12 cm. The second row of Fig. 9.6 displays the beam footprint on the ellipsoidal mirror. For better diagnostics, a point source of white light is used and the reflectivity of the top half of the split-mirror is set to only reflect green light, whereas the lower part reflects only blue light. Thus, the contributions of the upper and lower half can be traced in the optical path of the simulation. A minimum length of 157 mm is needed for the ellipsoidal mirror to focus the entire beam for all hub positions. In order to have options for alignment, the actual ellipsoidal mirror has a length of 180 mm.

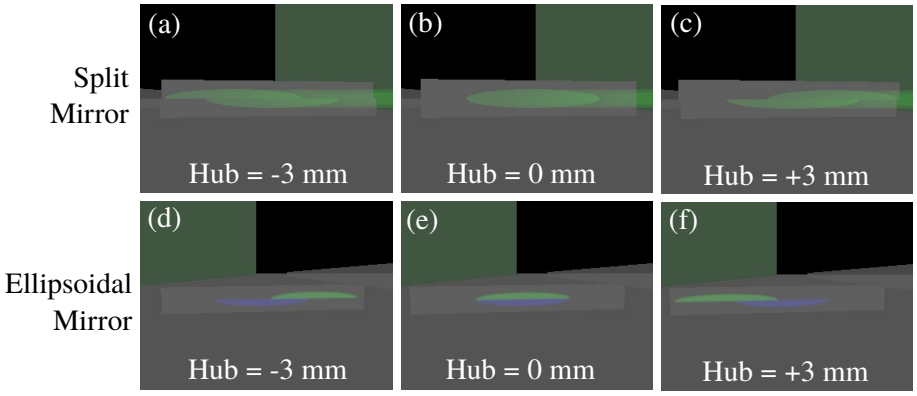

Figure 9.6: 1st row. View of the split-mirror for (a) maximum negative, (b) zero and (c) maximum positive hub. 2nd row. Same as 1st row, but for the ellipsoidal mirror.

9.3.2 Focal Spot Size

An ideal ellipsoidal mirror images a point-source into a point-focus (see Fig. 9.14). The first row of Fig. 9.7 shows a scan through the focus along the beam direction. The source distance is set to the design value of the ellipsoidal mirror. The so-called photon radius, i.e., the radial size of the propagated rays, is set to 0.5 µm and defines the smallest possible focus diameter. Fig. 9.7 (a) displays the beam diameter on the target screen −1 mm before the nominal focal distance. The contributions from the upper (green) and lower split-mirror half (blue) are well distinguishable. At this position, the beam diameter is 10 µm. At the nominal focal distance (Fig. 9.7 (b)), a single turquoise spot is visible on the screen. Thus, the simulation returns the results expected for imaging with an ideal ellipsoidal mirror. The beam diameter at a position +1 mm after the focal distance is shown in Fig. 9.7 (c). The diameter is the same as for −1 mm, but the contributions from the upper and lower mirror half have interchanged.

Depending on the wavelength and machine parameters of the FEL, the source point within the undulator can change on the order of some meters. To simulate this, the source distance is varied from 60 m to 65 m. The results are shown in the second row of Fig. 9.7. At the nominal focal distance, the beam diameter is now larger than 10 µm and the blue contribution from the lower mirror is at the top, i.e., the new focus is closer to the source (see Fig. 9.7 (d)). For a source distance of 65 m, the best focus is found at a position ~ -1.3 mm before the nominal focal distance (see Fig. 9.7 (e)). Concerning the experimental setup, this implies that it is crucial to have sufficient manipulation options to move the ellipsoidal mirror along the beam axis in order to hit the center of the gas jet with the smallest focus.

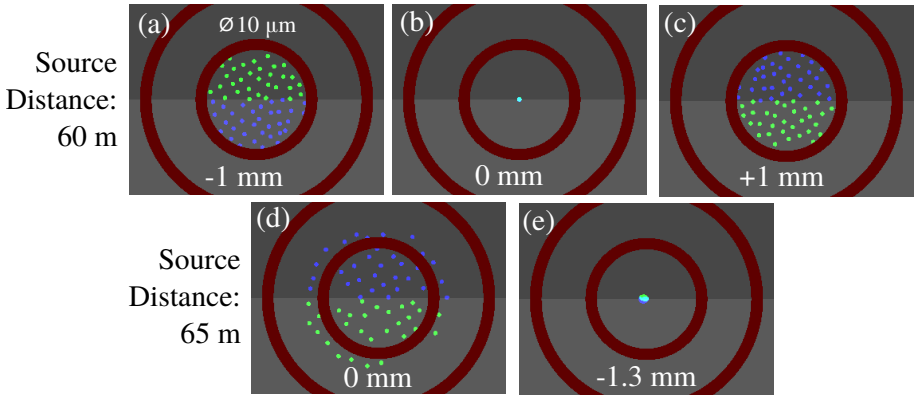

Figure 9.7: 1st row. Scan through the focus for the source distance of 60 m, which is the design value of the ellipsoidal mirror of the simulation. 2nd row. Same as 1st row, but for a source distance of 65 m.

9.3.3 Delay Scans and Angular Corrections

As pointed out in Sec. 9.2, an angular tilt correction is necessary to maintain spatial overlap of both foci during delay scans. The displacement in the focal plane for maximum delay settings and without angular corrections is shown in Fig. 9.8 (a) and (b). According to this, the focus of the upper mirror (green) is displaced by ± 200 µm for ± 3 mm hub. In addition, the beam size is enlarged compared to the spot of the resting mirror. If the angular tilt correction is switched on, the two foci can be spatially overlapped at the nominal focal spot and the movable focus is not enlarged. The underlying coordinate system of the upper mirror half is depicted in the upper right corner of Fig. 9.8. The subfigures (c)-(e) depict a scan through the focus for maximum positive hub and a tilt correction of 49.5 µrad.
Besides the tilt correction, the upper split mirror can do a tip rotation to overlap the foci in the vertical direction. Fig. 9.8 (f) shows a vertical displacement of 5 mm of the movable focus for a tip of 17.5 mrad. A displacement of 5 mm in the focal plane is sufficient according to experiences with the previous back-reflecting setup.

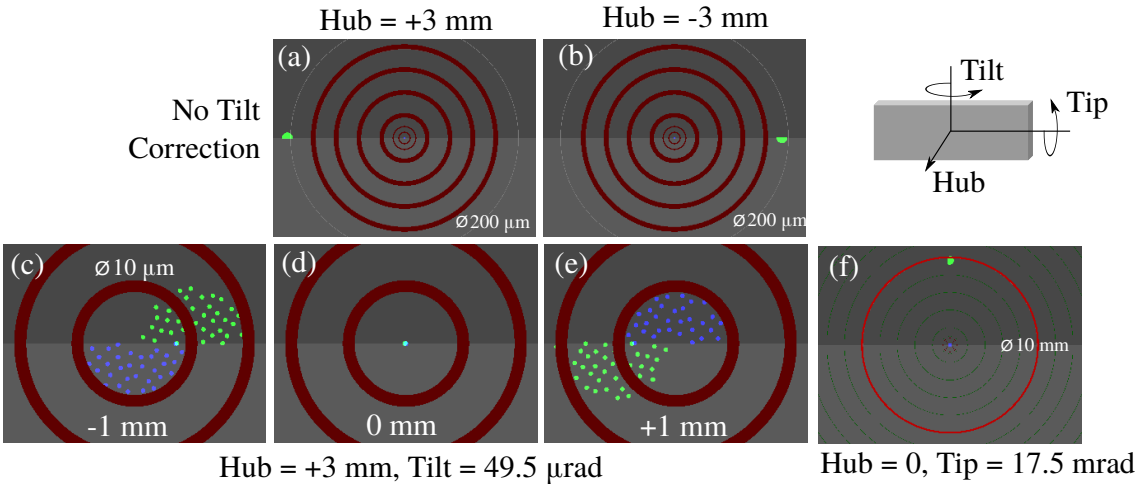

Figure 9.8: 1st row. Displacement of the movable focus (green spot) without tilt correction. The focus from the resting mirror (blue spot) stays centered. 2nd row, (c)-(e). Scan through the focus for maximum positive hub and tilt correction switched on. (f) Displacement in focal plane for a tip rotation of 17.5 mrad

9.3.4 Positioning of the Ellipsoidal Mirror

In this section, the sensitivity of the positioning of the ellipsoidal mirror is examined. It is crucial to hit the ellipsoidal mirror at the correct position and the right incidence angle. Otherwise, the focus will be corrupted due to imaging errors like aberrations. In the simulation, not the incidence angle is changed, but the ellipsoidal mirror is rotated around different axis, which likewise simulates an inappropriate positioning. The underlying coordinate system is depicted on the left of Fig. 9.9.

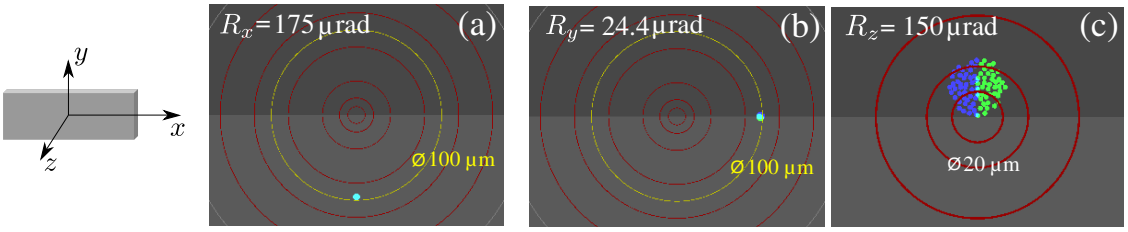

Figure 9.9: (a) Displacement of the focus (turquoise spot) in the focal plane for a rotation of the ellipsoidal mirror around the x-axis of $R_x = 175\,\mu\text{rad}$. The underlying coordinate system is drawn on the left. (b) Focal spot for $R_y = 24.4\,\mu\text{rad}$. (c) Focal spot for $R_z = 150\,\mu\text{rad}$.

Fig. 9.9 (a) shows the focal spot on the target screen for a rotation of the ellipsoidal mirror around the x-axis of $R_x = 175\,\mu\text{rad}$. The focal spot is vertically displaced by 50 µm and gets enlarged. A rotation of $R_y = 24.4\,\mu\text{rad}$ has the effect of a lateral displacement of 50 µm and a the focus gets elongated vertically (see Fig. 9.9 (b)).

The rotation around R_z primarily effects the focus size, which is enlarged to a diameter $> 20\,\mu m$ at the nominal focus position (see Fig. 9.9 (c)). According to the simulation, the angular resolution of the mirror kinematics should be better than $10\,\mu rad$ to get a small focus at the nominal position. The focus size is very sensitive to the rotation R_z.

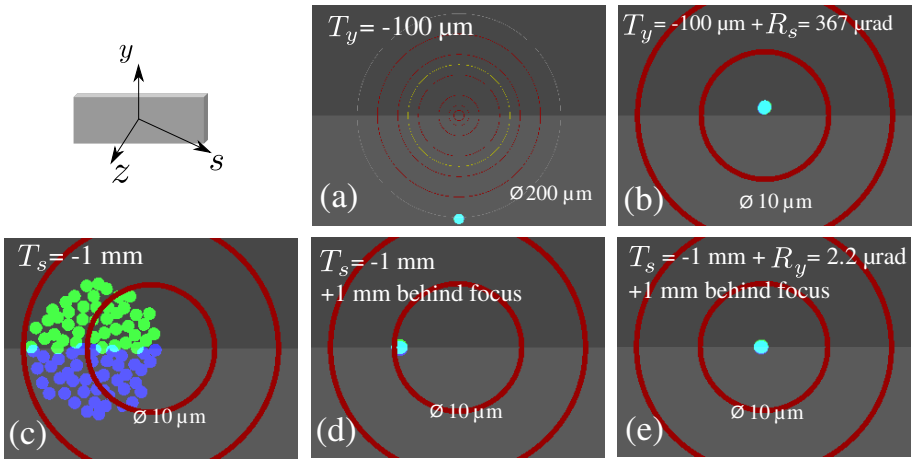

Figure 9.10: (a) Displacement of the focus (turquoise spot) in the focal plane for a translation along the y-axis of $T_y = -100\,\mu m$. The underlying coordinate system is drawn in the upper left corner. (b) Same as (a), but with angular correction Rs. (c) Focal spot for $T_s = -1\,mm$ at the nominal position. (d) Focal spot for $T_s = -1\,mm$ and $+1\,mm$ behind the focus. (e) Same as (d), but with angular correction R_y.

The results for translations of the ellipsoidal mirror are summarized in Fig. 9.10. The corresponding coordinate system is shown in the upper left corner. It has an axis s, which accounts for a translational along the direction of the outgoing beam. A vertical translation of the mirror affects the vertical position of the focus strongly (see Fig. 9.10 (a)). This offset can be compensated by a rotation around s of $R_s = 367\,\mu rad$ (see Fig. 9.10 (b)). In the 2^{nd} row, a misalignment along the s-axis is illustrated. For a translation of $T_s = -1\,mm$, the focus gets enlarged and also laterally displaced (see Fig. 9.10 (c)). The green/blue color-coding imprinted from the upper and lower half of the split-mirror tells that the actual focus should be further upstream with respect to the nominal focus. At a position $+1\,mm$ behind the nominal focus, the focal spot is small, but still displaced to the left (see Fig. 9.10 (d)). This can be compensated by a rotation R_y (see Fig. 9.10 (e)).
According to the simulation, the positioning accuracy for the ellipsoidal mirror should be better than $10\,\mu m$ (see Sec. 9.4). The simulations on positioning the split-mirror show similar results, because a misalignment of it directly affects the incidence angle and the position where the ellipsoidal mirror is hit.

In conclusion, the simulation shows that the resolution to position both mirrors should be $\leq 10\,\mu\text{rad}$ in angle and $\leq 10\,\mu\text{m}$ in translation in order to get the design focus of $\varnothing\,10\,\mu\text{m}$ at the nominal position in the center of the REMI spectrometer.

9.4 Final Configuration

9.4.1 Hexapod Kinematics

To obtain best focussing and high transmission for all delay values, the split and the ellipsoidal mirror need to be individually adjusted in all three rotational and translational dimensions with µrad- and µm-precision. The importance of a precise alignment of grazing incidence optics is already known from existing setups, e.g., Ref. [49], and is also the outcome of the ray tracing simulation presented in Sec. 9.3. A so-called hexapod [170, 256] is a parallel kinematics machine, which allows rotations and translations in all six degrees of freedom[78]. Therefore, it is optimal suited to position the mirrors in space. The hexapod kinematics used for the in-line split-delay optics is shown in Fig. 9.11.

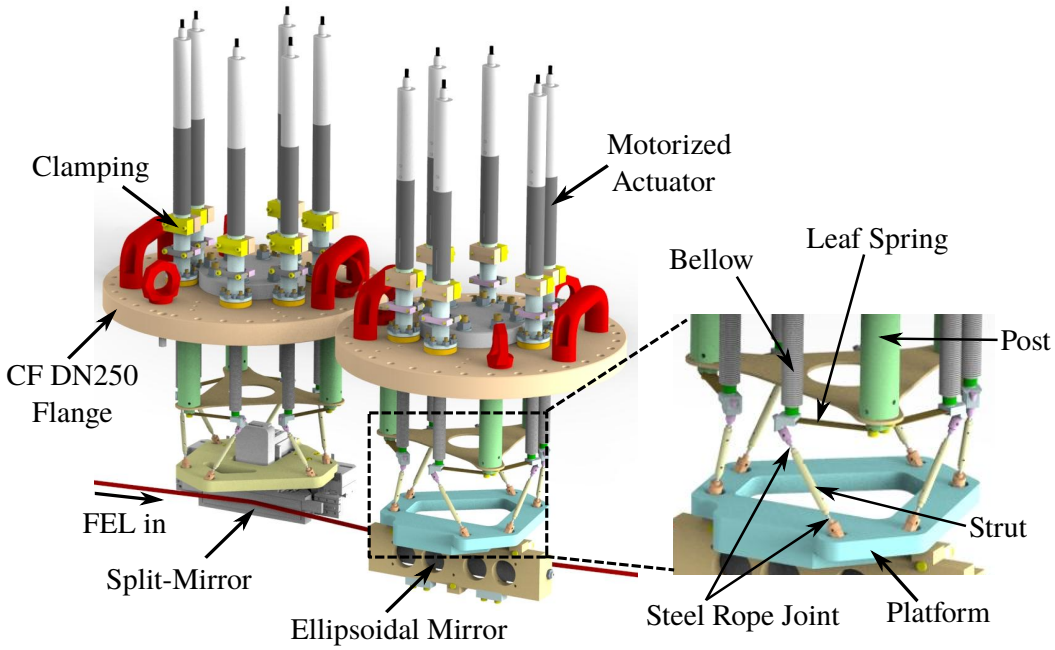

Figure 9.11: 3D CAD drawing of the in-line split-delay optics with labels of the main parts.

The split and the ellipsoidal mirror have their individual kinematics, which are mounted on two separate CF DN250 flanges and are not directly mechanically linked. A decoupled adjustment of both mirrors is essential for beam alignment

[78] Three rotations and three translations.

and also indispensable to compensate manufacturing tolerances[79], or uncertainties from the topographic survey of the mirror chamber[80]. The mounting on two separate supporting flanges also enables an independent removal of both mirrors in case of trouble-shooting.
The general design of the kinematics has been developed by a group around T. Noll and Th. Zeschke from the *Helmholtz Zentrum Berlin (HZB) / BESSY II*, which is specialized on the instrumentation of synchrotrons. The hexapod kinematics has six legs, each consisting of two steel rope joints, a connection strut, a leaf spring, a bellow and a motorized actuator (see Fig. 9.11). By linearly pulling or pushing the actuators, the legs react dynamically and the platform moves. An illustrative way to think about the hexapod kinematics is to compare its functionality to that of a puppet play. If the motor controls of all six actuators is done in a synchronized way, the platform and all parts attached to it will move in a controlled manner. A basic idea of the design is to use stable steel rope joints instead of conventional bearings, which increases the overall stiffness. The flexible copper-beryllium leaf springs are needed to prevent a lateral displacement of the upper joint in stressed positions of the joints[81]. Different to usual hexapods, the driving motors are not directly part of the moving assembly. This decreases the total mass and outgassing electrical parts are banned from the vacuum. Bellows separate the actuators from the vacuum.
The kinematics is designed for rotations $R_x, R_y, R_z = \pm 0.5°$ and translations of $T_x, T_y = \pm 3\,\text{mm}$ laterally and $T_z = \pm 5\,\text{mm}$ vertically. The working point is limited by the hub of the actuators and the breaking limit of the leaf springs. As long as the hub of all actuators is within the limits of $\pm 5\,\text{mm}$, also positions out of the aforementioned parameter space are reachable. For the split mirror, a vertical travel of $T_z = \pm 5\,\text{mm}$ is important, because this allows to put the complete FEL beam of 10 mm diameter onto one of the mirror halves, which is essential for experiments not applying an XUV-pump XUV-probe scheme (see Sec. 9.5).
Tests show that the resolution in all translations is $\Delta T_{x,y,z} \approx 0.1\,\mu\text{m}$ and in all rotations $\Delta R_{x,y,z} \approx 1\,\mu\text{rad}$. This values are in agreement with a test report by the HZB group for a similar kinematics. Due to the steel rope joints, the system shows hysteresis effects in the reproducibility of distinct positions. However, if the positions are always reached from one side, the hysteresis decreases notably. Tab. 9.1 summarizes the benchmarks of the 6D hexapod kinematics.

[79] For example errors in the parallelism of the flanges of the vacuum chamber which holds the supporting flanges. If emphasis is put on the manufacturing, tolerances in the order of some 1/10 mm are realized.
[80] The topographic survey is precise on the level of some 1/10 mm.
[81] Simulations show that for a hub of 3 mm and 5 mm, the lateral displacement of the upper joint is 0.11 mm and 0.31 mm, respectively.

Table 9.1: Benchmarks of the 6D hexapod kinematics.

Translations	T_x	T_y	T_z
Range [mm]	± 3	± 3	± 5
Resolution [µm]	0.1	0.1	0.1
Reproducibility [µm]	1	1	1
Rotations	R_x	R_y	R_z
Range [°]	± 0.5	± 0.5	± 0.5
Resolution [µrad]	1	1	1
Reproducibility [µrad]	10	10	10

The hexapod kinematics were manufactured by *FMB Berlin*[82]. The motorized actuators are *PI*[83] *M-230.25* high-resolution linear actuators with a DC gear motor and a rotary encoder. The maximum hub range is 25 mm with smallest increments of 0.05 µm. The unidirectional repeatability is specified to 0.1 µm. The rotary encoder is based on the Hall effect and its calculative resolution is stated to be typically 0.0046 µm. Each actuator is controlled via an individual *PI C-863 Mercury* servo controller.
A *LabVIEW*[84] program calculates the target position of the mirrors in space. Based on this, the corresponding hub values for the actuators are computed. The program needs the positions of the upper and the lower joints as input parameters. The procedure to calculate and to move to a target position entails the following steps:

1. The calculation starts from the zero positions $\mathbf{r}_i^0 = (x_i^0, y_i^0, z_i^0), i = 1, 2, ..., 6$ of the lower joints.

2. The end positions $\mathbf{r}_i^{\mathrm{rot}} = (x_i^{\mathrm{rot}}, y_i^{\mathrm{rot}}, z_i^{\mathrm{rot}})$ of the lower joints for global rotations R_x,R_y and R_z are calculated.

3. The displacement vector $\Delta\mathbf{r}_i^{\mathrm{rot}} = \mathbf{r}_i^{\mathrm{rot}} - \mathbf{r}_i^0$ to translate each lower joint to the new positions is computed.

4. For global translations T_x, T_y and T_z, an additional vector $\Delta\mathbf{r}_i^{\mathrm{trans}}$ is added.

5. In sum, the target positions of the lower joints read: $\mathbf{r}_i = \mathbf{r}_i^0 + \Delta\mathbf{r}_i^{\mathrm{rot}} + \Delta\mathbf{r}_i^{\mathrm{trans}}$.

6. Based on this, the target positions of each upper joint $\mathbf{R}_i$, i.e., the hub of the actuator, is calculated.

[82]FMB Feinwerk- und Meßtechnik GmbH, Friedrich-Wöhler-Straße 2, 12489 Berlin, Germany.
[83]Physik Instrumente (PI) GmbH & Co. KG, Auf der Römerstraße 1, 76228 Karlsruhe, Germany.
[84]Version: LabVIEW 2013. The core part of the program has been gratefully adopted from J.P. Müller from the *TU Berlin*.

7. Taking the equation which describes a sphere around the target position $\mathbf{r}_i$ of the lower joint with the radius being the leg length L yields: $(\mathbf{R}_i - \mathbf{r}_i)^2 = L^2$.

8. The resulting position $\mathbf{R}_i$ is required to be on the motor axis: $\mathbf{R}_i = \Delta\alpha_i \cdot \mathbf{n} + \mathbf{R}_i^0$ with $\mathbf{R}_i^0$ being the upper joint position before the movement and $\mathbf{n}$ being the actuator axis unit vector.

9. Then, the quadratic equation is solved for $\Delta\alpha_i$ and the actuator is moved by this distance.

10. The solution is $\Delta\alpha_i = -\frac{p}{2} \pm \sqrt{\left(\frac{p}{2}\right)^2 - q}$ with $p = 2\mathbf{n}_i \cdot \mathbf{k}_i$, $q = \mathbf{k}_i^2 - L^2$, $\mathbf{k}_i = \mathbf{r}_i - \mathbf{R}_i^0$ and the solution where the leg stays below the upper joint is taken.

Also the global movements of the hexapod kinematics are not encoded, each of the actuators is equipped with a rotatory encoder and a reference switch. Hence, the kinematics can be globally referenced by means of the reference switches of each actuator. The limits for the hub are set to $\Delta h = \pm 5\,\mathrm{mm}$ in order to avoid too much stress on the steel rope joints and the leaf springs. For safety reason, the hub limits are not just set in the *LabVIEW* software, but also stored directly on the servo controllers.

9.4.2 Split-Mirror

The split-mirror is the centerpiece of the pump-probe setup. It is designed to geometrically separate an incoming FEL beam of 10 mm diameter at a grazing angle of $\theta = 8°$ and consists of two plane mirror halves (clear aperture $120 \times 10.5\,\mathrm{mm}^2$), whereof the upper half is movable. The split-mirror unit is shown in Fig. 9.12.
In order achieve femtosecond pump-probe resolution and a pointing stability $\leq 1\,\mu\mathrm{m}$, which guarantees spatial overlap of both foci for all delay values, the upper mirror is movable by a custom-made[85] 3D parallel kinematics based on piezo positioners. The kinematics allows a hub-dependent angular correction around the vertical (tilt) and the horizontal (tip) axis to maintain spatial overlap during delay scans. The underlying coordinate system is defined in Fig. 9.12. The rotational axes are set along the mirror surface. As discussed in Sec. 9.2, the maximum hub range of $h = \pm 3\,\mathrm{mm}$ translates into a maximum delay range of $t_d = \pm 2.7\,\mathrm{ps}$. Rotations of some degrees are possible for the tilt. The maximum tip rotation $\pm 20\,\mathrm{mrad}$ is limited by the minimal allowed gap distance of 100 µm between the mirror halves. The gap is intended to be as small as possible in order to minimize photon losses. The substrates of the mirrors are chamfered to increase the freedom of movement and to avoid collisions between the mirror halves. The distance between the mirrors can be manually adjusted by three spring mounted fine thread screws (not shown in Fig. 9.12).

[85] SmarAct GmbH, Schütte-Lanz-Straße 9, 26135 Oldenburg, Germany.

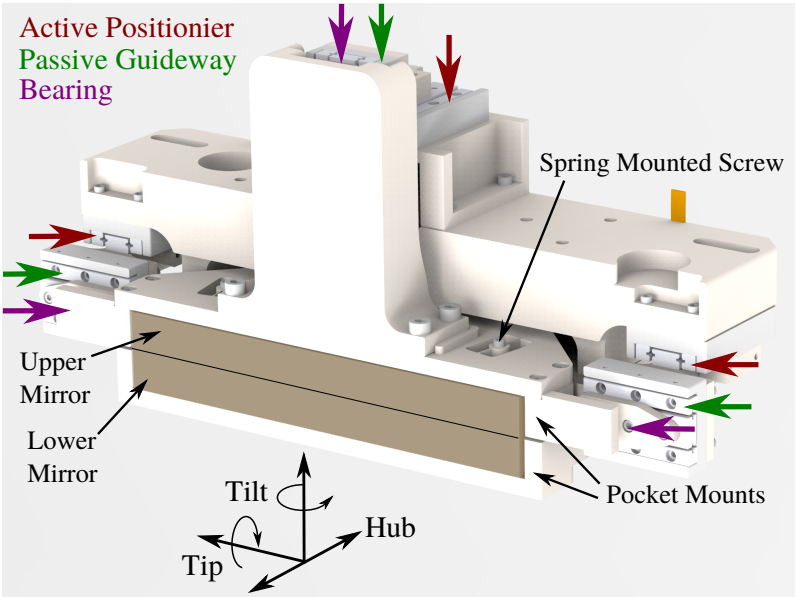

Figure 9.12: 3D parallel kinematics of the split-mirror. The upper mirror half is movable in the three dimensions tilt, tip and hub according to the shown coordinate system. The active positioniers, guideways and bearings are marked by red, green and purple arrows, respectively.

The 3D parallel kinematics is made up of three active linear piezo actuators, three passive linear guideways and three bearings (see Fig. 9.12). The parallel movement of all active actuators defines the current position status of the upper mirror. The controls software and a *.dll*-library are provided by the manufacturer, which allows to access the movement commands[86] via *LabVIEW*.
The piezo positioners are the *SmarAct SLC-1730*[87] nanometer precision linear positioners, which are stick-slip/friction-inertia piezo drivers [50, 114, 129, 150, 292]. An exemplary sketch showing the operation mode of such type of piezo drive is depicted in Fig. 9.13 (a). In the stick-phase, the piezo actuator expands and the runner adiabatically follows its motion, because it is linked by friction. In the slip-phase, the piezo contracts rapidly, but the runner is unable to follow due to its inertia and stays in place. Repeating this cycle many times by applying a periodic sawtooth control voltage allows to travel long distances (see Fig. 9.13 (b)), although only a single piezo actuator is used. Common piezo inertia actuators are operated at kHz frequencies which allows fast driving velocities ($\sim$ mm/s). It was observed that these drivers can show a back-stepping effect of $\sim 50\,\text{nm}$ during the slip-phase [150].
The manufacturer specific the positioners to have a resolution of $<1\,\text{nm}$ during the stick-phase. Each positionier features three piezos, which are installed in series.

[86] Executable commands are: move(*hub*, *tip*, *tilt*), speed, encoder referencing, encoder calibration.
[87] `http://www.smaract.com/products/linear-positioners/slc-series/slc-1730`, last request: 11/16/2017.

The complete stick-phase, i.e., the complete expansion length of all three piezos together, is 4.5 µm. All three positioners are operated in closed-loop mode with an encoder resolution of 4 nm and a repeatability of ± 60 nm. The maximum operation frequency is 18.5 kHz. The drivers are controlled by the *SmarAct MCS*[88] module with the *Advanced Sensor Calibration (ASC)* option. Tests on the pointing stability of the split-delay kinematics are presented in Sec. 9.6.2. The achieved benchmarks are summarized in Tab. 9.2.

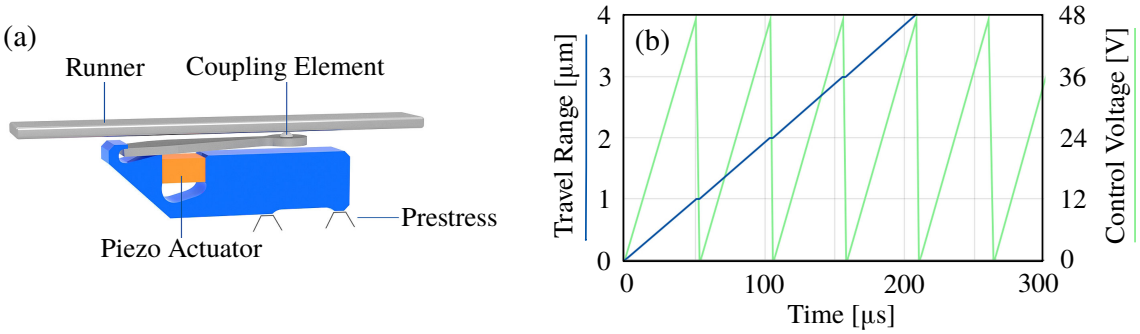

Figure 9.13: (a) Illustration of a piezo inertia drive. (b) Travel range of a stick-slip drive as a function of time. Also shown is the corresponding control voltage. Both figures are taken from Ref. [129].

The mono-crystalline silicon mirror substrates are custom-made by *Carl Zeiss SMT GmbH*[89] and the reflective surface is coated with 30 nm of carbon by *optiXfab GmbH*[90]. The quality of the split mirrors is similar to the ellipsoidal mirror and more information is given in Sec.9.4.3. Finite element method (FEM) simulations were applied to design the shape of the substrate and the corresponding mount to minimize any stress and deformations of the reflective mirror face. Viewed from aside, the mirrors have a L-like shape, which makes them fit perfectly into the respective pocket mounts. The fixation to the pocket is done by three spring mounted screws which gently press onto the rear part of the substrate.

[88] `http://www.smaract.com/products/control-systems/mcs/`, last request: 11/16/2017.
[89] Carl Zeiss SMT GmbH, Rudolf-Eber-Straße 2, 73447 Oberkochen, Germany.
[90] optiXfab GmbH, Hans-Knöll-Straße 6, 07745 Jena, Germany.

Table 9.2: Benchmarks of the 3D piezo kinematics.

Translations	Hub	
Range [mm]	± 3	
Resolution [nm]	≤ 1	
Reproducibility [nm]	± 60	
Rotations	Tip	Tilt
Range	some $^\circ$	± 20 mrad
Resolution [µrad]	≤ 1	≤ 1
Reproducibility [µrad]	1	1
Delay		
Range [ps]	± 2.7	
Resolution [fs]	≤ 1	
Closed-loop	Yes	

9.4.3 Ellipsoidal Mirror

An ellipsoidal mirror is perfectly shaped for point-to-point imaging, i.e., radiation emitted under varying angles from one focus will always be collected in the other focus. An ellipse is the two-dimensional cut through an rotationally symmetric ellipsoid. The layout and the nomenclature of an ellipse is shown in Fig. 9.14 .

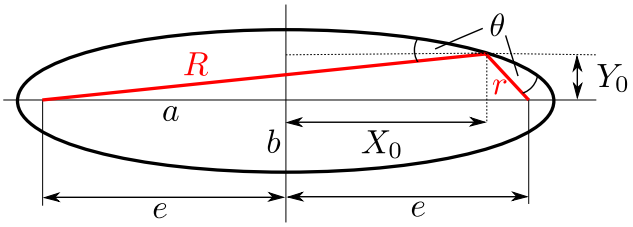

Figure 9.14: Layout of an ellipse and nomenclature. Taken and adapted from Ref. [111].

The present ellipsoidal mirror is designed for $R = 85\,\text{m}$, $r = 1\,\text{m}$ for $\theta = 8°$. The basic parameters are listed in the following [111].

- Major semi-axis: $a = \frac{R+r}{2} = 43000.00\,\text{mm}$
- $\varepsilon = \sqrt{\frac{R^2+r^2-2rR\,\cos(2\theta)}{4a^2}}$
- Minor semi axis: $b = \sqrt{a^2(1-\varepsilon^2)} = 1283.11\,\text{mm}$
- Incidence point in y: $Y_0 = \frac{rR\,\sin(2\theta)}{2a\varepsilon} = 272.55\,\text{mm}$

- Incidence point in x: $X_0 = a\sqrt{1 - \left(\frac{Y_0}{b}\right)^2} = 42018.71\,\text{mm}$
- Eccentricity: $e = \sqrt{a^2 - b^2} = 42980.85\,\text{mm}$

The machining of the mirror substrate was done by *Carl Zeiss SMT GmbH*[91]. The substrate consists of mono-crystalline silicon and is $180 \times 30 \times 20\,\text{mm}^3$ in dimensions. The clear aperture is $180 \times 20\,\text{mm}^2$. The fabrication of an ellipsoidal mirror is technically challenging in terms of maintaining contour accuracy while polishing and elaborated techniques like ion beam milling are of need [169]. The quality of a mirror depends on its contour accuracy, e.g., its slope error, and its surface roughness. The quality inspection of the manufacturer specifies the slope errors to 0.84 arcsec (rms) tangential and 1.2 arcsec (rms) sagittal. The surface roughness is measured to be $0.19 - 0.24\,\text{nm}$, e.g., $\lambda/50$ for $\lambda = 10\,\text{nm}$. Simulations specify a design focal spot size of $d \approx 10\,\mu\text{m}$.
For high transmission in the XUV photon energy range, the mirror is coated with a 30 nm thin layer of carbon by *optiXfab GmbH*[92]. The layer thickness has a relative error of $\pm\,5\,\%$ and the lateral homogeneity is $> 97\,\%$. Fig. 9.15 shows that the mirror has a high reflectivity of $\sim 80\%$ over a broad photon energy range from $30 - 150\,\text{eV}$.

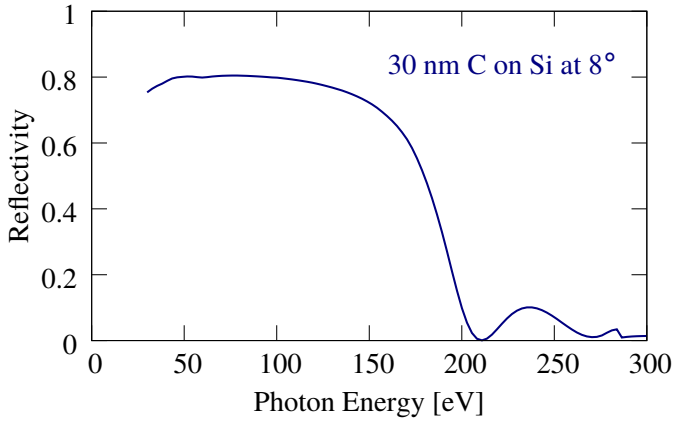

Figure 9.15: Calculated reflectivity curve at a grazing angle of $\theta = 8°$. Data from Ref. [100].

Like the split-mirror mount, the mount of the ellipsoidal mirror is designed to reduce the stress and deformations on the mirror surface (see Fig. 9.16). The weight of the mirror is held by two spherically shaped supporting rods. To prevent the mirror from dropping forward, it is mounted by three clamps, which fit into two lateral notches of the mirror substrate. Four additional spring mounted screws allow a gentle fixation. The mount was manufactured by *FMB Berlin*[93].

[91] Carl Zeiss SMT GmbH, Rudolf-Eber-Straße 2, 73447 Oberkochen, Germany.
[92] optiXfab GmbH, Hans-Knöll-Straße 6, 07745 Jena, Germany.
[93] FMB Feinwerk- und Meßtechnik GmbH, Friedrich-Wöhler-Straße 2, 12489 Berlin, Germany.

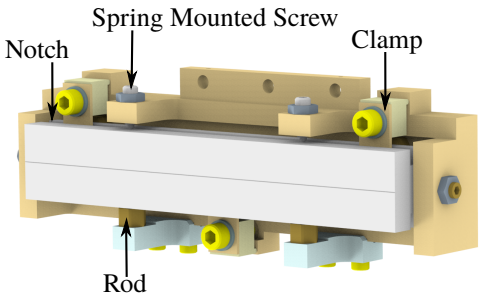

Figure 9.16: Mount of the ellipsoidal mirror. Explanations are given in the text.

9.4.4 Vacuum Chamber and Manipulation Platforms

The hexapod kinematics for the split and the ellipsoidal mirror are mounted in an overhead configuration onto two separate CF DN250 flanges. The distance between the midpoints of the split and the ellipsoidal mirror is 288 mm. This means a sideways displacement of 79.4 mm for the FEL beam at the grazing incidence angle of $\theta = 8\,°$. In order to fit both kinematics in one vacuum chamber, a lying CF DN250 tube of $\sim$ 700 mm length, which is titled by 16° with respect to the FEL axis, is used. A CAD drawing of the mirror chamber is shown in Fig. 9.17 (a). Two CF DN250 top flanges hold the hexapod kinematics. The two vertical tubes at the top have a non-standard inner-diameter of 230 mm, which enables to remove both kinematics vertically. The four CF DN200 sideways flanges hold two turbo molecular pumps[94] and two vacuum viewports. The flange at the FEL entrance is a CF DN200 flange on which a CF DN63 tube is welded under 16°. Similarly, a CF DN40 tube is welded on the CF DN200 exit flange. Two UHV gauges and one thermocouple, which is needed to monitor the temperature inside the chamber during bake-out, are mounted sideways on CF DN40 ports. In addition, a CF DN40 port which points upwards by 45° holds a xyz-manipulator[95]. It is used to insert a 25×25 mm^2 Ce:YAG fluorescence screen into the beam path between the mirrors. The chamber can be encapsulated from the surrounding vacuum sections by two pneumatic UHV window valves[96].
The chamber walls are made of annealed 1.4435 stainless steel. For the flanges, forged and annealed 1.4429 ESU stainless steel is chosen in order to minimize the outgassing rate from the surfaces. The chamber was manufactured by *FMB Berlin*[97].

[94] Pfeiffer Vacuum HiPace 700 turbopump with hybrid bearings, `https://www.pfeiffer-vacuum.com/de/produkte/turbopumpen/hybridgelagert/hipace-700/`, last request: 12/06/2017.
[95] VACGEN miniax XYZ manipulator with 50 mm z-travel, `http://www.vacgen.com/pages/miniax-xyz-manipulators`, last request: 12/06/2017.
[96] VAT Series 010 Mini UHV gate valves, pneumatic, with windows, `http://www.vatvalve.com/business/valves/catalog/A/010_1_V`, last request: 12/07/2017.
[97] FMB Feinwerk- und Meßtechnik GmbH, Friedrich-Wöhler-Straße 2, 12489 Berlin, Germany.

The 12 motorized linear actuators of the kinematics are clamped by a special construction and can be removed for bake-out or in case of malfunction. All used materials and components, including the mirrors and the split-delay kinematics, are suitable for bake-out temperatures of up to 150 °C. After bake-out at 120 °C for 24 h, a pressure of 1×10^{-10} mbar is reached in the chamber.
In order to position the chamber in space, a stack of four manipulation platforms is employed. The lowest platform is used to adjust the height of the chamber. The next platform allows to rotate the chamber around the vertical axis to adjust the angle with respect to the FEL axis. On top of this, a further translational platform enables lateral movements. The topmost platform sits on two high-precision linear guides[98] to translate the chamber along the beam direction. This allows to tune the distance between ellipsoidal mirror and the interaction point. In order to perform all movements under vacuum, the chamber is connected to the surrounding vacuum sections by flexible bellows.
The surveying, i.e., the precise placement of the mirrors to their nominal position in space, includes two steps. A transfer measurement references the mirror surfaces to several survey points mounted on the CF DN250 top flanges. Afterwards, the survey points are leveled to the coordinate system of the experimental hall by interferometric laser tracking. In the end, the absolute positions of the mirrors within the hall coordinate system are known with a precision of 1/10 mm.
The chamber and the manipulation platforms are mounted on a granite block to damp vibrations. Fig. 9.17 (b) shows a photography of the chamber on-site.

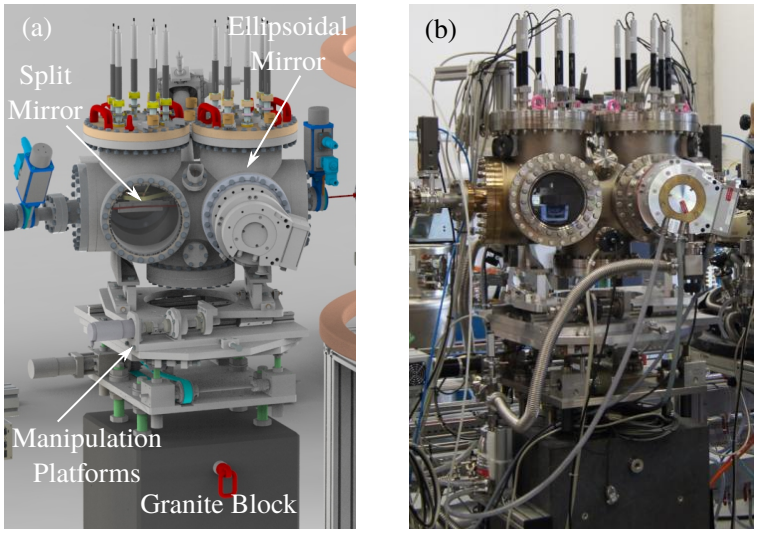

Figure 9.17: (a) 3D CAD drawing of the mirror chamber mounted on manipulation platforms, which are fixed on a granite block. (b) Photography of the mirror chamber on-site at beamline FL26 at FLASH2.

[98] Franke FDD non-magnetic linear guides, `https://www.franke-gmbh.com/linear-systems/products/linear-guides/fdd/`, last request: 12/06/2017.

9.5 Setup of the REMI Endstation at FLASH2

The in-line XUV split-delay optics (see Sec. 9.4) is integrated as a key part of the REMI endstation at beamline FL26 at FLASH2 (see Sec. 3.5). The REMI endstation is dedicated to gas-phase atomic, molecular and optical (AMO) physics experiments to study the ultrafast dynamics of small quantum systems (atoms, molecules, clusters) by combining pump-probe techniques with the high information potential of multi-particle coincidence spectroscopy (see Ch. 4). In its final stage, the endstation will allow to perform XUV-XUV, XUV-IR and FEL-HHG pump-probe experiments. The instrumentation will be also very flexible concerning the target preparation. Along these lines, an in-vacuum evaporation nozzle to inject liquid-phase targets has been developed [167]. An overview of the REMI endstation showing the main components is given in Fig. 9.18.

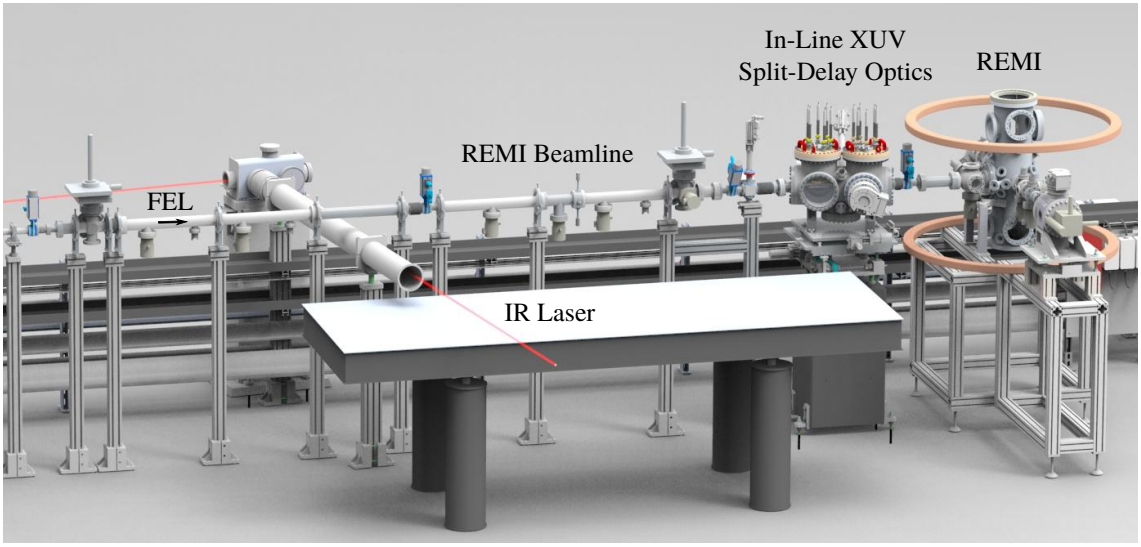

Figure 9.18: Overview of the REMI endstation at beamline FL26 at FLASH2.

After the undulators, the photons are guided over long distances to the REMI. On its way, the FEL beam can be characterized, manipulated and adjusted by several insertion devices in the tunnel section, in the experimental hall as well as in a dedicated REMI beamline. In the following, the components that have been installed at the time of this thesis are presented.

9.5.1 Tunnel Section and Experimental Hall

An overview of the photon transport and diagnostics at FLASH2 is given in Ref. [205]. In the tunnel section, beam position monitors based on gas ionization and a set of apertures[99] followed by fluorescence screens are used to monitor and to confine the

[99] Aperture diameter [mm]: 1, 2, 3, 5, 7.5 or 10 mm.

beam in space. The apertures are also utilized to adjust the intensity. The absolute intensity can be measured by a gas monitor detector (GMD) [264] or a multi-channel plate (MCP) tool. A non-invasive online photoionization spectrometer (OPIS) [27] measures the photon energy. The tunnel section closes with a gas attenuator[100], which allows for continuous intensity adjustment.
The photon diagnostics section in the experimental hall is equipped similar to the tunnel section. A second GMD and a further set of apertures[101] are installed. To date, there is no pulse length characterization available at FLASH2. Transmission filters are used to regulate the intensity and to suppress higher harmonics [264]. The filters of different materials and thicknesses are mounted on two motorized wheels. Depending on the photon energy and intensity, different filters and filter combinations can be chosen[102] [103]. Fig. 9.19 shows the transmission curves of some of the available filters.

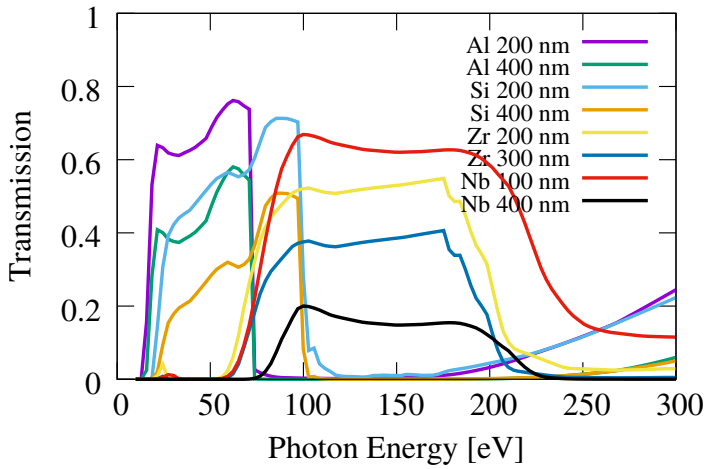

Figure 9.19: Transmission curves of filters as a function of photon energy. The specifications in nm refers to the thickness of the filters. Data taken from Ref. [100].

9.5.2 REMI Beamline

The beamline section in front of the REMI is designed to match the demands of multi-particle coincidence experiments (see Sec. 4.7). The beamline is shown in a schematic lateral cut in Fig. 9.20.

[100] Xe, N_2, Kr or Ar can be chosen as attenuation gases.
[101] Aperture diameter [mm]: 1, 2, 3, 5, 7.5, 10 or 14.
[102] First filter wheel: Al 205 nm, Al 402 nm, Zr 200 nm, Zr 295 nm, Si 200 nm, Si 401 nm, Nb 197 nm, Nb 405 nm, Nb 987 nm.
[103] Second filter wheel: Al 102 nm, Al 200 nm, Al 402 nm, Zr 200 nm, Zr 295 nm, Si 200 nm, Si 401 nm, Nb 197 nm, Nb 405 nm, Nb 987 nm.

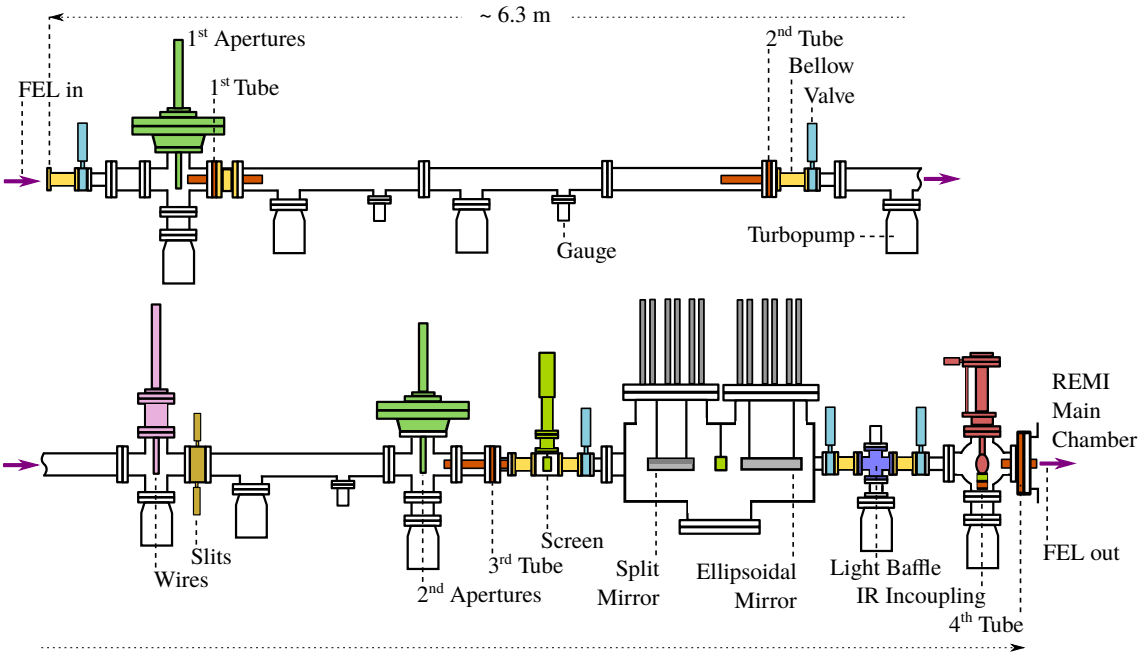

Figure 9.20: Schematic lateral cut through the beamline in front of the REMI including the new mirror chamber. Explanations are given in the text.

The FEL beam enters from the left. In order to protect the UHV conditions in the REMI main chamber ($\leq 10^{-11}$ mbar) from the vacuum conditions in the FLASH beamline ($\sim 10^{-7}$ mbar), the beamline is separated by four differential tubes (colored orange in Fig. 9.20) and a light baffle (colored blue in Fig. 9.20) into five differentially pumped vacuum sections. The differential tubes are configured to reduce stray light. At the two openings, sharp-chamfered copper apertures are clamped into the tube. The chamfer is manufactured as sharp as possible in order to minimize the area where photons can potentially scatter. The apertures have an inner diameter of 18 mm, while the tubes themselves have an inner diameter of 26 mm. This configuration acts as a light baffle for photons which are scattered to off-axis directions. Each flange, which holds one of the differential tubes, is followed by a flexible bellow (colored yellow in Fig. 9.20). This allows a convenient alignment of the tubes with respect to the beam axis.
After the mirror chamber, a further light baffle (colored blue in Fig. 9.20) is installed to prevent stray light in the vicinity of the REMI detectors. The light baffle consists of a CF DN40 cross, which holds two apertures made of roughened 625 µm thick silicon wafers with an inner diameter of 14 mm and 12 mm, respectively. The silicon apertures have the same purpose as the copper apertures of the differential tubes, i.e., to soak up undirected scattered photons. Silicon is chosen as material, because it absorbs strongly over a broad XUV photon energy range[104]. If necessary, the

[104]Between 10-100 eV, the absorption of 650 nm Si is ~70 %, between 100-200 eV nearly 100 % [100].

apertures can be exchanged without venting the mirror or the REMI chamber as the light baffle is enclosed by two gate valves (colored light-blue in Fig. 9.20).
At two distinct positions along the beamline, aperture units[105] (colored dark-green in Fig. 9.20) are integrated. The apertures are used to collimate the beam and to fix its position in space. To reproduce the aperture settings in a controlled way, the position of each aperture is gauged onto the beam axis. Each aperture unit is movable by a triaxial xyz-manipulator. The apertures are chamfered with the sharp edge pointing towards the incoming beam for reasons of stray light reduction. Additionally, the apertures' surfaces facing the beam are coated with a fluorescent ZnS powder, which facilitates the beam alignment during the experiment. A third aperture[106] can be put into the beam path directly in front of the REMI.
In total three fluorescence screens (colored light-green in Fig. 9.20) can be inserted to monitor the position and the shape of the beam. The first screen ($20 \times 20\,\mathrm{mm}^2$) is located in front of the mirror chamber and enables to observe the unsplit beam. A second screen ($25 \times 25\,\mathrm{mm}^2$) can be placed between the split and the ellipsoidal mirror (see Sec. 9.4) and allows to monitor the shape and the illumination uniformity of the split beams. A third screen ($20 \times 20\ \mathrm{mm}^2$) is located in front of the REMI[107]. Each screen consists of a 200 µm thin Ce:YAG crystal and a roughened silicon plate (thickness: 625 µm) on top of each other. The Ce:YAG crystal glows upon illumination with XUV photons. The silicon plates reduces reflexes from the Ce:YAG and additionally enables to observe the visible beamline alignment laser.
Horizontally stressed wires (colored pink in Fig. 9.20) can be driven into the beam path to cast a shadow over the gap of the split-mirror. It is an option to prevent stray light from the edges of the split-mirror. A pair of horizontal slits (colored light-brown in Fig. 9.20) can be used to block the upper or the lower part of the beam.
The incoupling mirror for an IR laser is installed (colored light-red in Fig. 9.20) in analogy to the setup described in Ch. 5. A holey 2 inch silver-coated plane mirror is mounted on a precision rotational feed-through, which is sitting on top of a triaxial xyz-manipulator. To overlap the FEL and the IR beam co-linearly, the IR beam is deflected by 90° and the mirror has a hole of 4 mm diameter for the focussed FEL beam to straightly pass through. The IR laser will be focussed by a lens ($f \approx 40\,\mathrm{cm}$) outside of the vacuum. The differential tube (4^{th} tube in Fig. 9.20) between IR incoupling and main chamber has an inner diameter of 22 mm. Thus, an IR beam of $\leq 35\,\mathrm{mm}$ diameter at the position of the lens can pass the tube without clipping.

[105] Diameters first unit [mm]: 4, 5, 6, 7, 8, 9 and 10, second unit [mm]: 4, 5, 6, 7, 8, 9, 10 and 11.
[106] Diameter: 10 mm, sharply chamfered. The aperature is screwed to the frame which holds the IR incoupling mirror.
[107] This screen is mounted underneath the IR incoupling mirror (see below).

9.5.3 Main Chamber and Photon Dump

In order to spatially overlap the foci at the nominal interaction point, a fluorescence screen can be moved into the center of the REMI main chamber (see Ch. 4). The screen is $10 \times 10\,\mathrm{mm}^2$ and coated with a thin film of Ce:YAG powder. A CCD camera[108] in combination with an optical magnification system is used to image the fluorescence of the foci.
After having passed the main chamber, the FEL beam is disposed in a photon dump. A schematic lateral cut is shown in Fig. 9.21.

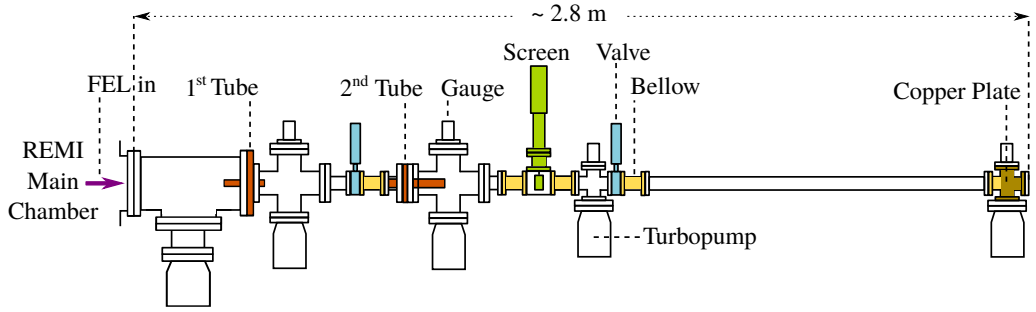

Figure 9.21: Schematic lateral cut through the photon dump. Explanations in the text.

The vacuum of the main chamber is separated from the FEL dump by two differential tubes (colored orange in Fig. 9.21). The first tube has an inner diameter of 26 mm. The split FEL beams, which are in sum 11 mm in diameter at this position, have enough space to pass the tube without clipping. The second tube is of the same type as the tubes in the REMI beamline[109].
The beam profile and position can be monitored by a Ce:YAG fluorescence screen (20×20 mm^2) (colored light-green in Fig. 9.21).
The fluorescence screen is followed by a long CF DN40 tube. Two bellows (colored yellow in Fig. 9.21) at each end allow to translate the entire tube. This can be helpful for stray light reduction.
The photon dump is terminated by a copper plate, which is electrically connected (colored brown in Fig. 9.21). The voltage signals induced by impinging FEL pulses serve as a reference for the energy per pulse.
From the first gate valve onwards (colored light-blue in Fig. 9.21), the entire photon dump is mounted to a single supporting frame. It can be quickly removed for setting up a parasitic experiment behind the REMI.

[108] Basler acA1300-30gc camera with Sony ICX445 CCD sensor, `https://www.baslerweb.com/en/products/cameras/area-scan-cameras/ace/aca1300-30gc/`, last request: 04/12/2018.
[109] Sharply chamfered copper apertures with inner diameter 18 mm.

9.6 Commissioning Results

The in-line split-delay optics has been commissioned on-site at FLASH2. The system is benchmarked and compared to its design values. Important parameters are the focal spot size (see Sec. 9.6.1), pointing and temporal stability (see Sec. 9.6.2 and 9.6.3). The reduction of stray light is observed in first REMI experiments (see Sec. 9.6.4). Furthermore, electron-ion coincidences (see Sec. 9.6.5) and delay-dependent KER spectra (see Sec. 9.6.6) are recorded.

9.6.1 Focal Spot Size

The focal spot area A is an important parameter as it is directly linked to the intensity $I \propto 1/A$ at the interaction spot. The focal diameter obtained by the previous back-reflecting split-delay optics (see Sec. 9.1) is estimated to $d \approx 30\,\mu\text{m}$ (FWHM). The design value of the new ellipsoidal mirror is $d \approx 10\,\mu\text{m}$ (FWHM). Due to the scaling of intensity like $I \propto E_{\text{pulse}}/A$, a reduction of the focal spot A is advantageous, because same intensities can be reached for lower FEL pulse energies E_{pulse}.

Wave Front Sensor

A wave front sensor (WFS) is used to analyze the optical properties of the focus [127] by comparing the actual wave front to that of a reference wave. Thereto, a thin metal plate, which has an asymmetrical grid of small holes imprinted[110], is put at $\sim 10\,\text{cm}$ distance in front of a CCD chip[111]. A distorted wave front hitting the so-called Hartmann plate will be transmitted to different positions on the CCD chip compared to a spherical reference wave. By analyzing the local intensity and slope of each spot on the CCD chip, information on wave front intensity and phase can be extracted. A back-propagation algorithm[112] uses a basis set of Zernike polynomials[113] [276] to reconstruct the wave front at arbitrary positions along the beam path.
The used WFS allows an online monitoring of the optical aberrations. Following an iterative approach, the focus is optimized by adjusting the position of the ellipsoidal mirror in space using the kinematics described in Sec. 9.4. The measurement is done in single bunch mode at a photon energy of $\hbar\omega = 56\,\text{eV}$. The results of the wave front reconstruction for the optimized focus are depicted in Fig. 9.22. The intensity profile of the smallest achieved focus is shown in Fig. 9.22 (b). The focus has a diameter

[110] Typical diameters $\sim 75\,\mu\text{m}$.
[111] For the present measurement, the *Compact Hartmann Sensor* is used. Detailed informations about this WFS can be found in Ref. [127].
[112] *MrBeam*, Laser-Laboratorium Göttingen, `https://www.llg-ev.de/willkommen/index.html`.
[113] Zernike polynomials are the appropriate choice for circular beams, for rectangular beams, Legendre polynomials are used.

$d = 3\,\mu\text{m}$ (FWHM), which is a factor of ~ 3 better than the design value[114]. WFS measurements for the KB optics at the CAMP endstation at FLASH1 yield a focus of $2 \times 4\,\mu\text{m}^2$ (FWHM) [126]. For the KB optics at the PG1 beamline, a vertical focus of $4\,\mu\text{m}$ (FWHM) is reported [49]. Assuming a typical pulse energy of $E_{\text{pulse}} = 10\,\mu\text{J}$ and a pulse duration of $T = 50\,\text{fs}$, intensities of $I \approx 10^{15}\,\text{W/cm}^2$ should be possible.

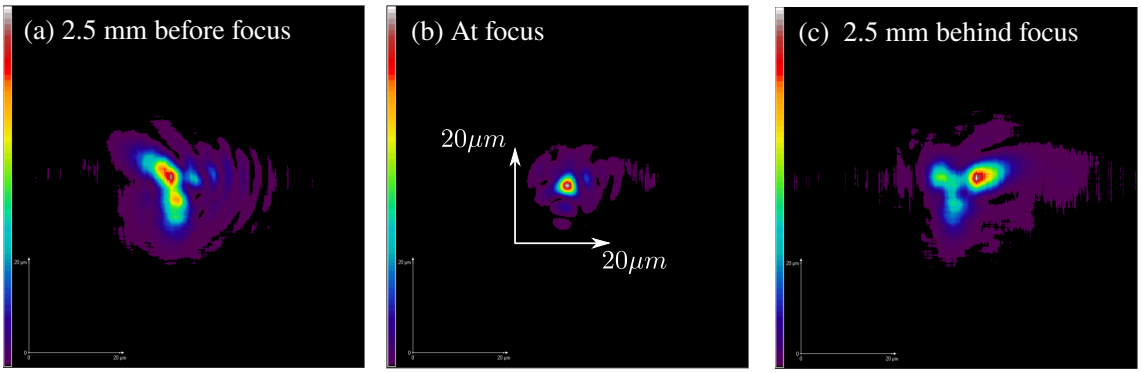

Figure 9.22: Intensity profile along the beam obtained by wave front reconstruction. (a) 2.5 mm before the focus. (b) At the focus. (c) 2.5 mm behind the focus.

Intensity Estimation by Xenon Charge States

The observed charge states in multi-photon ionization of xenon are a further benchmark of the focus size. Sorokin *et al.* [253] studied multiple ionization of xenon at FLASH at $\hbar\omega = 93\,\text{eV}$ in an intensity range from $10^{12} - 10^{16}\,\text{W/cm}^2$. The focus diameter was $d = (2.6 \pm 0.5)\,\mu\text{m}$ and the FEL pulse duration $T = (10 \pm 2)\,\text{fs}$. At maximum intensity ($I = 7.8 \times 10^{15}\,\text{W/cm}^2$), charge states up to Xe^{21+} were observed. In a similar experiment, Richter *et al.* [214] found charge states up to Xe^{19+} at $I = 2 \times 10^{15}\,\text{W/cm}^2$. Fig. 9.23 shows a TOF mass spectrum of xenon recorded with the present setup at a photon energy of $\hbar\omega = 100\,\text{eV}$ and a pulse energy of $E_{\text{pulse}} \approx 20\,\mu\text{J}$. For this measurement, the entire FEL beam is put onto the lower half of the split-mirror in order to avoid losses due to the slit between the mirror halves. The accumulations of close-by TOF peaks is attributed to the isotopy of xenon. The charge states are marked by arrows. Xe^{15+} is the highest charge state. In Ref. [214], Xe^{14+} is reached at $I = 1.7 \times 10^{15}\,\text{W/cm}^2$ and Ref. [253] sees Xe^{15+} at $I = 2 \times 10^{15}\,\text{W/cm}^2$. Taking those measurements as reference, the intensity reached with the ellipsoidal mirror can be estimate to be on the order of $1 - 2 \times 10^{15}\,\text{W/cm}^2$. This is in accordance with the focal spot size measured with the WFS for the present pulse energy of $E_{\text{pulse}} \approx 20\,\mu\text{J}$ and a pulse duration of $T = 50\,\text{fs}$. To reach Xe^{15+}, up to 32 photons need to be absorbed [253].

[114] Comparative measurements between WFS reconstruction and ablation imprints [32, 33] for the KB optics at beamline FL24 at FLASH2 [205] showed perfect agreement [204].

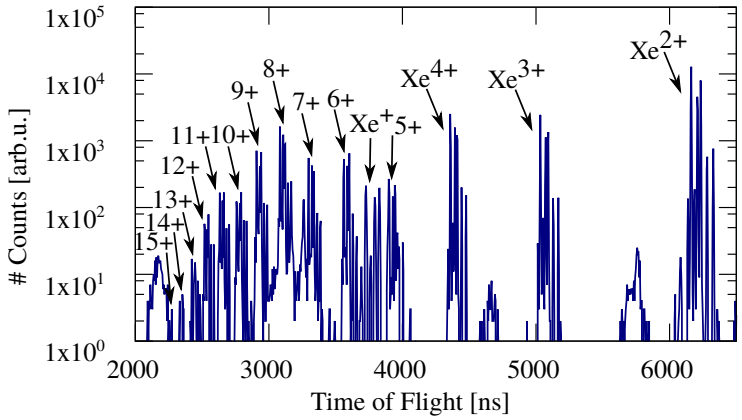

Figure 9.23: TOF mass spectrum of xenon ions recorded at $\hbar\omega = 100\,\mathrm{eV}$. For this measurement, the entire FEL beam of $E_{\mathrm{pulse}} \approx 20\,\mu\mathrm{J}$ is put onto the lower half of the split-mirror. $\mathrm{Xe}^{(1-15)+}$ ions are marked by arrows.

In XUV pump-probe operation, the FEL beam is equally distributed on the two mirror halves. The TOF spectrum recorded under this condition is depicted in Fig. 9.24. The highest recorded charge state is now Xe^{11+}, which after Ref. [253] yields an intensity of $I \approx 5 \times 10^{14}\,\mathrm{W/cm^2}$. Hence, a non-negligible amount of pulse energy is lost in the slit between the mirror halves.

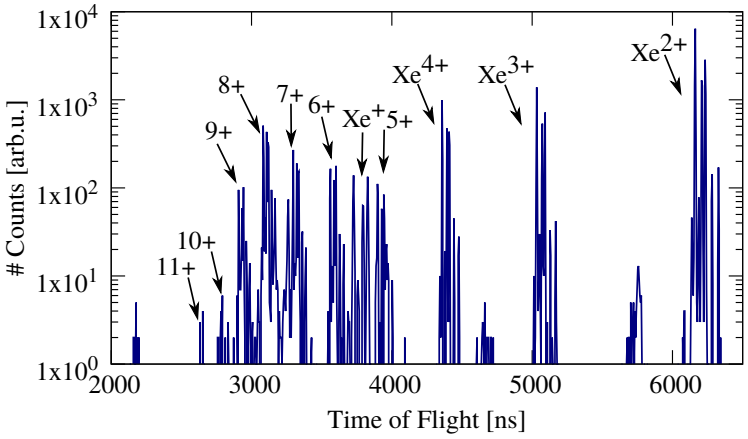

Figure 9.24: TOF mass spectrum of xenon ions recorded at $\hbar\omega = 100\,\mathrm{eV}$. For this measurement, the FEL beam of $E_{\mathrm{pulse}} \approx 20\,\mu\mathrm{J}$ is distributed equally on both halves of the split-mirror. $\mathrm{Xe}^{(1-11)+}$ ions are marked by arrows with their charge state.

9.6.2 Pointing Stability

The spatial overlap of both foci is a crucial for any pump-probe experiment. In order to determine the pointing stability, the position of the movable focus is observed on the fluorescence screen in the center of the REMI main chamber by means of the CCD camera with an optical magnification system (see Sec. 9.5). The centroid of the focal spot is determined in horizontal and vertical position. The horizontal offset Δx is plotted as a function of the delay in Fig. 9.25 (a). The absolute difference between -2000 to $+2000$ fs amounts to 45 µm. Additionally, anharmonic oscillations are superimposed. The origin of these non-linear behavior is unclear. It might be caused by a not perfectly synchronized movement of the three piezo actuators. In order to compensate the slope and the anharmonic behavior, the data is interpolated by a spline, which is then used for a correction. For each delay step, the corresponding spline value is used to correct to $\Delta x \stackrel{!}{=} 0$ fs by rotating the mirror accordingly. The delay scans shown in Fig. 9.25 (b) are recorded with the correction switched on. Now, the offset is $|\Delta x| \leq 2$ µm over the entire delay range. In the vertical direction Δy, corrections are also necessary and a stability of $|\Delta y| \leq 2$ µm is achieved as well.

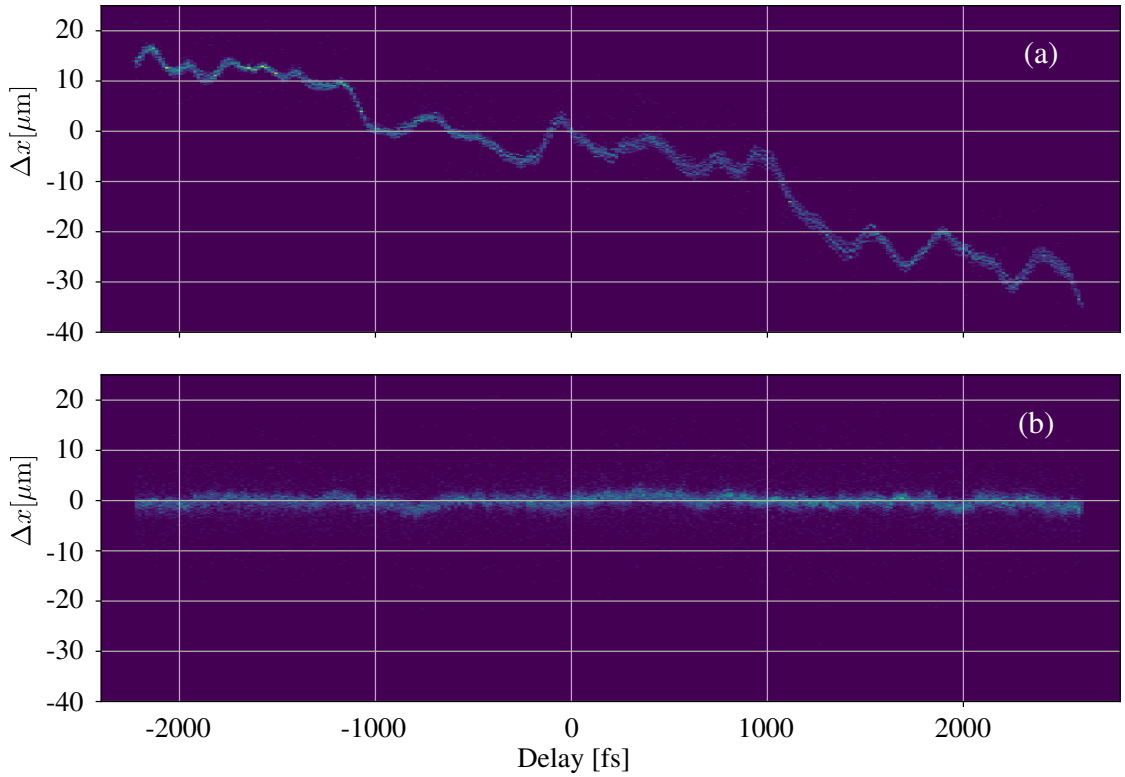

Figure 9.25: Centroid position Δx of the movable focus on the fluorescence screen as function of the delay. (a) Without correction. (b) With correction. For both plots, the delay range is scanned four times.

9.6.3 Temporal Stability

The interference pattern of an optical laser is used to calibrate the conversion factor between the covered hub $h\,[\mu\text{m}]$ and the corresponding temporal delay $t_d\,[\text{fs}]$. The laser beam is aligned to the nominal FEL beam axis, is divided by the split-mirror and focussed by the ellipsoidal mirror. The two foci are spatially overlapped on the fluorescence screen. The movable mirror half is continuously scanned and the overlapping foci are observed by the CCD camera with optical magnification system (see Sec. 9.5). Light wave interference of the split beams induces a modulation of the focal intensity. Fig. 9.26 (a) shows the modulation as a function of the hub h. The period of the modulation p_{hub} corresponds to the optical period of the laser $T = \lambda/c$ with $\lambda = 658\,\text{nm}$,

$$p_{\text{hub}} \propto T = \frac{\lambda}{c}. \tag{9.2}$$

The Fourier transform in Fig. 9.26 (b) reveals a period of $p_{\text{hub}} = 2.375\,\mu\text{m}$ and the conversion is given by

$$t_d\,[\text{fs}] = 0.923\,[\text{fs}/\mu\text{m}] \cdot h\,[\mu\text{m}]. \tag{9.3}$$

After Eq. 9.1, the conversion is geometrically given by $t_d^{\text{geo}} = (2h/c)\sin(8°)$ and

$$t_d^{\text{geo}}\,[\text{fs}] = 0.928\,[\text{fs}/\mu\text{m}] \cdot h\,[\mu\text{m}]. \tag{9.4}$$

The small difference between Eq. 9.3 and 9.1 could be for example explained by a deviation of the incidence angle on the split-mirror. For experiments, the delay axis is calibrated after Eq. 9.3.

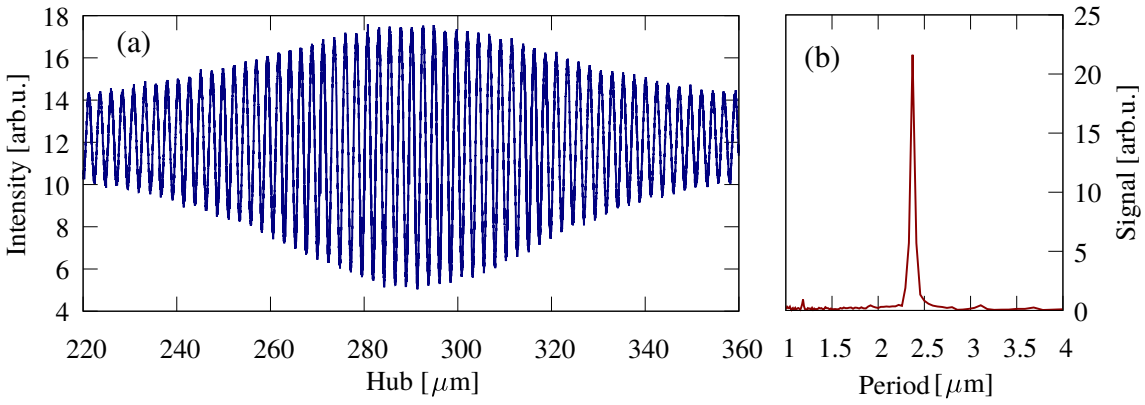

Figure 9.26: (a) Modulations of the focal intensity induced by the interference of the split beams of the optical beamline alignment laser. (b) Fourier transform of (a).

9.6.4 Stray Light Reduction

A major reason to switch to the in-line geometry is the need of stray light reduction in order to measure electron-ion coincidences. Fig. 9.27 (a) compares the stray light of the previous back-reflecting and the new in-line setup by means of counts on the ion MCP per FEL shot. Prompt photons in the range between 0 to 5 ns are almost inexistent for the new setup, whereas they contribute most for the old setup. The peak at ∼23 ns in the spectrum of the new setup can be assigned to scattered photons from the closing of the photon dump, because the corresponding path difference of ∼7 m is about twice the length of the photon dump. The similar strength of the proton peaks (see Fig. 9.27 (b)) shows that the experimental parameters are well normalized. Overall, a significant reduction of stray light is achieved.

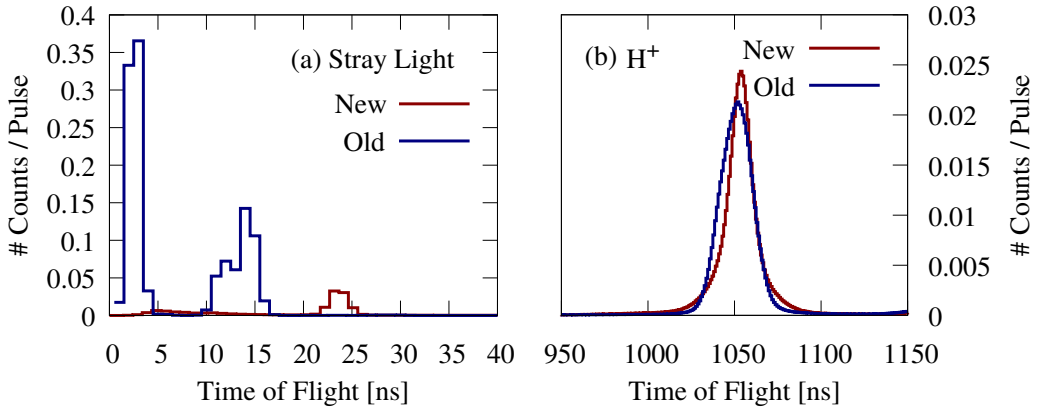

Figure 9.27: (a) Comparison of the stray light peaks in the TOF spectrum of the ion MCP for the old and the new setup. (b) Proton peaks as reference.

9.6.5 Electron-Ion Coincidences

Sequential two-photon double-ionization (TPDI) of noble gas atoms gained interest, as a careful theoretical treatments predicts the two ejected electrons to be correlated [74, 86, 87, 89, 131]. This is counter-intuitive as one naively would consider sequential TPDI as two separate ionization events. According to theory, correlations between the electrons are reflected in the angular distribution of the first ejected electron. In order to measure this distribution, the first electron of TPDI needs to be distinguished from that of single-ionization events. This can only unambiguously be done in a kinematically complete experiment, i.e., measuring the momenta of the doubly charge ion and the two electrons in coincidence [141]. Otherwise, only information about the second electron can be extracted [28].
Besides the aforementioned angular correlations of the electrons, which can be determined in a static experiment [141], sequential TPDI is also interesting from a time-dependent perspective. The idea is to map the spin-orbit wave packet, which

is induced by the superposition of the $^2P_{3/2}$ and $^2P_{1/2}$ configuration of the ionic Ne^+ state (see Fig. 9.28). A first photon launches the wave packet of 42 fs period. Afterwards, it is probed by a delayed second photon to Ne^{2+} (see Fig. 9.28). A quantum entanglement of the electrons is predicted by Ref. [192] and should be observable in the time-dependent angular correlation of the two electrons.
With the significantly reduced stray light background (see Sec. 9.6.4), the time-dependent sequential TPDI of neon is studied at a photon energy of $\hbar\omega = 44\,\text{eV}$ using the new setup. The underlying energy level scheme is depicted in Fig. 9.28.

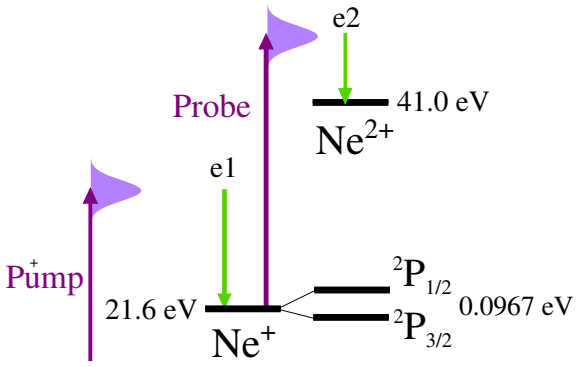

Figure 9.28: Energy level scheme illustrating the experiment on sequential TPDI of neon at $\hbar\omega = 44\,\text{eV}$. Explanations are given in the text.

A prerequisite of the experiment is the detection of the Ne^{2+} and the two electrons in coincidence. A so-called Photoelectron-Photoelectron-Photoion Coincidence (PePePiCo) map gives a first feedback. In such a plot, the TOFs of the ions are plotted against the sum of the TOFs of the first and the second electron impinging on the detector. The PePePiCo plot for the present case is shown in Fig. 9.29.
For a coincidence event, the sum of the TOFs of all particles is in first approximately constant. Thus, the diagonal line indicates the coincident detection of the three particles. The positive slope is explained by the geometry of the REMI spectrometer (see Sec. 4.2). Ions, which have an initial momentum that points towards the ion detector, have short TOFs. Consequently, the corresponding electrons start with initial momenta towards the electron detector and the sum TOF1 + TOF2 is also short. In the opposite case, ions are initially flighting towards the electron detector. The ion TOF is large and thus also the sum TOF1 + TOF2 of the corresponding electrons. Fig. 9.29 demonstrates that the new setup allows to record electron-ion coincidences, which was not possible with the previous back-reflecting setup (see Sec. 9.1). The delay-dependent analysis of the TPDI experiment is not presented in this thesis as it is part of another PhD project.

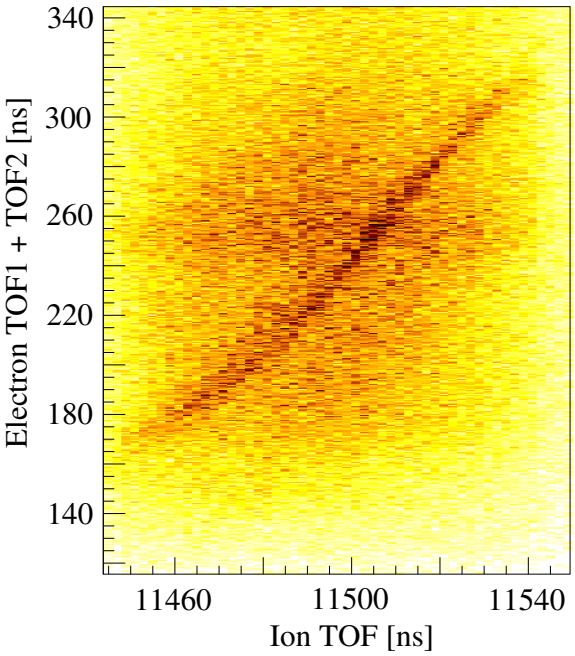

Figure 9.29: Photoelectron-Photoelectron-Photoion Coincidence (PePePiCo) map. On the horizontal axis, the ion TOF is plotted. On the vertical axis, the sum of the TOFs of the first and second detected electron is plotted.

9.6.6 Delay-Dependent KER Spectra

In order to test the pump-probe capability of the new setup, the fragmentation of Ar_2 is studied at a photon energy of $\hbar\omega = 24.8\,\text{eV}$ and FEL intensities of $I_{\text{FEL}} = 10^{13} - 10^{14}\,\text{W/cm}^2$. The KER of $Ar^+ + Ar^+$ and $Ar^{2+} + Ar^+$ ions measured in coincidence is recorded as function of the delay. An absolute delay range of 4.8 ps is scanned, i.e., close to the design value of 5.4 ps.

KER vs. Delay of $Ar^+ + Ar^+$ Ions

In Fig. 9.30, the KER of the $Ar^+ + Ar^+$ coincidence channel is plotted as a function of the delay t_d. For negative and positive delays, delay-independent contributions at $\sim 3.8\,\text{eV}$ and $\sim 5.3\,\text{eV}$ are present. They stem from uncorrelated absorption of two photons within the pump and the probe pulse. The contribution at $\sim 3.8\,\text{eV}$ is due to the direct fragmentation at the equilibrium internuclear distance R_{eq}. Thereto, two photons of $\hbar\omega = 24.8\,\text{eV}$ need to be absorbed. According to the findings of Sec. 8.1, this happens sequentially via an intermediate $Ar^+(3p^{-1}) - Ar$ state (see Fig. 9.31). The contribution at $\sim 5.3\,\text{eV}$ is induced by an ICD of an $Ar^+(3p^{-2}nl) - Ar$ state, i.e., similar to the one described in Eq. 8.4 in Sec. 8.1. The decay into $Ar^+(3p^{-1}) + Ar^+(3p^{-1})$ happens at an internuclear distance $R < R_{\text{eq}}$, which results in a higher KER compared to the fragmentation at R_{eq} (see Fig. 9.31).

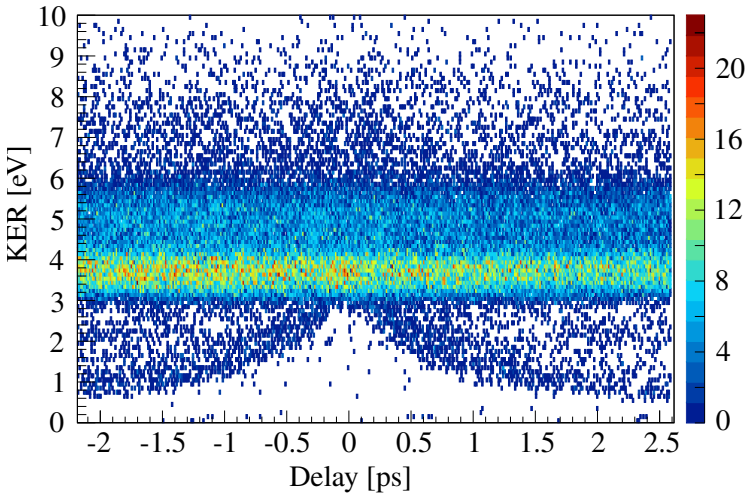

Figure 9.30: KER of $Ar^+ + Ar^+$ ions as a function of the pump-probe delay. The data are recorded at a photon energy of $\hbar\omega = 24.8\,\text{eV}$.

Besides the delay-independent contributions, Fig. 9.30 also shows a pump-probe signal. It starts at $t_d = 0\,\text{ps}$ at KER $\sim 3.8\,\text{eV}$ and ends asymptotically at KERs of $\sim 1.0\,\text{eV}$ for large delays. This signal is attributed to the dissociative photoionization channel. The pump pulse initiates the dissociation of the dimer:

$$\text{Pump} : \text{Ar} - \text{Ar} \xrightarrow{\text{XUV}} \text{Ar}^+(3p^{-1}) - \text{Ar} + e^-. \tag{9.5}$$

The delayed probe pulse interrupts the dissociation by ionizing to doubly charged states:

$$\text{Probe} : \text{Ar}^+(3p^{-1}) - \text{Ar} \xrightarrow{\text{XUV}} \text{Ar}^+(3p^{-1}) - \text{Ar}^+(3p^{-1}) + e^-. \tag{9.6}$$

The overall KER is given by that accumulated on the initial $\text{Ar}^+(3p^{-1}) - \text{Ar}$ and the final $\text{Ar}^+(3p^{-1}) - \text{Ar}^+(3p^{-1})$ curve:

$$\text{KER} = E_{\text{init}}(R_{\text{eq}}) - E_{\text{init}}(R(t_d)) + E_{\text{final}}(R(t_d)) - E_{\text{final}}(R \to \infty). \tag{9.7}$$

For large delays $|t_d| \to \infty$, $E_{\text{final}}(R(|t_d| \to \infty)) = E_{\text{final}}(R \to \infty)$ and no KER is accumulated on the final $\text{Ar}^+(3p^{-1}) - \text{Ar}^+(3p^{-1})$ curve. Thus, the asymptotically measured $Ar^+ + Ar^+$ KER of $\sim 1.0\,\text{eV}$ is a signature of the $\text{Ar}^+(3p^{-1}) - \text{Ar}$ precursor state. The asymptotic KER is reached at large delays $|t_d| \geq 2\,\text{ps}$, which corresponds to a slow dissociation. The visibility of the signal over a range of at least $\pm 2\,\text{ps}$ confirms the long-range pump-probe capability and implies that the new setup allows to trace dynamics on this time-scale.

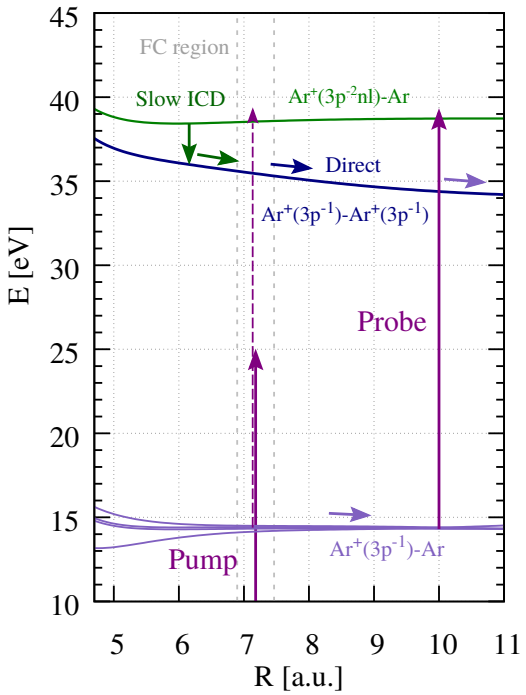

Figure 9.31: PECs of the argon dimer between $10-45\,\mathrm{eV}$. The potential energy E is given with respect to the $\mathrm{Ar}-\mathrm{Ar}$ ground state. For simplification, only a single PEC is plotted to represent $\mathrm{Ar}^+(3p^{-2}nl)-\mathrm{Ar}$ (dark-green) and $\mathrm{Ar}^+(3p^{-1})-\mathrm{Ar}^+(3p^{-1})$ (blue) states. All curves are taken from Refs. [258] and [178]. The purple vertical arrows indicate photons of $\hbar\omega$ =24.8 eV. The dashed arrow indicates the absorption of a second photon in the pump pulse. The Franck-Condon (FC) region lies within the two vertical dashed grey lines.

KER vs. Delay of $Ar^{2+}+Ar^{+}$ Ions

The KER of $\mathrm{Ar}^{2+}+\mathrm{Ar}^{+}$ ions as a function of the delay t_d is plotted in Fig. 9.32. It shows a delay-independent contribution, which is present over the entire delay range. According to Sec. 8.1.2, this contribution at KER $\sim 7.3\,\mathrm{eV}$ is due to direct fragmentation into $\mathrm{Ar}^{2+}+\mathrm{Ar}^{+}$ at R_{eq}. This is a highly non-linear processes, because it requires the absorption of four photons (see Fig. 9.33). The overall intensity is highest, if the two pulses do temporally overlap. This leads to an enhancement of the signal around delay zero. The delay-dependent signal shows two asymptotic limits. The first, strong signal has an asymptotic KER of $\sim 3.8\,\mathrm{eV}$. Thus, it coincides with the KER of fragmentation into $\mathrm{Ar}^{+}+\mathrm{Ar}^{+}$ at R_{eq} and precedes via the following scheme:

$$\mathrm{Pump}:\mathrm{Ar}-\mathrm{Ar}\xrightarrow{2\times\mathrm{XUV}}\mathrm{Ar}^{+}(3p^{-1})-\mathrm{Ar}^{+}(3p^{-1})+2e^{-}, \tag{9.8}$$

$$\mathrm{Probe}:\mathrm{Ar}^{+}(3p^{-1})-\mathrm{Ar}^{+}(3p^{-1})\xrightarrow{2\times\mathrm{XUV}}\mathrm{Ar}^{2+}(3p^{-1})-\mathrm{Ar}^{+}(3p^{-1})+e^{-}. \tag{9.9}$$

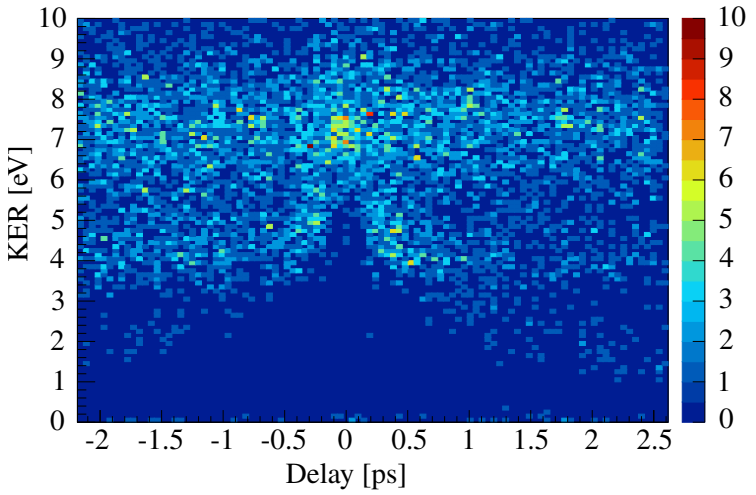

Figure 9.32: KER of $Ar^{2+} + Ar^{+}$ ions as a function of the pump-probe delay. The data are recorded at a photon energy of $\hbar\omega = 24.8\,\text{eV}$.

Fig. 9.30 shows that the asymptotic limit of this channel is reached at delays of $|t_d| \sim 0.7\,\text{ps}$. This implies that the fragmentation into $Ar^{+}(3p^{-1}) + Ar^{+}(3p^{-1})$ is much faster compared to the dissociation into $Ar^{+}(3p^{-1}) + Ar$ (see Fig. 9.30).
As shown in Fig. 9.33, two photons are absorbed in the pump and the probe step. The observation of a delay-dependent signal, which is non-linear in the pump and the probe step, points to a good performance of the new setup in terms of photon transmission. For negative delays, however, the count rate is higher compared to positive delays (see Fig. 9.32). An explanation of this phenomenon could be the loss of spatial overlap or a change in the focal spot size. This could be induced by a non-perfect alignment of the optical path with respect to the ellipsoidal mirror, when scanning the positive delay range. In the present case, such an effect is especially pronounced due to the non-linearity in the pump and the probe step. Usually, however, the photon energy is chosen such that only one photon needs to be absorbed in the pump and the probe step [237, 238]. Along these lines, the delay-dependent $Ar^{+} + Ar^{+}$ channel, i.e., one-photon pump one-photon probe, shows no inequality in the count rate between the positive and negative delay range (see Fig. 9.30).
The second delay-dependent channel is much weaker and reaches an asymptotic value of $\sim 1.0\,\text{eV}$ (see Fig. 9.32). This implies a pump-probe scheme including a $Ar^{+}(3p^{-1}) + Ar$ precursor state and the absorption of one photon in the pump and three photons in the probe step:

$$\text{Pump} : \text{Ar} - \text{Ar} \xrightarrow{\text{XUV}} \text{Ar}^{+}(3p^{-1}) - \text{Ar} - e^{-}, \tag{9.10}$$

$$\text{Probe} : \text{Ar}^{+}(3p^{-1}) - \text{Ar} \xrightarrow{3\times\text{XUV}} \text{Ar}^{2+}(3p^{-1}) - \text{Ar}^{+}(3p^{-1}) + 2e^{-}. \tag{9.11}$$

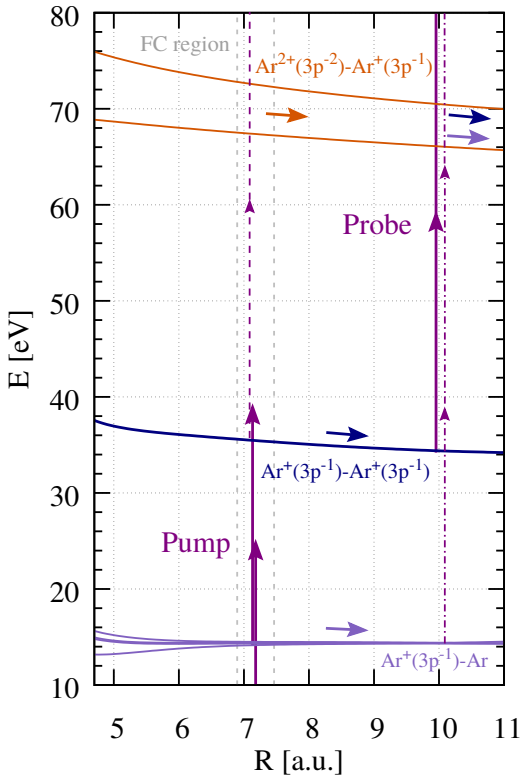

Figure 9.33: PECs of the argon dimer between $10-80\,\mathrm{eV}$. The potential energy E is given with respect to the Ar − Ar ground state. For simplification, only a single PEC (blue) is plotted to represent $\mathrm{Ar}^+(3p^{-1}) - \mathrm{Ar}^+(3p^{-1})$ states. Of the $\mathrm{Ar}^+(3p^{-1}) - \mathrm{Ar}^+(3p^{-1})$ states, the lowest and highest-lying PECs are plotted (orange). All curves are taken from Refs. [258] and [178]. The purple vertical arrows indicate photons of $\hbar\omega$ =24.8 eV. The dashed arrows indicate the absorption of two further photons in the pump step. The dashed-dotted arrows represent the probe from initial $\mathrm{Ar}^+(3p^{-1})$ – Ar states (violet). The Franck-Condon (FC) region lies within the two vertical dashed grey lines.

10 Conclusions

In this thesis, atomic argon, molecular hydrogen and argon dimers are studied in XUV-IR pump-probe experiments.
All three experiments exploit the unique properties of FEL radiation in terms of XUV pulses of few tens of femtosecond pulse duration and unprecedented high intensities (see Ch. 3). The absorption of multiple high-energetic photons within a single XUV pulse leads to a high degree of ionization and excitation of the system under investigation. In order to analyze and understand the mechanisms at work, the basic theoretical concepts of the interaction of photons with atoms, the description of many-electron atoms, the structure of diatomic molecules, interatomic relaxation mechanisms of argon dimers and the formalism of Landau-Zener transitions are summarized in Ch. 2.
With increasing complexity of the system under investigation, i.e., from atoms over diatomic molecules to dimers, also the number of ionization and relaxation channels increases. In order to follow these processes, pulses of an IR laser ($\lambda = 800\,\mathrm{nm}$, $\hbar\omega = 1.55\,\mathrm{eV}$) are employed in addition to the XUV FEL pulses. IR photons are especially advantageous for the present studies because they efficiently probe highly-excited electronic states, which are usually hard to ionize by XUV photons.
The experimental observables for the argon experiment are the yields of multiply charged Ar^{n+} ions, which are recorded as a function of the FEL intensity and the delay between XUV and IR pulse. In the experiments on H_2 and Ar_2, the kinetic energy release (KER) of the ionic fragments allows to distinguish different relaxation channels. The dynamical evolution of the processes at work is resolved by measuring the KER as a function of the pump-probe delay.
In order to detect the ions and their kinetic energy, multi-particle coincidence spectroscopy using a reaction microscope (REMI) is employed. The functionality and basic features of this instrument are presented in Ch. 4. This chapter also includes a section about the requirements and challenges of operating a REMI at an FEL. The setup for the XUV-IR experiments is presented in Ch. 5.
The conclusions drawn from the three experiments are summarized in the following in the Secs. 10.1, 10.2 and 10.3.
Furthermore, the design and the implementation of a new in-line XUV split-delay optics for the REMI endstation at the FEL FLASH2 is part of this thesis. Conclusions based on first commissioning results are compiled in Sec. 10.4.

10.1 Summary of the Argon Experiment

In Ch. 6, the multi-photon ionization of argon atoms at a photon energy of $\hbar\omega = 27\,\mathrm{eV}$ is studied at FEL intensities of $10^{13} - 10^{14}\,\mathrm{W/cm^2}$.
In an experiment using single XUV pulses, the Ar^{n+} ion yields are analyzed as a function of the FEL intensity. By "counting" the number of absorbed photons, the sequential ionization channel is found to dominate over the non-sequential. The highest charge state observed is Ar^{5+}, which requires the absorption of at least nine photons within one FEL pulse. High-lying Ar^{+*} resonances just below the Ar^{2+} double ionization threshold allow to explain the observed intensity-dependent yields of Ar^{2+} and Ar^{3+} ions.
To further investigate the role of the intermediate resonances, an IR laser pulse is used to probe the XUV multi-photon ionization pathway. The Ar^{n+} ion yields are examined as a function of the delay between the pulses as well as of their intensity. Largest delay-dependent effects on the yields are observed for Ar^{2+} ions. For the IR pulse arriving late with respect to the XUV excitation, one XUV photon less is needed to reach Ar^{2+}. This is explained by efficient population transfer from the Ar^{+*} states to the Ar^{2+} continuum by the IR pulse.

$$\mathrm{Ar} \xrightarrow{\mathrm{XUV}} \mathrm{Ar}^{+} + e^{-} \xrightarrow{\mathrm{XUV}} \mathrm{Ar}^{+*}, \tag{10.1}$$

$$\mathrm{Ar}^{+*} \xrightarrow{\mathrm{IR}} \mathrm{Ar}^{2+} + e^{-}. \tag{10.2}$$

The influence of the IR pulse on the ion yields of higher charge states is less pronounced, however, further resonances along the multi-photon ionization pathway are resolved.
The results of the argon experiment demonstrate that intermediate resonances are important to describe multi-photon multiple-ionization of an atom at XUV photon energies. It is shown that an additional IR laser pulse can be employed to reveal such resonances. The study is unique, because light-matter interaction at XUV photon energies on such a high level of non-linearity is up to now only possible at FELs. Furthermore, the results show, how different channels in a highly non-linear process like XUV multi-photon ionzation can be controlled by an assisting IR laser pulse.

10.2 Summary of the H_2 Experiment

In Ch. 7, the dissociation and fragmentation dynamics of H_2 at a photon energy of $\hbar\omega = 28.2\,\text{eV}$ and FEL intensities of $I \sim 10^{13}\,\text{W/cm}^2$ is studied by means of the KER of the final H^+ fragments.
Contributions below 1 eV to the KER distribution are attributed to non-resonant dissociative photoionization of the molecule:

$$H_2 + \hbar\omega \rightarrow H_2^+\ {}^2\Sigma_g^+(1s\sigma_g) + e^- \rightarrow H^+ + H(nl) + e^-. \tag{10.3}$$

Two further dissociation channels via excited states are identified in the KER region between $3 - 20\,\text{eV}$. The first channel requires the sequential absorption of two photons, where the second step is resonant:

$$H_2 + \hbar\omega \rightarrow H_2^+\ {}^2\Sigma_g^+(1s\sigma_g) + e^-, \tag{10.4}$$

$$H_2^+\ {}^2\Sigma_g^+(1s\sigma_g) + \hbar\omega \rightarrow H_2^+\ {}^2\Sigma_u^+(3p\sigma_u) \rightarrow H^+ + H^*. \tag{10.5}$$

The second channel is triggered by one-photon absorption. The measured KER distribution can be explained by contributions of doubly-excited H_2^{**} states, which decay via autoionization,

$$H_2 + \hbar\omega \rightarrow H_2^{**}\ Q_1\ {}^1\Sigma_u^+ \rightarrow H_2^+\ {}^2\Sigma_g^+(1s\sigma_g) + e^- \rightarrow H^+ + H(1s) + e^-, \tag{10.6}$$

and the dissociation of $H_2^+\ {}^2\Sigma_u^+(2p\sigma_u)$ states:

$$H_2 + \hbar\omega \rightarrow H_2^+\ {}^2\Sigma_u^+(2p\sigma_u) + e^- \rightarrow H^+ + H(1s) + e^-. \tag{10.7}$$

The KER of $H^+ + H^+$ ions reveals that sequential two-photon ionization via the bound intermediate $H_2^+\ {}^2\Sigma_g^+(1s\sigma_g)$ state is the dominant double ionization mechanism at work.

$$H_2\ X^1\Sigma_g^+ + \hbar\omega \rightarrow H_2^+\ {}^2\Sigma_g^+(1s\sigma_g) + e^-, \tag{10.8}$$

$$H_2^+\ {}^2\Sigma_g^+(1s\sigma_g) + \hbar\omega \rightarrow H^+ + H^+ + e^-. \tag{10.9}$$

By applying an additional IR laser pulse, the ground-state dissociation of H_2^+ is used as an intrinsic tool to find and quantify the temporal overlap between the XUV and the IR pulse. The scheme can be generalized and employed for any XUV-IR pump-probe experiment on gas-phase samples with XUV photon energies in the range of $20 - 30\,\text{eV}$, where commonly applied techniques like the dissociation of nitrogen or oxygen cannot be applied [270].

10.3 Summary of the Ar_2 Experiment

The relaxation dynamics of argon dimers after the absorption of multiple photons of $\hbar\omega = 27\,\mathrm{eV}$ is discussed in Ch. 8.
At first, the interaction with a single XUV pulse is studied. Different channels are identified by means of their specific KER. The FEL intensity is used as a control knob to adjust the number of absorbed photons and thus to successively open different relaxation channels.
At low intensities ($I = 1-5\times10^{13}\,\mathrm{W/cm^2}$), the KER distribution of $Ar^+ + Ar^+$ ions shows contributions of direct fragmentation via sequential two-photon absorption at the equilibrium internuclear distance R_{eq} (KER $\sim 3.8\,\mathrm{eV}$) and a higher KER component at $\sim 5.3\,\mathrm{eV}$, which is a signature of nuclear dynamics during the relaxation. This contribution is assigned to an ICD from a one-site ionized and excited state onto the repulsive $Ar^+(3p^{-1}) - Ar^+(3p^{-1})$ state:

$$Ar^+(3p^{-2}(^1D)4d\ ^2S) - Ar \xrightarrow{\mathrm{ICD}} Ar^+(3p^{-1}) - Ar^+(3p^{-1}) + e^-_{\mathrm{ICD}}. \tag{10.10}$$

The $Ar^+(3p^{-2}(^1D)4d\ ^2S) - Ar$ state is reached by two photons with the absorption of the second photon being resonant ($3p \to 4d$). The state has a binding character and a wave packet, which is excited at R_{eq}, moves towards smaller internuclear distances $R < R_{\mathrm{eq}}$ before it decays. Consequently, the KER is higher compared to the direct fragmentation at R_{eq}.
At high intensities ($I = 5\times10^{13}-1\times10^{14}\,\mathrm{W/cm^2}$), more photons can be absorbed and new relaxation pathways open up. This is manifested by additional contributions to the KER of $Ar^+ + Ar^+$ ions.
If the third photon removes a $3p$ electron at the already ionized and excited site, a one-site doubly ionized and excited $Ar^{2+}(3s^{-1}3p^{-1}\,^1P(+3p^{-3}(^2D)3d\,^1P))$ state is accessed. This state is of binding character with a potential minimum at $R \approx 5.5\,\mathrm{a.u.} < R_{\mathrm{eq}}$ and is crossed by repulsive curves of $Ar^+(3p^{-2}nl) - Ar^+(3p^{-1})$ character. At the curve crossings, charge can be non-adiabatically transferred:

$$Ar^{2+}(3s^{-1}3p^{-1}\,^1P(+3p^{-3}(^2D)3d\,^1P)) \xrightarrow{\mathrm{CT}} Ar^+(3p^{-2}nl) - Ar^+(3p^{-1}). \tag{10.11}$$

The crossings are situated at internuclear distances $R < R_{\mathrm{eq}}$ and the repulsive $Ar^+(3p^{-2}nl) - Ar^+(3p^{-1})$ states are steeper compared to $1/R$ Coulomb potential curves. Thus, the final KER of the $Ar^+(3p^{-2}nl) + Ar^+(3p^{-1})$ fragments is higher compared to fragmentation at R_{eq}. The charge transfer (CT) channel gives rise to KERs of $\sim 5.3\,\mathrm{eV}$ of $Ar^+ + Ar^+$ ions.
If the third photon is absorbed at the neutral site, high-lying $Ar^+(3p^{-2}nl) - Ar^+(3p^{-1})$ Rydberg states just below the triple ionization threshold are excited. These states fragment via so-called frustrated triple ionization and the final $Ar^+ + Ar^+$ ions have KERs of $\sim 7.2\,\mathrm{eV}$, i.e., close to that of $Ar^{2+} + Ar^+$ ions exploding at R_{eq} ($\sim 7.5\,\mathrm{eV}$).

By employing an XUV-IR pump-probe scheme, the mean lifetime of the CT process is determined. A delayed IR pulse probes the population of the $Ar^+(3p^{-2}nl) - Ar^+(3p^{-1})$ states after CT has occurred by ionizing the nl electron to triply ionized states:

$$Ar^+(3p^{-2}nl) - Ar^+(3p^{-1}) \xrightarrow{IR} Ar^{2+}(3p^{-2}) + Ar^+(3p^{-1}) + e^-_{nl}. \tag{10.12}$$

The delay-dependent yield of Coulomb-exploded Ar^{2+} and Ar^+ ions is the experimental observable, which contains the mean CT lifetime. A window condition on the KER is applied to select the respective ions. The mean CT lifetime of $\tau_{exp} = (531 \pm 136)\,fs$ is extracted from exponential fits to the delay-dependent Ar^{2+} and Ar^+ yields. The experiment is modeled by a classical simulation, which confirms the applied method of extracting the CT lifetime. Furthermore, the experimentally determined lifetime is compared to the value of $\tau_{LZ} = 430\,fs$ obtained by calculations of Ref. [177], which are based on Landau-Zener probabilities (see Sec.2.4.5). The calculated value underestimates the experimentally determined lifetime, however, agrees within the error bars of the fit.
The additional IR pulse also allows to probe the relaxation channel of frustrated triple ionization. The IR pulse ionizes the nl electron of the $Ar^+(3p^{-2}nl) - Ar^+(3p^{-1})$ Rydberg states and final triply ionized $Ar^{2+}(3p^{-2}) - Ar^+(3p^{-1})$ states are reached. Thus, for the IR pulse arriving late with respect to the XUV pulse, the high KER component around $\sim 7.2\,eV$ vanishes in the KER distribution of $Ar^+ + Ar^+$ ions.

The last section of Ch. 8 contains the KER distributions of higher charge states. Ion pairs with multiple charges $q_1 \cdot q_2 \leq 9$ are detected. The increasing deviation from a Coulomb explosion model with increasing multiple charge shows that the multi-photon cascade is accompanied by nuclear dynamics during the ionization steps.

10.4 Summary of the XUV Split-Delay Optics

The need to perform experiments that are at the same time capable of following nuclear dynamics and also being sensitive to electronic states, calls for an approach, which combines an XUV pump-probe scheme with the coincident detection of ions and electrons. In order to achieve such conditions, a new in-line XUV split-delay optics has been developed (see Ch. 9). Its design is based on XUV grazing incidence optics, which allows to split and delay the FEL pulses before sending them onto the target. Furthermore, the grazing incidence geometry features a high transmission between $20 - 150\,eV$ and thus allows to fully exploit the photon energy tunability of FLASH2.
The split-mirror is a plane mirror, which is horizontally cut into two halves. By moving the upper mirror back and forth, a path difference can be introduced, which

translates into a relative time delay between the pulse replicas. The delay can be scanned over a range of $\pm 2.7\,\mathrm{ps}$ with a fs-resolution by custom-made piezo-driven kinematics. In order to spatially overlap the foci in the middle of the REMI spectrometer, the upper mirror is also rotatable around the horizontal and vertical axis. This allows to spatially overlap the two foci with a precision of $\leq 2\,\mu\mathrm{m}$ for all delay values.
The split-mirror is followed by a focussing ellipsoidal mirror. The achieved focal diameter is measured to $d = 3\,\mu\mathrm{m}$ (FWHM) by a wave front sensor. This is at least a factor of five smaller compared to the previous setup. Using this small focus, xenon ion charge states up to 15+ are measured. According to literature, this corresponds to an intensities of $1 - 2 \times 10^{15}\,\mathrm{W/cm^2}$.
In the in-line geometry, the FEL beam passes the REMI spectrometer only once. This is a major advantage to a previous back-reflecting setup. It is shown that the new geometry tremendously reduces stray light background. This improvement enables to record delay-dependent electron-ion coincidence spectra, which is demonstrated in an experiment on two-photon double-ionization of neon.
The pump-probe capability over a wide delay-range of $\pm\,2\,\mathrm{ps}$ is successfully tested in an experiment on the fragmentation dynamics of argon dimers. At a photon energy of $\hbar\omega = 24\,\mathrm{eV}$, delay-dependent KER spectra are measured for the $Ar^+ + Ar^+$ and $Ar^{2+} + Ar^+$ coincidence channel.

10.5 Outlook

The results presented within this thesis demonstrate the rich knowledge gain on light-induced processes in small quantum systems, which is achieved by the combination of FEL radiation, optical laser pulses and multi-particle momentum spectroscopy. However, there is still room for future improvements. The new split-delay optics opens the window to perform time-dependent electron-ion coincidence spectroscopy at XUV photon energies. The detection of the ejected electrons will provide the so far missing piece of information on the electronic structure and thus will allow to study dynamical processes in their full entirety. For example, the present study on H_2 is not sensitive to the electronic states. This is different to single-photon experiments at synchrotrons, which strongly benefit from also detecting the electrons. At synchrotrons, however, the intensity is not sufficient to allow for multi-photon absorption studies or for time-resolved experiments in an XUX pump-probe scheme [121, 237, 238]. To date, FELs are the only radiation sources where such types of experiments can be performed.
Referring to this thesis, a pioneering study of this kind could be the observation of multiple interatomic relaxation channels in argon dimers in an XUV pump-probe experiment. The experimental observable is the time-dependent KER of argon dimer fragments, which have the signature of the nuclear dynamics of the different relax-

ation pathways imprinted. Measuring the emitted electrons in coincidence allows to unambiguously assign the involved electronic states.
The wavelength tunability of FLASH2 can be employed to trigger distinct relaxation pathways. Three possible channels (fast ICD, slow ICD and RCT) and the respective pump-probe schemes are depicted in Fig. 10.1.

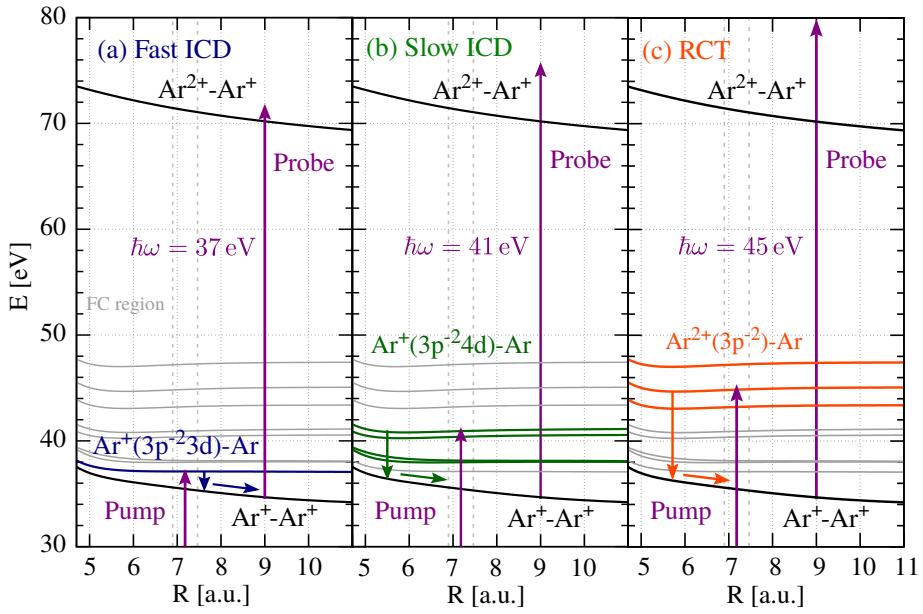

Figure 10.1: Illustration of three relaxation channels in the argon dimer. A Fast ICD (a), a slow ICD (b) and an RCT (c) can be investigated by an XUV pump-probe experiment.

Another idea for an XUV pump-probe on Ar_2 is to study the nuclear-wave-packet oscillation in the ionic Ar_2^+ state. A first XUV pulse launches a nuclear wave packet in Ar_2^+, which is mapped by a succeeding XUV pulse onto the repulsive $Ar^+ - Ar^+$ curve. The delay-dependent KER of $Ar^+ + Ar^+$ ions will contain information about the temporal evolution of the wave packet. The period of the nuclear wave packet oscillation is $\sim 270\,\mathrm{fs}$ [285], which should be resolvable with $\leq 50\,\mathrm{fs}$ FEL pulses.
An IR pump-probe laser [263] is the next upgrade of the FLASH2 facility. It will also be available at the REMI endstation. The laser system is OPCPA based and will provide pulses of sub-20 fs within bursts with a repetition rate of 10 Hz and an intra-burst repetition rate of 50 kHz. Each pulse can reach energies of 0.5 mJ at a center wavelength of 800 nm. The timing jitter between laser and FEL pulses is intended to be $<50\,\mathrm{fs}$ (rms) and peak intensities of $>10^{15}\,\mathrm{W/cm^2}$ should be reachable in the focus. The incoupling mirror of the laser is already installed in the last section of the REMI beamline (see Sec. 9.5). The laser system is supposed to be operational by the mid of 2018.

The higher repetition rate will help to collect more statistics in a shorter period of time, which is especially advantageous for REMI experiments.
With shorter IR pulses and a stable FEL-IR laser synchronization, one might repeat the experiment on IR-assisted multi-photon of argon with a better temporal resolution. This will allow to observe Rabi oscillations not only for the $Ar^+ \leftrightarrow Ar^{+*}$ transition (see Ref. [69]), but also for resonant transitions for higher charge states.
Furthermore, in cooperation with a group at the University of Hanover, a HHG source will be integrated into the REMI beamline. This will further extend the portfolio of available radiation sources and allow for two-color XUV pump-probe spectroscopy.

Appendix

A Atomic Units

The system of atomic units is commonly used in atomic and molecular physics. It is based on setting the following quantities to unity.

- Electron mass m_e
- Elementary charge e
- Classical Bohr radius a_0
- Planck's constant $\hbar$
- $\frac{1}{4\pi\epsilon_0}$ with the electric constant ϵ_0

The abbreviation used for all quantities given in atomic units is "a.u.". An overview of quantities in atomic units and their conservation to SI units is given in Tab. A.1.

Table A.1: Atomic units. Taken from Ref. [246].

Quantity	Expression	Value in SI units
Mass	m_e	$9.109 \times 10^{-31}\,\mathrm{kg}$
Charge	e	$1.602 \times 10^{-19}\,\mathrm{C}$
Length	a_0	$5.292 \times 10^{-11}\,\mathrm{m}$
Angular Momentum	$\hbar = h/(2\pi)$	$1.055 \times 10^{-34}\,\mathrm{kg\,m^2\,s^{-1}}$
Energy	$\hbar^2/(m_e a_0^2)$	$4.360 \times 10^{-18}\,\mathrm{J}$
Time	$m_e a_0^2/\hbar$	$2.419 \times 10^{-17}\,\mathrm{m\,s^{-1}}$
Velocity	$\hbar/(m_e a_0^2) = c\alpha$	$2.188 \times 10^{6}\,\mathrm{kg}$
Momentum	$\hbar/a_0$	$1.993 \times 10^{-24}\,\mathrm{kg\,m\,s^{-1}}$

B Reconstruction of Electron Momenta

Transverse Electron Momentum

Because of momentum conservation $\mathbf{p}_{\text{ion}} = -\mathbf{p}_{\text{electron}}$, electrons with the same initial momentum as the associated ion have a m_{ion}/m_e-times higher velocity[115]. Already for the lightest ion, the proton, the mass ratio is $m_{\text{proton}}/m_e \approx 1800$. Hence, under typical experimental conditions, i.e., electric field strength in the order of few tens V/cm, most of the electrons, especially those emitted transversally, would not reach the electron detector. However, the magnetic field B in z-direction forces the electrons of mass m_e on cyclotron orbits of frequency $\omega_c = eB/m_e$ (see Fig. B.1 (a)). The radius r of a cyclotron orbit is proportional to the initial transverse electron momentum $p_{(x,y)}$:

$$r = \frac{p_{(x,y)}}{m_e \omega_c} = \frac{p_{(x,y)}}{eB}. \tag{B.1}$$

Experimentally, the cyclotron radius r is not directly measurable. In analogy to the ions, the interaction point is projected onto the center-of-mass of the electrons' spatial distribution on the detector due to symmetry reasons. Some geometrical considerations are needed to determine the cyclotron radius r by measuring the radial distance R between a point of impact on the detector and the center-of-mass of the electron distribution (see Fig. B.1 (b)). The vector from the origin to the point of impact depends on the angle of revolution $\alpha = w_c t$ during the time of flight t. The evaluation of the sketch shown in Fig. B.1 (b) results in a cyclotron radius

$$r = \frac{R}{2 \left| \sin\left(\frac{w_c t}{2}\right)\right|}. \tag{B.2}$$

Here, R is the length of the vector pointing from the origin to the impact position. Equating Eq. B.1 with Eq. B.2 yields the absolute value of the transverse electron momentum[116]:

$$p_{(x,y)} = \frac{eRB}{2 \left| \sin\left(\frac{w_c t}{2}\right)\right|}. \tag{B.3}$$

The initial emission direction of the electron is defined by an angle φ relative to an arbitrarily chosen reference axis in the detector plane[117]. To compute φ, the angle θ between the vector to the impact position and the reference axis as well as the rotation angle α crossed during the time of flight t is needed:

$$\varphi = \theta \pm \alpha = \arctan\left(\frac{y}{x}\right) \pm \frac{\omega_c t}{2}. \tag{B.4}$$

[115] This section is compiled from Ref. [234].

[116] In atomic units: $p_{(x,y)}[\text{a.u.}] = \left(4.02 \cdot 10^{-3} \frac{\text{a.u.}}{\text{mm Gs}}\right) \frac{RB}{\left|\sin\left(\frac{w_c t}{2}\right)\right|}$ with $[R]$=mm, $[B]$=Gs.

[117] Here defined in x-direction.

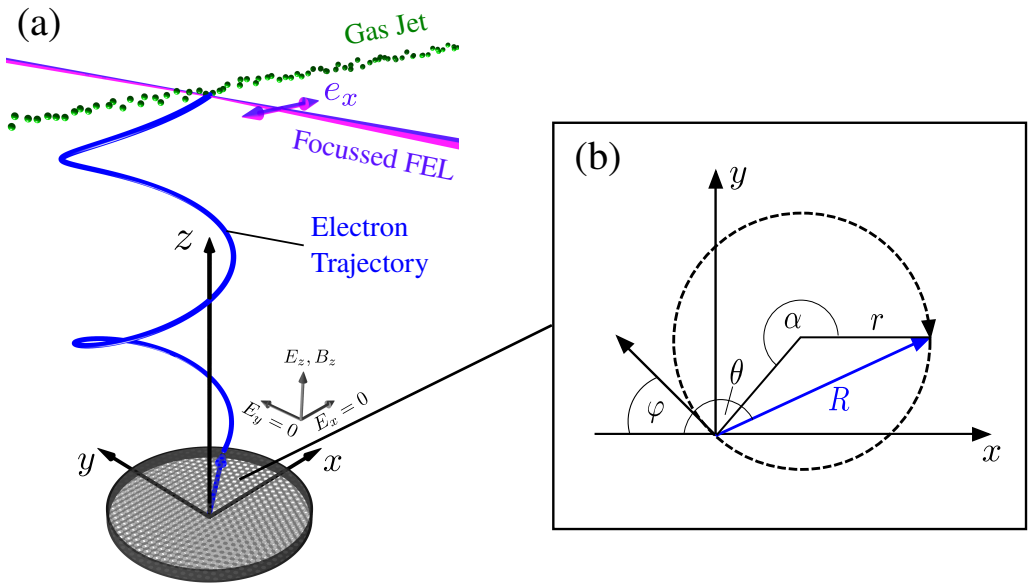

Figure B.1: Determination of the transverse electron momentum. (a) Schematic representation of an electron trajectory (blue) on a cyclotron orbit from the interaction point, i.e., the crossing point of the gas jet (green balls) with the focussed FEL beam (purple), to the detector. (b) Geometrical considerations necessary to determine the cyclotron radius r. Thereto, the radius R and the angle θ are measured. By accounting for the cyclotron frequency ω_c and the time of flight t, the angle of revolution $\alpha = w_c t$ is determined.

The sign of α is defined by the sense of rotation, which depends on the direction of the magnetic field. From Eqs. B.3 and B.4, it becomes clear that besides the impact position also the absolute time of flight t is needed in order to determine the transverse momentum $p_{(x,y)}$.
The periodicity of the cyclotron motion in 2π entails that electrons, whose time of flight is an integer multiple of the cyclotron period $T_c = 2\pi/\omega_c$, are imaged into one spot on the detector independent from their initial momentum. The transverse momentum of such electrons cannot be resolved. If the radius R is plotted versus the time of flight, the cyclotron period T_c is determinable by looking for the temporal distance between two so-called wiggles, i.e., the accumulations of minimum transverse momenta (see Fig. B.2). If the time of flight is known to the precision of one cyclotron period, the absolute time of flight can be determined to the accuracy achieved in measuring the cyclotron period T_c.

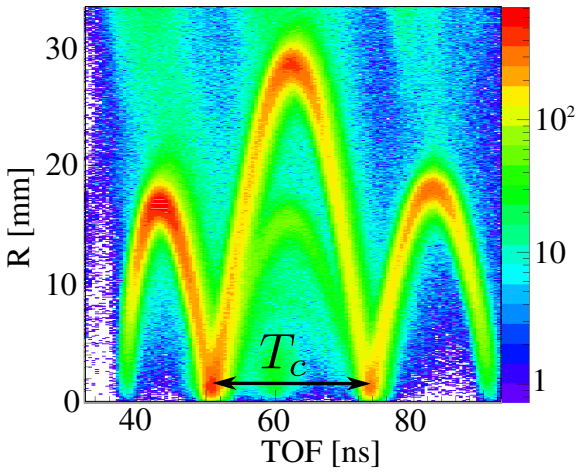

Figure B.2: Wiggle plot. The electron radius R on the detector is plotted against the time of flight (TOF) of electrons. The cyclotron period T_c is determined by looking at the distance between two wiggles.

Longitudinal Electron Momentum

The magnetic field does not affect the electron trajectory in time of flight direction. Thus, as for the ions, the longitudinal electron momentum is determined by the time of flight t. The voltage U and the corresponding acceleration length l_a have to be known in addition. In analogy to ions (see Eq. 4.10), the longitudinal electron momentum is given by

$$p_z = \frac{l_a m_e}{t} - \frac{qUt}{2l_a}. \tag{B.5}$$

List of Publications

The results of this thesis have not been published in other references.

Publications with own contributions:

K. Schnorr, A. Senftleben, M. Kurka, A. Rudenko, L. Foucar, G. Schmid, A. Broska, T. Pfeifer, K. Meyer, D. Anielski, R. Boll, D. Rolles, M. Kübel, M.F. Kling, Y.H. Jiang, S. Mondal, T. Tachibana, K. Ueda, T. Marchenko, M. Simon, G. Brenner, R. Treusch, S. Scheit, V. Averbukh, J. Ullrich, C.D. Schröter, and R. Moshammer Time-Resolved Measurement of Interatomic Coulombic Decay in Ne_2. *Physical Review Letters*, 111(9):093402, 2013.

K. Schnorr, A. Senftleben, M. Kurka, A. Rudenko, G. Schmid, T. Pfeifer, K. Meyer, M. Kübel, M. F. Kling, Y. H. Jiang, R. Treusch, S. Düsterer, B. Siemer, M. Wöstmann, H. Zacharias, R. Mitzner, T. J. M. Zouros, J. Ullrich, C. D. Schröter, and R. Moshammer. Electron Rearrangement Dynamics in Dissociating I_2^{n+} Molecules Accessed by Extreme Ultraviolet Pump-Probe Experiments. *Physical Review Letters*, 113:073001, 2014.

K. Schnorr, A. Senftleben, G. Schmid, S. Augustin, M. Kurka, A. Rudenko, L. Foucar, A. Broska, K. Meyer, D. Anielski, R. Boll, D. Rolles, M. Kübel, M.F. Kling, Y.H. Jiang, S. Mondal, T. Tachibana, K. Ueda, T. Marchenko, M. Simon, G. Brenner, R. Treusch, S. Scheit, V. Averbukh, J. Ullrich, T. Pfeifer, C. D. Schröter, and R. Moshammer. Multiple ionization and fragmentation dynamics of molecular iodine studied in IR-XUV pump-probe experiments. *Faraday Discussions*, 171:41-56, 2014.

K. Schnorr, A. Senftleben, G. Schmid, S. Augustin, M. Kurka, A. Rudenko, L. Foucar, A. Broska, K. Meyer, D. Anielski, R. Boll and D. Rolles, M. Kübel, M.F. Kling, Y.H. Jiang, S. Mondal, T. Tachibana, K. Ueda, T. Marchenko, M. Simon, G. Brenner, R. Treusch, S. Scheit, V. Averbukh, J. Ullrich, T. Pfeifer, C. D. Schröter, and R. Moshammer. Time-resolved study of ICD in Ne dimers using FEL radiation. *Journal of Electron Spectroscopy and Related Phenomena*, 204:245-246, 2015

T. Schlathölter, G. Reitsma, D. Egorov, O. Gonzalez-Magaña, S. Bari, L. Boschman, E. Bodewits, K. Schnorr, G. Schmid, C.D. Schröter, R. Moshammer, and R. Hoekstra. Multiple Ionization of Free Ubiquitin Molecular Ions in Extreme Ultraviolet Free-Electron Laser Pulses *Angewandte Chemie*, 55:10741-10745, 2016.

Bibliography

[1] T. Åberg. Theory of X-Ray Satellites. *Physical Review*, 156:35–41, 1967.

[2] W. Ackermann *et al.* Operation of a free-electron laser from the extreme ultraviolet to the water window. *Nature Photonics*, 1:336–342, 2007.

[3] P. Agostini and L. F. DiMauro. The physics of attosecond light pulses. *Reports on Progress in Physics*, 67(6):813, 2004.

[4] H. Aksela and S. Aksela. Photoionization and Auger decay in free atoms, molecules and small clusters. *Radiation Physics and Chemistry*, 76:370–374, 2007.

[5] E. Allaria *et al.* Highly coherent and stable pulses from the FERMI seeded free-electron laser in the extreme ultraviolet. *Nature Photonics*, 6(10):699–704, 2012.

[6] A. S. Alnaser *et al.* Subfemtosecond steering of hydrocarbon deprotonation through superposition of vibrational modes. *Nature Communications*, 5:3800, 2014.

[7] M. Altarelli. From 3rd- to 4th-generation light sources: Free-electron lasers in the x-ray range. *Crystallography Reports*, 55(7):1145–1151, 2010.

[8] M. V. Ammosov, N. B. Delone, and V. P. Krainov. Tunnelionization of complex atoms and of atomic ions in an alternating electromagnetic field. *Soviet Physics Journal of Experimental and Theoretical Physics*, 64(6):1191–1194, 1986.

[9] T. Aoto *et al.* Dissociative photoionization of H_2 at high photon energies: uncovering new series of doubly excited states. *Chemical Physics Letters*, 389(1):145–149, 2004.

[10] S. Askeland and M. Førre. Probing two-center interference in $H_2{}^+$ using chirped pulses. *Physical Review A*, 88:043411, 2013.

[11] D. Attwood and A. Sakdinawat. *X-Rays and Extreme Ultraviolet Radiation: Principles and Applications*. Cambridge University Press, 2017.

[12] V. Averbukh, I. B. Müller, and L. S. Cederbaum. Mechanism of Interatomic Coulombic Decay in Clusters. *Physical Review Letters*, 93:263002, 2004.

[13] V. Ayvazyan *et al.* First operation of a free-electron laser generating GW power radiation at 32 nm wavelength. *The European Physical Journal D - Atomic, Molecular, Optical and Plasma Physics*, 37:297–303, 2006.

[14] S. Barmaki and H. Bachau. Coulomb explosion of H_2^+ wave packet in ultrashort XUV laser fields. *Journal of Physics B: Atomic, Molecular and Optical Physics*, 40(3):463, 2007.

[15] U. Becker and D. A. Shirley. *VUV and Soft X-ray Photoionization*. Springer, 1996.

[16] C. Benvenuti *et al.* A novel route to extreme vacua: the non-evaporable getter thin film coatings. *Vacuum*, 53(1):219–225, 1999.

[17] C. Benvenuti *et al.* Vacuum properties of TiZrV non-evaporable getter films. *Vacuum*, 60(1):57–65, 2001.

[18] C. Beylerian, S. Saugout, and C. Cornaggia. Non-sequential double ionization of H_2 using ultrashort 10 fs laser pulses. *Journal of Physics B: Atomic, Molecular and Optical Physics*, 39(6):L105, 2006.

[19] J. Bjorken and S. Drell. *Relativistic Quantum Mechanics*. McGraw-Hill Education, 1998.

[20] I. Bocharova. *Laser Coulomb Explosion Imaging of Molecular Dynamics*. Lap Lambert Academic Publishing GmbH KG, 2011.

[21] R. Bonifacio, F. Casagrande, and G. Casati. Cooperative and chaotic transition of a free electron laser Hamiltonian model. *Optics Communications*, 40(3):219–223, 1982.

[22] R. Bonifacio, C. Pellegrini, and L. M. Narducci. Collective instabilities and high-gain regime in a free electron laser. *Optics Communications*, 50(6):373–378, 1984.

[23] M. Born and R. Oppenheimer. Zur Quantentheorie der Molekeln. *Annalen der Physik*, 389(20):457–484, 1927.

[24] B. Boudaiffa *et al.* Resonant Formation of DNA Strand Breaks by Low-Energy (3 to 20 eV) Electrons. *Science*, 287(5458):1658–1660, 2000.

[25] T. Brabec and F. Krausz. Intense few-cycle laser fields: Frontiers of nonlinear optics. *Reviews of Modern Physics*, 72:545–591, 2000.

[26] B. H. Bransden and C. J. Joachain. *Physics of Atoms and Molecules*. Longman Group, 1983.

[27] M. Braune *et al.* A non-invasive online photoionization spectrometer for FLASH2. *Journal of Synchrotron Radiation*, 23(1):10–20, 2016.

[28] M. Braune *et al.* Electron angular distributions of noble gases in sequential two-photon double ionization. *Journal of Modern Optics*, 63(4):324–333, 2016.

[29] A. Broska. *Koinzidenter Nachweis von Elektronen und Xenonionen am Freie-Elektronen-Laser in Hamburg.* Bachelor Thesis, University Heidelberg, 2012.

[30] L. S. Cederbaum and W. Domcke. *Theoretical Aspects of Ionization Potentials and Photoelectron Spectroscopy: A Green's Function Approach*, pages 205–344. John Wiley & Sons, Inc., 2007.

[31] L. S. Cederbaum, J. Zobeley, and F. Tarantelli. Giant Intermolecular Decay and Fragmentation of Clusters. *Physical Review Letters*, 79:4778–4781, 1997.

[32] J. Chalupský *et al.* Characteristics of focused soft x-ray free-electron laser beam determined by ablation of organic molecular solids. *Optics Express*, 15(10):6036–6043, 2007.

[33] J. Chalupský *et al.* Spot size characterization of focused non-gaussian x-ray laser beams. *Optics Express*, 18(26):27836–27845, 2010.

[34] Z. Chang, P. B. Corkum, and S. R. Leone. Attosecond optics and technology: progress to date and future prospects (invited). *Journal of the Optical Society of America B*, 33(6):1081–1097, 2016.

[35] J. A. Clarke. *The Science and Technology of Undulators and Wigglers.* Oxford Series on Synchrotron Radiation. OUP Oxford, 2004.

[36] J. Coe and P. Fromme. Serial Femtosecond Crystallography Opens New Avenues for Structural Biology. *Protein and Peptide Letters*, 23(3):255–272, 2016.

[37] R. Colle, A. Mitrushenkov, and S. Simonucci. Ab initio study of valence correlation satellites in photoelectron spectra of neon. *Journal of Electron Spectroscopy and Related Phenomena*, 123(1):85–96, 2002.

[38] J. E. Collin. Autoionization in atomic and molecular physics. *Endeavour*, 1(3):122–128, 1977.

[39] Wikimedia Commons. Franck-Condon-Prinzip, 2007.

[40] P. B. Corkum and F. Krausz. Attosecond science. *Nature Physics*, 3(6):381–387, 2007.

[41] P. Cörlin. *Tracing ultra-fast molecular dynamics in O_2^+ and N_2^+ with XUV-IR pump-probe experiments.* PhD Thesis, University Heidelberg, 2015.

[42] G. Y. Csanak, H. S. Taylor, and R. Yaris. Green's function technique in atomic and molecular physics. volume 7 of *Advances in Atomic and Molecular Physics*, pages 287–361. Academic Press, 1971.

[43] S. De *et al.* Following dynamic nuclear wave packets in N_2,O_2, and CO with few-cycle infrared pulses. *Physical Review A*, 84:043410, 2011.

[44] D. A. G. Deacon *et al.* First operation of a free-electron laser. *Physical Review Letters*, 38:892–894, 1977.

[45] W. Demtröder. *Atoms, Molecules and Photons: An Introduction to Atomic-, Molecular- and Quantum Physics*. Graduate Texts in Physics. Springer Berlin Heidelberg, 2010.

[46] G. Doumy *et al.* Nonlinear Atomic Response to Intense Ultrashort X Rays. *Physical Review Letters*, 106:083002, 2011.

[47] S. Düsterer *et al.* Spectroscopic characterization of vacuum ultraviolet free electron laser pulses. *Optics Letters*, 31(11):1750–1752, 2006.

[48] K. G. Dyall and F. P. Larkins. Satellite structure in the argon 2s photoelectron spectrum. *Journal of Physics B: Atomic and Molecular Physics*, 15(7):1021, 1982.

[49] S. Dziarzhytski *et al.* Microfocusing at the PG1 beamline at FLASH. *Journal of Synchrotron Radiation*, 23(1):123–131, 2016.

[50] C. Edeler, I. Meyer, and S. Fatikow. *Simulation and Measurements of Stick-Slip-Microdrives for Nanorobots*, pages 109–116. Springer Netherlands, Dordrecht, 2010.

[51] A. Einstein. Über einen die Erzeugung und Verwandlung des Lichtes betreffenden heuristischen Gesichtspunkt. *Annalen der Physik*, 322(6):132–148, 1905.

[52] P. Emma. First lasing and operation of an angstrom-wavelength free-electron laser. *Nature Photonics*, 4(9):641–647, 2010.

[53] T. Ergler *et al.* Time-Resolved Imaging and Manipulation of H_2 Fragmentation in Intense Laser Fields. *Physical Review Letters*, 95(9):093001, 2005.

[54] T. Ergler *et al.* Ultrafast mapping of H_2^+ (D_2^+) nuclear wave packets using time-resolved Coulomb explosion imaging. *Journal of Physics B: Atomic, Molecular and Optical Physics*, 39(13):S493, 2006.

[55] B. Erk. *Fragmentation Dynamics of Small Molecules upon Multiple Ionization by X-Ray Free-Electron Laser Pulses*. PhD Thesis, University Heidelberg, 2013.

[56] B. Erk *et al.* Ultrafast Charge Rearrangement and Nuclear Dynamics upon Inner-Shell Multiple Ionization of Small Polyatomic Molecules. *Physical Review Letters*, 110:053003, 2013.

[57] B. Erk *et al.* Imaging charge transfer in iodomethane upon x-ray photoabsorption. *Science*, 345(6194):288–291, 2014.

[58] B. Faatz *et al.* Simultaneous operation of two soft x-ray free-electron lasers driven by one linear accelerator. *New Journal of Physics*, 18(6):062002, 2016.

[59] L. Fechner. *High resolution experiments on strong-field ionization of atoms and molecules: test of tunneling theory, the role of doubly excited states, and channel-selective electron spectra*. PhD Thesis, University Heidelberg, 2014.

[60] J. Feldhaus, J. Arthur, and J. B. Hastings. X-ray free-electron lasers. *Journal of Physics B: Atomic, Molecular and Optical Physics*, 38(9):S799, 2005.

[61] J. Fernández and F. Martín. Autoionizing $^1\Sigma_u^+$ and $^1\Pi_u$ states of H_2 above the third and fourth ionization thresholds. *Journal of Physics B: Atomic, Molecular and Optical Physics*, 34(21):4141, 2001.

[62] J. Fernández and F. Martín. Electron and ion angular distributions in resonant dissociative photoionization of H_2 and D_2 using linearly polarized light. *New Journal of Physics*, 11(4):043020, 2009.

[63] B. Feuerstein and U. Thumm. Mapping of coherent and decohering nuclear wave-packet dynamics in D_2^+ with ultrashort laser pulses. *Physical Review A*, 67:063408, 2003.

[64] A. Fischer. *Dissociative Photoionization of Molecular Hydrogen*. PhD Thesis, University Heidelberg, 2015.

[65] A. Fischer *et al.* Molecular wave-packet dynamics on laser-controlled transition states. *Physical Review A*, 93:012507, 2016.

[66] B. Fischer *et al.* Steering the Electron in $H_2{}^+$ by Nuclear Wave Packet Dynamics. *Physical Review Letters*, 105:223001, 2010.

[67] D. Fischer *et al.* Ion-Lithium Collision Dynamics Studied with a Laser-Cooled In-Ring Target. *Physical Review Letters*, 109:113202, 2012.

[68] L. B. Fletcher *et al.* Ultrabright X-ray laser scattering for dynamic warm dense matter physics. *Nature Photonics*, 9(4):274–279, 2015.

[69] M. Flögel *et al.* Rabi oscillations in extreme ultraviolet ionization of atomic argon. *Physical Review A*, 95:021401, 2017.

[70] R. L. Fork *et al.* Compression of optical pulses to six femtoseconds by using cubic phase compensation. *Optics Letters*, 12(7):483–485, 1987.

[71] M. Førre, S. Barmaki, and H. Bachau. Nuclear Interference in the Coulomb Explosion of H_2^+ in Short vuv Laser Fields. *Physical Review Letters*, 102:123001, 2009.

[72] M. Förstel. Autoionization Mediated by Electron Transfer. *Physical Review Letters*, 106:033402, 2011.

[73] R. R. Freeman *et al.* Above-threshold ionization with subpicosecond laser pulses. *Physical Review Letters*, 59(10):1092–1095, 1987.

[74] S. Fritzsche *et al.* Angular distributions and angular correlations in sequential two-photon double ionization of atoms. *Journal of Physics B: Atomic, Molecular and Optical Physics*, 41(16):165601, 2008.

[75] U. Frühling *et al.* Single-shot terahertz-field-driven X-ray streak camera. *Nature Photonics*, 3(10):523–528, 2009.

[76] G. Fujimoto *et al.* Generation and measurement of optical pulses as short as 16 fs. *Applied Physics Letters*, 44:832–834, 1984.

[77] H. Fukuzawa *et al.* Photoelectron spectroscopy of sequential three-photon double ionization of Ar irradiated by EUV free-electron laser pulses. *Journal of Physics B: Atomic, Molecular and Optical Physics*, 43(11):111001, 2010.

[78] H. Fukuzawa *et al.* Deep Inner-Shell Multiphoton Ionization by Intense X-Ray Free-Electron Laser Pulses. *Physical Review Letters*, 110:173005, 2013.

[79] J. W. Gallagher *et al.* Absolute Cross Sections for Molecular Photoabsorption, Partial Photoionization, and Ionic Photofragmentation Processes. *Journal of Physical and Chemical Reference Data*, 17(1):9–153, 1988.

[80] K. Gokhberg. Private communication. 2017.

[81] K. Gokhberg *et al.* Site- and energy-selective slow-electron production through intermolecular Coulombic decay. *Nature*, 505:661–663, 2013.

[82] M. Göppert-Mayer. Über Elementarakte mit zwei Quantensprüngen. *Annalen der Physik*, 401(3):273–294, 1931.

[83] E. Goulielmakis *et al.* Single-Cycle Nonlinear Optics. *Science*, 320(5883):1614–1617, 2008.

[84] I. P. Grant. *Relativistic Quantum Theory of Atoms and Molecules: Theory and Computation*. Springer Series on Atomic, Optical, and Plasma Physics. Springer New York, 2007.

[85] I. Grguras *et al.* Ultrafast X-ray pulse characterization at free-electron lasers. *Nature Photonics*, 6:852–857, 2012.

[86] A. N. Grum-Grzhimailo *et al.* Angular distributions and correlations in sequential two-photon atomic double ionization. *Journal of Physics: Conference Series*, 194(1):012004, 2009.

[87] E. V. Gryzlova *et al.* Angular correlations between two electrons emitted in the sequential two-photon double ionization of atoms. *Journal of Physics B: Atomic, Molecular and Optical Physics*, 43(22):225602, 2010.

[88] E. V. Gryzlova *et al.* Doubly resonant three-photon double ionization of Ar atoms induced by an EUV free-electron laser. *Physical Review A*, 84:063405, 2011.

[89] E. V. Gryzlova *et al.* Similarity between the angular distributions of the first- and second-step electrons in sequential two-photon atomic double ionization. *Journal of Electron Spectroscopy and Related Phenomena*, 204:277–283, 2015.

[90] R. Guichard *et al.* Multiple ionization of neon by soft x-rays at ultrahigh intensity. *Journal of Physics B: Atomic, Molecular and Optical Physics*, 46(16):164025, 2013.

[91] M. H. Hablanian. *High-Vacuum Technology: A Practical Guide, Second Edition*. CRC Press, 2017.

[92] S. Hädrich *et al.* High photon flux 70 ev hhg source for applications in molecular and solid state physics. In *High-Brightness Sources and Light-Driven Interactions*, page HT1B.2. Optical Society of America, 2016.

[93] H.-J. Hagemann, W. Gudat, and C. Kunz. Optical constants from the far infrared to the x-ray region: Mg, Al, Cu, Ag, Au, Bi, C, and Al_2O_3. *Journal of the Optical Society of America*, 65(6):742–744, 1975.

[94] O. F. Hagena. Nucleation and growth of clusters in expanding nozzle flows. *Surface Science*, 106(1):101–116, 1981.

[95] O. F. Hagena. Cluster ion sources (invited). *Review of Scientific Instruments*, 63(4):2374–2379, 1992.

[96] A. M. Halpern and E. D. Glendening. Exploring the Nature of the H_2 bond. 2. Using Ab Initio Molecular Orbital Calculations To Obtain the Molecular Constants. *Journal of Chemical Education*, 90(11):1459–1462, 2013.

[97] H. Hasegawa *et al.* Multiphoton ionization of He by using intense high-order harmonics in the soft-x-ray region. *Physical Review A*, 71:023407, 2005.

[98] W. Heitler and F. London. Wechselwirkung neutraler Atome und homöopolare Bindung nach der Quantenmechanik. *Zeitschrift für Physik*, 44(6):455–472, 1927.

[99] W. Helml *et al.* Measuring the temporal structure of few-femtosecond free-electron laser X-ray pulses directly in the time domain. *Nature Photonics*, 8(12):950–957, 2014.

[100] B. L. Henke, E. M. Gullikson, and J. C. Davis. X-ray Interactions: Photoabsorption, Scattering, Transmission, and Reflection at $E = 50 - 30,000\,\mathrm{eV}$, $Z = 1 - 92$. *Atomic Data and Nuclear Data Tables*, 54(2):181–342, 1993.

[101] U. Hergenhahn. Interatomic and intermolecular coulombic decay: The early years. *Journal of Electron Spectroscopy and Related Phenomena*, 184(3-6):78–90, 2011.

[102] O. Herrwerth. *Atomic and molecular ionization dynamics in strong IR and XUV fields probed by time-resolved coincidence spectroscopy.* PhD Thesis, Ludwig Maximilian University of Munich, 2011.

[103] I. V. Hertel and C. P. Schulz. *Atoms, Molecules and Optical Physics 1: Atoms and Spectroscopy.* Graduate Texts in Physics. Springer Berlin Heidelberg, 2015.

[104] I. V. Hertel and C. P. Schulz. *Atoms, Molecules and Optical Physics 2: Molecules and Photons - Spectroscopy and Collisions.* Graduate Texts in Physics. Springer Berlin Heidelberg, 2015.

[105] Y. Hikosaka *et al.* Multiphoton Double Ionization of Ar in Intense Extreme Ultraviolet Laser Fields Studied by Shot-by-shot Photoelectron Spectroscopy. *Physical Review Letters*, 105:133001, 2010.

[106] Y. Hikosaka *et al.* Resonances in three-photon double ionization of Ar in intense extreme-ultraviolet free-electron laser fields studied by shot-by-shot photoelectron spectroscopy. *Physical Review A*, 88:023421, 2013.

[107] A. Hofmann. *The Physics of Synchrotron Radiation.* Cambridge Monographs on Particle Physics, Nuclear Physics and Cosmology. Cambridge University Press, 2004.

[108] D. M. P. Holland, K. Codling, G. V. Marr, and J. B. West. Multiple photoionisation in the rare gases from threshold to 280 eV. *Journal of Physics B: Atomic and Molecular Physics*, 12(15):2465, 1979.

[109] J. M. Hollas. *Symmetry in molecules.* textbook series. Chapman and Hall, 1972.

[110] K. Hoshina *et al.* Dissociative ATI of H_2 and D_2 in intense soft x-ray laser fields. *Journal of Physics B: Atomic, Molecular and Optical Physics*, 39(4):813, 2006.

[111] M. R. Howells *et al.* Theory and practice of elliptically bent x-ray mirrors. *Optical Engineering*, 39:39–39–15, 2000.

[112] S. Huang *et al.* Generation of subterawatt-attosecond pulses in a soft x-ray free-electron laser. *Physical Review Accelerators and Beams*, 19:080702, 2016.

[113] R. Hubele *et al.* Electron and recoil ion momentum imaging with a magneto-optically trapped target. *Review of Scientific Instruments*, 86(3):033105, 2015.

[114] M. Hunstig. Piezoelectric Inertia Motors - A Critical Review of History, Concepts, Design, Applications, and Perspectives. *Actuators*, 6(1), 2017.

[115] T. Ishikawa *et al.* A compact x-ray free-electron laser emitting in the sub-angstrom region. *Nature Photonics*, 6(8):540–544, 2012.

[116] K. Ito, R. I. Hall, and M. Ukai. Dissociative photoionization of H_2 and D_2 in the energy region of 25-45 eV. *The Journal of Chemical Physics*, 104(21):8449–8457, 1996.

[117] O. Jagutzki *et al.* Multiple Hit Readout of a Microchannel Plate Detector With a Three-Layer Delay-Line Anode. *Nuclear Science, IEEE Transactions*, 49(5):2477–2483, 2002.

[118] T. Jahnke. *Interatomic Coulombic Decay: Experimentelle Untersuchung eines neuartigen, interatomaren Abregungsmechanismus.* PhD Thesis, University Frankfurt a.M., 2005.

[119] T. Jahnke *et al.* Experimental Observation of Interatomic Coulombic Decay in Neon Dimers. *Physical Review Letters*, 93:163401, 2004.

[120] Y. H. Jiang *et al.* EUV-photon-induced multiple ionization and fragmentation dynamics: from atoms to molecules. *Journal of Physics B: Atomic, Molecular and Optical Physics*, 42(13):134012, 2009.

[121] Y. H. Jiang *et al.* Investigating two-photon double ionization of D_2 by XUV-pump-XUV-probe experiments. *Physical Review A*, 81(5):051402, 2010.

[122] Y. H. Jiang *et al.* Temporal coherence effects in multiple ionization of N_2 via XUV pump-probe autocorrelation. *Physical Review A*, 82(4):041403, 2010.

[123] Y. H. Jiang *et al.* Tracing direct and sequential two-photon double ionization of D_2 in femtosecond extreme-ultraviolet laser pulses. *Physical Review A*, 81:021401, 2010.

[124] Y. H. Jiang *et al.* Ultrafast Extreme Ultraviolet Induced Isomerization of Acetylene Cations. *Physical Review Letters*, 105:263002, 2010.

[125] R. Johnsen and M. A. Biondi. Measurements of radiative charge-transfer reactions of doubly and singly charged rare-gas ions with rare-gas atoms at thermal energies. *Physical Review A*, 18:996–1003, 1978.

[126] B. Keitel. Private communication. 2017.

[127] B. Keitel *et al.* Hartmann wavefront sensors and their application at FLASH. *Journal of Synchrotron Radiation*, 23(1):43–49, 2016.

[128] L. V. Keldysh. Ionization in the field of a strong electromagnetic wave. *Soviet Physics Journal of Experimental and Theoretical Physics*, 20(5):1307–1314, 1965.

[129] Physik Instrumente (PI) GmbH & Co. KG. Piezoelectric inertia drives. `https://www.physikinstrumente.com/en/technology/piezoelectric-drives/piezo-inertia-drives/?_ga=2.60076525.1994746946.1510743509-850607658.1433922893`, last request: 16/11/2017.

[130] S. Khan. Free-electron lasers. *Journal of Modern Optics*, 55(21):3469–3512, 2008.

[131] A. S. Kheifets. Sequential two-photon double ionization of noble gas atoms. *Journal of Physics B: Atomic, Molecular and Optical Physics*, 40(22):F313, 2007.

[132] M. Kimura *et al.* Controlling Low-Energy Electron Emission via Resonant-Auger-Induced Interatomic Coulombic Decay. *The Journal of Physical Chemistry Letters*, 4(11):1838–1842, 2013.

[133] M. Kimura *et al.* Efficient site-specific low-energy electron production via interatomic Coulombic decay following resonant Auger decay in argon dimers. *Physical Review A*, 87:043414, 2013.

[134] K. Klünder *et al.* Probing single-photon ionization on the attosecond time scale. *Physical Review Letters*, 106(14):143002, 2011.

[135] I. S. Ko *et al.* Construction and commissioning of PAL-XFEL Facility. *Applied Sciences*, 7(5):479, 2017.

[136] R. Koopmann *et al.* In vivo protein crystallization opens new routes in structural biology. *Nature Methods*, 9:259–262, 2012.

[137] A. Kramida, Y. Ralchenko, and J. Reader and NIST ASD Team. NIST Atomic Spectra Database (ver. 5.3), [Online]. Available: `http://physics.nist.gov/asd` [2017, April 6]. National Institute of Standards and Technology, Gaithersburg, MD., 2015.

[138] J. Kunz. *Analysis of Time Delays in Photoionization of N_2 in XUV-THz Pump-Probe Experiments at FLASH.* Master Thesis, University Heidelberg, 2013.

[139] C. Kupitz *et al.* Serial time-resolved crystallography of photosystem II using a femtosecond X-ray laser. *Nature*, 513:261–265, 2014.

[140] M. Kurka. *Zwei- und Drei-Photonen Doppelionisation von Helium und Neon am Freie-Elektronen Laser in Hamburg.* Diploma Thesis, University Heidelberg, 2007.

[141] M. Kurka *et al.* Two-photon double ionization of Ne by free-electron laser radiation: a kinematically complete experiment. *Journal of Physics B: Atomic, Molecular and Optical Physics*, 42(14):141002, 2009.

[142] M. Kurka *et al.* Differential cross sections for non-sequential double ionization of He by 52 eV photons from the Free Electron Laser in Hamburg, FLASH. *New Journal of Physics*, 12(7):073035, 2010.

[143] P. Lablanquie *et al.* Appearance of interatomic Coulombic decay in Ar, Kr, and Xe homonuclear dimers. *The Journal of Chemical Physics*, 127(15):154323, 2007.

[144] P. Lambropoulos, L. A. A. Nikolopoulos, and M. G. Makris. Signatures of direct double ionization under xuv radiation. *Physical Review A*, 72:013410, 2005.

[145] M. Lampton, O. Siegmund, and R. Raffanti. Delay line anodes for microchannel-plate spectrometers. *Review of Scientific Instruments*, 58(12):2298–2305, 1987.

[146] L. Landau. Zur Theorie der Energieübertragung. ii. *Physikalische Zeitschrift der Sowjetunion*, 2:46–51, 1932.

[147] C. Langbrandtner. *Experimente zur Ionisation von atomarem Wasserstoff in Ionenstössen*. Diploma Thesis, University Heidelberg, 2007.

[148] C. J. Latimer *et al.* Photoionization of hydrogen and deuterium. *The Journal of Chemical Physics*, 102(2):722–725, 1995.

[149] C. J. Latimer *et al.* The dissociative photoionization of methane in the VUV. *Journal of Physics B: Atomic, Molecular and Optical Physics*, 32(11):2667, 1999.

[150] J. Li *et al.* Design and experimental research of an improved stick-slip type piezo-driven linear actuator. *Advances in Mechanical Engineering*, 7(9):1687814015595016, 2015.

[151] K. Liu *et al.* Enhanced dissociation of H_2^+ into highly excited states by UV pulses. *Molecular Physics*, 113(21):3247–3252, 2015.

[152] L. B. Madsen, M. Plummer, and J. F. McCann. Multiphoton ionization of H_2^+ by intense light: A comparison of Floquet and wave-packet results. *Physical Review A*, 58:456–465, 1998.

[153] E. Majorana. Atomi orientati in campo magnetico variabile. *Il Nuovo Cimento*, 9(43), 1932.

[154] M. G. Makris and P. Lambropoulos. Theoretical interpretation of multiphoton ionization of neon by soft-x-ray intense radiation. *Physical Review A*, 77:023401, 2008.

[155] B. Manschwetus *et al.* Mechanisms underlying strong-field double ionization of argon dimers. *Physical Review A*, 82:013413, 2010.

[156] S. Marburger *et al.* Experimental Evidence for Interatomic Coulombic Decay in Ne Clusters. *Physical Review Letters*, 90:203401, 2003.

[157] G. V. Marr and J. B. West. Absolute photoionization cross-section tables for helium, neon, argon, and krypton in the vuv spectral regions. *Atomic Data and Nuclear Data Tables*, 18(5):497–508, 1976.

[158] F. Martín. Ionization and dissociation using b-splines: photoionization of the hydrogen molecule. *Journal of Physics B: Atomic, Molecular and Optical Physics*, 32(16):R197, 1999.

[159] F. Martín *et al.* Single Photon-Induced Symmetry Breaking of H_2 Dissociation. *Science*, 315(5812):629–633, 2007.

[160] H. Mashiko, A. Suda, and K. Midorikawa. Focusing multiple high-order harmonics in the extreme-ultraviolet and soft-x-ray regions by a platinum-coated ellipsoidal mirror. *Applied Optics*, 45(3):573–577, 2006.

[161] A. Matsuda *et al.* Visualizing hydrogen atoms migrating in acetylene dication by time-resolved three-body and four-body coulomb explosion imaging. *Physical Chemistry Chemical Physics*, 13:8697–8704, 2011.

[162] J. Matsumoto *et al.* Asymmetry in Multiple-Electron Capture Revealed by Radiative Charge Transfer in Ar Dimers. *Physical Review Letters*, 105:263202, 2010.

[163] S. Matsuura *et al.* Characteristics of the Newly Developed MC and its Assembly. *Nuclear Science, IEEE Transactions*, 32(1):350–354, 1985.

[164] V. May and O. Kühn. *Charge and Energy Transfer Dynamics in Molecular Systems*. Wiley, 2011.

[165] B. W. J. McNeil and N. R. Thompson. X-ray free-electron lasers. *Nature Photonics*, 4:814 –821, 2010.

[166] A. McPherson *et al.* Studies of multiphoton production of vacuum-ultraviolet radiation in the rare gases. *Journal of the Optical Society of America B*, 4(4):595–601, 1987.

[167] S. Meister. *XUV Free-Electron Laser Experiments on Weakly Bound Dimers: Construction of a Water-Dimer Jet Source and Resonance-Enhanced ICD in Ne_2*. Master Thesis, University Heidelberg, 2016.

[168] L. Meitner. Über die Beta-Strahl-Spektra und ihren Zusammenhang mit der Gamma-Strahlung. *Zeitschrift für Physik*, 9(131), 1922.

[169] R. Mercier *et al.* Ion beam milling fabrication of a small off-axis ellipsoidal mirror, diffraction limited to 1 μm resolution at 14 nm. *Review of Scientific Instruments*, 72(2):1559–1564, 2001.

[170] J. P. Merlet. *Parallel Robots*. Solid Mechanics and Its Applications. Springer Netherlands, 2006.

[171] E. Mevel *et al.* Atoms in strong optical fields: Evolution from multiphoton to tunnel ionization. *Physical Review Letters*, 70(4):406–409, 1993.

[172] M. Meyer, J. T. Costello, S. Düsterer, W. B. Li, and P. Radcliffe. Two-colour experiments in the gas phase. *Journal of Physics B: Atomic, Molecular and Optical Physics*, 43(19):194006, 2010.

[173] Y. Mi *et al.* Electron-nuclear coupling through autoionizing states after strong-field excitation of H_2 molecules. *Physical Review Letters*, 118:183201, 2017.

[174] F. H. Mies. Configuration Interaction Theory. Effects of Overlapping Resonances. *Phys. Rev.*, 175:164–175, 1968.

[175] C. J. Milne *et al.* SwissFEL: The Swiss X-ray Free Electron Laser. *Applied Sciences*, 7(7):720, 2017.

[176] S. V. Milton *et al.* Exponential Gain and Saturation of a Self-Amplified Spontaneous Emission Free-Electron Laser. *Science*, 292(5524):2037–2041, 2001.

[177] T. Miteva. Private communication. 2018.

[178] T. Miteva *et al.* Interatomic Coulombic decay following resonant core excitation of Ar in argon dimer. *The Journal of Chemical Physics*, 141(6):064307, 2014.

[179] T. Miteva *et al.* Ionization satellites of the ArHe dimer. *The Journal of Chemical Physics*, 140(20):204320, 2014.

[180] R. Mitzner *et al.* Spatio-temporal coherence of free electron laser pulses in the soft x-ray regime. *Optics Express*, 16(24):19909–19919, 2008.

[181] R. Mitzner *et al.* Direct autocorrelation of soft-x-ray free-electron-laser pulses by time-resolved two-photon double ionization of He. *Physical Review A*, 80:025402, 2009.

[182] N. Miyauchi *et al.* Three-photon double ionization of Ar studied by photoelectron spectroscopy using an extreme ultraviolet free-electron laser: manifestation of resonance states of an intermediate Ar^+ ion. *Journal of Physics B: Atomic, Molecular and Optical Physics*, 44(7):071001, 2011.

[183] T. Mizuno *et al.* Time-resolved observation of interatomic excitation-energy transfer in argon dimers. *The Journal of Chemical Physics*, 146(10):104305, 2017.

[184] Y. Morishita *et al.* Experimental Evidence of Interatomic Coulombic Decay from the Auger Final States in Argon Dimers. *Physical Review Letters*, 96:243402, 2006.

[185] R. Moshammer *et al.* A 4π recoil-ion electron momentum analyzer: a high-resolution "microscope" for the investigation of the dynamics of atomic, molecular and nuclear reactions. *Nuclear Instruments and Methods in Physics Research Section B: Beam Interactions with Materials and Atoms*, 108(4):425–444, 1996.

[186] R. Moshammer *et al.* Few-Photon Multiple Ionization of Ne and Ar by Strong Free-Electron-Laser Pulses. *Physical Review Letters*, 98:203001, 2007.

[187] R. Moshammer *et al.* Second-order autocorrelation of XUV FEL pulses via time resolved two-photon single ionization of He. *Optics Express*, 19(22):21698–21706, 2011.

[188] K. Motomura *et al.* Multiple ionization of atomic argon irradiated by EUV free-electron laser pulses at 62 nm: evidence of sequential electron strip. *Journal of Physics B: Atomic, Molecular and Optical Physics*, 42(22):221003, 2009.

[189] K. Motomura *et al.* Sequential multiphoton multiple ionization of atomic argon and xenon irradiated by x-ray free-electron laser pulses from SACLA. *Journal of Physics B: Atomic, Molecular and Optical Physics*, 46(16):164024, 2013.

[190] R. Neutze *et al.* Potential for biomolecular imaging with femtosecond X-ray pulses. *Nature*, 406:752–757, 2000.

[191] C. Nicolas *et al.* Dissociative photoionization of N_2 in the 24-32 eV photon energy range. *Journal of Physics B: Atomic, Molecular and Optical Physics*, 36(11):2239, 2003.

[192] L. A. A. Nikolopoulos. Time-Dependent Theory of Angular Correlations in Sequential Double Ionization. *Physical Review Letters*, 111:093001, 2013.

[193] G. Ogurtsov and D. Dowek. *Dynamical Processes in Atomic and Molecular Physics*. Bentham Science Publishers, 2012.

[194] C. Ott *et al.* Reconstruction and control of a time-dependent two-electron wave packet. *Nature*, 516:374–378, 2014.

[195] R. H. Page *et al.* High-resolution photoionization spectrum of water molecules in a supersonic beam. *The Journal of Chemical Physics*, 88(4):2249–2263, 1988.

[196] K. Patkowski *et al.* Accurate ab initio potential for argon dimer including highly repulsive region. *Molecular Physics*, 103(15-16):2031–2045, 2005.

[197] P. M. Paul *et al.* Observation of a Train of Attosecond Pulses from High Harmonic Generation. *Science*, 292(5522):1689–1692, 2001.

[198] H. Pauly. *Atom, Molecule, and Cluster Beams I: Basic Theory, Production and Detection of Thermal Energy Beams*. Atom, Molecule, and Cluster Beams. Springer, 2000.

[199] C. Pellegrini. X-ray free-electron lasers: from dreams to reality. *Physica Scripta*, 2016(T169):014004, 2016.

[200] C. Pellegrini, A. Marinelli, and S. Reiche. The physics of x-ray free-electron lasers. *Reviews of Modern Physics*, 88:015006, 2016.

[201] T. Pfeifer *et al.* Partial-coherence method to model experimental free-electron laser pulse statistics. *Optics Letters*, 35(20):3441–3443, 2010.

[202] T. Pflüger. *Electron Impact Ionization Studies of Small Rare Gas Clusters*. PhD Thesis, University Heidelberg, 2012.

[203] M. Pitzer *et al.* Direct Determination of Absolute Molecular Stereochemistry in Gas Phase by Coulomb Explosion Imaging. *Science*, 341(6150):1096–1100, 2013.

[204] E. Plönjes. Private communication. 2017.

[205] E. Plönjes *et al.* FLASH2: Operation, beamlines, and photon diagnostics. *AIP Conference Proceedings*, 1741(1):020008, 2016.

[206] J. H. Posthumus. The dynamics of small molecules in intense laser fields. *Reports on Progress in Physics*, 67(5):623, 2004.

[207] M. Protopapas, C. H. Keitel, and P. L. Knight. Atomic physics with super-high intensity lasers. *Reports on Progress in Physics*, 60(4):389, 1997.

[208] D. Püschner. *Quantitative Rechenverfahren der Theoretischen Chemie: Ein Einstieg in Hartree-Fock, Configuration Interaction und Dichtefunktionale*. essentials. Springer Fachmedien Wiesbaden, 2017.

[209] P. Radcliffe *et al.* Single-shot characterization of independent femtosecond extreme ultraviolet free electron and infrared laser pulses. *Applied Physics Letters*, 90(13):131108, 2007.

[210] P. Radcliffe *et al.* Atomic photoionization in combined intense XUV free-electron and infrared laser fields. *New Journal of Physics*, 14(4):043008, 2012.

[211] H. Redlin *et al.* The FLASH pump-probe laser system: Setup, characterization and optical beamlines. *Nuclear Instruments and Methods in Physics Research Section A: Accelerators, Spectrometers, Detectors and Associated Equipment*, 635:S88–S93, 2011.

[212] X. Ren *et al.* Direct evidence of two interatomic relaxation mechanisms in argon dimers ionized by electron impact. *Nature Communications*, 7:11093, 2016.

[213] X. Ren *et al.* Observation of fast and slow interatomic Coulombic decay in argon dimers induced by electron-impact ionization. *Physical Review A*, 96:032715, 2017.

[214] M. Richter *et al.* Extreme Ultraviolet Laser Excites Atomic Giant Resonance. *Physical Review Letters*, 102(16):163002, 2009.

[215] R. Riedel *et al.* Single-shot pulse duration monitor for extreme ultraviolet and X-ray free-electron lasers. *Nature Communications*, 4:1731, 2013.

[216] J. Rist *et al.* A comprehensive study of Interatomic Coulombic Decay in argon dimers: Extracting R-dependent absolute decay rates from the experiment. *Chemical Physics*, 482:185–191, 2017.

[217] J. Rossbach. A VUV free electron laser at the TESLA test facility at DESY. *Nuclear Instruments and Methods in Physics Research Section A: Accelerators, Spectrometers, Detectors and Associated Equipment*, 375(1):269–273, 1996.

[218] B. Rudek. Ultra-efficient ionization of heavy atoms by intense X-ray free-electron laser pulses. *Nature Photonics*, 6:858–865, 2012.

[219] A. Rudenko *et al.* Fragmentation dynamics of molecular hydrogen in strong ultrashort laser pulses. *Journal of Physics B: Atomic, Molecular and Optical Physics*, 38(5):487, 2005.

[220] A. Rudenko *et al.* Exploring few-photon, few-electron reactions at FLASH: from ion yield and momentum measurements to time-resolved and kinematically complete experiments. *Journal of Physics B: Atomic, Molecular and Optical Physics*, 43(19):194004, 2010.

[221] J. R. Rumble, editor. *Ionization energies of atoms and atomic ions*. Internet Version. CRC Press/Taylor & Francis, Boca Raton, FL, 2018.

[222] J. R. Rumble, editor. *Work function of the elements*. Internet Version. CRC Press/Taylor & Francis, Boca Raton, FL, 2018.

[223] D. Rupp *et al.* Coherent diffractive imaging of single helium nanodroplets with a high harmonic generation source. *Nature Communications*, 8(1):493, 2017.

[224] J. D. Sadler *et al.* Compression of X-ray Free Electron Laser Pulses to Attosecond Duration. *Scientific Reports*, 5:16755, 2015.

[225] N. Saito *et al.* Evidence of radiative charge transfer in argon dimers. *Chemical Physics Letters*, 441(1-3):16–19, 2007.

[226] N. Saito and I. H. Suzuki. Multiple photoionization in Ne, Ar, Kr and Xe from 44 to 1300 eV. *International Journal of Mass Spectrometry and Ion Processes*, 115(2):157–172, 1992.

[227] K. Sakai *et al.* Electron-transfer-mediated decay and interatomic coulombic decay from the triply ionized states in argon dimers. *Physical Review Letters*, 106:033401, 2011.

[228] J. A. R. Samson and R. B. Cairns. Total Absorption Cross Sections of H_2, N_2, and O_2 in the Region 550-200 Å. *Journal of the Optical Society of America*, 55(8):1035–1035, 1965.

[229] I. Sánchez and F. Martín. Multichannel Dissociation in Resonant Photoionization of H_2. *Physical Review Letters*, 82:3775–3778, 1999.

[230] R. Santra *et al.* Interatomic Coulombic Decay in van der Waals Clusters and Impact of Nuclear Motion. *Physical Review Letters*, 85:4490–4493, 2000.

[231] C. Sarkar, S. Bhattacharyya, and S. Saha. Role of higher excited electronic states on high harmonic generation in H_2^+ - A time-independent Hermitian Floquet approach. *The Journal of Chemical Physics*, 134:024304, 2011.

[232] J. Schirmer. Beyond the random-phase approximation: A new approximation scheme for the polarization propagator. *Physical Review A*, 26:2395–2416, 1982.

[233] J. Schirmer, L. S. Cederbaum, and O. Walter. New approach to the one-particle Green's function for finite Fermi systems. *Physical Review A*, 28:1237–1259, 1983.

[234] G. Schmid. *XUV-Pump THz-Probe Experiments on Neon at the Free-Electron Laser in Hamburg.* Master thesis, University Heidelberg, 2013.

[235] P. Schmüser, M. Dohlus, and J. Rossbach. *Ultraviolet and soft X-ray free-electron lasers.* Number 229 in Springer tracts in modern physics. Springer, 2008.

[236] K. Schnorr. *XUV Pump-Probe Experiments on Diatomic Molecules: Tracing the Dynamics of Electron Rearrangement and Interatomic Coulombic Decay.* Springer Theses. Springer International Publishing, 2014.

[237] K. Schnorr *et al.* Time-Resolved Measurement of Interatomic Coulombic Decay in Ne_2. *Physical Review Letters*, 111(9):093402, 2013.

[238] K. Schnorr *et al.* Electron Rearrangement Dynamics in Dissociating I_2^{n+} Molecules Accessed by Extreme Ultraviolet Pump-Probe Experiments. *Physical Review Letters*, 113:073001, 2014.

[239] K. Schnorr *et al.* Multiple ionization and fragmentation dynamics of molecular iodine studied in IR-XUV pump-probe experiments. *Faraday Discussions*, 171:41–56, 2014.

[240] K. Schnorr *et al.* Time-resolved study of ICD in Ne dimers using FEL radiation. *Journal of Electron Spectroscopy and Related Phenomena*, 204:245–256, 2015.

[241] S. Schreiber *et al.* Status of the FEL User Facility FLASH. In *Proceedings of FEL 2011, Shanghai, China*, 2011.

[242] S. Schreiber and B. Faatz. The free-electron laser FLASH. *High Power Laser Science and Engineering*, 3, 2015.

[243] M. Schultze *et al.* Delay in photoemission. *Science*, 328(5986):1658–1662, 2010.

[244] G. Scoles. *Atomic and Molecular Beam Methods: 1.* Atomic and Molecular Beam Methods. Oxford University Press, Incorporated, 1988.

[245] S. K. Semenov and N. A. Cherepkov. Generalization of the atomic RPA method for diatomic molecules: H_2 photoionization cross-section calculation. *Chemical Physics Letters*, 291(3):375–380, 1998.

[246] A. Senftleben. *Kinematically complete study on electron impact ionisation of aligned hydrogen molecules.* PhD Thesis, University Heidelberg, 2009.

[247] A. Senftleben *et al.* Characterization of Extreme Ultra-Violet Free-Electron Laser Pulses by Autocorrelation. In K. Yamanouchi and M. Katsumi, editors, *Multiphoton Processes and Attosecond Physics*, Springer Proceedings in Physics. Springer Berlin Heidelberg, 2012.

[248] C. D. Sherrill and H. F. Schäfer III. The configuration interaction method: Advances in highly correlated approaches. volume 34 of *Advances in Quantum Chemistry*, pages 143–269. Academic Press, 1999.

[249] C. Shih-I. Floquet theory and complex quasivibrational energy formalism for intense field molecular photodissociation. *The Journal of Chemical Physics*, 75(5):2215–2221, 1981.

[250] T. Shintake *et al.* A compact free-electron laser for generating coherent radiation in the extreme ultraviolet region. *Nature Photonics*, 2(9):555–559, 2008.

[251] A. S. Simonsen *et al.* Direct two-photon double ionization of H_2. *Physical Review A*, 85:063404, 2012.

[252] S. E. Sobottka and M. B. Williams. Delay line readout of microchannel plates. *Nuclear Science, IEEE Transactions*, 35(1):348–351, 1988.

[253] A. A. Sorokin *et al.* Photoelectric Effect at Ultrahigh Intensities. *Physical Review Letters*, 99:213002, 2007.

[254] A. A. Sorokin *et al.* X-ray-laser interaction with matter and the role of multiphoton ionization: Free-electron-laser studies on neon and helium. *Physical Review A*, 75:051402, 2007.

[255] E. Spiller. *Soft X-Ray Optics*. Spie Press Vol Pm15. SPIE Optical Engineering Press, 1994.

[256] D. Stewart. A Platform with Six Degrees of Freedom. *Proceedings of the Institution of Mechanical Engineers*, 180(1):371–386, 1965.

[257] J. Stohr. *Linac Coherent Light Source II (LCLS-II) Conceptual Design Report*. 2011.

[258] S. D. Stoychev *et al.* On the doubly ionized states of Ar_2 and their intra- and interatomic decay to Ar_2^{3+}. *The Journal of Chemical Physics*, 128:014307, 2008.

[259] E. C. G. Stueckelberg. *Theorie der unelastischen Stösse zwischen Atomen*. Birkhäuser Basel, 2009.

[260] K. Suffern. *Ray Tracing from the Ground Up*. CRC Press, 2016.

[261] Z. Sun *et al.* Current Status of Single Particle Imaging with X-ray Lasers. *Applied Sciences*, 8(1):132, 2018.

[262] X. Tang, G. A. Garcia, and L. Nahon. New insights onto dissociation of state-selected O_2^+ ions investigated by double imaging photoelectron photoion coincidence: The superimposed $3^2\Pi_u$ and $c^4\Sigma_u^-$ inner-valence states. *The Journal of Chemical Physics*, 148(12):124309, 2018.

[263] The FLASH2 pump-probe laser system. `http://photon-science.desy.de/facilities/flash/beamlines/optical_laser_systems/index_eng.html`, last request: 04/12/2018.

[264] K. Tiedtke *et al.* The soft x-ray free-electron laser FLASH at DESY: beamlines, diagnostics and end-stations. *New Journal of Physics*, 11(2):023029, 2009.

[265] W. K. Tobiska and A. A. Nusinov. Status of ISO draft international standard for determining solar irradiances (DIS 21348). *Advances in Space Research*, 2005.

[266] F. Trost. *Pulse Duration Measurement at FLASH2 by Intensity Autocorrelation in Neon and Argon.* Admission Thesis, University Heidelberg, 2017.

[267] P. Tzallas *et al.* Extreme-ultraviolet pump-probe studies of one-femtosecond-scale electron dynamics. *Nature Physics*, 7:781–784, 2011.

[268] K. Ueda *et al.* Electron-ion coincidence momentum spectroscopy: Its application to ar dimer interatomic decay. *Journal of Electron Spectroscopy and Related Phenomena*, 155(1-3):113–118, 2007.

[269] J. Ullrich *et al.* Recoil-ion and electron momentum spectroscopy: reaction-microscopes. *Reports on Progress in Physics*, 66(9):1463, 2003.

[270] J. Ullrich, A. Rudenko, and R. Moshammer. Free-Electron Lasers: New Avenues in Molecular Physics and Photochemistry. *Annual Review of Physical Chemistry*, 63(1):635–660, 2012.

[271] B. Ulrich *et al.* Double-ionization mechanisms of the argon dimer in intense laser fields. *Physical Review A*, 82:013412, 2010.

[272] S. Usenko *et al.* Attosecond interferometry with self-amplified spontaneous emission of a free-electron laser. *Nature Communications*, 8:15626, 2017.

[273] G. Vampa and D. M. Villeneuve. High-harmonic generation: To the extreme. *Nature Physics*, 11(7):529–530, 2015.

[274] P. W. van Amersfoort *et al.* First lasing with FELIX. *Nuclear Instruments and Methods in Physics Research Section A: Accelerators, Spectrometers, Detectors and Associated Equipment*, 318(1):42–46, 1992.

[275] H. Wabnitz *et al.* Multiple Ionization of Rare Gas Atoms Irradiated with Intense VUV Radiation. *Physical Review Letters*, 94:023001, 2005.

[276] J. Y. Wang and D. E. Silva. Wave-front interpretation with zernike polynomials. *Applied Optics*, 19(9):1510–1518, 1980.

[277] P. Q. Wang *et al.* Highlighting the angular dependence of bond softening and bond hardening of H_2^+ in an ultrashort intense laser pulse. *Journal of Physics B: Atomic, Molecular and Optical Physics*, 38(15):L251, 2005.

[278] T. Weber *et al.* Sequential and nonsequential contributions to double ionization in strong laser fields. *Journal of Physics B: Atomic, Molecular and Optical Physics*, 33(4):L127, 2000.

[279] T. Weber *et al.* Complete photo-fragmentation of the deuterium molecule. *Nature*, 431:437–440, 2004.

[280] H. Weise. The European XFEL-Status and Commissioning. In *25th Russian Particle Accelerator Conf.(RuPAC'16), St. Petersburg, Russia, November 21-25, 2016*, pages 11–15. JACOW, Geneva, Switzerland, 2017.

[281] K. Wille. Synchrotron radiation sources. *Reports on Progress in Physics*, 54(8):1005, 1991.

[282] C. Wittig. The Landau-Zener Formula. *The Journal of Physical Chemistry B*, 109(17):8428–8430, 2005.

[283] J. L. Wiza. Microchannel plate detectors. *Nuclear Instruments and Methods*, 162(1-3):587–601, 1979.

[284] J. Wu *et al.* Multiple Recapture of Electrons in Multiple Ionization of the Argon Dimer by a Strong Laser Field. *Physical Review Letters*, 107:043003, 2011.

[285] J. Wu *et al.* Steering the Nuclear Motion in Singly Ionized Argon Dimers with Mutually Detuned Laser Pulses. *Physical Review Letters*, 110:033005, 2013.

[286] S. Yan *et al.* Observation of interatomic Coulombic decay and electron-transfer-mediated decay in high-energy electron-impact ionization of Ar_2. *Physical Review A*, 88:042712, 2013.

[287] J. J. Yeh and I. Lindau. Atomic subshell photoionization cross sections and asymmetry parameters: $1 < Z < 103$. *Atomic Data and Nuclear Data Tables*, 32(1):1–155, 1985.

[288] L. Young *et al.* Femtosecond electronic response of atoms to ultra-intense X-rays. *Nature*, 466(7302):56–61, 2010.

[289] C. Zener. Non-adiabatic crossing of energy levels. *Proceedings of the Royal Society of London A: Mathematical, Physical and Engineering Sciences*, 137(833):696–702, 1932.

[290] A. H. Zewail. Laser Femtochemistry. *Science*, 242(4886):1645–1653, 1988.

[291] A. H. Zewail. Femtochemistry: Atomic-scale dynamics of the chemical bond. *The Journal of Physical Chemistry A*, 104(24):5660–5694, 2000.

[292] Z. M. Zhang *et al.* Piezoelectric friction-inertia actuator–a critical review and future perspective. *The International Journal of Advanced Manufacturing Technology*, 62(5):669–685, 2012.

[293] K. Zhao *et al.* Tailoring a 67 attosecond pulse through advantageous phase-mismatch. *Optics Letters*, 37(18):3891–3893, 2012.

[294] T. Z. Zhao *et al.* First lasing of an echo-enabled harmonic generation free-electron laser. *Nature Photonics*, 6(6):360–363, 2012.

[295] C. Zhu, Y. Teranishi, and H. Nakamura. *Nonadiabatic transitions due to curve crossings: complete solutions of the landau-zener-stueckelberg problems and their applications*, pages 127–233. John Wiley & Sons, Inc., 2007.

[296] G. Zhu *et al.* Controlling Two-Electron Threshold Dynamics in Double Photoionization of Lithium by Initial-State Preparation. *Physical Review Letters*, 103:103008, 2009.

[297] J. Zobeley, R. Santra, and L. S. Cederbaum. Electronic decay in weakly bound heteroclusters: Energy transfer versus electron transfer. *The Journal of Chemical Physics*, 115(11):5076–5088, 2001.

Danksagung

Zum Schluss möchte ich allen Menschen danken, die mich bei dieser Arbeit, am Institut und während meines Studiums unterstützt und begleitet haben. Mein besonderer Dank gilt hierbei:

- Robert,
  der mir diese interessante Doktorarbeit am MPIK und FLASH ermöglicht hat. Deine scharfsinnige und pragmatische Art und Weise physikalischen Fragestellungen zu begegnen, hat mich nachdrücklich beeindruckt und geprägt.

- Thomas,
  in dessen Abteilung ich diese Arbeit durchführen durfte. Deine Ideen bei Diskussionen an der Beamline waren immer inspirierend und haben zu einem anderen Blickwinkel auf die Experimente angeregt.

- Kirsten,
  für ihren unermütlichen Einsatz beim Aufbau, der Durchführung, der Analyse und der Interpretation sämtlicher Experimente. Ohne dich wäre das FLASHREMI nicht das, was es heute ist. Egal wann, was und wo, dir war nie eine Frage zu viel oder ein Weg zu weit. Neben den unzähligen Strahlzeiten an FLASH, sind die C60 Experimente am LCLS und die Zeit in Kalifornien unvergesslich.

- Sven,
  für die geduldige Beantwortung aller Computer- und Softwarefragen. Deine Programmierkünste haben es mitterweile unmöglich gemacht, die Datenaufnahme oder das Go4 zum Absturz zu bringen. Auch die fachmännische Zähmung der vielen kleinen "Teufelchen", die sich immer wieder in meinen Computer eingeschlichen haben, war phenomenal.

- Severin,
  für seinen tollen Einsatz und die innovativen Ideen beim Aufbau des Experiments, insbesondere bei den Manipulationsplattformen der Spiegelkammer. Der Einbau der Spiegel wäre ohne deine ruhigen Hände sicherlich nicht so "reibungslos" über die Bühne gegangen.

- Hannes,
  für seine unerschütterliche Ruhe und das genaue Lösen von Problemen. Insbesondere möchte ich dir für die LabView-Programmierung der neuen Spiegelkammersoftware danken, ohne die sich keiner der Spiegel bewegt hätte.

- Florian,
  für seine besonnene und hilfsbereite Art, die beim Aufbau als auch bei der Durchführung der Experimente sehr angenehm war.

- Claus-Dieter,
  dessen Erfahrung, Genauigkeit und Sorgfalt beim Aufbau der Experimente von bedeutender Rolle war.

- Bernd und Christian,
  ohne deren technische Unterstützung die Durchführung der Experimente nicht möglich gewesen wäre.

- allen aktuellen und ehemaligen Mitgliedern der Abteilung "Quantendynamik und -kontrolle" am MPIK.

- der WG STRASSER,
  also Chris, Franzi und Frieder, die mir während meiner Studienzeit tolle Mitbewohner waren.

- meiner Familie,
  auf die ich mich immer verlassen kann und die mir einen festen Rückhalt gibt.

- allen meinen Freunden.

- Cora,
  die ich sehr liebe!

Eigenständigkeitserklärung

Ich versichere, dass ich diese Arbeit selbständig verfasst und keine anderen als die angegebenen Quellen und Hilfsmittel benutzt habe.

Heidelberg, ...

Georg Schmid